Technical Report

VISCOUS REGION OF TURBULENT BOUNDARY LAYER

by

Henry W. Tieleman

U. S. Army Research Grant
DA-AMC-28-043-65-G20

FLUID MECHANICS PROGRAM
ENGINEERING RESEARCH CENTER
COLLEGE OF ENGINEERING
COLORADO STATE UNIVERSITY
FORT COLLINS, COLORADO

Technical Report

VISCOUS REGION OF TURBULENT BOUNDARY LAYER

by

Henry W. Tieleman

U. S. Army Research Grant
DA-AMC-28-043-65-G20

Fluid Dynamics and Diffusion Laboratory

College of Engineering

Colorado State University

Fort Collins, Colorado

December 1967

CER67-68HWT21

ABSTRACT

VISCOUS REGION OF TURBULENT BOUNDARY LAYER

The nature of mean and turbulent motion in the viscous sublayer of a thick boundary layer with zero pressure gradient has been investigated. Measurements have been made of the mean motion, two of the turbulent velocity components, the turbulent shear stress, and spectra of the longitudinal component of the velocity fluctuation. Traverses were made through approximately one-fifth of the boundary layer, which was approximately 32 inches thick. The boundary layer was developed along the floor of the wind tunnel test section for 85 feet.

The turbulent shear stresses and the turbulence intensities were evaluated from a single rotated wire. A detailed account is given of the theory concerning the yawed wire operation. Included are corrections for the results from normal and yawed hot wires when operated in large mean velocity gradients and/or turbulence intensity gradients.

By assuming local similarity, the semilogarithmic velocity distribution can be derived. However, when local similarity is assumed, it is required that $\frac{\partial U}{\partial x} = 0$ or that $\frac{\partial \tau}{\partial y} = 0$ in the region where the law of the wall is valid. The measurements confirm the existence of a constant shear-stress region near the wall. However, the results show that the constant shear layer does not exist as far out as where the semilogarithmic velocity distribution is valid. Cross-checks were made between mean flow measurements,

turbulence measurements and wall shear-stress measurements. The results were compared with existing theories for boundary layer flow near the wall.

Energy spectra of the streamwise turbulence component indicate that the theory of local isotropy can be applied to turbulent shear flows. This is especially true when the boundary layer is allowed to develop for a relatively long time. Measurements indicate that $\sqrt{\overline{v^2}}$ is much closer to $\sqrt{\overline{u^2}}$ in magnitude as compared to the results from small scale boundary layers. This study was made in connection with a program which intends to give criteria for the modeling of atmospheric boundary layers in the wind tunnel.

ACKNOWLEDGEMENTS

The author wishes to express his sincere appreciation for the guidance and suggestions received from his advisor, Professor V. A. Sandborn.

For their comments and review of the dissertation, gratitude is extended to Dr. J. E. Cermak, Dr. H. J. Koloseus, Dr. R. D. Haberstroh, and Dr. D. P. Squier.

The author also wishes to express his appreciation for the cooperation received from the shop personnel in construction and maintenance of the equipment. Special appreciation goes to Mr. Jay Burton for the use of his calibration device. This device was used for the calibration of the pitot-static tube.

The project was supported by the Integrated Army Meteorological Wind Tunnel Research Program under Grant DA-AMC-28-043-65-G20.

TABLE OF CONTENTS

TABLE OF CONTENTS - Continued

TABLE OF CONTENTS - Continued

LIST OF TABLES

LIST OF FIGURES

LIST OF SYMBOLS

Symbol	Definition	Dimensions
A	Constant of velocity function	
A', A_1	Constants in heat-loss equation	
B	Constant of velocity function	
B' , B_1	Constants in heat-loss equation	
C	Constant of velocity function	
C_1	Constant	
c_f	Local skin-friction coefficient	
D	External height of tube, or wire diameter	L
d	Displacement	L
E	Mean voltage	V
E_o	Mean voltage at zero velocity	V
$E(k)$	Three-dimensional spectrum function	
e	Voltage fluctuation	V
$\sqrt{\overline{e^2}}$	Root mean square of voltage fluctuation	V
F	Velocity function	
F_1	Velocity function	
$F(k)$	One-dimensional wave number spectrum function	L^3/T^2
$F(n)$	One-dimensional frequency spectrum function	T
f	Velocity function	
f_s	Instantaneous side force	ML/T^2

Symbol	Definition	Dimension
G	Constant	
G*	Constant	
H	Form factor	
I	Electrical current	A
I_1	Shape parameter	
K	Factor of proportionality	
k	Wave number	L^{-1}
k_η	Wave number	L^{-1}
k_s	Wave number	L^{-1}
k_1	Coefficient	
L	Dissipation length parameter	L
L_x	Integral scale of turbulence	L
ℓ	Mixing length or wire length	L
m	Exponent	
n	Frequency	T^{-1}
P	Mean static pressure	M/LT^2
P_m	Measured total pressure	M/LT^2
P_∞	Static pressure outside boundary layer	M/LT^2
p	Pressure fluctuation	M/LT^2
$\overline{q}^2$	Sum of mean squares of velocity fluctuations	L^2/T^2
R	Operating resistance of hot wire	Ω

LIST OF SYMBOLS - Continued

Symbol	Definition	Dimension
R_a	Resistance of hot wire at room temperature	Ω
Re_x	Reynolds number based on distance x and free stream velocity	
R_x, R_y, R_z	Velocity correlation coefficients	
S_U	Sensitivity of voltage w.r.t. velocity	VT/L
S_V	Sensitivity of voltage w.r.t. angle	VT/L
T(k)	Rate of energy transfer	
T(s)	Temperature along hot wire	
t	Time	T
t_w	Fluctuation of wall-shear stress	M/LT^2
U	Local mean velocity in x direction	L/T
U'	Local instantaneous velocity in x direction	L/T
U_M	Measured mean velocity without corrections	L/T
U_m	Measured mean velocity with correction for wall proximity only	L/T
U_o	Amplitude of oscillation of infinite plate	L/T
U_{TOT}	Total velocity component	L/T
U_τ	Shear velocity	L/T
U_∞	Free stream velocity	L/T
u'	Velocity correction for wall effect	L/T
u , v , w	Velocity fluctuations in x, y, z direction	L/T

LIST OF SYMBOLS - Continued

Symbol	Definition	Dimension
$\sqrt{\overline{u^2}}, \sqrt{\overline{v^2}}, \sqrt{\overline{w^2}}$	Root mean square of velocity fluctuations	L/T
$\overline{uv}$	Time mean value of product u and v	L^2/T^2
V	Local mean velocity in y direction	L/T
x	Distance along surface from downstream edge of gravel roughness	L
y	Distance normal to surface measured from the wall	L
z	Distance normal to x and y measured from center of tunnel	L
y^*	Constant	
α	Constant	
α_1	Constant	
β_1	Constant	
β_2	Constant	
γ	Turbulent kinematic viscosity	
δ	Boundary layer thickness	L
δ^*	Displacement thickness	L
ϵ	Rate of turbulent energy dissipation	L^2/T^3
ϵ_τ	Eddy viscosity	L^2/T
ζ	Angle of attack	
η	Non-dimensional distance from wall	
θ	Momentum thickness	L
λ	Micro scale of turbulence	L

LIST OF SYMBOLS - Continued

Symbol	Definition	Dimension
λ'	Average distance between streaks	L
λ^*	Non-dimensional distance between streaks	
μ	Absolute viscosity	M/LT
ν	Kinematic viscosity	L^2/T
ρ	Mass density	M/L^3
τ	Shear stress	M/LT^2
τ_w	Wall-shear stress	M/LT^2
ϕ'	Angle with x coordinate in x-y plane	
ϕ	Mean angle with x coordinate in x-y plane	
ϕ_1	Angle change	
ψ	Angle with x coordinate in x-z plane	
ω	Rotational velocity	T^{-1}

Chapter I

INTRODUCTION

Much progress has been made in the measurement of mean and fluctuating quantities of specialized turbulent shear flows. Most of the experiments have been made in free turbulent shear flows, because the absence of solid boundaries facilitates the measurements. Fully developed turbulent flow in pipes and channels has been investigated in great detail by Laufer and other investigators. The research in two-dimensional boundary layers has been limited to relatively thin boundary layers. The characteristics and structure of the turbulent boundary layer with zero pressure gradient has been investigated by Klebanoff (19) and Townsend (39). A great deal of emphasis was placed on the turbulent energy balance in these experiments. Sandborn and Slogar (30) investigated the distribution of terms appearing in the equation of motion in a turbulent boundary layer with a progressively increasing adverse pressure gradient. The results given by Schubauer and Klebanoff (34) show that the measured skin friction is higher than the expected values. This was observed in the region where the longitudinal pressure gradient was small. Sandborn and Slogar (30) report that the shear-stress measurements by Askenas, Riddell, and Rott at Cornell University were inconsistent with the expected values. They found that even for zero pressure-gradient flow, the measured shear-stress curves show a maximum away from the wall.

An adequate model for the turbulence is not yet available. Great mathematical complexities are encountered in the solution of the Navier-Stokes equations. In order to make any progress, hypotheses have been made. These hypotheses attempt to explain the physical processes occurring in turbulent boundary-layer flow. The mixing length theory is one of such attempts. Although this theory gives good engineering results, the theory does not give any insight into the physical characteristics of the production and dissipation of turbulence. A better model for the turbulence, which is consistent with recent observations concerning the detailed structure of the turbulence, is not yet available.

In the last two or three decades the statistical treatment of homogeneous isotropic turbulence has been quite successful. Kolmogoroff's theory (1) of local similarity of the small scale eddies of the turbulence has led to this success. Much time and effort has been spent to find an acceptable theory for the transfer of energy of large eddies to the small eddies. Based on existing evidence, the eddy-viscosity transfer theory due to Heisenberg (16) has been generally accepted. Many attempts have been made to apply similar methods to the study of turbulent shear flow. The merits of these methods have not been fully assessed, due to the difficulties encountered in measuring the energy dissipation and energy transfer of the turbulent energy.

Hot wire techniques have been used quite successfully to obtain an understanding of the mechanisms which are the cause of production and dissipation of the turbulence. However the uncertainty in the measurements using hot-wire techniques is appreciable and not completely evaluated. A number of assumptions are necessary to evaluate turbulent quantities from hot-wire anemometer measurements. Under direction of Professor Sandborn (32), a long term project has been undertaken at Colorado State University to improve on existing hot-wire techniques.

In this report, experimental studies of the operation of hot wires in turbulent shear flow are described. The experiment was carried out in connection with a program which has as its goal the modeling of atmospheric boundary layers in the wind tunnel. A detailed account is made of the sensitivity of hot-wire output with respect to changes in velocity and angle of yaw. The turbulent velocity component in the y-direction and turbulent shear stress are evaluated from yawed wire measurements. Cross checks are made between turbulence measurements, mean flow measurements and wall-shear measurements. The results cast doubt on the use of the basic assumptions in the evaluation of yawed wire or crossed-wire data. The uncertainty in the measurements is especially true in the presence of large mean-velocity gradients and large gradients of turbulence intensity which occur in the viscous sublayer. Finally, energy spectra

were measured in the viscous sublayer to see how far the theory of locally isotropic turbulence can be applied to turbulent shear flow.

Chapter II

THEORETICAL BACKGROUND

2.1 The Turbulent Boundary Layer

At the turn of the century, Prandtl showed how viscosity affects the flow past a solid body. For fluids with a low viscosity, this effect is limited to a thin layer in the immediate neighborhood of the solid boundary called the boundary layer. The flow in this layer can either be turbulent or laminar. The laminar boundary-layer problem has been solved. However, at the present the problem of the turbulent boundary layer is still far from solved. Attempts have been made to utilize the information from the laminar boundary-layer theory in the turbulent layer. Although several models have been introduced, a consistent model for the turbulent flow is still missing.

The development of the boundary layer is greatly influenced by the free-stream pressure gradient and the nature of the surface roughness. In order to keep the case simple, the boundary layer developing along a smooth flat plate with zero pressure gradient is being considered. When the flow is also considered to be two-dimensional and steady, the Reynolds equations of motion reduce to

$$U\frac{\partial U}{\partial x} + V\frac{\partial U}{\partial y} = \nu\frac{\partial^2 U}{\partial y^2} - \frac{\partial \overline{uv}}{\partial y} - \frac{\partial \overline{u}^2}{\partial x} - \frac{1}{\rho}\frac{\partial P}{\partial x} \qquad (2\text{-}1)$$

and

$$\frac{\partial \overline{uv}}{\partial x} + \frac{\partial \overline{v}^2}{\partial y} = -\frac{1}{\rho}\frac{\partial P}{\partial y} \quad . \qquad (2\text{-}2)$$

Neglecting the term $\frac{\partial \overline{uv}}{\partial x}$, one may obtain after integration of (2-2)

$$\frac{P}{\rho} = \frac{P_\infty}{\rho} - \overline{v}^2 \quad . \tag{2-3}$$

The x- and z-axes coincide with the surface of the flat plate, the x-axis being in the direction of the mean flow, and y-axis is at right angles to the surface (Figure 1). The Reynolds equations of motion are the result of the statistical averaging of the general Navier-Stokes equations and the required continuity condition. A mathematical solution for these equations has not been obtained due to their non-linear character.

Differentiation of equation (2-3) with respect to x and substitution in equation (2-1) gives

$$U\frac{\partial U}{\partial x} + V\frac{\partial U}{\partial y} = -\frac{1}{\rho}\frac{\partial P_\infty}{\partial x} + \nu\frac{\partial^2 U}{\partial y^2} - \frac{\partial \overline{uv}}{\partial y} - \frac{\partial}{\partial x}(\overline{u}^2 - \overline{v}^2) \quad . \tag{2-4}$$

Experimental evidence, such as given by Sandborn and Slogar (30), indicates that the terms $\frac{\partial \overline{v}^2}{\partial x}$ and $\frac{\partial \overline{u}^2}{\partial x}$ are unimportant as long as separation is not approached. When the condition of zero pressure gradient outside the boundary layer is imposed, the governing momentum equation becomes

$$U\frac{\partial U}{\partial x} + V\frac{\partial U}{\partial y} = \nu\frac{\partial^2 U}{\partial y^2} - \frac{\partial \overline{uv}}{\partial y} = \frac{1}{\rho}\frac{\partial \tau}{\partial y} \quad . \tag{2-5}$$

The boundary conditions are

for $y = 0$: $U = V = 0$ $\overline{uv} = 0$

for $y \to \infty$: $U = U_\infty$ $\overline{uv} = 0$.

The momentum equation is to be used in combination with the continuity equation,

$$\frac{\partial U}{\partial x} + \frac{\partial V}{\partial y} = 0 \quad . \tag{2-6}$$

The momentum equation is similar to the one for the laminar boundary layer, except for the term with the correlation of u and v. The term $-\rho\overline{uv}$ is known as the turbulent shear stress in the x-direction, also known as one of the Reynolds stresses. The total shear stress is made up of a turbulent part and a viscous part. Adjacent to the solid surface the viscous shear dominates, and away from the wall the turbulent shear dominates.

The momentum equation for the turbulent boundary layer together with the continuity equation form a set of equations which is indeterminate. There are more unknowns than there are equations. The problem is now to find a relation between the Reynolds stress and the mean flow. So far, a satisfactory solution to this problem has not been obtained.

2.1.1 Flow near the wall - Close to the wall, the flow is greatly influenced by the presence of the solid boundary. When the wall is approached, the effect of viscosity gradually increases with the result that the turbulence becomes less important. Consequently, the viscous shear stress increases in importance with respect to the turbulent shear stress. At the wall itself it is assumed that the turbulent shear stress vanishes completely. The wall-shear stress can be expressed as

$\tau_w = \mu \left(\frac{\partial U}{\partial y} \right)_{y=0}$. However, the region adjacent to the wall, where the viscous shear cannot be neglected, is relatively small with respect to the entire boundary-layer thickness. This means that the change from almost completely viscous flow to fully turbulent flow takes place in the "viscous sublayer". This sublayer may be subdivided into two regions. The first is the "linear sublayer" where the velocity profile is almost linear when no longitudinal pressure gradient is present. The remainder of the viscous sublayer includes the region where the turbulent shear stress cannot be ignored. At the outer edge of the viscous sublayer, the viscous shear becomes negligibly small in comparison with the turbulent shear.

Close to the solid boundary, the mean flow must be parallel to the floor. Consequently, the magnitude of the vertical component of the mean flow is zero or nearly zero. Away from the wall, the vertical component becomes larger but it always will be small compared to the longitudinal component of the mean velocity. If $V \simeq 0$ near the wall, the continuity equation demands that $\frac{\partial U}{\partial x}$ has an extremely small magnitude. An examination of the momentum equation shows that the slope of the shear stress at the wall is zero. It will be shown later that the term $\frac{\partial \overline{uv}}{\partial y}$ is zero at the wall. This requires that at the wall the term $\nu \frac{\partial^2 U}{\partial y^2}$ is zero, which leads to the requirement that $\frac{\partial U}{\partial y}\Big|_{y=0}$ = constant. In the viscous sublayer, the viscous shear changes from a large value at the wall to a negligible magnitude at the edge of the viscous sublayer. In the same distance, the turbulent

shear stress varies from a zero value at the wall to a large value. Therefore, it can be expected that the terms $\nu \frac{\partial^2 U}{\partial y^2}$ and $\frac{\partial \overline{uv}}{\partial y}$ are large in magnitude relative to the other terms in the momentum equation. For part of the viscous sublayer it can be assumed that

$$\nu \frac{\partial^2 U}{\partial y^2} - \frac{\partial \overline{uv}}{\partial y} = \frac{1}{\rho} \frac{\partial \tau}{\partial y} \simeq 0 \quad . \tag{2-7}$$

Upon integration of this expression, one obtains immediately

$$\nu \frac{\partial U}{\partial y} - \overline{uv} = \frac{\tau}{\rho} \simeq \frac{\tau_w}{\rho} \quad . \tag{2-8}$$

This means that the total shear stress in this region is constant and equal to the wall shear stress. The simplification of the momentum equation in the viscous sublayer can be interpreted as the vanishing of the inertia terms $U \frac{\partial U}{\partial x}$ and $V \frac{\partial U}{\partial y}$. If it is known how the term $\overline{uv}$ varies with respect to y, or how $\overline{uv}$ is related to the mean flow, then equation (2-8) may be integrated to obtain the velocity distribution in the region where it applies. Data taken by Sandborn (32) show that near the edge of the viscous sublayer the terms $\frac{\partial \overline{uv}}{\partial y}$ and $\nu \frac{\partial^2 U}{\partial y^2}$ are also relatively small in magnitude. Therefore, it can be expected that all the terms in the momentum equation are of the same order of magnitude. Consequently, equation (2-8) is no longer valid, and no further information can be obtained from this simplified momentum equation.

Beyond the viscous sublayer the viscous term in the equation of motion becomes negligibly small with respect to the other terms. The momentum equation reduces to

$$U\frac{\partial U}{\partial x} + V\frac{\partial U}{\partial y} = -\frac{\partial \overline{uv}}{\partial y} = \frac{1}{\rho}\frac{\partial \tau}{\partial y} \quad . \qquad (2\text{-}9)$$

This equation is similar to the equation of motion for the laminar boundary layer with zero pressure gradient. The exception is that the turbulent term $-\frac{\partial \overline{uv}}{\partial y}$ has taken the place of the viscous term $\nu\frac{\partial^2 U}{\partial y^2}$. The difficulty with equation (2-9) is the proper specification of its boundary conditions near the wall. If similarity for the velocity distribution exists and the term $\overline{uv}$ can be related to the mean flow, a solution for equation (2-9) may be found. Measurements made by Sandborn (32) in the Army wind tunnel indicate that the magnitude of the term $U\frac{\partial U}{\partial x}$ is larger than the other inertia term $V\frac{\partial U}{\partial y}$. The term $U\frac{\partial U}{\partial x}$ is negative while $V\frac{\partial U}{\partial y}$ is positive, which results in the necessity that $\frac{1}{\rho}\frac{\partial \tau}{\partial y}$ be negative. Consequently, as soon as the inertia terms can no longer be neglected, the shear stress, $-\rho\overline{uv} = \tau$, decreases in magnitude, until it vanishes near the edge of the boundary layer.

2.1.2 Similarity considerations - For laminar boundary-layer flow with a zero-pressure gradient, the velocity profiles are all of similar shape if a dimensionless coordinate system is introduced. For this type of flow, the profiles are identical, forming the well-known Blasius profile. This similarity will be maintained regardless of the Reynolds number of the flow or of the local skin friction. A similarity where the velocity profile is a universal function of one single parameter has not been found for the turbulent boundary layer. The solution

of the equations is not as simple for turbulent boundary layers as for the laminar boundary layer. For turbulent layers the presence of the turbulence introduces a new unknown, the turbulent shear stress. The assumptions which are made for the distribution of the turbulent shear stress are based on experiment.

When an obstacle is placed in a laminar boundary layer, the velocity profiles downstream from this disturbance do not resemble the Blasius profile. However, if the layer is allowed to develop far enough downstream, the velocity profiles slowly return to the Blasius profile. In turbulent layers, the effect of upstream disturbances is wiped out quite soon, and the velocity profiles return to a "normal" boundary layer profile. This phenomenon was experimentally investigated by Klebanoff and Diehl (18). Their results show that the inner portion of the turbulent layer returns more quickly to "normal" than the outer portion of the layer. This suggests that the flow close to the wall is relatively insensitive to the flow conditions away from the wall and to the upstream conditions. On the other hand, the flow away from the boundary is affected a great deal by upstream conditions. This leads to the two-layer concept for the turbulent boundary layer, and one cannot expect the entire boundary layer to be represented by a single universal profile as is the case in laminar boundary layers. The examination of the momentum equation in the previous section seems to support the above arguments for a two-layer concept.

Rotta (29) points out that the flow near the wall is completely determined by the distance from the wall, the wall-shear stress and the kinematic viscosity. Consequently, the mean velocity distribution can be expressed by the similarity law

$$\frac{U}{U_\tau} = f\left(\frac{yU_\tau}{\nu}\right) \tag{2-10}$$

which is called the law of the wall. This means that in a region close to the wall the flow is solely determined by the conditions existing at the wall. In the previous section, it was shown how integration of the equation of motion within the viscous sublayer led to equation (2-8). A subsequent integration of this equation will lead to

$$\frac{U}{U_\tau} = \frac{yU_\tau}{\nu} + \frac{1}{\nu U_\tau} \int \overline{uv}\ dy \ . \tag{2-11}$$

This equation is valid as long as the inertia terms in the equation of motion are negligibly small with respect to the other terms, and as long as the shear stress does not vary in the y-direction. If the turbulent shear stress can be expressed in terms of local flow conditions and of the wall shear, one may expect the law of the wall to be applicable in part of the viscous sublayer. For fully developed turbulent pipe flow, the turbulent shear stress can be expressed as

$$\overline{uv} = \nu \frac{\partial U}{\partial r} + \frac{r}{a} U_\tau^2 \tag{2-12}$$

where a is the radius of the pipe and r the radial coordinate. In this case, the turbulent shear stress is expressed in terms of local flow conditions and the shear velocity. If the flow near the wall is

affected very little by the flow in the outer layer, it can be assumed that all wall flows are similar (for the case $\partial P/\partial x = 0$). Consequently, the turbulent shear stress of a turbulent boundary layer in the region near the wall can be expected to depend on local flow conditions and the wall-shear stress only. Therefore, the law of the wall is compatible with the equation of motion in a region of the viscous sublayer where the inertia terms can be ignored. Experimental data seem to confirm the existence of a similarity law in the region adjacent to the solid boundary. The results also indicate that this similarity exists not only in the viscous sublayer but extends well out into the turbulent part of the boundary layer.

If the similarity law, equation (2-10), and the continuity requirement are introduced in the momentum equation (2-5), the following expression may be obtained.

$$\mu \frac{\partial U_\tau}{\partial x}\left[\left(\frac{U}{U_\tau}\right)^2 - \frac{\partial (U/U_\tau)}{\partial \eta}\int_0^{\frac{\eta\nu}{U_\tau}} \frac{U}{U_\tau}\, d\eta\right] = \frac{\partial \tau}{\partial \eta} \qquad (2\text{-}13)$$

where $\eta = \dfrac{yU_\tau}{\nu}$. Assume the function $f\left(\dfrac{yU_\tau}{\nu}\right)$ is a truly universal function for turbulent boundary-layer flow near a smooth wall. Now one may expect that when this universal function is introduced in the momentum equation an expression is obtained which is independent of x. Only when the derivative of the wall shear stress with respect to x is a constant can true similarity of the form $\dfrac{U}{U_\tau} = f\left(\dfrac{yU_\tau}{\nu}\right)$ exist. For flow within the viscous sublayer, the

term $U\frac{\partial U}{\partial x}$ was neglected, which is basically the same as neglecting the term $\frac{\partial U_\tau}{\partial x}$. The true similarity can only exist for very large Reynolds numbers where U_τ is nearly constant. The term $u\frac{\partial U_\tau}{\partial x}$ is extremely small in magnitude so that the deviation of the shear stress from its value at the wall is necessarily small. Therefore, the assumption of constant shearing stress leads to similarity. Even in regions where the wall-shear stress is no longer constant with distance away from the wall, similarity of prescribed form may still be successful.

Rotta (29) argues that the self preservation of the velocity profile in a turbulent boundary layer is a justification for the assumption of local similarity. The flow is locally similar when the distribution of the mean flow quantities, expressed in non-dimensional form, is independent of the x-coordinate. From experiment and general dimensional arguments, it was generally found that a similarity law for the outer part of the turbulent boundary layer exists when $\frac{U-U_\infty}{U_\tau}$ and $\frac{y}{\delta}$ are used as coordinates.

$$\frac{U-U_\infty}{U_\tau} = F\left(\frac{y}{\delta}\right) . \qquad (2\text{-}14)$$

This similarity law for the fully turbulent part of the boundary layer is usually referred to as the velocity-defect law. However, there is a great difference between the velocity-defect law and the Blasius profile. For the laminar layer, the ratios of momentum thickness and

displacement thickness with respect to the boundary layer thickness are constants. For turbulent layers, the ratios of the various thicknesses will vary with the skin friction. The velocity-defect law cannot be valid close to the wall, since the flow next to the wall must depend on the absolute value of the velocity and not on the velocity defect. For small values of y, the function $F(y/\delta)$ approaches $\frac{U_\infty}{U_\tau}$. At the other end of the boundary layer when y approaches δ, the function $F(y/\delta)$ goes to zero. For turbulent boundary-layer flow with a zero-pressure gradient, $F(y/\delta)$ is only a truly universal function when $\frac{U_\infty}{U_\tau}$ is independent of x or when $\frac{\partial U_\tau}{\partial x} = 0$. Previously, it was concluded that $\frac{\partial U_\tau}{\partial x}$ had to be at least a constant in order that the law of the wall should be truly a similarity law. In order to have complete similarity throughout the turbulent boundary layer, the shear velocity must be independent of x. In other words, the wall shear stress must be a constant in the x direction. These conditions can only be approached when the boundary layer Reynolds number, Re_x, has a very large value. These high Reynolds numbers have never been obtained in laboratory experiments. However, experimental results indicate that the variables $\frac{U}{U_\tau}$ and $\frac{yU_\tau}{\nu}$ correlate the data in the wall region, and the variables $\frac{U-U_\infty}{U_\tau}$ and $\frac{y}{\delta}$ correlate the data in the outer region. There is an overlap region where both methods of correlation can be used successfully. This leads to the conclusion that some relation between the two sets of parameters

must exist. Clauser (5) has shown that only when the function F and f are logarithmic a region of overlap can exist. For this region one has

$$\frac{U - U_\infty}{U_\tau} = A \log \left(\frac{y}{\delta} \right) + B \qquad (2\text{-}15)$$

and

$$\frac{U}{U_\tau} = A \log \left(\frac{yU_\tau}{\nu} \right) + C \quad . \qquad (2\text{-}16)$$

Equation (2-16) is only valid in the overlap region where the flow is fully turbulent. Adjacent to the wall in the linear sublayer, the velocity varies linearly with the distance away from the wall. Between the overlap region and the linear sublayer there exists a transition region where the velocity profile blends smoothly from the linear form into the semilogarithmic form.

In the large Army wind tunnel, the velocity profiles also show similarity in the outer region when $\frac{U}{U_\infty}$ is plotted versus y/δ. This similarity can be written as $\frac{U}{U_\infty} = F_1 \left(\frac{y}{\delta} \right)$. Close to the wall, the law of the wall applies. Again there is an overlap region where both correlation methods can be used. The correlation for the outer region can be written in the following form.

$$\frac{U}{U_\tau} = \frac{U_\infty}{U_\tau} \; F_1 \left(\frac{y}{\delta} \right) \quad . \qquad (2\text{-}17)$$

The law of the wall can be written as

$$\frac{U}{U_\tau} = f \left(\frac{y}{\delta} \cdot \frac{\delta U_\tau}{\nu} \right) \quad . \qquad (2\text{-}18)$$

The two functions F_1 and f should give similar results in the overlap region. This means that the multiplication of $\frac{\delta U_\tau}{\nu}$ inside the function f must have the same effect as the multiplicative term $\frac{U_\infty}{U_\tau}$ outside the function F_1. In order to satisfy this requirement, one has to resort to a power law. In the overlap region one has

$$\frac{U}{U_\infty} = \left(\frac{y}{\delta}\right)^m \tag{2-19}$$

and

$$\frac{U}{U_\tau} = C_1 \left(\frac{yU_\tau}{\nu}\right)^m \quad . \tag{2-20}$$

However, equation (2-20) does not apply all the way to the wall. Near the wall, the values of m and C_1 must be unity.

2.1.3 Hypothetical relations - Several empirical hypotheses have been introduced based on some simplified model of the turbulent motion. The older hypotheses are still being used at the present despite their shortcomings. This is due to the fact that the perfect relation is still missing.

Boussinesq was the first to attack the problem by introducing the concept of eddy viscosity. He assumed that the turbulent stresses act in the same way as the viscous stresses, implying that the turbulent stresses are proportional to the velocity gradient. The coefficient of proportionality was called the "eddy viscosity" and was defined by

$$-\rho \overline{uv} = \rho \epsilon_\tau \frac{\partial U}{\partial y} \quad . \tag{2-21}$$

The velocity profile of the turbulent boundary layer can now be calculated, provided a satisfactory distribution of the "eddy viscosity" can be assumed.

Prandtl tried to relate the turbulent shear stress to the mean velocity, using the characteristics of the turbulence. Analogous to the kinetic theory of gases, Prandtl assumed that the coefficient of "eddy viscosity" was equal to the product of a "mixing length" and some suitable velocity (mixing length theory). According to this theory, the turbulent shear stress in a turbulent boundary layer can now be calculated from the following expression.

$$-\rho\,\overline{uv} = \rho\,\ell^2 \left|\frac{\partial U}{\partial y}\right| \frac{\partial U}{\partial y} \quad . \tag{2-22}$$

The relation between the eddy viscosity and the mixing length becomes

$$\epsilon_\tau = \ell^2 \left|\frac{\partial U}{\partial y}\right| \quad . \tag{2-23}$$

Again, assumptions have to be made on the distribution of the mixing length in the turbulent boundary layer. Several assumptions concerning the distribution of the mixing length, ℓ , and the eddy viscosity have been tabulated by Rotta (29). However, no general relation for the distribution of these parameters is available. The most serious objection to the validity of these theories is that eddy viscosity as well as mixing length depend solely on the local flow conditions.

Townsend (40) has pointed out that the local conservation of turbulent kinetic energy supports these objections. Because the turbulent motion cannot sustain itself, a continuous supply of energy is

necessary to maintain the motion. The necessary energy is obtained from the mean flow working against the turbulent stresses. The local energy balance depends not only on the local production and dissipation of turbulent energy, but also on the transport of turbulent energy to and from other parts of the turbulent flow. Consequently, it can be expected that the local turbulent shear stress depends not only on local flow conditions, but also on conditions at other parts of the flow.

Prandtl assumed that the mixing length at relatively short distances from the wall had to be proportional to the distance y. He also assumed that outside the viscous layer the viscous shear can be neglected, so that $\tau = -\rho \overline{uv}$. Additionally he had to assume that the shear stress in this region is constant, so that $\tau = \tau_w$. Substitution of these assumptions in equation (2-22) leads, after integration to the well known equation for the velocity distribution, to

$$\frac{U}{U_\tau} = A \log \left(\frac{y U_\tau}{\nu} \right) + C \quad . \tag{2-24}$$

This expression for the velocity is similar to the expression obtained by Clauser in the overlap region, where either the law of the wall or the velocity defect law correlate the data. Since equation (2-24) was derived for the region where viscous shear can be neglected, one may expect this equation to fail in the immediate neighborhood of the wall. Approaching the wall, the logarithmic term tends to go to minus infinity. The same logarithmic velocity distribution is obtained when it is assumed that the eddy viscosity is proportional to the distance from the wall such that

$$\epsilon_\tau = \frac{1}{A} U_\tau y \quad . \tag{2-25}$$

2.1.4 Hypothetical relations for the viscous sublayer - Most of the existing hypothetical relations cover only part of the region where the law of the wall is applicable. Hama (14) obtained a universal relation between the dimensionless mixing length and the dimensionless distance from the wall. By the use of experimental results, the following universal relation was found,

$$\frac{\ell U_\tau}{\nu} = \left(\alpha' \frac{y U_\tau}{\nu} \right)^2 , \qquad (2\text{-}26)$$

where α' is a numerical constant of approximately 0.1. This universality seems to be valid for the entire viscous sublayer. Outside the viscous sublayer, Hama's solution is connected smoothly to the logarithmic velocity distribution. The most complete relations for the turbulent velocity profile near the wall are given by van Driest (7) and Reichardt (28). Both authors give continuous relations for the mean velocity and the turbulent shear stress for the regions where the law of the wall is expected to be valid.

Van Driest points out that the turbulence near the wall is expected to be damped by viscosity. This viscous effect is estimated by considering Stoke's second problem. This problem involves the solution of the Navier-Stokes equations for the flow about an infinite flat plate which is harmonically oscillated parallel to itself in an infinite fluid. The solution of this problem has the form of a damped harmonic

oscillation with an amplitude of $U_o e^{-y/G}$. Here U_o is the amplitude of the oscillation of the infinite plate. Consider the case where the plate is fixed and the fluid oscillates relative to the plate. The damping effect of the plate on the fluid can be expected to be of the form $(1 - e^{-y/G})$. In order to describe the velocity distribution in the viscous sublayer, Prandtl's mixing length needs to be modified to

$$\ell = \frac{y}{A} \left(1 - e^{-y/G}\right) \tag{2-27}$$

or in dimensionless form

$$\frac{\ell U_\tau}{\nu} = \frac{yU_\tau}{\nu A} \left[1 - \exp - \left(\frac{yU_\tau}{\nu G^*}\right)\right] . \tag{2-28}$$

This result can be substituted in the expression for the shear stress

$$\tau = \mu \frac{\partial U}{\partial y} + \rho \ell^2 \left(\frac{\partial U}{\partial y}\right)^2 . \tag{2-29}$$

With the assumption that $\tau = \tau_w$ the following relation for the mean velocity distribution is obtained.

$$\frac{U}{U_\tau} = \int_0^{\frac{yU_\tau}{\nu}} \frac{2d\left(\frac{yU_\tau}{\nu}\right)}{1 + \sqrt{1 + 4\left(\frac{\ell U_\tau}{\nu}\right)^2}} . \tag{2-30}$$

From empirical fitting of the experimental results, van Driest chose as magnitudes for the constants, $\frac{1}{A} = 0.4$ and $G^* = 26$.
For $\frac{yU_\tau}{\nu} > 100$, the above expression becomes

$$\frac{U}{U_\tau} = 5.24 + 5.75 \log \left(\frac{yU_\tau}{\nu}\right) . \tag{2-31}$$

For $\frac{yU_\tau}{\nu} < 5$ the velocity distribution becomes

$$\frac{U}{U_\tau} = \frac{yU_\tau}{\nu} \quad . \tag{2-32}$$

Therefore, this assumed distribution for the mixing length seems to fit the experimental data quite well for the entire region where the law of the wall is applicable. Reichardt (28) points out that, approaching the wall, the turbulent shear stress varies proportionally to y^3. Consequently, the eddy viscosity must vary in a similar manner, since in the linear sublayer $\frac{\partial U}{\partial y}$ is a constant. The eddy viscosity should change smoothly from a third power distribution to a linear distribution. Reichardt, therefore, proposes to use the following expression

$$\epsilon_\tau = \frac{\nu}{A}\left[\frac{yU_\tau}{\nu} - y^* \tanh\left(\frac{yU_\tau}{\nu} / y^*\right)\right] \quad . \tag{2-33}$$

It can be shown that

$$\frac{d\left(\frac{U}{U_\tau}\right)}{d\left(\frac{yU_\tau}{\nu}\right)} = \frac{\frac{\tau}{\tau_w}}{1 + \frac{\epsilon_\tau}{\nu}} \quad . \tag{2-34}$$

By substitution and assuming that $\frac{\tau}{\tau_w} = 1$,

$$\frac{U}{U_\tau} = \int_0^{\frac{yU_\tau}{\nu}} \frac{d\left(\frac{yU_\tau}{\nu}\right)}{1 + \frac{1}{A}\left[\frac{yU_\tau}{\nu} - y^* \tanh\left(\frac{yU_\tau}{\nu} / y^*\right)\right]} \tag{2-35}$$

where A and y^* are constants. Reichardt gives $A = 2.5$ and $y^* = 11$ as the best values for these constants.

Assuming that the simplified momentum equation (2-8) is valid, and introducing the concept of mixing length, one obtains in non-dimensional form

$$\frac{\partial(U/U_\tau)}{\partial\left(\frac{yU_\tau}{\nu}\right)} + \left(\frac{\ell U_\tau}{\nu}\right)^2 \left[\frac{\partial(U/U_\tau)}{\partial\,\frac{yU_\tau}{\nu}}\right]^2 = 1 \quad . \tag{2-36}$$

The solution of this quadratic equation is

$$\frac{U}{U_\tau} = \int_0^{\frac{yU_\tau}{\nu}} \frac{-1 + \sqrt{1 + 4\left(\frac{\ell U_\tau}{\nu}\right)^2}}{2\left(\frac{\ell U_\tau}{\nu}\right)^2}\, d\left(\frac{yU_\tau}{\nu}\right) \quad . \tag{2-37}$$

This equation is the same as equation (2-30). Van Driest's relation is compatible with the momentum equation for the viscous sublayer. However, this relation seems to fit the data also quite well in the region where the inertia terms can no longer be neglected.

2.1.5 Distribution of the turbulent quantities - No theory is available for the distribution of the turbulent velocities in the boundary layer. Only a solution of the total energy equation can give the distribution of the three turbulent velocity components. Measurement of these quantities have not led to any similarity. Usually these measured turbulent velocities are presented in the same nondimensional manner as the mean velocity is presented in the region where the law of the wall is valid. Measurements by Plate and Sandborn (27) of the longitudinal turbulent velocity in the Army wind tunnel seem quite insensitive to a variation in x distance. This is true when the turbulent

velocity is plotted with respect to the local velocity instead of with respect to free stream velocity or local shear velocity.

The distribution of the turbulent shear stress is of importance, since this term appears in the equation of motion. The turbulent velocities appear only in the energy equation, and so far there has been no need for a hypothetical relation for these velocity components Only in the immediate vicinity of the wall can predictions be made about the distribution of the turbulent shear stress and the turbulent velocity components. Rotta (29) shows, by means of the continuity requirement and the condition of no slip at the wall, how the term $\overline{uv}$ varies in this region. It is assumed that the three turbulent velocity components are zero at the wall.

$$u = v = w = 0 \quad , \quad \text{for} \quad y = 0 \quad . \tag{2-38}$$

This requires that

$$\frac{\partial u}{\partial x} = \frac{\partial u}{\partial z} = \frac{\partial v}{\partial x} = \frac{\partial v}{\partial z} = \frac{\partial w}{\partial x} = \frac{\partial w}{\partial z} = 0 \quad , \text{ for } \quad y = 0 \quad . \tag{2-39}$$

From the continuity equation it follows that

$$\frac{\partial v}{\partial y} = - \frac{\partial u}{\partial x} - \frac{\partial w}{\partial z} = 0 \quad , \quad \text{for} \quad y = 0 \quad . \tag{2-40}$$

However, the derivatives $\frac{\partial u}{\partial y}$ and $\frac{\partial w}{\partial y}$ and higher order derivatives with respect to y have finite values for $y = 0$. Therefore, the term $\frac{\partial^2 v}{\partial y^2}$ may have a finite value at the wall. Using these requirements, it turns out that the first two derivatives of $\overline{uv}$ with respect to y are zero at the wall. The third derivative may have a finite value at the wall, since the term $\overline{\frac{\partial u}{\partial y} \frac{\partial^2 v}{\partial y^2}}$

does not necessarily vanish at the wall. Close to the wall, the shear stress can be assumed to be equal to the wall shear stress

$$\tau = \mu \frac{\partial U}{\partial y} - \rho \overline{uv} \simeq \tau_w \quad . \tag{2-41}$$

The mean velocity close to the wall can be obtained by integration of the above expression and the use of the assumption that $\frac{\partial^3 \overline{uv}}{\partial y^3}$ is not zero for $y = 0$. The result is

$$U = \frac{\tau_w y}{\mu} + \frac{1}{24\,\nu} \left(\frac{\partial^3 \overline{uv}}{\partial y^3} \right)_{y=0} y^4 + \ldots . \tag{2-42}$$

The streamwise velocity fluctuation $u(x , y , z , t)$ is assumed to be analytic everywhere in the flow field. Consequently, this velocity fluctuation may be expanded in a Taylor's series. If $u(x , y , z , t)$ is expanded about a point y_1 close to the boundary, the fluctuation of u at $y = 0$ is, of course, zero. Therefore,

$$0 = u(x, y_1, z, t) + y_1 \frac{\partial}{\partial y} \left[u(x, y_1, z, t)\right] + \frac{1}{2} y_1^2 \frac{\partial^2}{\partial y^2} \left[u(x, y_1, z, t)\right] + \ldots . \tag{2-43}$$

Similarly for the vertical fluctuation

$$0 = v(x, y_1, z, t) + y_1 \frac{\partial}{\partial y} \left[v(x, y_1, z, t)\right] + \frac{1}{2} y_1^2 \frac{\partial^2}{\partial y^2} \left[v(x, y_1, z, t)\right] + \ldots . \tag{2-44}$$

or

$$u = - y \frac{\partial u}{\partial y} - \frac{1}{2} y^2 \frac{\partial^2 u}{\partial y^2} - \ldots \ldots \tag{2-45}$$

and

$$v = - y \frac{\partial v}{\partial y} - \frac{1}{2} y^2 \frac{\partial^2 v}{\partial y^2} - \ldots \ldots \tag{2-46}$$

Now in the immediate neighborhood of the wall

$$\overline{uv} = y^2 \overline{\frac{\partial u}{\partial y} \frac{\partial v}{\partial y}} + \frac{1}{2} y^3 \overline{\frac{\partial u}{\partial y} \frac{\partial^2 v}{\partial y^2}} + \frac{1}{2} y^3 \overline{\frac{\partial^2 u}{\partial y^2} \frac{\partial v}{\partial y}} + \frac{1}{4} y^4 \overline{\frac{\partial^2 u}{\partial y^2} \frac{\partial^2 v}{\partial y^2}} + \ldots\ldots . \quad (2\text{-}47)$$

It follows from the continuity equation that $\frac{\partial v}{\partial y} = 0$ for $y = 0$. Therefore, the terms $\overline{\frac{\partial u}{\partial y} \frac{\partial v}{\partial y}}$ and $\overline{\frac{\partial^2 u}{\partial y^2} \frac{\partial v}{\partial y}}$ are zero at the wall. The turbulent shear stress is clearly zero at the wall, as well as the first and second derivative with respect to y . However, the third derivative may have a finite value at the wall. According to this scheme it turns out that

$$\left.\frac{\partial^3 \overline{uv}}{\partial y^3}\right|_{y=0} = 9 \left.\overline{\frac{\partial u}{\partial y} \frac{\partial^2 v}{\partial y^2}}\right|_{y=0} . \quad (2\text{-}48)$$

This result is similar to the one obtained by Rotta except for the magnitude of the coefficient.

As shown before, the streamwise fluctuating velocity component may be expressed as

$$u = - y \frac{\partial u}{\partial y} - \frac{1}{2} y^2 \frac{\partial^2 u}{\partial y^2} - \ldots\ldots . \quad (2\text{-}49)$$

This leads to an expression for the mean square of the velocity fluctuation in the x-direction of

$$\overline{u^2} = y^2 \overline{\left(\frac{\partial u}{\partial y}\right)^2} + y^3 \overline{\frac{\partial u}{\partial y} \frac{\partial^2 u}{\partial y^2}} + \frac{1}{4} y^4 \overline{\left(\frac{\partial^2 u}{\partial y^2}\right)^2} + \ldots . \quad (2\text{-}50)$$

The velocity distribution adjacent to the wall is

$$\frac{U}{U_\tau} = \frac{yU_\tau}{\nu} \tag{2-51}$$

The distribution of the turbulent velocity with respect to the local velocity can be written as

$$\frac{\sqrt{\overline{u^2}}}{U} = \left[\frac{\overline{\left(\frac{\partial u}{\partial y}\right)^2}}{U_\tau^4/\nu^2} + \frac{y\,\overline{\frac{\partial u}{\partial y}\,\frac{\partial^2 u}{\partial y^2}}}{U_\tau^4/\nu^2} + \frac{\frac{1}{4}\,y^4\,\overline{\left(\frac{\partial^2 u}{\partial y^2}\right)^2}}{U_\tau^4/\nu^2} + \cdots \right]^{\frac{1}{2}} . \tag{2-52}$$

Therefore, at the wall the ratio $\frac{\sqrt{\overline{u^2}}}{U}$ does not vanish.

At the wall

$$\left.\frac{\sqrt{\overline{u^2}}}{U}\right|_{y=0} = \frac{\mu\sqrt{\overline{\left(\frac{\partial u}{\partial y}\right)^2}}}{\tau_w} \neq 0 \tag{2-53}$$

or

$$\left.\frac{\sqrt{\overline{u^2}}}{U}\right|_{y=0} = \frac{\sqrt{\overline{t_w^2}}}{\tau_w} \neq 0 \quad , \tag{2-54}$$

where t_w is the fluctuating part of the shear stress at the wall. Experimental evidence given by Mitchell and Hanratty (24) indicates that the ratio of the rms of the fluctuating velocity, $\sqrt{\overline{u^2}}$, and the mean velocity is 0.32 at the wall.

2.1.6 The energy equations - In a turbulent boundary layer, energy must be brought into the layer to make up for the loss of energy due to dissipation. The necessary energy is obtained from the mean flow working against the shear stresses. The shear stresses also act as the energy-transfer agent, so energy is transferred from the

outer layer of the turbulent boundary layer to the wall region. Here, some of this transferred mean energy is converted into turbulent energy, and finally most of this energy is dissipated into heat. Some of the turbulent energy produced near the wall is diffused to the outer layer to maintain its turbulence level. The conversion and transport of energy in the turbulent boundary layer is necessary because the turbulent motion cannot sustain itself. Therefore, a continuous supply of turbulent energy is necessary at all parts of the turbulent boundary layer to maintain the turbulent motion.

The energy balance at any point in the turbulent boundary layer can be discussed best by consideration of the individual terms in the energy equations for the mean flow and the turbulent flow. The mean flow energy equation for the turbulent boundary layer may be obtained by multiplying the boundary layer momentum equation by U, to obtain

$$U^2 \frac{\partial U}{\partial x} + UV \frac{\partial U}{\partial y} = \nu U \frac{\partial^2 U}{\partial y^2} - U \frac{\partial \overline{uv}}{\partial y} \quad . \tag{2-55}$$

Rearranging, one obtains

$$U \frac{\partial \left(\frac{1}{2} U^2 \right)}{\partial x} + V \frac{\partial \left(\frac{1}{2} U^2 \right)}{\partial y} - \overline{uv} \frac{\partial U}{\partial y} + \frac{\partial (U \overline{uv})}{\partial y}$$

$$- \frac{\nu}{2} \frac{\partial^2 U^2}{\partial y^2} + \nu \left(\frac{\partial U}{\partial y} \right)^2 = 0 \quad . \tag{2-56}$$

The first two terms represent the loss of kinetic energy of the mean flow due to its retardation, or the work done per unit time per unit

mass by the inertia forces. The term $\overline{uv}\ \frac{\partial U}{\partial y}$ is the well known production term. The next two terms represent the transfer of energy. The last term indicates the direct dissipation. Near the wall where the inertia terms in the momentum equation can be neglected, the mean flow energy equation reduces to

$$\frac{1}{2}\ \nu\ \frac{\partial^2 U^2}{\partial y^2} - \frac{\partial(U\ \overline{uv})}{\partial y} = \nu\left(\frac{\partial U}{\partial y}\right)^2 - \overline{uv}\ \frac{\partial U}{\partial y} = \frac{\tau_w}{\rho}\ \frac{\partial U}{\partial y} \quad . \quad (2\text{-}57)$$

In this region, the energy required to balance the loss due to direct dissipation and production of turbulent energy has to come from the outer part of the boundary layer. Outside the viscous sublayer where the viscous shear stress in the momentum equation can be neglected, the mean flow energy equation reduces to

$$U\ \frac{\partial\left(\frac{1}{2}\ U^2\right)}{\partial x} + V\ \frac{\partial\left(\frac{1}{2}\ U^2\right)}{\partial y} - \overline{uv}\ \frac{\partial U}{\partial y} + \frac{\partial\ (U\ \overline{uv})}{\partial y} = 0 \quad . (2\text{-}58)$$

For most of this region, the production term is small compared to the other terms. The energy lost from the mean flow, due to its retardation, is practically all transferred toward the wall. Closer to the wall this energy, transferred from the outer layer, is either converted into turbulent energy or dissipated directly into heat.

The turbulent energy equation can be obtained by multiplying the complete Navier-Stokes equations for the x, y, and z-direction by u, v, and w, respectively. After taking the mean values and summation of the three equations, the following equation for the conservation of turbulent energy is obtained [Rotta (29)].

$$U \frac{\partial \left(\frac{1}{2} \overline{q^2}\right)}{\partial x} + V \frac{\partial \left(\frac{1}{2} \overline{q^2}\right)}{\partial y} + (\overline{u^2} - \overline{v^2}) \frac{\partial U}{\partial x} + \overline{uv} \frac{\partial U}{\partial y}$$

$$+ \frac{\partial}{\partial y} \overline{v \left(\frac{1}{2} q^2 + \frac{p}{\rho}\right)} + \epsilon - \nu \frac{\partial^2}{\partial y^2} \left(\frac{1}{2} \overline{q^2} + \overline{v^2}\right) = 0 \qquad (2\text{-}59)$$

where $\overline{q^2} = \overline{u^2} + \overline{v^2} + \overline{w^2}$. The first two terms are indicative of the convective transport of turbulent energy by the mean flow. The next two terms are the production terms. The production terms $\overline{u^2} \frac{\partial U}{\partial x}$ and $\overline{v^2} \frac{\partial U}{\partial x}$ are an order of magnitude smaller than the term $\overline{uv} \frac{\partial U}{\partial y}$. The difference of these small terms may be neglected in well developed turbulent boundary layers. The term $\frac{\partial}{\partial y} \overline{v \frac{1}{2} q^2}$ represents the diffusion of turbulent energy in the y-direction by turbulent motion. The term $\frac{1}{\rho} \frac{\partial(\overline{vp})}{\partial y}$ is indicative of the transfer of energy under the action of pressure gradients. The turbulent dissipation is indicated by the term ϵ . The last term represents the transport of turbulent energy in the y-direction by the viscous forces. The mean flow-energy equation and the turbulent energy equation can be added to obtain the total energy equation in which the production term will disappear. The total energy equation indicates that the loss of mean-flow energy and turbulent energy is transported to other parts of the boundary layer where it is dissipated into heat by viscosity.

2.2 Turbulent Scales and Structure

The concept of local isotropy proposed by Kolmogoroff (1) has been generally accepted. However, these concepts can only be applied to flows whose Reynolds number is large enough. Unfortunately, the theory does not predict when the Reynolds number is large enough so that local isotropy can be assumed.

The theory of local isotropy states that the small-scale structure of the turbulence has statistical properties, which are invariant under a rotation of the coordinate system and under a reflection with respect to the coordinate planes. The low wave-number part of the energy spectrum consists of the energy-containing eddies. The structure of these eddies is determined by the mean flow from which they receive their energy. However, on the other end of the wave-number scale, the turbulence may be expected to be statistically independent of the energy-containing turbulence. This means that the small scale structure of the turbulence is statistically isotropic and approximately homogeneous in space and time. When this is the case, it may be assumed that local isotropy exists. So far, the statistical theory of turbulence has been limited to the treatment of homogeneous isotropic turbulence. Since no shear can be present in this type of turbulence, the turbulence must decay in the course of time. The basic concepts obtained from the study of homogeneous isotropic turbulence are introduced into the study of turbulent shear flow.

All of the dissipation of energy occurs in the high wave-number region of the energy spectrum. This region of the spectrum where the energy is dissipated contributes only a negligible amount to the total turbulence energy. During the decay process, the energy-containing eddies lose their energy to the smaller dissipative eddies. The energy of the turbulent motion is dissipated into heat through the action of viscosity. Due to the inertial forces, energy is passed on from the larger eddies to smaller ones, and these in turn break down into still smaller ones, and so on. When this process takes place, the viscous forces become gradually more effective in dissipating the energy. The effect of these two types of forces tends to bring about an equilibrium distribution of the energy. When the energy-containing eddies and the dissipative eddies are sufficiently far apart in size, the smaller eddies are in a state of statistical equilibrium and are independent of their origin. The properties of this type of turbulent motion can be summarized as follows:

1. For sufficiently large Reynolds numbers, the turbulent motion can be locally isotropic, independent of whether the energy-containing eddies are isotropic or not. This part of the spectrum is called the universal equilibrium range.

2. The eddies at the high wave-number range of the spectrum are governed by the viscous forces. It is in this region of the spectrum that the turbulent energy is dissipated into heat.

3. The eddies which lie between the two ends of the spectrum are not affected by viscosity. The statistical properties of this part of the turbulent motion depend solely on the rate of energy dissipation. This range in the spectrum is called the inertial subrange, which is the lower wave-number range of the universal equilibrium range.

A three-dimensional spectral density function $E(k)$ is defined, such that the total turbulent energy per unit mass is

$$\frac{1}{2}\left(\overline{u^2} + \overline{v^2} + \overline{w^2}\right) = \int_0^\infty E(k)\, dk \quad . \tag{2-60}$$

The time rate of change of the spectral-density function, $E(k)$, at any wave number consists of two parts. The rate of energy transfer, which is the net transfer of energy from one wave number to another, is denoted by $T(k)$. The second term is the rate of viscous dissipation which turns out to be $-2\nu k^2 E(k)$. Thus,

$$\frac{\partial}{\partial t} E(k) = T(k) - 2\nu k^2 E(k) \quad , \tag{2-61}$$

which is the dynamic equation for the energy-spectrum function, $E(k)$. Here is one equation with two unknowns, E and T. The theory of isotropic turbulence is concerned with the relationship between T and E. Several so-called "physical" transfer theories have been proposed. On the basis of existing evidence the eddy viscosity-transfer theory due to Heisenberg (16) seems to be more successful than the other theories. Heisenberg's theory is based on

the assumption that the mechanism which is governing the energy transfer is similar to the one governing the viscous dissipation. Consider the rate of change of energy from wave numbers zero to k; then

$$\frac{\partial}{\partial t} \int_0^k E(k')\, dk' = \int_0^k T(k')\, dk' - 2\nu \int_0^k k'^2 E(k')\, dk' \quad . \quad (2\text{-}62)$$

Heisenberg argued that the motion associated with wave numbers from zero to k can be considered as the mean motion. This is in contrast with the motion associated with wave numbers from k to infinity which is considered to be the turbulent motion. Analogous to turbulent boundary-layer flow, there is transfer of energy from the mean motion to the turbulent motion. Continuing the analogy, Heisenberg assumed that there exists a turbulent kinematic viscosity γ such that

$$\int_0^k T(k')\, dk' = -2\gamma \int_0^k k'^2 E(k')\, dk' \quad . \quad (2\text{-}63)$$

As was pointed out, γ depends on the smaller eddies and therefore can be expected to be of the form of an integral over all wave numbers larger than k. By dimensional reasoning, Heisenberg obtained the following expression for the turbulent kinematic viscosity:

$$\gamma(k) = \alpha \int_k^\infty \sqrt{\frac{E(k')}{k'^3}}\, dk' \quad (2\text{-}64)$$

where α is a constant. By substitution, one obtains the following expression:

$$\frac{\partial}{\partial t} \int_0^k E(k')\, dk' = -2 \left[\nu + \alpha \int_k^\infty \sqrt{\frac{E(k'')}{k''^3}}\, dk'' \right] \int_0^k k'^2 E(k')\, dk' . \tag{2-65}$$

A solution for the dynamic equation has been obtained for the universal equilibrium range. At wave numbers in this range, the term $\frac{\partial}{\partial t} E(k)$ is small, and consequently, the term

$$\frac{\partial}{\partial t} \int_k^\infty E(k)\, d\, k$$

is negligibly small as compared to the term

$$\frac{\partial}{\partial t} \int_0^\infty E(k)\, d\, k \quad .$$

This is true because the total energy lies almost entirely in the region of small wave numbers. The total transfer across the entire wave-number range is clearly equal to zero,

$$\int_0^\infty T(k)\, d\, k = 0 \quad . \tag{2-66}$$

It was pointed out that

$$\frac{\partial}{\partial t} \int_0^k E(k')\, d\, k' >> \frac{\partial}{\partial t} \int_k^\infty E(k')\, d\, k' \tag{2-67}$$

or

$$\frac{\partial}{\partial t} \int_0^k E(k')\, d\, k' \simeq \frac{\partial}{\partial t} \int_0^\infty E(k')\, d\, k' \quad . \tag{2-68}$$

Substituting these assumptions in the dynamic equation, one obtains

$$\frac{\partial}{\partial t} \int_0^\infty E(k')\, dk' = -2\nu \int_0^\infty k'^2 E(k')\, dk' = -\epsilon \qquad (2\text{-}69)$$

where ϵ is the total dissipation of turbulence per unit mass. Hence,

$$\epsilon = 2\left[\nu + \alpha \int_k^\infty \sqrt{\frac{E(k'')}{k''^3}}\, dk''\right] \int_0^k k'^2 E(k')\, dk' \,. \qquad (2\text{-}70)$$

The solution of this equation gives the expression for the spectrum in the universal equilibrium range,

$$E(k) = \left(\frac{8\epsilon}{9\alpha}\right)^{2/3} k^{-5/3} \left[1 + \frac{8\nu^3}{3\alpha^2\epsilon} k^4\right]^{-4/3} . \qquad (2\text{-}71)$$

The equation contains only the parameters ϵ and ν as was predicted by Kolmogoroff's theory. When $k << \left(\frac{3\alpha^2\epsilon}{8\nu^3}\right)^{1/4}$, the spectrum function reduces to the appropriate form for the inertial subrange of the spectrum

$$E(k) = \left(\frac{8}{9\alpha}\right)^{2/3} \epsilon^{2/3} k^{-5/3} . \qquad (2\text{-}72)$$

As was predicted, this part of the energy spectrum depends solely on the rate of dissipation of energy per unit mass. For large wave numbers when $k >> \left(\frac{3\alpha^2\epsilon}{8\nu^3}\right)^{1/4}$, the spectrum function reduces to

$$E(k) = \left(\frac{\alpha}{2\nu^2}\right)^2 \epsilon^2 k^{-7} . \qquad (2\text{-}73)$$

The presence of the dissipation and the kinematic viscosity in this expression is in agreement with Kolmogoroff's prediction for the high wave-number region of the energy spectrum.

Since no three-dimensional energy spectrum has been measured, it is necessary to transform this equation to the one-dimensional form. Using the theory of isotropic turbulence, these two spectrum functions can be related by the following expression:

$$E(k) = \frac{1}{2} k^2 \frac{\partial^2 F(k)}{\partial k^2} - \frac{1}{2} k \frac{\partial F(k)}{\partial k} \quad , \tag{2-74}$$

[Hinze (17)] . $F(k)$ is the one-dimensional spectrum of the longitudinal velocity fluctuations and defined as

$$\int_0^\infty F(k)\, dk = \overline{u^2} \quad . \tag{2-75}$$

The one-dimensional spectrum function for the universal equilibrium range becomes

$$F(k) = \frac{18}{55} \left(\frac{8\epsilon}{9\alpha}\right)^{2/3} k^{-5/3} \left[1 + \frac{8\nu^3}{3\alpha^2\epsilon} k^4\right]^{-4/3} . \tag{2-76}$$

Define a wave number k_η , such that $k_\eta = \left(\frac{3\alpha^2\epsilon}{8\nu^3}\right)^{1/4}$. This wave number lies in the intermediate range of the spectrum where both the inertia forces and viscosity play a role. By substitution, the one-dimensional spectrum function becomes

$$F(k) = \frac{18}{55} \left(\frac{2^{13}}{3^7}\right)^{1/4} \frac{(\epsilon\nu^5)^{1/4}}{\alpha^{3/2}} \left(\frac{k}{k_\eta}\right)^{-5/3} \left[1 + \left(\frac{k}{k_\eta}\right)^4\right]^{-4/3} . \tag{2-77}$$

For $\frac{k}{k_\eta} < 1$ $\quad F(k) = \frac{18}{55} \left(\frac{2^{13}}{3^7}\right)^{1/4} \frac{(\epsilon\nu^5)^{1/4}}{\alpha^{3/2}} \left(\frac{k}{k_\eta}\right)^{-5/3}$. (2-78

$$\text{For } \frac{k}{k_\eta} > 1 \qquad F(k) = \frac{18}{55}\left(\frac{2^{13}}{3^7}\right)^{1/4} \frac{(\epsilon\nu^5)^{1/4}}{\alpha^{3/2}} \left(\frac{k}{k_\eta}\right)^{-7} \quad . \tag{2-79}$$

However, k_η contains the constant α, whose magnitude is not exactly known, but is of the order of 0.5 (3). This constant may vary, depending on whether local isotropy exists or not. For the purpose of representing the data, the wave number k_s is used, where $k_s = \left(\frac{\epsilon}{\nu^3}\right)^{1/4}$, and $k_\eta \simeq 0.57\ k_s$. The data can be represented in non-dimensional form using the non-dimensional coordinates, $\frac{F(k)}{(\epsilon\nu^5)^{1/4}}$ and $\frac{k}{k_s}$.

The rate of turbulent energy per unit mass in isotropic turbulence is given by

$$\epsilon = 2\nu \int_0^\infty k^2\ E(k)\ dk \quad . \tag{2-80}$$

In terms of the longitudinal one-dimensional spectrum, F(k), this expression becomes

$$\epsilon = 15\nu \int_0^\infty k^2\ F(k)\ dk \quad . \tag{2-81}$$

Taylor (38) showed how the longitudinal correlation coefficient and $\frac{U\ F(n)}{2\sqrt{2\pi}}$ are Fourier transforms of each other.

$$F(n) = \frac{4}{U} \int_0^\infty R_x \cos \frac{2\pi nx}{U}\ dx \tag{2-82}$$

and

$$R_x = \int_0^\infty F(n) \cos \frac{2\pi nx}{U}\ dx \tag{2-83}$$

where $F(n)$ is defined such that $\int_0^\infty F(n)\,dn = 1$, and R_x is the longitudinal correlation coefficient. The definition for the micro-scale given by Taylor (37) is

$$\frac{1}{\lambda^2} = 2 \operatorname*{Lim}_{x \to 0} \left(\frac{1 - R_x}{x^2} \right) \quad . \tag{2-84}$$

Expanding $\cos \frac{2\pi n x}{U}$ in a Taylor series and substituting in the expression for the micro-scale, one obtains

$$\frac{1}{\lambda^2} = \frac{4\pi^2}{U} \int_0^\infty n^2 F(n)\,dn \quad . \tag{2-85}$$

The rate of dissipation per unit mass for isotropic turbulence is

$$\epsilon = 7.5\,\nu \overline{\left(\frac{\partial u}{\partial y}\right)^2} = 15\,\nu \overline{\left(\frac{\partial u}{\partial x}\right)^2} \quad . \tag{2-86}$$

Taylor (37) showed how the micro-scale can be expressed in terms of turbulent velocities

$$\lambda^2 = \frac{\overline{u^2}}{\overline{\left(\frac{\partial u}{\partial x}\right)^2}} \quad . \tag{2-87}$$

Therefore,

$$\epsilon = 15\,\nu \frac{\overline{u^2}}{\lambda^2} \tag{2-88}$$

and

$$\epsilon = 15\,\nu\,\overline{u^2}\,\frac{4\pi^2}{U} \int_0^\infty n^2 F(n)\,dn \quad . \tag{2-89}$$

By introduction of the wave-number notation, such that $k = \frac{2\pi n}{U}$ and $F(k) = \frac{U}{2\pi}\,\overline{u^2}\,F(n)$, one obtains

$$\epsilon = 15\nu \int_0^\infty k^2 F(k)\, dk \quad . \tag{2-90}$$

This result, of course, is similar to equation (2-81), which was obtained through the dynamic equation for isotropic turbulence. The micro-scale of the turbulence can now be obtained by measuring the one-dimensional energy spectrum.

$$\frac{\overline{u^2}}{\lambda^2} = \int_0^\infty k^2 F(k)\, dk \quad . \tag{2-91}$$

The other method is to assume that Taylor's hypothesis is valid, so that

$$\lambda^2 = \frac{U^2\, \overline{u^2}}{\overline{\left(\frac{\partial u}{\partial t}\right)^2}} \quad . \tag{2-92}$$

Liu and Sandborn (21) have shown that the time-derivative of the turbulent signal can be measured relatively, simply by means of a differentiating circuit.

Taylor (37) defined the average size of the eddies as

$$L_x = \int_0^\infty R_x\, dx \quad , \tag{2-93}$$

where R_x is the longitudinal correlation coefficient. By the use of equation (2-82) and $n = 0$, one obtains

$$F(n)_{n=0} = \frac{4}{U} \int_0^\infty R_x\, dx = \frac{4L_x}{U} \quad . \tag{2-94}$$

In wave-number notation, the macro-scale of turbulence is

$$L_x = \frac{\pi}{2\,\overline{u^2}}\, F(k)_{k=0} \quad . \tag{2-95}$$

To determine the magnitude of $F(k)_{k=0}$, the method of extrapolation as suggested by Sandborn and Slogar (30) has been used. Dryden (9) shows that, for large Re_λ ($Re_\lambda = \frac{\sqrt{\overline{u^2}}\,\lambda}{\nu}$), the energy spectrum can be expressed as

$$F(n) = \frac{4\,\frac{L_x}{U}}{1 + \frac{4\pi^2 n^2 L_x}{U^2}} \tag{2-96}$$

or

$$F(n) = \frac{F(n)_{n=0}}{1 + \frac{4\pi^2 n^2 L_x}{U^2}} \tag{2-97}$$

or

$$F(k) = \frac{F(k)_{k=0}}{1 + k^2\,\frac{\pi}{2\,\overline{u^2}}\,F(k)_{k=0}} \quad . \tag{2-98}$$

The value of $F(k)_{k=0}$ was determined by fitting this parabolic equation to a faired curve through the lower wave-number region of the energy spectra.

Chapter III

EXPERIMENTAL EQUIPMENT AND PROCEDURES

The entire experiment was performed in the large U.S. Army Meteorological wind tunnel located in the Fluid Dynamics and Diffusion Laboratory at Colorado State University. The purpose of this experiment was to survey the part of the boundary layer close to the rigid boundary. In this region the viscous contribution to the total shear cannot be neglected. The experiment and procedures used for this study will be discussed in the following sections. A special chapter will be devoted to analysis of data and corrections.

3.1 Wind Tunnel

Measurements were taken in the boundary layer which was allowed to develop along the floor of the 100 foot long test section of the large U.S. Army Meteorological Wind Tunnel (Figure 2). The cross section of the tunnel is approximately 6 by 6 feet, and the ceiling of this facility is adjustable in order to control the streamwise pressure gradient. The wind tunnel is of the recirculating type, and the air speed in the tunnel is controlled by means of a variable speed, variable pitch aircraft propeller. The air temperature in the tunnel can be maintained at a constant level by means of an air conditioning system. Detailed description of this facility has been given by Plate and Cermak (26). Damping screens and a 3:1 entrance contraction

produce a low free stream turbulence intensity, $\sqrt{\overline{u^2}}/U_\infty$. This turbulence intensity ranges from 0.00015 to 0.00027 at a free stream velocity of 20 fps to 80 fps, respectively (Figure 3). All measurements were made at a distance of 85 feet downstream from the inlet of the test section. The measurements were made in a vertical plane along the center of the tunnel. The boundary layers along the walls of the tunnel were artificially tripped by a saw tooth fence preceded by a four foot section of 1/2 inch gravel fastened around the perimeter of the tunnel just downstream from the entrance contraction. The roughness at the entrance of the test section was found to thicken the boundary layer providing the experimenter with a thicker boundary layer to explore. Another advantage of inducing transition as far upstream as possible was to have as long a period of turbulence development toward equilibrium as possible.

3.2 Instrumentation

3.2.1 Actuator - Measuring probes were moved vertically through the boundary layer by means of a precision actuator (Figure 4). The position of the probes could be changed accurately at one thousandth of one inch intervals. This was achieved by means of a counter which was connected to the actuator movement. The position of the probes with respect to the tunnel floor was determined from the counter reading when the probes were touching the floor. With a set of magnifying lenses it could be determined whether the

probes were touching the tunnel floor or not. The total movement of the actuator was approximately 7.5 inches. The actuator was fastened at the center of the tunnel floor, outside the tunnel, so that only the measuring probes were allowed to protrude into the boundary layer.

3.2.2 Pitot-static tube and static-pressure tube - Mean velocity measurements were made with a flattened total-head tube with a square cut end (Figure 5). This probe had a width of 0.050 inch, a height of 0.030 inch and a wall thickness of 0.005 inch. The total head tube, which was mounted directly to the actuator, could be moved by the actuator vertically away from the floor up to a distance of approximately 7.5 inches. The free stream velocity was measured by a standard 1/8 inch diameter pitot-static tube (Figure 5) at the axis of the tunnel perpendicular above the position where all other measurements were made. The pressure of the total-head tube in the boundary layer was measured against the pressure of the static openings of the pitot-static tube in the free stream.

An attempt was made to measure the static-pressure distribution in the boundary layer. For this purpose a static tube with a rounded nose and two static openings (0.016 inch diameter) was used. The diameter of the static tube was 0.043 inch and was 1.5 inch long (Figure 5). The static openings were located 0.75 inch from the rounded nose, opposite from each other in a plane parallel to the floor of the tunnel. The static pressure in the boundary layer

was measured against the pressure of the static openings of the pitot-static tube in the free stream.

The pressure probes were connected to a Trans-sonics Equibar Type 120B electronic manometer by means of plastic tubing.

3.2.3 Hot-wire probes - Turbulence measurements were made by means of the hot-wire technique. The hot wire, made of platinum coated tungsten with a diameter of 0.0002 inch, was operated by a constant temperature hot-wire anemometer designed at Colorado State University by Finn and Sandborn (11). The rms of the output signal of the hot-wire anemometer was measured by a true rms meter. After appropriate amplification, the fluctuating part of the output of the anemometer was recorded on F.M. magnetic tape. The streamwise velocity fluctuation, $\sqrt{\overline{u^2}}$, was measured by means of a hot wire which was positioned parallel to the floor and perpendicular to the axis of the tunnel. The 0.050 inch long wire was soldered at each end to a support which in turn protruded from a 3/32 inch diameter ceramic probe (Figure 5). The ceramic probe was placed in a vertical position and could be moved by the precision actuator in the same manner as described before.

A rotating single wire of similar description was used to measure the turbulent shear stress. The wire could be rotated 360^0 in a plane parallel to the flow and perpendicular to the floor of the tunnel. The movement of the rotating wire was provided by a low-speed electric motor, and the position of the wire was determined

from the output of a 10-turn potentiometer which was rotated by the motor through a set of connecting gears.

3.2.4 Wall shear-stress meter - The wall shear stress was measured by means of a pivoting-element gauge (Figure 6). The wall shear stress which acts on the horizontal surface of the pivoting element is magnified by a lever arm. The surface on which the shear stress acts was mounted flush with the floor of the tunnel; its center coincided with the point where all other measurements were made. The instrument was positioned in such a way that the surface was only allowed to move in a streamwise direction. The shear meter is used as a null-reading instrument. The measurements are obtained only when the horizontal surface of the pivoting element is flush with the floor of the tunnel. The pivoting element with the horizontal surface is held by two strain-gauge wires each at one side of the pivoting element. One end of each of the strain-gauge wires is fastened to the pivoting element just above the point of rotation; the other ends are fastened to micrometer movements. The micrometers are able to stress or relax each wire independently. When the wall shear acts on the horizontal surface of the pivoting element the strain-gauge wires are stressed accordingly. The different magnitudes of strain can be read as voltage changes from a Wheatstone bridge. The shear meter was calibrated with known weights, each of them representing a certain shear stress. One wire was used as a reference wire to determine the position of the horizontal surface. The other, called

the active wire, was used to determine the force on the horizontal surface. Two "dummy" wires of about the same length as the active and reference wires were mounted inside the instrument to act as temperature compensators. The active wire and one of the dummy wires made up two adjacent arms in one Wheatstone bridge; the reference wire and the other dummy wire made up two adjacent arms in the second Wheatstone bridge. If the two wires are identical in dimensions and resistance and if both wires are subjected to the same changes in temperature during the course of measurement, the resistance changes due to temperature alone will be the same for both of the Wheatstone bridge arms in which the wires are located. The effects of temperature on the wires will cancel and will not influence the measurement of the stress-induced strain at the active wires.

Sigmund Cohn #479 platinum alloy was used as the wire material; the wire diameter was 0.0005 inch and the resistance of each wire was approximately 350 ohms. The strain sensitivity of this type of wire was higher than that of most other materials and since it also had a relatively high tensile strength this type of wire material made an excellent sensing element for unbounded strain gauges. The pivoting element was supported by means of two tungsten-carbide pivots, each positioned carefully in sapphire vee-jewel bearings. The pivots were precision ground to match the geometry of the bearings in order to obtain almost frictionless movement. Each

Wheatstone bridge was excited by 4 volts D.C. The bridges were balanced with each wire in an unstressed state.

With the pivoting element locked in the null position, the reference wire was stressed until an unbalance of 0.004 volt was obtained. The pivoting element was then unlocked and allowed to move due to either the calibration weights or due to the actual wall-shear stress acting on the horizontal surface. The active wire was then stressed until the pivoting element had returned to the null position as indicated by a 0.004 volt unbalance of the Wheatstone bridge containing the reference wire. With the pivoting element in the null position, the unbalance of the Wheatstone bridge containing the active wire was read. This voltage is indicative of the streamwise shear force on the horizontal surface of the pivoting element. The calibration curve (Figure 7) shows a linear relationship between output voltage of the bridge and shear stress. The instrument was mounted in the wind tunnel, and shear measurements were obtained for a range of Reynolds numbers.

3.2.5 Integrator - Some mean quantities are difficult to establish due to the fact that these quantities are made up of a mean component and a fluctuating component. Therefore, it is necessary to employ some averaging method over a sufficient length of time so that a reliable average can be obtained. This can be done graphically or electronically. The graphic integration is not desirable for the evaluation of great quantities of data. An alternate approach is to

use an electronic integrating circuit that was developed at the Fluid Dynamics and Diffusion Laboratory at Colorado State University (Figures 8 and 9). The integrator uses an operational amplifier technique to insure proper frequency response. The integrator can easily be calibrated by introducing a non-fluctuating voltage from a power supply or a non-fluctuating output of the transducer for the required period of time. The integrator was used in conjunction with mean velocity measurements, space correlations, and turbulence spectra.

3.2.6 Differentiating circuit - A differentiating circuit was used to measure the average size of the smallest eddies. The differentiating circuit (Figure 10) was used to evaluate $\overline{\left(\frac{\partial u}{\partial t}\right)^2}$. This quantity was obtained indirectly from the calibration curve of the differentiating circuit (Figure 11). The output voltage of the differentiating circuit is equal to the product of a constant and the time derivative of the input voltage,

$$e_{out} = R.C. \frac{\left[d\ e_{in}(t)\right]}{dt} \quad . \qquad (3\text{-}1)$$

The magnitude of the constant, R.C. , depends on the magnitude of the resistive and capacitive elements in the differentiating circuit. The frequency response of the differentiating circuit was better than 2000 cps. To prevent saturation, the hot-wire signal from the F.M. tape had to be attenuated so that the magnitude of the rms of the signals was between 0.01 and 0.05 volt.

Chapter IV

CALIBRATION PROCEDURES AND DATA REDUCTION

4.1 Mean-Velocity Measurements

Instrumentation used to obtain measurements in a boundary layer especially close to the solid boundary needs to be small in dimensions, and the position needs to be known accurately. There are many uncertainties about pressure measurements in the immediate neighborhood of a solid boundary. Velocity measurements require corrections for low Reynolds number, turbulence and velocity-gradient effects and wall proximity. For boundary-layer exploration, the diameter of the total-head tube needs to be small because of the steep velocity gradient close to the solid boundary. In order to reduce the dimensions of the total-head tube in the direction normal to the wall, the tube is flattened to a roughly rectangular shape.

4.1.1 Calibration of pitot-static tube - A 1/8-inch diameter pitot-static tube was used as a standard throughout the entire experiment. It was calibrated against a temperature compensated heat-transfer device, which in turn was calibrated in a whirling-arm apparatus.

The temperature compensated heat-transfer device consists of two thin quartz crystals, each having a diameter of 0.5 inch. The crystals will resonate at their natural frequency, which depends on the geometry of the crystals and the environment in which the crystals

are placed. One of the crystals was provided with a resistive material, which acted as a heating device. A change in temperature will cause a comparable change in the natural frequency of the crystal. When the heated crystal is subjected to forced convection, the change in natural frequency will become a function of the velocity. The second crystal acts as a compensator for ambient temperature changes. The natural frequency of the reference crystal is subtracted from the natural frequency of the heated crystal. This difference in frequency is a function of the temperature difference between the two crystals. Assuming that other conditions do not alter the response of the crystals, their temperature difference will then be a function of the velocity when normal atmospheric conditions are maintained. The two crystals were mounted in a holder side by side and placed in the whirling-arm apparatus. The heating current to the active crystal was kept constant at 26 milliamperes throughout the experiment. The crystals were placed in such a position that they were parallel to the path of the probe. The probe was placed at the end of a horizontal arm which rotated about a vertical axis. The horizontal distance between the vertical axis and the heated crystal was 34.25 inches. The circumferential speed of the probe could be altered from 1 fps to 32 fps by using different pulley combinations. A set of brushes was used to transmit the electrical signal from the crystals to the electrical counter outside the whirling-arm apparatus. The horizontal arm rotated above a cylindrical tank. The probe rotated in the tank through

a narrow circular slit in the cover of the tank. Due to the motion of the probe, a circulatory air flow was set up in the tank, moving in the same direction as the probe. Two vertical baffles were placed in the tank to decrease the strength of this circulatory flow. Nevertheless, a correction for this flow had to be made. This correction was obtained by means of a pitot-static tube inserted horizontally through the side of the tank as close to the path of the heated crystals as possible. The dynamic pressure due to the swirl created by the moving probe is plotted against the calculated speed of the probe in Figure 12. The probe speed was obtained by counting the number of revolutions of the horizontal arm in a certain time span. The radial distance at which the heated crystal is mounted away from the vertical axis can be measured. Consequently, the speed at which the heated probe is traveling can be obtained. The relative velocity of the heated crystal with respect to the air in the immediate vicinity was obtained by subtracting the swirl velocity from the probe speed. The calibration curve of the probe (Figure 13) shows the frequency difference as a function of the relative velocity of the probe.

The next step was to calibrate the pitot-static tube against the crystal probe. This was done in the free stream outside the boundary layer in the wind tunnel. The probe was placed in the tunnel in such a way that the crystals were parallel to the mean flow. It was found that the maximum permissible error in alignment of the crystal probe was approximately $\pm 5^0$ up to a velocity of 32 fps. This was the

maximum obtainable speed with the swirling arm. Trying to get higher speeds resulted in slippage of the belt connecting the pulleys, with the result that the speed of the probe became unstable. The calibration of the 1/8-inch pitot-static tube against the crystal probe is shown in Figure 14. The results of this calibration show that the velocity head as measured by the pitot-static tube needed a correction of 1.73%.

4.1.2 Viscous effects on total-head tubes - MacMillan (22) has pointed out that the tube Reynolds number for total-head tubes at low velocity may become so small that viscous effects are important. He found that at low speeds the pressure in the circular total-head tube was greater than the true total pressure. For flattened, blunt nosed total-head tubes, the pressure in the tube is higher than the true total pressure as long as the tube Reynolds number based on the internal height is less than 15. For tube Reynolds numbers between 15 and 800, the pressure in the tube is lower than the true total pressure. For tube Reynolds numbers higher than 800, the effect of viscosity on total-head tubes can be neglected. The total-head tube used in the boundary layer exploration was calibrated in the free stream against the standard pitot-static tube, so that this calibration takes into account the viscous effects. It turned out that there was no detectable difference between the pressure as measured by the standard pitot-static tube and the pressure differential between the total-head tube

and the static pressure from the standard pitot-static tube (over the range of velocities encountered in the boundary layer).

The effects of shear, wall proximity and turbulence intensity on the velocity head readings in the boundary layer still need to be determined. Calibration took place in the center of the tunnel where the turbulence intensity is extremely small, the shear stress is zero and the wall is too far away to have any effect on velocity head readings.

4.1.3 The effect of shear on total-head tubes - MacMillan (23) found that the effect of shear alone could be conveniently expressed as a displacement d of the effective center of the tube toward the region of higher velocity. MacMillan found that the value of d/D was 0.15, independent of Reynolds number and velocity gradient. D is defined as the external height of the tube, which in the present case was 0.030 inch. Therefore, the displacement of the tube toward the region of higher velocity is 0.0045 inch.

4.1.4 Wall proximity effects on total-head tubes - MacMillan (23) gives a relation for wall effect expressed as a function of y/D. In this case, y is defined as the distance from the rigid boundary to the center of the total-head tube. When $y/D < 2$, this correction must be applied. It is expressed as a correction u' to be added to the measured velocity U_M. MacMillan also found that u'/U_M depends only on y/D and is independent of a Reynolds number, the latter being based on the shear velocity and the external height of the tube (Figure 15).

4.1.5 Turbulence effects on total-head tubes - Goldstein (13) obtained the following expression for the quantity which is measured by the total-head tube in a turbulent stream.

$$P_m = P + \frac{1}{2} \rho U^2 + \frac{1}{2} \rho \left(\overline{u^2} + \overline{v^2} + \overline{w^2} \right) . \qquad (4-1)$$

The following discussion is partly taken from the analysis Landweber (20) made for the effect of turbulence on total-head tubes.

The equation of motion for a two-dimensional incompressible boundary layer normal to the rigid boundary can be reduced to

$$\frac{\partial \overline{v^2}}{\partial y} = - \frac{1}{\rho} \frac{\partial P}{\partial y} . \qquad (4-2)$$

Integration with respect to y gives

$$\overline{v^2} = - \frac{P}{\rho} + \text{constant} . \qquad (4-3)$$

The constant of integration is determined by the condition outside the boundary layer, $\overline{v^2} = 0$, and the local mean pressure equals the external pressure P_∞. It follows then that

$$\frac{P}{\rho} = \frac{P_\infty}{\rho} - \overline{v^2} . \qquad (4-4)$$

When this equation is introduced in the expression for the quantity measured by a total-head tube, one obtains the following:

$$P_m = P_\infty + \frac{1}{2} \rho U^2 + \frac{1}{2} \rho \left[\overline{u^2} - \overline{v^2} + \overline{w^2} \right] . \qquad (4-5)$$

Putting $P_m - P_\infty = \frac{1}{2} \rho U_m^2$ and substituting in the above equation

$$\frac{1}{2} \rho U_m^2 = \frac{1}{2} \rho U^2 + \frac{1}{2} \rho \left(\overline{u^2} - \overline{v^2} + \overline{w^2} \right) \qquad (4\text{-}6)$$

or

$$U = U_m \left(1 - \frac{\overline{u^2}}{U_m^2} + \frac{\overline{v^2}}{U_m^2} - \frac{\overline{w^2}}{U_m^2} \right)^{\frac{1}{2}} . \qquad (4\text{-}7)$$

Assuming $\overline{v^2}/U_m^2$ equal to $\overline{w^2}/U_m^2$, the expression for the effect of turbulence on a total-head tube becomes

$$U = U_m \left(1 - \frac{\overline{u^2}}{U_m^2} \right)^{\frac{1}{2}} \qquad (4\text{-}8)$$

Hinze (17) questions Goldstein's expression for the quantity measured by the total-head tube. In the first place, due to the finite dimensions of the opening of the total-head tube, deviations from Goldstein's relation may be expected. Goldstein's expression might be correct if the tube were infinitely small in dimensions so that the total-head opening can be considered a true point. When the dimensions of this opening are of the same order of magnitude as the lateral or the vertical scale of the turbulence, a correction must be made. This correction is necessary because of the resulting averaging that will inevitably occur. The opening of the total-head tube had the following dimensions: height = 0.020 inch, width = 0.040 inch. The lateral integral scale of the turbulence close to the floor was measured to be 0.049 inch and 0.030 inch at free-stream velocities

of 20 fps and 40 fps, respectively. These scales are of the same order of magnitude as the width of the opening of the total-head tube. However, total-head tubes, which are too small and too fragile, are impractical for use in thick boundary layers.

Secondly, Hinze maintained that lateral and vertical velocity fluctuations will not produce the same effect as predicted by Goldstein. No systematic investigation is available concerning the effect of tube dimensions and the effect of turbulence on total-head tube readings. In view of this, and since no better method is available, the correction outlined above is applied to all the measurements with the total-head tube. Figure 16 shows the magnitude of the correction as applied to velocity measurements in the boundary layer at free-stream velocities of 20 fps, 30 fps, and 40 fps, respectively.

4.1.6 Mean-velocity calculations - The mean velocities are obtained through the following steps:

1. Obtain the pressure differential in mm Hg from the calibration curve for the integrator output versus Trans-sonics reading (Figure 17).
2. Apply the correction for the Trans-sonics from the calibration curve of the Meriam micromanometer versus Trans-sonics (Figure 18).
3. Apply the total-head tube correction of 1.73%, as obtained by calibration of total-head tube versus standard pitot-static tube.

4. Calculate the measured velocity from

$$\Delta h_{true} = \frac{1}{2} \rho U_M^2 \qquad (4\text{-}9)$$

5. Make correction for wall proximity. Obtain y/D and enter into Figure 15, to obtain $\frac{u'}{U_M}$, where u' is the correction for wall effect to be added to the measured velocity U_M

$$U_m = U_M + u' \quad . \qquad (4\text{-}10)$$

6. Correction for turbulence effects.

$$U = U_m \left(1 - \frac{\overline{u^2}}{U_m^2} \right)^{\frac{1}{2}} \quad . \qquad (4\text{-}11)$$

7. Correction for shear effects. d = 0.15D = 0.0045 inch. This correction is made toward the region of higher velocity.

4.2 Static-Pressure Measurements

The velocity fluctuations in a turbulent flow field go hand in hand with the static pressure fluctuations. The static-pressure fluctuations are the result of the non-linearity of the governing equations of motion. It has always been a difficult problem to evaluate the change in velocity and pressure fields due to the introduction of a probe in the stream. It is relatively easy to obtain reliable pressure measurements in a non-turbulent uniform flow. In such a case, the

reading of a static-pressure tube will depend on the shape of the nose and the distance of the supporting stem behind the openings. According to Fage (10), the reading obtained with a static-pressure tube is independent of the geometry of this tube as long as the following requirements are met. The static openings must be at least 6 tube diameters behind the nose and the supporting stem at least 15 stem diameters downstream from the static openings.

However, for turbulent flow the problem becomes much more complicated. Again, there is very little evidence in the literature of a systematic investigation of the effect of turbulence on the readings of the static-pressure tubes. Goldstein (13) argued that the difference of the measured static pressure and the true average static pressure is due to the effect of the impact pressure of the fluctuating cross velocities on the tube and its openings. This effect depends not only on the geometry of the tube and its openings but also on the magnitude and frequency of the cross velocities. Goldstein proposed that for a tube with a large number of small openings equally spaced around its periphery, the reading of the tube can be expressed as

$$P_m = P + k_1 \rho (\overline{v^2} + \overline{w^2}) \qquad (4\text{-}12)$$

where P is the true average static pressure and k_1 some coefficient. For isotropic turbulence, he expects k_1 to have a value of $\frac{1}{4}$. However, a reliable value for k_1 can only be obtained experimentally. It is also conceivable that the scale of the lateral velocity fluctuations

will affect the tube reading. This is especially true when this scale is of the same order of magnitude as the tube diameter. According to Hinze, the static pressure measured by a static-pressure tube will be too low. The cross turbulence affects the pressure distribution along the circumference of the tube. The statement that the measured static pressure is too low becomes evident when it is realized that normal flow around a cylinder gives a resultant negative pressure. Corcos (6) discussed the effect on the pressure field by the cross flow in a turbulent flow field. Instantaneously, the static-pressure probe will experience a cross flow which will cause an additional pressure field. The effect of the cross flow will depend on the probe geometry and the Reynolds number of the cross flow (based on the probe diameter). The instantaneous side force due to the instantaneous cross flow will depend on the Reynolds number of this cross flow. For high cross-flow Reynolds numbers, the side force is proportional to the area exposed, the velocity squared and the density,

$$\sqrt{f_s^2} \sim A_1 \rho \left(\overline{v^2} + \overline{w^2} \right) \quad . \tag{4-13}$$

At low Reynolds numbers in the Stokesian range, the side force is proportional to the diameter of the probe, the viscosity, and the velocity,

$$\sqrt{f_s^2} \sim d \mu \sqrt{\overline{v^2} + \overline{w^2}} \quad . \tag{4-14}$$

Chao (4) yawed his static-pressure probe, so that the probe could be subjected to a known cross flow. His probe had a diameter of 1/16 inch and four static openings of approximately 1/32 inch each. The openings were located at 90^0 intervals around the circumference of the probe. The pressure measured by the probe did not change when the probe was exposed to a known cross flow deliberately. Even with a 67% increase of the lateral force due to the yawing of the probe, Chao did not observe any appreciable changes in static pressures. From Chao's experiment, it can be inferred that the static-pressure tube is insensitive to small errors in alignment. In view of what is mentioned above, there does not seem to be a reliable method to calibrate and to correct the measurements taken with a static-pressure tube. An attempt was made to measure the static pressure in the boundary layer with respect to the static pressure in the free stream. This pressure differential was too small to be measured accurately with the available equipment.

4.3 Turbulence Measurements

4.3.1 Hot-wire sensitivity to velocity and angle of yaw - The measurement of transient velocity components was done exclusively by the constant-temperature hot-wire anemometer designed at Colorado State University by Finn and Sandborn (11).

The detecting element of a hot-wire anemometer consists of a very fine and short metal wire, which is heated above ambient

temperature by means of an electric current. By using a constant-temperature hot-wire anemometer the electric resistance of the wire and its temperature are kept constant. A slight variation in velocity will result in a variation in heat loss from the hot wire, which in turn produces an unbalance of a Wheatstone bridge. Any unbalance in the bridge is compensated for by means of an electronic feedback system. The feedback system senses the unbalance in the bridge and alters the current to the bridge to rebalance it. Such a feedback system operates almost instantaneously, and it can follow and balance the bridge for frequencies up to 50,000 cps or greater.

The amount of heat transferred from the hot wire depends on:

1. The velocity of the fluid
2. The difference in wire temperature and the temperature of the fluid
3. The physical properties of the fluid
4. The dimensions and physical properties of the wire
5. The orientation of the wire in the flow field.

The wire loses heat through conduction, free convection, forced convection and radiation. Generally, the effects of radiation and of free convection are neglected. The temperature distribution along the wire can be predicted by solving the steady-state problem of heat transfer from a finite hot wire with Joulean heating, conduction of heat into the wire supports and forced convection. Since we want to measure transient velocities rather than mean velocities, we need to

consider the heat transfer from the hot wire in the transient state. The transient solution can be approximated by assuming that the wire responds as a first order system. In hot-wire anemometry, it is assumed that the fluctuations can be evaluated from a calibration between the wire heat loss and the quantity to be measured. The wire heat loss must be known very accurately so that the first derivative of heat loss with respect to the quantity which changes the heat loss can be obtained.

The heat loss from a circular cylinder of infinite length has been found to be a function of velocity, temperature, fluid properties and angle of attack. For this experiment, it was assumed that the hot wire was used in flows where temperature and fluid properties were considered constant. It is assumed that the hot wire is operated ideally by the electronic circuit, so that problems of frequency response do not need to be considered. The problem is now to find a technique to obtain the turbulent velocities from the hot wire output and the calibration curves. The output of the constant-temperature hot-wire anemometer, which is indicative of the hot-wire heat loss, can now be assumed to be a function of velocity, U_{TOT} , and the angle of attack, ζ , provided the geometry and physical properties of the wire remain constant,

$$E_{OUT} = E(U_{TOT}, \zeta) . \qquad (4\text{-}15)$$

The total velocity seen by the hot wire at any moment is

$$U_{TOT} = \sqrt{(U + u)^2 + v^2 + w^2} \quad . \tag{4-16}$$

The rectangular coordinate system is rotated so that the mean velocity U is directed in x-direction only. The angle ζ is the total angle between the direction of total velocity and the position of the hot wire. The angle ζ can be thought of as being made up of two angles ϕ and ψ . Angle ϕ is the angle the hot wire makes with the x-axis when rotated in the x-y plane, and angle ψ is the angle the hot wire makes with the x-axis when rotated in the x-z plane (Figures 19, 20, and 21). Any combination of ϕ and ψ coincides with one value for angle ζ . When the wire is perfectly aligned in the x-y plane, the value of $\frac{\partial E}{\partial \psi}$ is zero. However, the heat loss is quite sensitive to angle of yaw for small deviations from perfect alignment (32). Therefore, it is essential that a wire yawed in the x-y plane is aligned exactly in this plane. Considering now only angles of yaw in the x-y plane, the output of the constant-temperature hot-wire anemometer can now be assumed to be a function of total velocity vector, U_{TOT} , and the angle of attack, ϕ ,

$$E_{OUT} = E\,(U_{TOT}\ ,\ \phi) \quad . \tag{4-17}$$

In terms of differentials, one obtains

$$dE_{OUT} = \frac{\partial E}{\partial U_{TOT}}\ d\,U_{TOT} + \frac{\partial E}{\partial \phi}\ d\,\phi \quad . \tag{4-18}$$

The differential of the total velocity is

$$dU_{TOT} = \frac{1}{\sqrt{(U+u)^2 + v^2 + w^2}} \left[(U+u)\,du + v\,dv + w\,dw \right] \tag{4-19}$$

Generally, it is assumed that $U >> u$, v or w, so that the above equation reduces simply to

$$d\,U_{TOT} \simeq d\,u \quad . \tag{4-20}$$

For large magnitudes of turbulence, the complete expression of dU_{TOT} must be utilized. If the fluctuations of the velocity are large in reference to the mean velocity, it is nearly impossible to evaluate the output of a hot wire anemometer. From Figure 19, it can be easily seen that the instantaneous angle of attack can be written as

$$\phi' = \phi + \tan^{-1} \frac{v}{(U+u)} \quad . \tag{4-21}$$

Its differential may be expressed as

$$d\phi = \frac{(U+u)\,dv - v\,du}{(U+u)^2 + v^2} \quad . \tag{4-22}$$

By substitution, one obtains

$$dE_{OUT} = \frac{\partial E}{\partial U} \frac{1}{\sqrt{(U+u)^2 + v^2 + w^2}} \left[(U+u)\,du + v\,dv + w\,dw \right] +$$

$$\frac{\partial E}{\partial \phi} \left[\frac{(U+u)\,dv - v\,du}{(U+u)^2 + v^2} \right] \quad . \tag{4-23}$$

The above equation is still impossibly complex, and additional assumptions seem necessary to obtain a less complex expression in which the terms can be evaluated.

It is now assumed that the mean velocity U is much greater than the turbulent velocities (i.e., $U >> u$, v or w). Substituting these assumptions in the above equation, one obtains the following relation:

$$dE_{OUT} = \frac{\partial E}{\partial U} du + \frac{\partial E}{\partial \phi} d\phi \qquad (4\text{-}24)$$

or consequently,

$$E_{OUT} = E(U, \phi) \quad . \qquad (4\text{-}25)$$

Assuming now that $E(U, \phi)$ is analytic everywhere in the flow field, the above function may be expanded in a Taylor series about some convenient point of operation. The deviations of the velocity and angle from its mean values are assumed to be small and will be denoted by $u = U' - U$ and $\phi_1 = \phi' - \phi$, respectively. Expanding the output of the hot wire about U and ϕ, the following is obtained,

$$E(U', \phi') = E(U, \phi) + \left(\frac{\partial E}{\partial U}\right)_m u + \left(\frac{\partial E}{\partial \phi}\right)_m \phi_1 + \frac{1}{2!}\left(\frac{\partial^2 E}{\partial U^2}\right)_m u^2 + \left(\frac{\partial^2 E}{\partial U \partial \phi}\right)_m u\phi_1 + \frac{1}{2!}\left(\frac{\partial^2 E}{\partial \phi^2}\right)_m \phi_1^2 + \ldots\ldots \quad . \qquad (4\text{-}26)$$

The deviation of the wire voltage from its mean is denoted by e, where $e = E(U', \phi') - E(U, \phi)$. The partial derivatives with

subscript m denote the evaluation of these partial derivatives at the point of operation (U , ϕ) .

Neglecting higher order terms, the expansion can be rewritten as

$$e = \left(\frac{\partial E}{\partial U}\right)_m u + \left(\frac{\partial E}{\partial \phi}\right)_m \phi_1 \quad . \tag{4-27}$$

$\left(\frac{\partial E}{\partial U}\right)_m$ is the sensitivity of the hot wire voltage to a deviation in velocity from its mean, and $\left(\frac{\partial E}{\partial \phi}\right)_m$ is the sensitivity of the hot wire voltage to a deviation in angle from its mean. From now on, the subscript m of the partial derivatives of E will be omitted with the understanding that all partial derivatives are being evaluated at the mean.

From Figure 19, it can easily be seen that

$$\sin \phi_1 = \frac{v}{\sqrt{(U + u)^2 + v^2}} \quad . \tag{4-28}$$

After expansion,

$$\phi_1 = \frac{v}{\sqrt{(U + u)^2 + v^2}} + \frac{1}{6}\left[\frac{v}{\sqrt{(U + u)^2 + v^2}}\right]^3 + \ldots\ldots \tag{4-29}$$

Previously, it was assumed that the mean velocity, U , is much larger than the turbulent fluctuations, consequently $\phi_1 \simeq \frac{v}{U}$ and

$$e = \frac{\partial E}{\partial U} u + \frac{1}{U} \frac{\partial E}{\partial \phi} v \quad . \tag{4-30}$$

To employ this expression, it must be written in terms of quantities which can be measured such as root-mean squares or mean squares

of fluctuating quantities. Therefore, the above equation is squared and averaged. This leads to

$$\overline{e^2} = \left(\frac{\partial E}{\partial U}\right)^2 \overline{u^2} + 2\left(\frac{\partial E}{\partial U}\right)\left(\frac{1}{U}\frac{\partial E}{\partial \phi}\right)\overline{uv} + \left(\frac{1}{U}\frac{\partial E}{\partial \phi}\right)^2 \overline{v^2} \quad . \quad (4-31)$$

Letting $\frac{\partial E}{\partial U} = S_U$ and $\frac{1}{U}\frac{\partial E}{\partial \phi} = S_V$, one obtains

$$\overline{e^2} = \left(S_U\right)^2 \overline{u^2} + 2\, S_U S_V \overline{uv} + \left(S_V\right)^2 \overline{v^2} \quad . \quad (4-32)$$

The above equation requires that the hot wire has to be calibrated with respect to angle and velocity in order to obtain a value for $\overline{uv}$ from which the turbulent shear stress in the x-direction can be obtained. These sensitivities themselves vary with angle and velocity, however, it was found that the two sensitivity terms S_U and S_V are of equal magnitude at an angle of $\phi = 40^0$. Based on this information and previous experiments it was decided to operate the hot wire at angles of plus and minus 40^0 from the x-axis in the x-y plane. For the case of $\phi = 90^0$, or when the wire is perpendicular to the mean flow, the angle sensitivity is zero (Figure 22) and the above equation becomes

$$\overline{e^2} = \left(S_U\right)^2 \overline{u^2} \quad . \quad (4-33)$$

From this expression, the magnitude of $\overline{u^2}$ can be obtained when the wire is properly calibrated against velocity, and the mean velocity at the point of measurement is known.

Knowing the magnitude of $\overline{u^2}$, values of $\overline{v^2}$ and $\overline{uv}$ can now be obtained by using the measurements of $\overline{e^2}$ at the wire

positions of plus and minus 40^0. Examining a plot (Figure 22) of hot wire voltage versus angle of attack, it can be seen that for positive angles of ϕ, S_V is a positive quantity, and for negative angles of attack S_V is a negative quantity. Therefore, two equations can now be constructed; one for the positive angle of attack,

$$(\overline{e^2})_{+40} = (S_U^2)_{+40} \overline{u^2} + 2(S_U)_{+40} (S_V)_{+40} \overline{uv} + (S_V)^2_{+40} \overline{v^2} \tag{4-34}$$

and the other for the negative angle of attack,

$$(\overline{e^2})_{-40} = (S_U^2)_{-40} \overline{u^2} + 2(S_U)_{-40} (S_V)_{-40} \overline{uv} + (S_V)^2_{-40} \overline{v^2} \ . \tag{4-35}$$

4.3.2 Hot-wire calibrations - All hot wires used for this experiment were calibrated in the free stream outside the boundary layer in the Army wind tunnel, so that accurate values for the hot-wire voltage could be obtained. The wire which was used for the turbulent shear measurements was calibrated for angles of attack of $\pm 90^0$ and $\pm 40^0$. In these positions, the output voltage from the hot wire was obtained for mean velocities ranging from 5 to 40 fps. From these results, the velocity sensitivity, $S_U = \frac{\partial E}{\partial U}$, was obtained for the three different angles: 90^0, $+40^0$, and -40^0. In order to insure a high degree of accuracy, the velocity sensitivities were obtained in two different manners. The most straight-forward way is to obtain the slope directly from the calibration curve of the wire voltage versus velocity. However, the measurement of the

velocity sensitivity in this manner is subject to a relatively great amount of error.

From previous experiments, it was found that the mean heat loss from hot wires in subsonic continuum flow was quite well predicted by King's Law,

$$\frac{I^2 R}{R - R_a} = A' + B' \sqrt{U} \quad . \tag{4-36}$$

In order to obtain an accurate value for the velocity sensitivity, the equation not only must represent the data but also give a good first derivative. It was found that the power of the velocity in King's Law varies with the wire Reynolds number. The relation between the mean heat loss and the mean velocity appears to be expressed best by the relation

$$\frac{I^2 R}{R - R_a} = A' + B' U^m \quad . \tag{4-37}$$

For constant temperature operation, one can write:

$$\frac{E^2}{R(R - R_a)} = A' + B' U^m \quad . \tag{4-38}$$

If the temperature of the fluid and of the wire is constant, the term $R(R - R_a)$ is a constant and

$$E^2 = A_1 + B_1 U^m \quad . \tag{4-39}$$

If for no-flow the wire voltage is E_o, one gets

$$E^2 - E_o^2 = B_1 U^m \quad . \tag{4-40}$$

Since the wire voltage for the no-flow condition can be measured very accurately, the term $E^2 - E_o^2$ is plotted versus the velocity on a log-log plot. As it turns out, this plot is not quite a straight line. However, straight lines can be fitted for certain ranges of velocity. For the velocity range of 1.5 - 4 fps, m is usually larger than 0.5. For the velocity range of 4 - 12.5 fps, m is close to 0.5. For velocities greater than 12.5 fps, m turns out to be smaller than 0.5.

The derivative of equation 4-40 with respect to U yields an expression from which the velocity sensitivity can be obtained. For each velocity range where the data can be fitted with a straight line, accurate values for m and B may be obtained and the velocity sensitivity calculated. The results for the velocity sensitivity of both methods are similar except for velocities below 3 fps. In this velocity range, m changes so rapidly that no straight line can be fitted to the data. This method to obtain the velocity sensitivity was used for all three angles of yaw.

For an absolutely symmetrical wire, the velocity sensitivity curves should be the same for $+ 40^0$ and $- 40^0$; it turns out that there is a slight difference in the two curves (Figures 23 and 24). Figure 25 shows the variation of velocity sensitivity with velocity for a wire normal to the flow. The angle sensitivity $S_V = \frac{1}{U} \frac{\partial E}{\partial \phi}$ at $\phi = + 40^0$ and $\phi = - 40^0$ was obtained by measuring the hot wire voltage at seven different angles ranging from $\phi = + 35^0$ to $\phi = + 45^0$, and from $\phi = - 35^0$ to $\phi = - 45^0$, respectively.

The results show that no difference in angle sensitivity between the positive and negative angle of yaw could be discerned because of the scatter of the data (Figure 26).

4.3.3 Calibration of the differentiating circuit - The average size of the smallest eddies, which are mainly responsible for the turbulent energy dissipation, can be measured directly by means of a differentiating circuit. The size of the smallest eddies, λ, called the micro-scale, can also be obtained from the power spectrum. The micro-scale is defined by Taylor (37) as

$$\frac{1}{\lambda^2} = 2 \lim_{x \to 0} \frac{1 - R_x}{x^2} = \lim_{y \to 0} \left(\frac{1 - R_y}{y^2} \right) . \quad (4\text{-}41)$$

For isotropic turbulence, it turns out that $R_x = R_y$ when $x = y\sqrt{2}$. The micro-scale, λ, is the intercept on the y axis of a parabola of correct curvature drawn in such a manner that it touches the (R_y, y) curve at its maximum when $y = 0$. Taylor shows that

$$R_y = 1 - \frac{1}{2!} \frac{y^2}{\overline{u^2}} \overline{\left(\frac{\partial u}{\partial y} \right)^2} + \frac{1}{4!} \frac{y^4}{\overline{u^2}} \overline{\left(\frac{\partial^2 u}{\partial y^2} \right)^2} - \cdots . \quad (4\text{-}42)$$

Neglecting higher order terms,

$$\overline{\left(\frac{\partial u}{\partial y} \right)^2} = 2 \overline{u^2} \lim_{y \to 0} \left(\frac{1 - R_y}{y^2} \right) \quad (4\text{-}43)$$

or

$$\overline{\left(\frac{\partial u}{\partial y} \right)^2} = \frac{2 \overline{u^2}}{\lambda^2} . \quad (4\text{-}44)$$

For isotropic turbulence

$$\overline{\left(\frac{\partial u}{\partial x}\right)^2} = \frac{1}{2}\overline{\left(\frac{\partial u}{\partial y}\right)^2} \quad . \tag{4-45}$$

Therefore,

$$\lambda^2 = \frac{\overline{u^2}}{\overline{\left(\frac{\partial u}{\partial x}\right)^2}} \quad . \tag{4-46}$$

Assuming that Taylor's hypothesis is valid, the previous equation can be written as

$$\lambda = \frac{U\sqrt{\overline{u^2}}}{\sqrt{\overline{\frac{\partial u}{\partial t}^2}}} \quad . \tag{4-47}$$

For a wire normal to the mean flow, the instantaneous output voltage is related to the instantaneous velocity by

$$e(t) = S_u\, u(t) \quad . \tag{4-48}$$

The micro-scale can now be directly expressed in terms of the hot-wire anemometer output voltage, $e(t)$,

$$\lambda = \frac{U\sqrt{\overline{e^2}}}{\sqrt{\overline{\left(\frac{\partial e}{\partial t}\right)^2}}} \quad , \tag{4-49}$$

where $\sqrt{\overline{e^2}}$ is the rms of the signal which is fed into the differentiating circuit. The magnitude of $\sqrt{\overline{\left(\frac{\partial e}{\partial t}\right)^2}}$ is obtained from the calibration curve (Figure 11).

Assume that the input signal to the differentiating circuit is a sine wave, $e = A \sin \omega t$. It can easily be shown that the rms of this signal is $\sqrt{\overline{e^2}} = \frac{A}{\sqrt{2}}$. Now $\frac{de}{dt} = A\,\omega \cos \omega t$ and

$$\sqrt{\overline{\left(\frac{de}{dt}\right)^2}} = \frac{A\omega}{\sqrt{2}} = \sqrt{\overline{e^2}}\;\omega \qquad (4\text{-}50)$$

where $\omega = 2\pi n$. Therefore, the rms of the derivative of the input-sine wave can be calculated when its frequency and the magnitude of its rms are known. It is possible to obtain a calibration of the differentiating circuit of the output voltage, $\sqrt{\overline{e^2}}$, versus the calculated value for $\sqrt{\overline{\left(\frac{\partial e}{\partial t}\right)^2}}$ (Figure 11). The micro-scale, λ , can be calculated since all the terms in the expression for λ can be obtained.

4.3.4 Possible sources of error in turbulence measurements - The measurement of turbulent velocity components seems relatively easy following the previous discussions. However, these measurements are subject to a great deal of uncertainty. In this section, the possible sources of error in turbulence measurements will be pointed out.

a. Effect of the solid boundary on turbulence measurements

When a hot wire is used close to a solid boundary, errors are introduced due to the effect of the boundary on the rate of heat loss from the wire. When a tungsten wire is used at an overheating ratio

of $R/R_a = 1.5$, the wire temperature is approximately 250^0 F. Consequently, when this hot wire is used near a solid boundary the wire can be 180^0F hotter than the surface. Besides losing heat to the air due to forced convection, the wire may lose additional heat to the surface, due to conduction. Piercy, Richardson and Winny (25) used potential-flow theory to determine the conduction-heat loss due to the presence of a solid surface. These results cannot be expected to apply to the boundary layer, since different velocity profiles are involved. Wills (42) showed the effect of the solid boundary for laminar flow. The air velocity at the wire was found from the known laminar velocity profile. Using the same channel, the boundary layer was allowed to become turbulent. The same values for U_τ were used in order to maintain the same velocity gradient at the wall. As could be expected, the laminar correction was too big to be used in turbulent flow. The results indicated that close to the wall a correction approximately half as big as for the laminar case was a good estimate.

No exact correction for the effect of a solid surface on the heat transfer from a wire can be obtained, unless one resorts to experimental methods. The effect of the boundary on the heat transfer from the hot wire for the no-flow condition is shown in Figure 27. For this condition, the effect of the surface becomes negligible when the wire is 0.1 inch away from this surface. For the turbulent boundary layer with a free stream velocity of approximately 20 fps, surface

effects were detected when the wire was within 0.01 inch of the surface. At such distances from the surface, 10% discrepancies in estimating the clearance between the wire and the boundary exist. The fact that the surface is not perfectly smooth adds to this problem. In this experiment, data within 0.02 inch of the surface are subject to these uncertainties. It was found that at distances greater than 0.02 inch from the surface the velocity measurements from the hot wire and the total-head tube coincide quite well.

b. Effect of wire length on turbulence measurements

When the integral scale of the turbulence in the direction of the hot wire is of the same order of magnitude as the length of the wire, the turbulence measurements are in error. Hot wires approximately 0.05 inch long were used for the turbulence measurements. It could very well be that velocity fluctuations on one part of the wire are not completely correlated with those on another part. This means that the dominating eddies are of the same size or smaller than the length of the wire. The lack of correlation causes the rms voltage to be reduced. This reduction depends on the falling-off of the correlation curve of the turbulence in the direction of the wire. This reduction must be taken into account in all turbulence measurements, including turbulence intensity, correlations, turbulent shear and energy-density spectra. For maximum signal output, however, it is required to have a relatively long hot wire. The space resolution

requires a hot wire of zero length. These two requirements are in conflict and some sort of compromise has to be made.

Dryden, et al. (8), Frenkiel (12), and Uberoi and Kovasznay (41) came to the same conclusion about the space-resolution correction for the turbulent voltage:

$$\frac{\overline{e_\ell^2}}{\overline{e^2}} = \frac{2}{\ell^2} \int_0^\ell (\ell - z)\, R_z(z)\, dz \quad , \tag{4-51}$$

where $\overline{e_\ell^2}$ is the measured mean square of the fluctuating voltage. However, before an attempt is made to correct the turbulent voltage for space resolution, it is important to realize the influence of conduction into the wire supports. The effective length of the wire is shorter than its actual length due to the drop in local temperature of the wire toward its supports.

The correction for wire length was calculated using the measured lateral correlation coefficient, R_z. This correlation coefficient was measured by means of two vertical wires, each being approximately 0.01 inch long. The centers of these wires were located at a distance of 0.015 inch above the tunnel floor. The calculations were made for a free stream velocity of 40 fps. For this case, the measured lateral integral scale was 0.030 inch. The correction factor, C_1, was found to be 1.15. This correction factor is defined by

$$\overline{e^2} = C_1\, \overline{e_\ell^2} \quad , \tag{4-52}$$

so that,

$$\frac{1}{C_1} = \frac{2}{\ell^2} \int_0^{\ell} (\ell - z)\, R_z\, dz \quad . \tag{4-53}$$

For ℓ , the actual wire length of 0.05 inch was used. For the worst possible case, the correction for finite wire length is 15%. This result was obtained using the actual wire length and not a shorter length due to end effects. It can be expected that this lateral integral scale will increase rapidly with increasing distance from the solid boundary. This would then result in a rapid decrease in the correction factor C_1 . No turbulence measurements are considered accurate within 0.02 inch of the tunnel floor. The lateral correlation measurements were made with wires which were positioned vertically and close to the tunnel floor. The vertical velocity gradient and the vertical gradient of the longitudinal velocity fluctuations are of large magnitude close to the solid boundary. Under such conditions, the measurements of hot wires seem to be exaggerated as will be shown later. For these reasons, and lack of reliable measurements, no correction for finite wire length was made as far as the turbulence-intensity measurements and the turbulence-shear measurements were concerned.

Also the one-dimensional energy spectra need to be corrected for wire length. The contribution to the energy by high wave-number turbulence of small scale will be too low, due to the finite length of

the hot wire. Betchov (2) corrected his results for the effect of the finite length of the hot wire. The uncorrected spectrum falls as k^{-7} in the viscous range. However, after the correction is made the spectrum falls off as k^{-6}. The true one-dimensional spectrum can be recovered from the measured spectrum using the correction equation given by Uberoi and Kovasznay (41).

$$F(k) \simeq \frac{1}{\pi \ell} \int_k^{\infty} \frac{F'(k')\, dk'}{\sqrt{k' - k^2}} \qquad (4\text{-}54)$$

where $F'(k')$ is the measured one-dimensional spectrum which will approach the true one-dimensional spectrum, $F(k)$, when ℓ approaches zero. The correction equation is derived with the assumption that the temperature distribution is uniform along the wire. If it is assumed that $F'(k') = B\, k^{-7}$, the true one-dimensional spectrum becomes

$$F(k) = \frac{B}{\ell} \frac{15}{96} k^{-7} . \qquad (4\text{-}55)$$

This result shows that the spectrum function still falls off as k^{-7}. Betchov's results after the correction showed a slope of -6 on a log-log plot. The two methods of correction for finite wire length do not give similar results.

Since the hot wire has a finite length and does not give a point measurement, the recorded signal is an integral of the turbulence over the wire length. For eddy sizes several times smaller than the wire length, it is possible that two or more such eddies strike the

wire simultaneously. The result would be that the measured power at such high wave numbers tends to be larger than the true power. Previously, it has been argued that if the scale of the eddies in the direction of the wire was of the same magnitude or slightly smaller than the length of the wire, the rms voltage was reduced.

The wire length should be small compared to the wave length of a particular frequency. However, it is questionable how well the wave length represents the true scale of the eddies at this particular frequency. The wire length (0.05 inch) corresponds to a wave number of 1500 feet^{-1}. This would indicate that the viscous regions of spectra measured close to the wall ($y < 0.5$ inch) may need to be corrected.

The effect of wire length may be determined by obtaining the energy spectrum with wires of varying length. Extrapolation for zero wire length could give the proper value for the spectrum function at a given wave number. Difference in logarithmic slope of the viscous region of the spectrum was observed by comparing two recorded signals, taken under the same flow conditions but at different times. This would indicate that the measurements taken at different times are sensitive to slight changes in behavior of the electronic equipment. In view of this, and since no reliable method is available, no correction was made for the effect of the wire length on measured power spectra.

c. Effect of velocity gradient and turbulence-intensity gradient on turbulence measurements

For heat transfer from a finite hot wire in the steady state with a uniform velocity distribution normal to the wire, the temperature distribution along the wire can be written as

$$\frac{d^2T}{ds^2} - \beta_1 T = -\beta_2 \quad . \tag{4-56}$$

In this case, β_1 and β_2 are constants. However, with a steady non-uniform flow normal to the wire the above equation becomes more complicated. Both β_1 and β_2 now are functions of s . This is due to the fact that the convective heat-transfer coefficient varies with the velocity distribution along the wire. The equation for the temperature distribution along the wire becomes

$$\frac{d^2\,T(s)}{ds^2} - T(s)\,\beta_1(s) = -\beta_2(s) \quad . \tag{4-57}$$

The general solution of this differential equation does not seem to be expressible in terms of simple functions of β_1 and β_2 . When a hot wire is operated in a velocity gradient, the heat transfer along the wire is non-uniform. This results in a shift of the effective center of the wire toward that part of the wire with the higher heat transfer. If the wire also experiences a turbulence-intensity gradient in the direction of the wire, a mathematical solution for the temperature distribution is almost impossible to obtain.

Hot wires operating close to the solid boundary in the turbulent boundary layer and projected partly or completely in the y-direction are subject to the above mentioned gradients. When operated under such conditions, the measurements with a vertical and a horizontal hot wire positioned normal to the mean flow do not give the same value of turbulence intensity. Figures 28 and 29 demonstrate the results obtained for $\sqrt{\overline{u^2}}/U$ with the horizontal and vertical wire. The discrepancy in results from the horizontal and vertical wire seems to increase with increasing Reynolds numbers. It is reasonable to assume that the measurements with the horizontal wire are more nearly correct. When this is true, it seems that the vertical wire is affected by a large mean-velocity gradient that exists along its length or possibly by the existence of a turbulence gradient $\partial \sqrt{\overline{u^2}}/\partial y$. For measurements of the longitudinal turbulence intensity, the wire can be placed such that these large gradients are not present along the wire. However, for measurements of the turbulent shear stress, the wire must be yawed so that it is partly projected in the y-direction.

Results show that total shear obtained from measurements with the hot wire were systematically higher than the expected values obtained from the mean velocity distribution. The wall-shear stress was obtained experimentally with the wall-shear stress meter and theoretically from the Ludwig-Tillman equation for local skin friction.

In the viscous region close to the solid boundary, it is possible to neglect the inertia terms in the equation of motion. The result is that the vertical gradient in total shear is zero if the longitudinal pressure gradient is also zero. Since the wall shear is known, the turbulent shear in this viscous region can now be calculated by subtracting the viscous shear from the total shear. However, the experimental results were systematically higher than the calculated results (Figures 30 and 31). Close to the wall, in the region with an appreciable velocity gradient, the longitudinal turbulence intensity measured with the vertical wire was generally larger in magnitude than the one measured with the horizontal wire. The turbulent shear stresses measured with the yawed wire are larger in magnitude than the calculated values obtained from the momentum equation. This leads to the conclusion that the measurements with hot wires, which are partly or completely exposed to velocity gradients, are generally exaggerated. Plotting $\sqrt{\overline{u^2}}$ versus distance from the tunnel floor (Figures 32 and 33), it was noted that $\sqrt{\overline{u^2}}$ measured with the vertical wire already differed from the true value of $\sqrt{\overline{u^2}}$ before the term $\frac{\partial \sqrt{\overline{u^2}}}{\partial y}$ becomes significant. Therefore, it was believed that the mean velocity gradient had much more effect on the hot wire output than the gradient of the longitudinal velocity fluctuations.

The measurements were corrected in the following manner. The rms output of the vertical hot wire was compared with the rms calculated from the true turbulence intensity, $\frac{\sqrt{\overline{u^2}}}{U}$, obtained

from the measurements with the horizontal wire. For each distance from the floor, a ratio for the difference in rms voltage and measured rms voltage can be obtained. This same ratio was used to correct the measurements of the yawed wire. By correcting the output of the yawed wire it is assumed that the calculated terms $\overline{uv}$ and $\overline{v^2}$ are corrected for effects of velocity and turbulence gradient.

d. Effect of turbulence on heat transfer from hot wires

The heat transfer from cylinders placed in a turbulent flow is affected by the Reynolds number, the intensity of the turbulence and the ratio between the scale of the turbulence and the cylinder diameter. These effects were investigated by van der Hegge Zijnen (15). The results show that for very small or very large magnitudes of the ratio L_x/D, the turbulence intensity has hardly any effect on the heat transfer from the cylinder. When the scale of the turbulence is of the same order of magnitude as the cylinder diameter ($L_x/D = 1.5$), an increase in turbulence intensity will markedly increase the heat transfer especially for high Reynolds numbers. In this experiment, the wires were calibrated in the free stream with a very low turbulence intensity. It is possible that the heat transfer increases when the same wire is operated in the boundary layer at much higher turbulence intensity. So far, it has been assumed that the mean heat transfer is the same whether the turbulence intensity is low (free stream) or the turbulence intensity is high (boundary

layer), as long as the mean flow does not change. A change in heat transfer due to turbulence intensity would result in a change in hot wire voltage. However, the measured mean velocities near the boundary were in good agreement with the velocities obtained from the hot-wire calibration. This indicates that the heat transfer from the wire is not affected by turbulence intensity as long as the scale of the turbulence is sufficiently large with respect to the wire diameter.

e. Effect of linearization on turbulence calculations

The sensitivity of the hot wire anemometer to velocity fluctuations was explained in section 4.3.1. The expression for the differential of the hot wire output was too complex and additional assumptions had to be made. The classical assumption was made that the magnitude of the mean flow was much larger than the magnitude of the fluctuations.

By using the expression for the differential of the hot-wire output, it is assumed that the calibration curve of the hot wire is linear around the point of operation. This assumption may be adequate for small turbulence intensities at high mean velocities. But the assumption of the velocity-voltage curve being linear over the range required by $dE_{out} \simeq e$ must be questioned. The possible error due to non-linear averaging of the hot-wire anemometer was checked graphically from the calibration curve. For a fluctuation

intensity of $\sqrt{\overline{u^2}}/U = 0.30$, the maximum error of 3% was found when $U = 20$ fps . For lower velocities and at the same turbulence intensity the error was found to be less. Therefore, it can be concluded that for all turbulent measurements the non-linearity of the voltage versus velocity calibration curve is unimportant.

f. Effect of large turbulence components on hot wire measurements

In the previous section, some light was shed on the effect of large velocity fluctuations in the same direction as mean flow. The maximum possible error to be expected under the conditions encountered in this experiment was 3%. Next to the solid surface, the scale of the turbulence in the longitudinal direction is ten times as large as either the lateral or vertical turbulence scales. For a wire normal to the flow and parallel to the tunnel floor, the wire sees a relatively large fluctuation in the x-direction and a comparatively small fluctuation in the other two directions. The maximum longitudinal turbulence intensity encountered in this experiment was of the order of 0.3 close to the wall. Therefore, one might expect that the intensities of the lateral and the vertical turbulence components, $\sqrt{\overline{v^2}}/U$ and $\sqrt{\overline{w^2}}/U$ would be of the order of 0.03. In the region close to the wall, the assumption that $U >> v$ or w can therefore be accepted without introduction of a great deal of error. Schraub and Kline (33) have attempted to estimate the errors

due to large turbulence fluctuations along a hot wire. The results show that errors of the order of 5% are possible for turbulence intensities of approximately 35%. The maximum value for this turbulence intensity, encountered in a region away from the wall was approximately 10%. Therefore, it can be concluded that the effect of v and w turbulence components is relatively small (less than 5%), so this effect has been ignored.

Chapter V

RESULTS AND DISCUSSION

5.1 The Nature of the Turbulent Boundary Layer

The presence of the gravel roughness at the entrance to the test section of the Army wind tunnel results in a large increase in skin friction. This increased skin friction means an increased wall-shear stress and a higher loss in momentum. Therefore, momentum has to enter the boundary layer to make up for this increased loss of momentum. The only way for more momentum to enter the boundary layer is for the boundary layer to increase in thickness at a faster rate. Downstream from the gravel roughness, the velocity profile is expected to return to a "normal" boundary layer profile. The only difference is that the roughness has helped to develop the boundary layer at a much faster rate than would have been the case without the roughness.

For the zero-pressure gradient turbulent boundary layer, the form factor, H, depends solely on the skin friction. Rotta (29) gives an expression for the variation of form factor with skin friction.

$$\frac{1}{H} = 1 - \frac{U_\tau}{U_\infty} I_1 \quad , \tag{5-1}$$

where

$$I_1 = \int_0^\infty \left[\frac{U_\infty - U}{U_\tau} \right]^2 d\left(\frac{yU_\tau}{\delta^* U_\infty} \right)$$

and

$$\frac{U_\tau}{U_\infty} = \sqrt{\frac{c_f}{2}} \quad .$$

Since the boundary-layer thickness can be defined in several ways, Rotta introduces the dimensionless wall distance, $\frac{yU_\tau}{\delta^* U_\infty}$, instead of y/δ . The parameter I_1 can be expected to be a constant, assuming that similarity of the velocity defect exists. The calculated value of the parameter I_1 is given by Rotta as 6.1. Figure 34 shows the calculated variation of form factor with skin friction, as well as the experimental results of Smith and Walker (36) and the results obtained in this experiment. The experimental results seem to fall above the calculated curve. The same is true for the experimental results of Schultz-Grunow and Hama as presented in Figure 13.6 of reference 29. All the velocity profiles of the Army wind tunnel seem to have the same value for form factor. This is in agreement with the similarity of the profiles when $\frac{U}{U_\infty}$ is plotted versus y/δ (Figures 35 and 36). According to the theory, this would mean no change in skin friction. When turbulent velocity profiles are plotted as was done for laminar layers, using U/U_∞ versus y/δ , the profiles seem to become similar notwithstanding the change in skin friction. However, it must be noted that Reynolds numbers, based on the distance from the virtual origin, of magnitude 3×10^8 were obtained. Reynolds numbers of such high magnitudes are not generally obtained in laboratory experiments. In Table I,

the important profile parameters are given for the measured velocity profiles along the test section of the tunnel. This table includes the results from the profiles at the station for which x = 85 feet. The skin friction was calculated from the empirical relation due to Ludwig and Tillman

$$c_f = 0.246 \times 10^{-0.678\,H} (U_\infty\, \theta/\nu)^{-0.268} \quad . \qquad (5\text{-}2)$$

The values for the distance from the virtual origin were obtained by means of the resistance law due to Smith and Walker (36).

The von Karman momentum-integral equation,

$$c_f = 2\frac{d\,\theta}{dx} \quad , \qquad (5\text{-}3)$$

gives values for the local skin friction which are 2.5 to 3 times as large as the values obtained from the Ludwieg-Tillman equation. However, the Ludwieg-Tillman equation seems more reliable since its results agree well with the values for local skin friction as obtained from the shear meter (Figure 37). The momentum-integral equation gives exaggerated values for local skin friction as compared with the results obtained from the shear meter. These exaggerated values for local skin friction are a result of the fact that the flow in the tunnel is not completely two-dimensional. Due to the increased momentum loss in the corners of the tunnel, more momentum has to be delivered by the free stream. This gives rise to the development of a secondary flow where high velocity fluid is transported from the center of the tunnel toward the corners. The necessary result is

that slow moving fluid is transported laterally away from the corners along the boundary and finally transported back to the free stream along the center line of the tunnel. This secondary flow tends to increase the boundary layer thickness at the center of the tunnel. The momentum thickness increases faster than is expected, resulting in an exaggeration of the local skin friction.

In Chapter II, it has been pointed out that for local similarity of the outer part of the turbulent boundary layer the term $\frac{\partial U_\tau}{\partial x}$ has to vanish (when longitudinal pressure gradient is absent). Rotta (29) found the following requirements for local similarity of the turbulent boundary layer flow:

$$\left.\begin{aligned} \frac{d(U_\tau / U_\infty)}{dx} &= 0 \\ \frac{d(\delta^* U_\infty / U_\tau)}{dx} &= \text{constant} \quad . \end{aligned}\right\} \qquad (5\text{-}4)$$

Figure 38 shows that this first requirement for local similarity is not fulfilled. However, this figure shows that the shear velocity varies almost linearly with the x-distance. This means that the law of the wall applies, or that the function $f\left(\frac{yU_\tau}{\nu}\right)$ is a truly universal function for turbulent shear flow near a smooth wall. Rotta's second requirement for local similarity is fulfilled, as can be seen from Figure 39.

5.2 The Flow Near the Wall at Station: x = 85 feet

The mean velocity distributions for approximately 1/5 of the boundary-layer thickness are shown in Figures 40, 41, and 42. Included in these figures are the slopes of the velocity profile at the wall, obtained from the wall shear-stress meter. The magnitudes of the wall-shear stress are plotted in Figure 37. In this figure, the measured and calculated values for the wall-shear stress are plotted versus a ratio of free stream velocity and kinematic viscosity. The values of the wall-shear stress obtained with the Ludwieg-Tillman skin-friction formula are slightly higher than the measured values obtained with the shear meter. Comparing the measured velocity distribution with the slope of the velocity at the wall, one can see that the region of linear velocity distribution is limited to a region of 0.020 inch from the wall. The thickness of this region varies with the Reynolds number of the flow.

Figure 43 shows the distribution of the term $\frac{-\overline{uv}}{U^2}$ versus y/δ . When these terms are plotted, one notices immediately a great deal of similarity. In the immediate neighborhood of the wall, equations (2-42) and (2-47) lead to the following expression

$$-\frac{\overline{uv}}{U^2} = \frac{\mu^2 \overline{\frac{\partial u}{\partial y}\frac{\partial v}{\partial y}}}{\tau_w^2} + \frac{1}{2} y \mu^2 \frac{\overline{\frac{\partial u}{\partial y}\frac{\partial^2 v}{\partial y^2}}}{\tau_w^2} + \ldots . \quad (5\text{-}5)$$

However, continuity requires that the term $\overline{\frac{\partial u}{\partial y}\frac{\partial v}{\partial y}}$ is zero at the wall. Consequently, the term $\frac{\overline{uv}}{U^2}$ should vanish at the wall. From

the data in Figure 43, it cannot be concluded whether the term $\frac{-\overline{uv}}{U^2}$ goes to zero at the wall or not. The turbulent shear stress cannot be measured close enough to the wall, because a yawed wire has to be used to make this measurement.

The viscous shear stress and the turbulent shear stress distributions are shown in Figures 44 and 45. Only in the immediate neighborhood of the wall is the viscous shear of any importance. For the case $U_\infty \simeq 40$ fps, a slight positive pressure gradient was measured. When the inertia terms are neglected, the equation of motion (2-4) reduces to

$$\frac{\partial P}{\partial x} = \frac{\partial \tau}{\partial y} \quad . \tag{5-6}$$

The accuracy of the turbulent shear stress measurements is within ± 10%. Evidence is found that difficulties are encountered when a hot wire is operated in a region where large mean and turbulent velocity gradients exist. In this light, it is nearly impossible to expect that the term $\overline{uv}$ can be measured within an uncertainty level of less than 10%. The measurements indicate that the total shear stress is constant only in a relatively small region adjacent to the wall. Beyond this region, the inertia terms can no longer be neglected. Several attempts were made to measure the longitudinal mean-velocity gradient, $\frac{\partial U}{\partial x}$. However, this term is extremely small for thick boundary layers, especially in the region close to the wall. The results seem to indicate that there is a very small region next

to the wall where the velocity profile varies linearly with y. However, the measurements so close to the wall are not accurate enough to substantiate this assumption. Near the surface, the term $\nu \frac{\partial^2 U}{\partial y^2}$ is zero or nearly zero. Beyond this region, the viscous term becomes relatively large until it reaches a maximum and thereafter decreases rapidly. The term $\frac{\partial \overline{uv}}{\partial y}$ follows a similar pattern. There is a relatively large region where both the viscous term $\nu \frac{\partial^2 U}{\partial y^2}$ and the turbulent term $\frac{\partial \overline{uv}}{\partial y}$ are relatively small. This is the transition region between the viscous sublayer and the fully turbulent part of the turbulent layer. In this transition region, the inertia terms are probably of the same order of magnitude as either the viscous term or the turbulent term of the equation of motion. Beyond the transition region, only the viscous term can be neglected from the equation of motion.

Figure 46 shows the distribution of τ/τ_w versus y/δ for two different free stream velocities. For $y/\delta > 0.05$, the curves are similar. Close to the wall, the similarity breaks down due to the existing pressure gradient at $U_\infty \simeq 40$ fps. It was found that close to the floor the output of the vertical and yawed hot wires show much larger voltage excursions than the output of the horizontal wire. The output of the hot wire seems to oscillate about one point, then makes a large excursion and oscillates about another point. Consequently, it is extremely difficult to obtain a reliable average of the

rms of the fluctuating voltage. For the horizontal wire these difficulties are less severe, and a better average can be obtained. A change in rms voltage of less than 5% may result in completely erroneous results of the terms $\overline{uv}$ and $\overline{v^2}$. This is another reason why the measurements of the turbulent shear stress close to the wall are subject to a great deal of uncertainty. The large fluctuations in rms voltage from yawed hot wires can possibly be related to the streaky structure of the turbulence near the wall (33).

The distributions of the longitudinal turbulence intensity $\frac{\sqrt{\overline{u^2}}}{U}$ are given in Figure 47. At the wall, this ratio should not vanish but must have a finite value (equation (2-53)). According to the data, this finite value could be 0.30 or slightly higher. This is in agreement with the results of Mitchell and Hanratty (24), who claim a value of 0.32 for the ratio $\frac{\sqrt{\overline{u^2}}}{U}$ when $y = 0$. In Figure 48, the distribution of the vertical velocity fluctuation, $\frac{\sqrt{\overline{v^2}}}{U}$, is shown. For the distribution near the wall, one may write from equation (2-46),

$$\overline{v^2} = y^2 \overline{\left(\frac{\partial v}{\partial y}\right)^2} + y^3 \overline{\frac{\partial v}{\partial y}\frac{\partial^2 v}{\partial y^2}} + \frac{1}{4} y^4 \overline{\left(\frac{\partial^2 v}{\partial y^2}\right)^2} + \ldots . \quad (5\text{-}7)$$

However, at the wall the first two terms to the right of the equal sign are zero. The term $\frac{\partial v}{\partial y} = 0$ at the wall, as is required by the continuity equation. Consequently, one may expect the ratio $\frac{\sqrt{\overline{v^2}}}{U}$ to vanish at the wall. The distribution of U near the wall is given by equation (2-42). The data in Figure 48 indeed indicate that $\frac{\sqrt{\overline{v^2}}}{U}$

tends to zero near the wall. Figures 49 and 50 show the comparison of the longitudinal and the vertical turbulent intensities. The two intensities are of the same order of magnitude except for the region extremely close to the wall. Klebanoff's results (19) indicate that the lateral turbulent intensity falls between the longitudinal and vertical turbulent intensities. The results from this experiment indicate that the three turbulent intensities are much closer in magnitude than those encountered by Klebanoff. This observation may be attributed to the fact that the flow in this experiment had more time to develop than in Klebanoff's boundary layer. Due to the action of the correlations $\overline{p\frac{\partial u}{\partial x}}$, $\overline{p\frac{\partial v}{\partial y}}$ and $\overline{p\frac{\partial w}{\partial z}}$, energy is transferred from the larger turbulence components to the smaller ones (29). Therefore, the turbulence tends to become more isotropic. The three turbulence components must have the same magnitude when the flow is completely isotropic.

The large excursions seen by the vertical and yawed hot wires close to the wall can possibly be related to the observations made by Schraub and Kline (33). They found that the pattern of flow appears to consist of an array of "islands of hesitation". Longitudinal vortices are formed at the edge of these "islands of hesitation". After the vortex has been carried away from the wall, it will break up into unoriented turbulence. The "islands of hesitation" are interspersed with areas of faster moving fluid. An attempt was made to do similar

studies in air. Schraub and Kline did their observations in water boundary layers, with the help of dye and the hydrogen-bubble technique. A "mammoth" hot wire was placed normal to the flow and close to the wall. In order to make observations, a Schlieren method was used. Close to the wall, darker lines interspersed with lighter lines were shed from the heated wire. This indicates that density gradients exist in a direction normal to the flow. The spacing of these lines seems to vary with the Reynolds number of the flow. For higher Reynolds numbers, the distance between streaks is smaller than for the lower Reynolds numbers. This agrees with the observations of Kline and Schraub (33). When the "mammoth" hot wire was placed in the same direction, but away from the wall, these streaks were no longer observed. The fact that density gradients exist across the flow, downstream from the wire, when the latter is placed close to the wall, indicates that the heat transfer from the wire is not constant along the wire. This can be interpreted as a passage of alternate fast and slow moving air past the wire. However, the density gradients are small and consequently, the contrast between light and dark areas is small. It was difficult to obtain photographs from which measurements could be made. Rough estimates show that the parameter $\lambda^* = \frac{\lambda' U_\tau}{\nu}$ is of the order of 100. Here λ' is the average spacing of the streaks. The results of Schraub and Kline indicate the value of $\lambda^* = 102 \pm 10$. This suggests that the

instability which produces the streaks depends on wall shear stress and viscosity.

The similarity law for flow near the wall,

$$\frac{U}{U_\tau} = f\left(\frac{yU_\tau}{\nu}\right) \tag{5-8}$$

seems to be valid. When the coordinates $\frac{U}{U_\tau}$ and $\frac{yU_\tau}{\nu}$ are used, either in a linear or in a semilogarithmic plot, the data collapse to one curve (Figures 51 and 52). The solid line in the linear plot is the semilogarithmic velocity distribution as was obtained by van Driest (7). The semilogarithmic law fits the data quite well in the range $40 < \frac{yU_\tau}{\nu} < 1000$. The semilogarithmic law was first derived by Prandtl using the mixing length theory. He had to assume that the mixing length was proportional to the distance from the wall and that the shear stress is constant, so that $\tau = \tau_w$. However, for the region where the semilogarithmic velocity distribution fits the data the ratio $\frac{\tau}{\tau_w}$ decreases from 1 to about 0.7 or 0.8, depending on the Reynolds number of the flow. Therefore, the assumption made by Prandtl is subject to a 20% to 30% error in this case. The reason why Prandtl did not make a serious error with this assumption can be obtained from equation (2-13). The assumption of constant shear stress leads to the similarity law for the flow near the wall. Clauser (5) arrives at the logarithmic velocity distribution by assuming that near the wall, the law of the wall, and for the outer flow the velocity defect law is valid. However, the

assumption of the law of the wall leads to the requirement that $\frac{\partial \tau}{\partial \eta}$ is at least a constant. The term $\mu \frac{\partial U_\tau}{\partial x}$ is extremely small, which implies that $\frac{\partial \tau}{\partial \eta}$ is almost zero.

The relation given by van Driest fits the data quite well for the range $0 < \frac{yU_\tau}{\nu} < 1000$. Possibly there is a Reynolds number effect. The high Reynolds-number data are best fit by Hama's curve in the region $5 < \frac{yU_\tau}{\nu} < 40$. Reichardt's curve and van Driest's curve are identical for the region $0 < \frac{yU_\tau}{\nu} < 40$. For high values of $\frac{yU_\tau}{\nu}$, Reichardt's expression reduces to $\frac{U}{U_\tau} = 5.25 + 5.5 \log \frac{yU_\tau}{\nu}$. Van Driest's constants in the semilogarithmic expression for the velocity distribution are 5.24 and 5.75, respectively. Reichardt fixed his relation for the turbulent shear stress such that the term $\overline{uv}$ varied proportionally to y^3 in the immediate neighborhood of the wall. This is in agreement with equation (2-48). Away from the wall, the Reynolds shear stress gradually changes to a linear distribution. Van Driest's relation allows the turbulent shear stress to vanish at the wall with the fourth power of y. Similarly, using Hama's relation, the turbulent shear stress vanishes like y^4 at the wall. In Figure 53, the relations for the mixing length given by Hama and van Driest are compared with the measured data. The assumption of a linear distribution for the mixing length is valid in the range $40 < \frac{yU_\tau}{\nu} < 400$. Within the viscous sublayer, Hama's relation for the mixing length seems

adequate. The data also indicate that $\frac{\ell U_\tau}{\nu}$ is a function of $\frac{yU_\tau}{\nu}$ in the region where the law of the wall is valid.

The semilogarithmic velocity distribution fits the data best in the range $40 < \frac{yU_\tau}{\nu} < 1000$. The linear sublayer can be expected in the range $0 < \frac{yU_\tau}{\nu} < 4$. The viscous sublayer extends from $\frac{yU_\tau}{\nu} = 0$ to $\frac{yU_\tau}{\nu} \simeq 60$. Beyond the viscous sublayer, the inertia terms can no longer be neglected. All terms in the equation of motion are of the same order of magnitude. Only the viscous term can be measured with any degree of accuracy. The other terms are either difficult to measure or are subject to error.

The balance of the mean energy equation (2-56) is difficult to obtain. The terms include the loss of kinetic energy of the mean flow due to its retardation. The term, $\frac{\partial U}{\partial x}$, was too small to be measured accurately in thick boundary layers, especially near the surface. The energy transfer term $\frac{\partial(U\,\overline{uv})}{\partial y}$ is a difficult term to measure. The distribution of the turbulent shear stress is subject to error. This means that the y-derivative of the term $U\,\overline{uv}$ becomes very unreliable. In order to show the order of magnitude of the terms in equation (2-58), it was assumed that $\frac{\tau_w}{\rho} - \nu \frac{\partial U}{\partial y} = -\overline{uv}$. Knowing the wall-shear stress and the mean velocity distribution, the turbulent shear stress can be obtained. In the viscous sublayer, the mean energy equation becomes

$$-\overline{uv}\,\frac{\partial U}{\partial y} + \frac{\partial(U\,\overline{uv})}{\partial y} - \frac{\nu}{2}\,\frac{\partial^2 U}{\partial y^2} + \nu\left(\frac{\partial U}{\partial y}\right)^2 = 0 \qquad (5\text{-}9)$$

or

$$\frac{\partial(U\,\overline{uv})}{\partial y} - \overline{uv}\,\frac{\partial U}{\partial y} - \nu\, U\,\frac{\partial^2 U}{\partial y^2} = 0 \quad . \qquad (5\text{-}10)$$

Figure 54 shows the distribution of the direct dissipation, the transfer of energy due to viscous diffusion and the work done by the viscous shear per unit time. The latter term is balanced by the first two terms. The distribution of the terms appearing in equation (5-10) is shown in Figure 55. Close to the wall, the dissipation due to the mean velocity gradient is more important than the turbulent energy dissipation. The flow is almost completely viscous. However, within a short distance the effect of viscosity becomes relatively unimportant. From here on, the turbulent energy dissipation dominates the total dissipation. In the region away from the wall, the kinetic energy, lost by the mean motion due to its retardation is mostly transferred to the wall region by the term $\frac{\partial(U\,\overline{uv})}{\partial y}$ (Figure 13.12 of reference 29). In the outer region, this last term is relatively large but of opposite sign when compared to the viscous sublayer. The total dissipation in the viscous sublayer is large compared to the dissipation in the outer layer. Most of the energy which is dissipated into heat comes from the outer layer due to the transfer of the energy which was taken away from the mean flow. According to Schubauer (35), 40 % of the energy lost by the mean flow is directly dissipated into heat, without going through the stage of turbulence. The remaining 60% of energy lost by the mean flow is transferred

into turbulent energy. The maximum rate of turbulence production takes place just outside the layer where the velocity profile is linear. The terms in the turbulent energy equation are difficult to measure. The turbulent dissipation, ϵ , has been obtained from the turbulence spectra, assuming local isotropy. The results will be discussed in the next section.

5.3 Energy Spectra and Turbulence Scales at Station: x = 85 feet

Further insight into the characteristics of turbulence in the boundary layer can be obtained by examining the spectral distribution of turbulent energy. Energy enters the spectrum through the large eddies and is then transferred through the spectrum to the smaller eddies where it is finally dissipated. Chapter II shows how the theory of local isotropy leads to expressions for the distribution of the one-dimensional spectrum function (equation (2-77)). In turbulent shear flow, it is not known how the one-dimensional spectrum function is related to the three-dimensional spectrum function. However, it is assumed that the one-dimensional spectrum function is still an integral effect of the three-dimensional spectrum function. In spite of these and other experimental difficulties, the study of the energy spectra may lead to very interesting conclusions.

In order to test the spectra for similarity, the data should be presented with $\frac{F(k)}{(\epsilon\, \nu^5)^{1/4}}$ and $\frac{k}{k_s}$ as coordinates. In Figure 56, a number of spectra of the longitudinal turbulent velocity are

represented in non-dimensional form. Included in this plot is the non-dimensional form of the one-dimensional energy spectrum function as was obtained by Heisenberg (equation (2-77)). The results show that equation (2-77) is a similarity law for the longitudinal energy spectra. Each spectrum branches away from Heisenberg's theoretical formula at a different point, depending on the size of the large scale eddies. In the region $10^{-1} < \frac{k}{k_s} < 1$, the experimental values of the non-dimensional spectrum seem to fall below the values predicted by Heisenberg. At the high frequency end of the spectra, the scatter of the data is appreciable. This is partly due to the fact that the spectra at 0.005 inch and 0.003 inch from the wall can no longer be predicted by Heisenberg's theoretical formula. The spectra at varying distances from the wall show varying extents of the inertial subrange, depending on the size of the large scale eddies. For example, the spectrum at $y = 0.022$ inch and $U_\infty = 20$ fps joins with Heisenberg's expression at the end of the inertial subrange. Consequently, the spectrum at this point will show only a very small region where $F(k)$ varies as $k^{-5/3}$. The spectrum at a point where the Reynolds number of the flow is much higher, for instance the spectrum at $y = 7.0$ inches and $U_\infty = 40$ fps, shows an appreciable region where $F(k)$ varies as $k^{-5/3}$. Sandborn and Marshall (31) have compared the spectra taken in the Army wind tunnel with spectra taken in flows with extremely high Reynolds numbers. These flows

included flow in an ocean tidal channel, and the flow of the atmosphere over water waves. These high Reynolds-number flows show a still larger region where $F(k)$ varies as $k^{-5/3}$.

The question is, what are the criteria for a turbulent shear flow to be considered locally isotropic? The theory does not predict when the turbulence may be considered to be locally isotropic. Bradshaw (3) compared the factor of proportionality, K, of equation (5-13) for power spectra obtained from grid turbulence and from turbulent shear flow. He found that the value of K in the spectrum formula $F(k) = K \epsilon^{2/3} k^{-5/3}$ is constant for homogeneous grid turbulence as well as for turbulent shear flow. The constancy of the factor K is true as long as the micro-scale Reynolds number, Re_λ, is not smaller than 100. A necessary condition for local isotropy to exist is the requirement $k >> \frac{1}{L_x}$. Here, L_x is the longitudinal integral scale of the turbulence as is defined in equation (2-93). The results of Figure 56 indicate the existence of the inertial subrange up to $\frac{k}{k_s} = 0.1$. The lower limit of the inertial subrange depends on the magnitude of the integral scale L_x. According to Figure 56, the $-\frac{5}{3}$ region of the energy spectrum shrinks to zero at about $Re_\lambda = 25$. The magnitudes for the micro-scale were obtained from the wave number spectra using equation (2-91). Bradshaw (3) points out that it is possible for the energy spectra to obey the local-isotropic relations in spite of the

fact the shear-stress spectra do not. The requirement for local similarity could follow from Kolmogoroff's postulate that in the inertial subrange the energy spectra depend on k and ϵ only. This leads to the similarity of the energy spectra when the data are presented using $\frac{k}{k_s}$ and $\frac{F(k)}{(\epsilon \nu^5)^{1/4}}$ as coordinates.

Figures 57 and 58 show the distribution of the macro-scales and the micro-scales. The scales decrease to zero at the surface, as might be expected, and seem to become constant in the fully turbulent part of the boundary layer. The macro-scales were determined by the use of equation (2-98). The micro-scales were determined either by using equation (2-91) or by use of equation (2-92). The results obtained by the method of integration of the second moment of the energy spectra seem to be more reliable than the results obtained from the differentiating circuit. The results show that the micro-scale obtained by the differentiation method are consistently higher. Based on the comparison of the magnitude of the turbulent dissipation with the magnitude of the production of turbulent energy, it can be concluded that the method of integration gives more reliable results.

Figures 59 and 60 show the distribution of the turbulent production and the turbulent dissipation. The turbulent dissipation was obtained by the use of equation (2-90). The necessary assumption of local isotropy seems to hold beyond the viscous sublayer. The

dissipation measurements are subject to a great deal of uncertainty. In equation (2-90), the major contribution comes from the inertial subrange. The energy spectrum, F(k), rapidly decreases in this range; on the other hand the square of the wave number increases rapidly. The product, k^2 F(k) , is therefore subject to a great deal of uncertainty, and consequently so are the values for the turbulent dissipation. Any conclusions concerning the validity of local isotropy in the relation for the turbulent dissipation are difficult to draw. First, reliable measurements are difficult to obtain especially close to the solid boundary. It is in this region where the bulk of the turbulent dissipation takes place. Secondly, it is not known how the production, diffusion and convection of turbulence affects the assumption of locally isotropic turbulence. Thirdly, only the one-dimensional spectrum can be measured. For isotropic turbulence this is no problem since the three-dimensional spectrum function can be expressed in terms of the one-dimensional spectrum function (equation (2-74)). Whether or not this expression is valid for turbulent shear flow is still an unanswered question.

Figures 59 and 60 show the distribution of the turbulent production and the turbulent dissipation. Since the turbulent convection and diffusion are small terms, one expects the production to be of the same order of magnitude as the turbulent dissipation. For U_∞ = 20 fps, the two terms are of the same order of magnitude in

the range $\frac{yU_\tau}{\nu} > 30$. For $U_\infty = 40$ fps, the production and dissipation are of the same order of magnitude in the range $\frac{yU_\tau}{\nu} > 130$. The assumption of locally isotropic turbulence seems valid outside the viscous sublayer. The criterion for validity of this assumption will depend also on the Reynolds number of the flow. When the flow has more time to develop, the turbulence will tend to become more isotropic. In this experiment, the boundary layer has developed for 85 feet. This is considerably longer than the 10.5 feet in Klebanoff's experiment. In Figure 61, the production term and the direct dissipation term are compared with Klebanoff's results. When plotted in dimensionless terms, a great deal of similarity can be observed. Figure 62 shows the comparison of the production term and the turbulent dissipation term with Klebanoff's data. The distributions of the dimensionless production term show excellent similarity. The turbulent dissipation term shows some scatter. However, since the turbulent dissipation is a difficult term to measure it probably falls well within the uncertainty limits.

Heisenberg's theoretical expression which fits the data (Figure 56) is

$$\frac{F(k)}{(\epsilon\nu^5)^{1/4}} = 0.48 \left(\frac{k}{k_s}\right)^{-5/3} \left[1 + 10.67 \left(\frac{k}{k_s}\right)^4\right]^{-4/3} . \quad (5\text{-}11)$$

For the inertial subrange one has

$$\frac{F(k)}{(\epsilon \nu^5)^{1/4}} = 0.48 \left(\frac{k}{k_s} \right)^{-5/3} \qquad (5\text{-}12)$$

or

$$F(k) = 0.48 \ \epsilon^{2/3} \ k^{-5/3} \ . \qquad (5\text{-}13)$$

Consequently, all spectra which can be represented by Heisenberg's theoretical expression must yield a proportionality factor, K , of 0.48. Bradshaw found from several sets of experimental data a value of 0.5. He used the following formula for the turbulent dissipation:

$$\epsilon = \frac{U_\tau^3}{L} \ . \qquad (5\text{-}14)$$

Here, L is the dissipation length parameter, and is represented as $L = \frac{1}{A} y = 0.4 y$, for the inner part of the turbulent boundary layer. In dimensionless form, equation (5-14) becomes:

$$\frac{\nu \epsilon}{U_\tau^4} = \frac{2.5}{y U_\tau / \nu} \ . \qquad (5\text{-}15)$$

This expression for the turbulent dissipation shows a remarkable similarity with Klebanoff's data (Figure 62), in the range $10 < \frac{y U_\tau}{\nu} < 2000$. Table II gives the parameters calculated from the energy spectra using the relations for isotropic turbulence.

In Figure 63, the one-dimensional energy spectra are plotted for different values of y . The plot shows how, for small distances of y , more energy is contained at higher wave numbers. At larger

distances away from the wall (y = 0.5 inch), less energy is contained at high wave numbers. For $\frac{yU_\tau}{\nu} > 120$, the value of ϵ changes very little as compared to the value of ϵ in the range $\frac{yU_\tau}{\nu} < 120$ (Figure 62). Consequently, the one-dimensional energy spectra in the range $\frac{yU_\tau}{\nu} > 120$ tend to become similar (equation (5-13)). Table III gives the numerical values of $F(k)/\overline{u^2}$ for all measured spectra.

As mentioned before, measurements were made of the lateral velocity correlation coefficients. The results are shown in Figures 64 and 65. These measurements were made with two vertical wires, parallel to each other and positioned as close to the wall as possible. It was estimated that the centers of the wires were approximately 0.015 inch from the wall. From these measurements, the lateral integral scale of the eddies close to the wall can be measured. It is observed that the lateral correlation coefficient becomes negative for larger separation distances. This is similar to the results of correlation measurements made by Willmarth and Tu (43). These authors give a model for the turbulence structure in the immediate neighborhood of the wall. Vortex lines which are originally parallel to the wall in the z-direction are bent and stretched in the direction of the flow at some angle to the wall. This model explains why, close to the wall, areas of faster moving fluid are alternated with areas of slower moving fluid. This phenomenon was observed by Schraub and

Kline (33), and also in the present experiment with the "mammoth" hot wire in the wind tunnel.

Chapter VI

CONCLUSIONS

The turbulent boundary layer can be considered to be divided into three regions. The first region is in the immediate neighborhood of the wall, where the inertia terms in the equation of motion are small compared to the other terms. The second region makes up the largest part of the boundary layer, where the flow is fully turbulent. In this region, the viscous term in the equation of motion is small compared to the other terms. Between these two regions exists a transition region where all the terms in the equation of motion are small, but of the same order of magnitude. The present study was carried out to evaluate the flow quantities in the wall region of the turbulent boundary layer. While the concepts of a constant shear layer have been discussed in the literature, no detailed measurements for this region are available.

The existence of local similarity close to the wall and in the outer portion of the turbulent boundary layer has been experimentally justified in this experiment as well as many others. It has been pointed out that $\frac{\partial U_\tau}{\partial x}$ has to be independent of x in order that the law of the wall is a similarity law. Similarly, $\frac{\partial U_\tau}{\partial x}$ has to vanish in order that the velocity defect law is a similarity law. Experimental data have indicated that both methods of correlation overlap in a region outside the viscous sublayer. Therefore, it can be concluded

that $\frac{\partial U_\tau}{\partial x} = 0$ is a requirement for local similarity. When the similarity law, $\frac{U}{U_\tau} = f\left(\frac{yU_\tau}{\nu}\right)$, is introduced into the equation of motion it can be concluded that $\frac{\partial \tau}{\partial y} = 0$, since it is required that $\frac{\partial U_\tau}{\partial x} = 0$. This means that for boundary layer flow with zero pressure gradient, a constant shear layer must exist in the region where the law of the wall is valid. Experimental evidence shows that the law of the wall is valid in the region $0 < \frac{yU_\tau}{\nu} < 1000$. Consequently, one may expect the constant shear layer to exist in the same region.

The experimental results indicate that a constant shear layer exists in the region $0 < \frac{yU_\tau}{\nu} < 60$. This, in spite of the fact that the law of the wall correlates the data in the region $0 < \frac{yU_\tau}{\nu} < 1000$. It was found that turbulent shear-stress measurements can be subject to considerable error. In order to investigate this problem, measurements were made for $\sqrt{\overline{u^2}}$ with a hot wire in a horizontal and a vertical position. The results from the vertical wire showed a definite increase in the magnitude of $\sqrt{\overline{u^2}}$, especially near the surface. It was concluded that in this region the measurements from the vertical wire were influenced by the gradient of the mean velocity in the y-direction. The result was that the heat transfer along the wire was not uniform, and incorrect values for the rms voltage were obtained. The measurements with the yawed hot wire were corrected for the effect of velocity gradient using the results from the vertical and

horizontal wire. After these corrections were made the turbulent shear stress could be obtained within an uncertainty range of ±10%.

The local similarity of the flow near the wall was established experimentally. The semilogarithmic expression for the velocity distribution is derived for the region where the law of the wall and the velocity defect law overlap. The semilogarithmic velocity distribution fits the data best in the range $40 < \frac{yU_\tau}{\nu} < 1000$. For the outer layer, a great deal of similarity is observed when $\frac{U}{U_\infty}$ and $\frac{y}{\delta}$ are used as coordinates. For boundary layers with a Reynolds number of the order of 10^8 to 10^9, the local skin-friction coefficient varies very little with x, and similarity of the above mentioned form is observed.

Van Driest's relation for the velocity distribution in the region where the law of the wall is valid fits the data quite well. In the region $40 < \frac{yU_\tau}{\nu} < 1000$, van Driest's expression becomes $\frac{U}{U_\tau} = 5.24 + 5.75 \log \frac{yU_\tau}{\nu}$. The assumption of a linear distribution for the mixing length is in agreement with the measurements in the range $40 < \frac{yU_\tau}{\nu} < 400$. In the viscous sublayer, Hama's relation for the mixing length coincides quite well with the measurements.

It was difficult to obtain a reliable average of the rms voltage from a hot wire which was partly or completely projected in the y-direction. This is especially true for measurements close to the wall. The idea was conceived that this observation could be related

to the "streaky" structure of the turbulence near the surface as was observed by Schraub and Kline. A Schlieren image from a "mammoth" hot wire normal to the flow and close to the wall of the wind tunnel showed alternating areas of fast and slow moving fluid. The distance between these areas varied with the magnitude of the Reynolds number of the flow. Measurements of the lateral velocity correlation coefficient are in agreement with these observations.

The energy density spectra of the longitudinal turbulence component show a great deal of similarity when plotted in non-dimensional form. Except for spectra of points within 0.010 inch of the wall, Heisenberg's expression correlates the data quite well. However, this does not include the low wave-number range. Although the data correlate well with Heisenberg's expression it cannot therefore be concluded that the turbulence is locally isotropic everywhere in the turbulent boundary layer. The term $\epsilon^{1/4}$ appears in Heisenberg's expression; consequently, this expression is insensitive to changes in ϵ. The existence of the inertial subrange where the spectrum falls off as $k^{-5/3}$ is also an inconclusive argument for the existence of local isotropy. Every spectrum varies as $k^{-5/3}$ at some point. A better way to decide whether or not local isotropy exists is to check the magnitude of the factor of proportionality, K, in the spectrum formula $F(k) = K\epsilon^{2/3}k^{-5/3}$. This expression is more sensitive to changes in ϵ than Heisenberg's equation. The most reliable way to check the existence of local isotropy is to

measure the individual terms in the expression for the turbulent dissipation by means of hot-wire anemometry, and to compare these results with the calculated values from the expression $\epsilon = 15\nu \int_0^\infty k^2 F(k)\, dk$.

The conclusions can be summarized as follows:

1. The existence of local similarity of the form $\frac{U}{U_\tau} = f\left(\frac{yU_\tau}{\nu}\right)$ demands the existence of a constant shear layer.
2. Experimental results show that the constant shear layer exists only in the region $0 < \frac{yU_\tau}{\nu} < 60$.
3. Turbulent shear measurements are usually too high close to the wall where large mean velocity gradients occur.
4. The existence of local similarity was well established for high Reynolds number boundary layers.
5. The "streaky" structure of the turbulence close to the wall as described by Schraub and Kline was confirmed.
6. The longitudinal and vertical turbulence components are much closer in magnitude than previous published results would indicate.
7. Local isotropy seems to exist outside the viscous sublayer of turbulent boundary layers whose Reynolds numbers are sufficiently large.

BIBLIOGRAPHY

BIBLIOGRAPHY

1. Batchelor, G. K., Kolmogoroff's theory of locally isotropic turbulence. Proceedings Cambridge Philosophical Society, 43:533-559, 1947.

2. Betchov, R., On the fine structure of turbulent flows. Journal of Fluid Mechanics, 3:205-216, 1957.

3. Bradshaw, P., Conditions for the existence of an inertial subrange in turbulent flow. NPL Aero Report 1220, A.R.C. 28 664, F. M. 3798, 1967.

4. Chao, J. L., Turbulent momentum transfer in a three-dimensional wall jet. Ph. D. Dissertation, Colorado State University, Fort Collins, Colorado, June 1965.

5. Clauser, F. H., The turbulent boundary layer. Advances in Applied Mechanics 4:1-51, 1954.

6. Corcos, G. M., Pressure measurements in unsteady flows. Symposium on Measurement in Unsteady Flow, American Society of Mechanical Engineers, Worcester, Mass., 1962.

7. van Driest, E. R., On turbulent flow near a wall. Journal of the Aeronautical Sciences. 23:1007-1011, 1956.

8. Dryden, H. L., Schubauer, G. B., Mock, Jr., W. C. and Skramstad, H. K., Measurements of intensity and scale of wind tunnel turbulence and their relation to the critical Reynolds number of spheres. NACA T. R. 581, 1937.

9. Dryden, H. L., A review of the statistical theory of turbulence. Quarterly of Applied Mathematics. 1:7-42, 1943.

10. Fage, A., On the static pressure in fully developed turbulent flow. Proceedings of the Royal Society, A 155;576-596, 1936.

11. Finn, C. L. and Sandborn, V. A., The design of a constant temperature hot-wire anemometer. U.S. Army Research Grant DA-AMC-28-043-65-G20 and NASA, NGR-06-002-038, CER 66-67 CLF-36, Colorado State University, Fort Collins, Colorado, March 1967.

12. Frenkiel, F. N., Effects of wire length in turbulence investigations with hot-wire anemometer. Aeronautical Quarterly, 5:1-24, 1954.

13. Goldstein, S., Modern developments in fluid dynamics. Volume I, Dover Publications, Inc., New York, 1965.

14. Hama, F. R., On the velocity distribution in the laminar sublayer and transition region in turbulent shear flows. Journal of the Aeronautical Sciences. 20:648-649, 1953.

15. van der Hegge Zijnen, B. G., Heat transfer from horizontal cylinders to a turbulent airflow. Applied Scientific Research, Section A, 7:205-223, 1958.

16. Heisenberg, W., On the statistical theory of turbulence. Translation of: Zur Statistischen Theory der Turbulenz. Zeitschrift für Physic, 124, 1948. NACA TM 1431, 1958.

17. Hinze, J. O., Turbulence: An introduction to its mechanism and theory. McGraw-Hill Book Company, Inc., New York, 1959.

18. Klebanoff, P. S., and Diehl, Z. W., Some features of artificially thickened fully developed turbulent boundary layers with zero pressure gradient. NACA Rep. 1110, 1952.

19. Klebanoff, P. S., Characteristics of turbulence in a boundary layer with zero pressure gradient. NACA TN 3178, 1954.

20. Landweber, L., Reanalysis of flat-plate boundary-layer data. Proceedings of Ninth International Towing Tank Conference, Paris, September 1960.

21. Liu, C.Y. and Sandborn, V. A., Evaluation of the turbulent energy dissipation from time derivative measurements. U.S. Army Research Grant DA-AMC-28-043-64-G-9, CEM 65 CYL-VAS5, Colorado State University, Fort Collins, Colorado, April 1965.

22. MacMillan, F. A., Viscous effects on flattened pitot tubes at low speeds. Journal of the Royal Aeronautical Society. 58:837-839, 1954.

23. MacMillan, F. A., Experiments on pitot-tubes in shear flow. A.R.C., Reports and Memoranda No. 3028, 1956.

24. Mitchell, J. E. and Hanratty, T. J., Study of turbulence at a wall using an electro-chemical wall shear-stress meter. Journal of Fluid Mechanics. 26:199-221, 1966.

25. Piercy, N. A. V., Richardson, E. G., and Winny, H. F., On the convection of heat from a wire moving through air close to a cooling surface. The Proceedings of the Physical Society, 69B:731-742, 1956.

26. Plate, E. J. and Cermak, J. E., Micro-meteorological wind tunnel facility. Final Report, Fluid Dynamics and Diffusion Laboratory, Colorado State University, Fort Collins, Colorado, 1963.

27. Plate, E. J. and Sandborn, V. A., Modeling of a thermally stratified boundary layer. U.S. Army Research Grant DA-AMC-28-043-65-G20, CEM 66 EJP-VAS8, Colorado State University, Fort Collins, Colorado, April 1966.

28. Reichardt, H., Vollständige Darstellung der turbulenten Geschwindigkeitsverteilung in glatten Leitungen. Zeitschrift für angewandte Mathematik und Mechanik. 31:208-219, 1951.

29. Rotta, J. C., Turbulent boundary layers in incompressible flow. Progress in Aeronautical Sciences, Volume 2, Boundary Layer Problems, Edited by Ferri, A. et al., New York, N.Y., The Macmillan Company, 1962.

30. Sandborn, V. A. and Slogar, R. J., Study of the momentum distribution of turbulent boundary layers in adverse pressure gradients. NACA TN 3264, 1955.

31. Sandborn, V. A., and Marshall, R. D., Local isotropy in wind tunnel turbulence. U.S. Army Research Grant DA-AMC-28-043-64-G-9, CER 65 VAS-RDM 71, Colorado State University, Fort Collins, Colorado, October 1965.

32. Sandborn, V. A., Hot-wire anemometer measurements in large-scale boundary layers. U.S. Army Research Grant DA-AMC-28-043-65-G20, CER66-67VAS32, Colorado State University, Fort Collins, Colorado, March 1967.

33. Schraub, F. A. and Kline, S. J., A study of the structure of the turbulent boundary layer with and without longitudinal pressure gradients. Stanford University Report MD - 12, 1965.

34. Schubauer, G. B. and Klebanoff, P. S., Investigation of separation of the turbulent boundary layer. NACA TN 2133, 1950.

35. Schubauer, G. B., Turbulent processes as observed in boundary layer and pipe. Journal of Applied Physics, 25:188-196, 1954.

36. Smith, D. W. and Walker, J. H., Skin-friction measurements in incompressible flow. NASA Rep. R-26, 1959.

37. Taylor, G. I., Statistical theory of turbulence, Part I - IV. Proceedings of the Royal Society, A151:421-478, 1935.

38. Taylor, G. I., The spectrum of turbulence. Proceedings of the Royal Society, A164:192-215, 1938.

39. Townsend, A. A., The structure of the turbulent boundary layer. Proceedings Cambridge Philosophical Society, 47:375-395, 1950.

40. Townsend, A. A., The structure of turbulent shear flow. Cambridge University Press, 1956.

41. Uberoi, M. S. and Kovasznay, L. S. G., On mapping and measurements of random fields. Quarterly of Applied Mathematics. 10:375-393, 1953.

42. Wills, J. A. B., The correction of hot-wire readings for proximity to a solid boundary. Journal of Fluid Mechanics, 12:388-396, 1962.

43. Willmarth, W. W. and Tu, B. J., An experimental study of the structure of turbulence near the wall through correlation measurements in a thick turbulent boundary layer. University of Michigan, Technical Report 02920-3-T, 1966.

APPENDIX

APPENDIX

COMMERCIAL INSTRUMENTATION

Pressure Transducer

A Trans-sonics Type 120B Equibar pressure meter was used to obtain pressure measurements. The instrument is a portable differential micromanometer which operates over a total pressure range of 0 - 30 mm Hg in eight full-scale ranges. The pressure sensor is a differential capacitance device consisting of a stretched diaphragm clamped between two glass discs. Capacitor electrodes are formed on the concave surfaces of the discs, adjacent to the diaphragm. These two capacitances form two arms of an A. C. bridge. Any pressure differential causes an unbalance of the bridge. This signal is amplified and fed to a detector circuit, which provides a voltage to the meter and to the D.C. output terminals. The D.C. output varies from 0 - 30 millivolts ± 2%, proportional to the pressure differential. This output is the same for each scale range. The accuracy of the meter reading is listed as 3% full scale of each selected range. Since the kinetic pressure measurements in the turbulent boundary layer were subject to a great deal of fluctuation, it was necessary to integrate the output of the Trans-sonics over a suitable period of time in order to obtain an accurate measurement. The D.C. output of the Trans-sonics was first amplified one hundred times by

means of a D.C. amplifier, and then integrated over a time span of 200 seconds. A calibration curve (Figure 17) of pressure in mm Hg versus integrator output voltage was obtained for each scale range of the Trans-sonics. Since the D.C. output of the Trans-sonics varied from 0 - 30 millivolts for each scale setting, these calibration curves were all similar when plotted on the proper scale. A Meriam Model 34FB2TM micromanometer was used as standard to calibrate the Trans-sonics electronic manometer. A calibration curve (Figure 18) for each scale range was obtained.

True R.M.S. Voltmeter

In order to measure the A.C. output of the constant temperature hot-wire anemometer, a Brüel and Kjear electronic voltmeter type 2416 was used. This instrument is able to make A.C. voltage measurements in the frequency range of 2 cps to 200,000 cps and has eleven voltage ranges varying from 10 millivolts to 1,000 volts full scale deflection in 10 db steps.

A two-stage amplifier is followed by rectifying and squaring circuits for rms, average and peak measurements, and a moving coil meter. A large capacitor can be connected across the meter to obtain accurate readings. Since the amplifier is provided with an output jack, the instrument can be used as a calibrated amplifier having a maximum gain of 60 db. The frequency response of the instrument is linear within 2% rms from 2 cps to 200,000 cps. The accuracy of the

meter scale is listed as better than 1% of the full scale deflection. This instrument was used as an amplifier for the A.C. signal from the hot-wire anemometer before it was recorded on F.M. magnetic tape.

Wave Analyzer

The spectra of the turbulence signals from the hot-wire anemometer were determined from magnetic tape and analyzed by means of a Technical Products Company wave-analyzer system. A signal of approximately 1.0 volts rms from the magnetic tape was fed in the input of the T.P. -627 analyzer. The second input to the T.P. -627 analyzer came from the T.P.-626 oscillator which provided the heterodyne signal for the analyzer. The T.P.-627 analyzer was used with a filter having an effective band width of 1.12 cps. The output of the filter will be the power in the 1.12 cps filter band at the frequency to which the T.P.-626 oscillator is tuned. This output was fed to the T.P.-633 power integrator where the signal was squared. Additional circuitry in the T.P.-633 power integrator provides the functions of integrating over a certain time period up to 100 seconds and multiplying the signal by the reciprocal of the integrating time. After the T.P.-633 power integrator performs the necessary functions to obtain the power spectrum, the output can either be fed to an X-Y recorder or the output can be read immediately on a built-in meter.

In order to obtain accurate readings, the output of the T.P. -633 was integrated for two minutes by means of the integrator circuit. Occasionally, the results of the Technical Products Company wave analyzer were checked against the results of a spectrum analyzer type 2109, manufactured by Brüel and Kjear. These passive filters were of the octave type, varying in band width approximately proportional to the center frequency.

Multiplier

For the two point lateral-space correlation, a Philbrick multiplier was used. The output of the multiplier is a D.C. voltage which was fed into the integrator in order to obtain accurate results. The correlation coefficient can be written as

$$R_z = \frac{\overline{u_1 u_2}}{\sqrt{\overline{u_1^2}}\ \sqrt{\overline{u_2^2}}} \quad .$$

The multiplier was calibrated in such a way that the correlation coefficient could be obtained from

$$R = \frac{25 \quad E_{out}}{\sqrt{\overline{e_1^2}}\ \sqrt{\overline{e_2^2}}} \quad ,$$

where E_{out} is the D.C. output of the multiplier. Since the sensitivity coefficients cancel, the required velocity correlation coefficient can be obtained directly from the measured voltages.

TABLES

TABLE I - TURBULENT BOUNDARY-LAYER PARAMETERS

x	U_∞	U_τ	c_f	τ_w	δ	δ^*	θ	H	Re_x	x'	ν
ft	fps	fps		lbs/ft^2	inches	inches	inches			ft	$ft^2/sec.$
12	30.30	1.011	2.228×10^{-3}	1.900×10^{-3}	11.04	1.66	1.22	1.37	2.23×10^{-7}	155	2.10×10^{-4}
22	29.35	0.995	2.299 x	1.836 x	14.70	2.10	1.61	1.30	1.73 x	124	2.10 x
32	29.56	0.967	2.139 x	1.731 x	18.77	2.61	1.99	1.31	3.14 x	223	2.10 x
42	29.50	0.948	2.063 x	1.658 x	22.10	3.02	2.30	1.31	4.30 x	308	2.11 x
52	29.33	0.916	1.952 x	1.551 x	24.12	3.59	2.72	1.32	6.80 x	490	2.12 x
62	29.44	0.897	1.859 x	1.489 x	27.06	3.95	2.96	1.34	1.03×10^{-8}	737	2.11 x
72	29.47	0.889	1.822 x	1.463 x	30.14	4.41	3.32	1.33	1.21 x	864	2.11 x
85	30.84	0.903	1.713 x	1.564 x	33.75	4.86	3.64	1.33	2.14 x	1377	1.99 x
85	20.25	0.610	1.817 x	0.715 x	35.04	4.59	3.44	1.34	1.24 x	1216	1.99 x
85	41.40	1.186	1.642 x	2.701 x	32.46	4.57	3.46	1.32	3.10 x	1487	1.99 x

TABLE II - PARAMETERS OBTAINED FROM SPECTRUM CALCULATIONS
$U_\infty \simeq 20$ fps

y inches	$\frac{yU_\tau}{\nu}$	λ inches	L_x inches	ϵ ft^2/sec^3	$\frac{\sqrt{\overline{u^2}}\lambda}{\nu}$
0.005	1.21	0.028	0.090	20.2	2.7
0.008	1.94	0.034	0.156	32.5	4.3
0.010	2.42	0.043	0.207	32.4	6.8
0.014	3.39	0.058	0.302	32.2	12.5
0.022	5.33	0.071	0.339	47.6	22.7
0.032	7.66	0.092	0.471	50.7	39.1
0.050	12.1	0.110	0.660	53.1	57.5
0.150	36.4	0.129	0.754	34.2	62.7
0.200	48.5	0.135	0.905	28.5	63.1
0.300	72.7	0.133	1.093	25.7	58.2
0.400	97.0	0.152	1.206	19.0	65.5
0.500	121	0.163	1.320	16.3	69.4
0.500	121	0.224	1.282	9.32	93.5
1.0	242	0.259	1.357	6.70	106
1.5	364	0.297	1.494	4.66	116
2.0	485	0.324	1.847	3.66	123
3.0	727	0.361	2.074	2.63	129
4.0	970	0.383	2.167	2.25	134
5.0	1212	0.393	2.357	2.19	139
6.0	1454	0.427	2.357	1.87	152
7.0	1697	0.437	2.431	1.79	156

TABLE II - PARAMETERS OBTAINED FROM SPECTRUM CALCULATIONS - Cont'd.
$U_\infty \simeq$ 40 fps

y inches	$\frac{yU_\tau}{\nu}$	λ inches	L_x inches	ϵ ft^2/sec^3	$\frac{\sqrt{u^2}\ \lambda}{\nu}$
0.003	1.40	0.017	0.132	286	3.2
0.007	3.27	0.040	0.198	260	16.6
0.010	4.67	0.056	0.358	253	31.
0.013	6.07	0.070	0.452	255	47.
0.018	8.41	0.088	0.490	246	76.
0.023	10.7	0.106	0.603	212	98.
0.028	13.1	0.117	0.754	195	122.
0.058	27.1	0.142	0.905	141	155.
0.108	50.4	0.164	1.06	96.7	171.
0.208	97.2	0.191	1.32	71.3	201.
0.308	144	0.217	1.47	55.0	227.
0.408	191	0.239	1.62	44.7	247.
0.508	237	0.261	1.89	37.3	270.
0.5	234	0.202	2.45	65.0	200.
1.0	467	0.244	2.83	40.7	231.
1.5	701	0.265	2.92	32.0	242.
2.0	934	0.296	3.20	23.9	260.
3.0	1400	0.329	3.30	17.4	275.
4.0	1868	0.360	3.58	13.7	292.
5.0	2335	0.388	3.77	10.8	302.
6.0	2802	0.395	3.96	9.52	293.
7.0	3270	0.401	4.15	8.48	306.

TABLE III - NUMERICAL VALUES OF MEASURED ONE-DIMENSIONAL SPECTRUM FUNCTIONS $U_\infty \simeq 40$ fps

y = 0.003 inch		y = 0.007 inch		y = 0.010 inch		y = 0.013 inch		y = 0.018 inch		y = 0.023 inch	
k	$F(k)/\overline{u^2}$	k	$F(k)/\overline{u^2}$	k	$F(k)/\overline{u^2}$	k	$F(k)/\overline{u^2}$	k	$F(k)/\overline{u^2}$	k	$F(k)/\overline{u^2}$
17.3	7.02×10^{-3}	7.32	9.9×10^{-3}	5.11	1.88×10^{-2}	3.93	2.08×10^{-2}	2.85	2.49×10^{-2}	2.36	2.83×10^{-2}
25.9	6.20	11.0	1.02×10^{-2}	7.67	1.59	5.90	1.87	4.28	2.33	3.54	2.51
34.6	5.19	14.6	9.11×10^{-3}	10.2	1.44	7.87	1.64	5.71	2.00	4.72	2.17
43.2	4.10	18.3	8.46	12.8	1.20	9.84	1.39	7.14	1.90	5.90	1.98
51.9	3.78	22.0	6.48	15.3	1.09	11.8	1.23	8.56	1.65	7.08	1.65
60.5	3.46	25.6	6.61	17.9	9.26×10^{-3}	13.8	1.02	9.99	1.49	8.26	1.73
69.1	3.05	29.3	5.87	20.4	9.21	15.7	1.10	11.4	1.40	9.44	1.61
86.4	2.48	36.6	5.93	25.6	7.83	19.7	9.11×10^{-3}	14.3	1.22	11.8	1.40
108.0	2.24	45.8	4.79	31.9	7.05	24.6	8.09	17.8	1.08	14.7	1.24
138	1.87	58.6	4.41	40.9	6.06	31.5	6.98	22.8	9.39×10^{-3}	18.9	1.04
173	1.67	73.2	3.51	51.1	5.00	39.3	6.06	28.5	8.11	23.6	9.13×10^{-3}
216	1.42	91.5	2.87	63.9	4.06	49.2	5.25	35.7	6.97	29.5	7.51
277	1.16	117	2.34	81.8	3.30	63.0	4.26	45.7	5.85	37.7	6.37
346	8.49×10^{-4}	146	1.82	102	2.52	78.7	3.39	57.1	4.52	47.2	5.36
432	5.87	183	1.46	128	1.98	98.4	2.42	71.4	3.62	59.0	4.39
540	3.82	229	1.13	160	1.68	123	1.84	89.2	2.95	73.7	3.41
691	2.54	293	7.34×10^{-4}	204	1.09	157	1.50	114	2.30	94.4	2.63
864	1.56	366	5.19	256	8.49×10^{-4}	197	1.14	143	1.76	118	2.08
1080	1.00	458	3.29	319	5.35	246	8.37×10^{-4}	178	1.12	147	1.69
1383	6.30×10^{-5}	586	2.03	409	4.09	315	5.67	228	1.10	189	1.27
1729	4.03	732	1.27	511	2.36	393	3.72	285	7.98×10^{-4}	236	9.75×10^{-4}
2161	2.83	915	7.52×10^{-5}	639	1.01	492	2.05	357	3.99×10^{-4}	295	4.23
2766	2.04	1171	4.14	818	4.86×10^{-5}	630	5.95×10^{-5}	457	8.83×10^{-5}	377	1.04
3457	9.16×10^{-6}	1464	1.08	1022	1.14×10^{-5}	787	1.60×10^{-5}	571	2.38×10^{-5}	472	2.89×10^{-5}
4321	1.60×10^{-6}	1830	2.32×10^{-6}	1278	3.0×10^{-6}	984	3.0×10^{-6}	714	3.99×10^{-6}	590	4.55×10^{-6}
5402	3.65×10^{-7}	2288	6.30×10^{-7}	1597	5.28×10^{-7}	1230	5.56×10^{-7}	892	8.89×10^{-7}	737	9.10×10^{-7}
6914	8.18×10^{-8}	2929	1.25×10^{-7}	2044	1.24×10^{-7}	1574	1.37×10^{-7}	1142	2.37×10^{-7}	944	2.54×10^{-7}
8643	3.56×10^{-8}	3661	4.05×10^{-8}	2555	4.72×10^{-8}	1967	6.51×10^{-8}	1427	9.84×10^{-8}	1180	8.13×10^{-8}
						2459	4.46×10^{-8}			1475	5.20×10^{-8}

y = 0.028 inch		y = 0.058 inch		y = 0.108 inch		y = 0.208 inches		y = 0.308 inches		y = 0.408 inches	
k	$F(k)/\overline{u^2}$	k	$F(k)/\overline{u^2}$	k	$F(k)/\overline{u^2}$	k	$F(k)/\overline{u^2}$	k	$F(k)/\overline{u^2}$	k	$F(k)/\overline{u^2}$
2.10	3.87×10^{-2}	1.60	4.66×10^{-2}	1.44	5.18×10^{-2}	1.30	6.79×10^{-2}	1.23	7.49×10^{-2}	1.19	8.30×10^{-2}
3.14	3.27	2.40	3.82	2.16	4.56	1.95	6.36	1.85	6.54	1.78	7.66
4.19	3.20	3.20	3.30	2.88	4.12	2.60	6.00	2.47	6.00	2.38	7.04
5.24	2.80	4.00	3.25	3.60	3.49	3.26	5.21	3.08	5.53	2.97	6.42
6.29	2.42	4.80	2.85	4.32	3.26	3.91	4.47	3.70	4.98	3.56	5.75
7.34	2.15	5.60	2.56	5.04	2.88	4.56	3.85	4.32	4.62	4.16	4.62
8.39	1.95	6.40	2.18	5.76	2.58	5.21	3.45	4.93	3.90	4.75	4.03
10.5	1.68	8.00	1.96	7.20	2.03	6.51	2.76	6.17	3.54	5.94	3.42
13.1	1.46	10.0	1.71	9.00	1.75	8.14	2.43	7.71	2.71	7.42	2.91
16.8	1.22	12.8	1.45	11.5	1.48	10.4	2.02	9.87	2.22	9.50	2.43
21.0	1.02	16.0	1.22	14.4	1.21	13.0	1.63	12.3	1.70	11.9	2.05
26.2	8.5×10^{-3}	20.0	9.92×10^{-3}	18.0	1.06	16.3	1.27	15.4	1.36	14.8	1.62
33.5	6.68	25.6	7.78	23.0	8.74×10^{-3}	20.8	9.37×10^{-3}	19.7	1.12	19.0	1.26
41.9	5.41	32.0	6.41	28.8	7.00	26.0	7.45	24.7	8.86×10^{-3}	23.8	9.34×10^{-3}
52.4	4.29	40.0	5.26	36.0	6.05	32.6	6.29	30.8	7.16	29.7	6.51
65.5	3.48	50.0	4.31	45.0	4.96	40.7	5.02	38.6	4.94	37.1	4.71
83.9	2.70	64.0	3.47	57.6	4.48	52.1	4.08	49.3	4.13	47.5	3.99
104.8	2.24	80.0	3.28	72.0	4.09	65.1	3.18	61.7	3.75	59.4	3.43
131	2.05	100	2.73	90.0	3.36	81.4	2.75	77.1	3.07	74.2	3.09
168	1.47	128	2.10	115	2.58	104	2.15	98.7	2.56	95.0	2.57
210	1.00	160	2.00	144	2.02	130	1.50	123	1.87	119	1.89
262	5.80×10^{-4}	208	6.86×10^{-4}	187	8.0×10^{-4}	169	4.87×10^{-4}	160	4.91×10^{-4}	154	4.00×10^{-4}
335	1.22×10^{-4}	256	1.71×10^{-4}	230	2.16×10^{-4}	208	1.78×10^{-4}	197	1.53×10^{-4}	190	1.24×10^{-4}
419	3.34×10^{-5}	320	4.69×10^{-5}	288	7.12×10^{-5}	260	4.53×10^{-5}	247	3.49×10^{-5}	238	2.74×10^{-5}
524	7.5×10^{-6}	400	9.92×10^{-6}	360	1.3×10^{-5}	326	1.02×10^{-5}	308	9.0×10^{-6}	297	5.93×10^{-6}
655	2.0×10^{-6}	500	2.70×10^{-6}	450	2.26×10^{-6}	407	2.17×10^{-6}	386	1.78×10^{-6}	371	1.38×10^{-6}
839	4.0×10^{-7}	640	5.72×10^{-7}	576	6.36×10^{-7}	521	5.13×10^{-7}	493	4.39×10^{-7}	475	4.26×10^{-7}
1048	1.08×10^{-7}	800	1.91×10^{-7}	720	1.96×10^{-7}	651	1.40			594	2.14×10^{-7}
						814	1.50				

TABLE III - NUMERICAL VALUES OF MEASURED ONE-DIMENSIONAL SPECTRUM FUNCTIONS $U_\infty \geq 40$ fps - Cont'd.

y = 0.508 inch		y = 0.50 inch		y = 1.00 inch		y = 1.50 inch		y = 2.00 inch		y = 3.00 inch	
k	$F(k)/\overline{u^2}$	k	$F(k)/\overline{u^2}$	k	$F(k)/\overline{u^2}$	k	$F(k)/\overline{u^2}$	k	$F(k)/\overline{u^2}$	k	$F(k)/\overline{u^2}$
1.15	9.36×10^{-2}	1.15	1.25×10^{-1}	1.05	1.46×10^{-1}	0.993	1.27×10^{-1}	0.958	1.69×10^{-1}	0.911	1.66×10^{-1}
1.73	8.69	1.73	1.22	1.57	1.26	1.49	1.36	1.44	1.54	1.37	1.68
2.31	7.36	2.31	1.08	2.10	1.09	1.99	1.26	1.92	1.24	1.82	1.43
2.89	6.19	2.88	1.01	2.62	9.06×10^{-2}	2.48	1.02	2.39	1.16	2.28	1.15
3.46	5.35	3.46	7.62×10^{-2}	3.15	8.98	2.98	1.02	2.87	9.43×10^{-2}	2.73	1.12
4.04	4.85	4.04	6.90	3.67	7.24	3.48	8.32×10^{-2}	3.35	7.82	3.19	9.89×10^{-2}
4.62	4.35	4.61	5.66	4.19	6.51	3.97	7.75	3.83	6.89	3.65	8.71
5.77	3.68	5.77	4.55	5.24	4.77	4.97	6.21	4.79	6.26	4.56	6.62
7.22	3.09	7.21	3.67	6.55	4.14	6.21	4.32	5.99	4.20	5.70	4.63
9.24	2.34	9.23	2.68	8.39	3.01	7.95	3.21	7.66	3.01	7.29	3.30
11.5	1.84	11.5	2.04	10.5	2.06	9.93	2.17	9.58	2.22	9.11	2.08
14.4	1.37	14.4	1.63	13.1	1.57	12.4	1.56	12.0	1.61	11.4	1.67
18.5	1.07	18.5	1.12	16.8	1.03	15.9	1.18	15.3	1.05	14.6	1.05
23.1	8.02×10^{-3}	23.1	8.34×10^{-3}	21.0	7.70×10^{-3}	19.9	8.20×10^{-3}	19.2	8.44×10^{-3}	18.2	7.93×10^{-3}
28.9	6.68	28.8	5.84	26.2	5.60	24.8	5.96	23.9	5.54	22.8	5.43
36.1	5.51	36.0	3.70	32.8	3.33	31.0	3.98	29.9	3.89	28.5	3.92
46.2	3.85	46.1	2.66	41.9	2.28	39.7	2.71	38.3	2.62	36.5	2.52
57.7	3.09	57.7	1.71	52.4	1.53	49.7	1.42	47.9	1.87	45.6	1.68
72.2	2.76	72.1	1.41	65.5	1.37	62.1	1.34	59.9	1.29	57.0	1.32
92.4	2.04	92.3	9.92×10^{-4}	83.9	9.71×10^{-4}	79.5	9.84×10^{-4}	76.6	9.50×10^{-4}	72.9	8.80×10^{-4}
115	1.09	115	8.16	105	7.12	99.3	6.68	95.8	5.94	91.1	5.99
144	5.85×10^{-4}	144	5.39	131	4.32	124	4.28	120	3.92	114	3.76
185	1.27×10^{-4}	185	2.78	168	2.57	159	2.72	153	2.38	146	2.27
231	2.51×10^{-5}	231	1.41	210	1.31	199	1.31	192	1.17	182	1.08
289	6.69×10^{-6}	288	8.65×10^{-5}	262	5.87×10^{-5}	248	5.36×10^{-5}	239	5.36×10^{-5}	228	5.22×10^{-5}
361	1.32×10^{-6}	360	2.70	328	2.51	310	2.45	299	2.46	285	1.95×10^{-5}
462	2.68×10^{-7}	461	1.27	419	1.11	397	1.05	383	1.01	365	9.02×10^{-6}
577	1.09×10^{-7}	577	6.58×10^{-6}	524	4.96×10^{-6}	497	4.62×10^{-6}	479	4.32×10^{-6}	456	3.55×10^{-6}
		721	2.22×10^{-6}	655	1.80×10^{-6}	621	1.84×10^{-6}	599	1.30×10^{-6}	570	1.26×10^{-6}
		923	7.77×10^{-7}	839	7.00×10^{-7}	795	7.22×10^{-7}	766	6.37×10^{-7}	729	6.13×10^{-7}
		1153	5.13×10^{-7}	1048	5.33×10^{-7}						

y = 4.00 inches		y = 5.00 inches		y = 6.00 inches		y = 7.00 inches	
k	$F(k)/\overline{u^2}$	k	$F(k)/\overline{u^2}$	k	$F(k)/\overline{u^2}$	k	$F(k)/\overline{u^2}$
0.882	1.81×10^{-1}	0.859	1.76×10^{-1}	0.843	2.00×10^{-1}	0.829	2.19×10^{-1}
1.32	1.86	1.29	1.88	1.26	1.94	1.24	2.03
1.76	1.56	1.72	1.54	1.69	1.56	1.66	1.80
2.20	1.31	2.15	1.37	2.11	1.45	2.07	1.58
2.65	1.14	2.58	1.09	2.53	1.12	2.49	1.20
3.09	1.06	3.01	1.06	2.95	1.12	2.90	1.10
3.53	8.36×10^{-2}	3.44	8.15×10^{-2}	3.37	9.23×10^{-2}	3.32	1.02
4.41	6.35	4.30	6.41	4.21	6.22	4.15	7.01×10^{-2}
5.51	4.65	5.37	4.63	5.27	4.41	5.18	4.55
7.05	3.22	6.87	2.96	6.74	3.42	6.64	3.18
8.82	2.20	8.59	2.33	8.43	2.34	8.29	2.15
11.0	1.44	10.7	1.46	10.5	1.80	10.4	1.58
14.1	9.90×10^{-3}	13.8	1.02	13.5	1.02	13.3	1.04
17.6	6.64	17.2	6.81×10^{-3}	16.9	6.80×10^{-3}	16.6	7.96×10^{-3}
22.0	4.19	21.5	5.01	21.1	4.76	20.7	6.21
27.6	2.89	26.9	2.82	26.3	3.30	25.9	3.79
35.3	1.87	34.4	2.09	33.7	2.06	33.2	2.06
44.1	1.60	43.0	1.69	42.1	1.83	41.5	1.74
55.1	1.36	53.7	1.27	52.7	1.21	51.8	1.29
70.5	8.91×10^{-4}	68.7	8.58×10^{-4}	67.4	8.94×10^{-4}	66.4	8.45×10^{-4}
88.2	5.80	85.9	6.76	84.3	5.44	82.9	5.47
110	3.85	107	3.52	105	3.72	104	3.71
141	1.74	138	1.78	135	1.82	133	1.63
176	1.02	172	9.91×10^{-5}	169	9.37×10^{-5}	166	9.46×10^{-5}
220	4.44×10^{-5}	215	3.87×10^{-5}	211	4.92	207	5.29×10^{-5}
276	2.01×10^{-5}	269	2.08×10^{-5}	263	1.74	259	1.97×10^{-5}
353	8.40×10^{-6}	344	8.75×10^{-6}	337	8.16×10^{-6}	332	7.77×10^{-6}
441	3.54×10^{-6}	430	3.13×10^{-6}	421	3.37×10^{-6}	415	3.58×10^{-6}
551	1.09×10^{-6}	537	1.20×10^{-6}	527	1.06×10^{-6}	518	1.26×10^{-6}
705	5.41×10^{-7}			674	4.86×10^{-7}	664	6.73×10^{-7}

TABLE III - NUMERICAL VALUES OF MEASURED ONE-DIMENSIONAL SPECTRUM FUNCTIONS $U_\infty \geq 20$ fps - Cont'd.

y = 0.001 inch		y = 0.003 inch		y = 0.004 inch		y = 0.005 inch		y = 0.008 inch		y = 0.010 inch	
k	$F(k)/\overline{u^2}$	k	$F(k)/\overline{u^2}$	k	$F(k)/\overline{u^2}$	k	$F(k)/\overline{u^2}$	k	$F(k)/\overline{u^2}$	k	$F(k)/\overline{u^2}$
199.5	8.46×10^{-4}	60.1	2.77×10^{-3}	44.6	3.51×10^{-3}	35.9	4.11×10^{-3}	22.9	8.16×10^{-3}	18.3	1.03×10^{-2}
299	7.90	90.2	2.29	66.9	3.12	53.9	3.39	34.3	7.63	27.5	9.39×10^{-3}
399	6.67	120	2.20	89.1	2.63	71.8	3.33	45.8	6.82	36.7	8.66
489	6.03	150	1.80	111	2.23	89.8	3.05	57.2	6.90	45.8	8.39
598	5.66	180	1.61	134	1.94	108	2.58	68.7	6.30	55.0	7.27
698	4.87	210	1.56	156	1.88	126	2.56	80.1	5.49	64.2	6.26
798	4.35	241	1.44	178	1.71	144	2.28	91.6	4.93	73.3	5.97
997	3.53	300	1.15	223	1.69	180	2.08	114	4.17	91.7	5.21
1247	2.99	376	1.16	279	1.15	224	1.58	143	3.16	115	4.06
1596	3.31	481	8.21×10^{-4}	357	1.12	287	1.11	183	2.77	147	3.06
1995	1.78	601	5.06	446	7.47×10^{-4}	359	7.71×10^{-4}	229	1.75	183	2.27
2494	1.19	752	4.67	557	5.84	449	5.35	286	1.26	229	1.86
3192	6.34×10^{-5}	962	1.92	713	2.94	575	3.33	366	9.69×10^{-4}	293	1.15
3990	4.67	1203	1.05	891	1.54	718	2.18	458	6.15	367	6.11×10^{-4}
4987	2.05	1503	8.14×10^{-5}	1114	6.79×10^{-5}	898	9.33×10^{-5}	572	2.51	458	3.84
6234	1.03	1879	3.75	1393	3.65	1122	5.00	715	1.53	573	1.68
7980	4.80×10^{-6}	2405	1.50	1783	1.95	1436	2.41	916	6.40×10^{-5}	733	6.84×10^{-5}
9975	2.06	3007	7.50×10^{-6}	2228	9.68×10^{-6}	1795	1.10	1145	2.90	917	3.40
12470	1.17	3758	4.09	2786	4.89	2244	6.81×10^{-6}	1431	1.28	1146	1.81
15960	4.94×10^{-7}	4811	1.09	3565	1.67	2873	1.99×10^{-6}	1831	5.92×10^{-6}	1467	6.21×10^{-6}
19950	1.32×10^{-7}	6013	9.04×10^{-7}	4457	4.53×10^{-7}	3591	8.09×10^{-7}	2289	2.56×10^{-6}	1834	3.58
25930	5.00×10^{-8}	7817	2.60×10^{-7}	5794	1.88	4668	2.53	3663	2.00×10^{-7}	2384	1.05
31920	2.34×10^{-8}	9621	1.00×10^{-7}	7131	1.12	5745	1.32	4578	1.21×10^{-7}	2934	4.70×10^{-7}
				8914	5.43×10^{-8}	7182	5.85×10^{-8}			3667	1.77
										4584	1.04

y = 0.014 inch		y = 0.022 inch		y = 0.032 inch		y = 0.050 inch		y = 0.150 inch		y = 0.200 inch	
k	$F(k)/\overline{u^2}$	k	$F(k)/\overline{u^2}$	k	$F(k)/\overline{u^2}$	k	$F(k)/\overline{u^2}$	k	$F(k)/\overline{u^2}$	k	$F(k)/\overline{u^2}$
13.4	1.51×10^{-2}	8.89	1.69×10^{-2}	6.38	2.37×10^{-2}	4.54	3.48×10^{-2}	3.07	4.26×10^{-2}	2.89	4.41×10^{-2}
20.1	1.51	13.3	1.72	9.58	2.02	6.82	3.18	4.60	3.29	4.33	3.63
26.8	1.35	17.8	1.50	12.8	1.93	9.09	2.80	6.14	2.82	5.78	3.12
33.5	1.21	22.2	1.47	16.0	1.63	11.4	2.63	7.67	2.85	7.22	2.68
40.2	1.19	26.7	1.32	19.2	1.70	13.6	2.38	9.20	2.38	8.67	2.34
46.9	9.29×10^{-3}	31.1	1.20	22.3	1.55	15.9	1.94	10.7	2.18	10.1	2.07
53.6	9.07	35.5	1.24	25.5	1.45	18.2	2.02	12.3	2.06	11.6	1.92
67.0	7.43	44.4	9.03×10^{-3}	31.9	1.07	22.7	1.55	15.3	1.60	14.5	1.75
83.8	6.25	55.5	7.85	39.9	1.01	28.4	1.37	19.2	1.50	18.1	1.56
107	5.01	71.1	6.45	51.1	7.48×10^{-3}	36.4	1.12	24.5	1.36	23.1	1.20
134	3.12	88.9	4.34	63.8	6.42	45.4	7.91×10^{-3}	30.7	1.00	28.9	1.03
168	2.25	111	3.45	79.8	5.03	56.8	7.19	38.3	5.88×10^{-3}	36.1	7.24×10^{-3}
214	1.87	142	2.78	102	4.02	72.7	6.00	49.1	4.83	46.2	5.93
268	1.01	178	1.84	128	2.81	90.9	3.51	61.4	3.28	57.8	4.97
335	6.48×10^{-4}	222	1.10	160	1.42	114	2.70	76.7	2.34	72.2	2.89
419	2.33	278	6.34×10^{-4}	200	7.22×10^{-4}	142	1.62	95.9	2.24	90.3	2.50
536	1.03	355	3.44	255	3.70	182	8.00×10^{-4}	123	1.44	116	1.54
670	5.00×10^{-5}	444	1.18	319	2.00	227	4.03	153	1.00	145	1.08
838	2.22×10^{-5}	555	5.80×10^{-5}	399	1.03	284	2.22	192	6.02×10^{-4}	181	5.78×10^{-4}
1072	9.88×10^{-6}	711	2.68	511	5.12×10^{-5}	364	1.03	245	3.00	231	3.50
1340	3.70	889	1.31	638	3.15	454	6.04×10^{-5}	307	1.88	289	1.95
1742	1.92	1155	5.62×10^{-6}	836	1.16	591	2.52×10^{-5}	399	1.02	376	1.10
2144	3.77×10^{-7}	1422	2.08×10^{-6}	1022	2.36×10^{-6}	727	4.97×10^{-6}	491	2.99×10^{-5}	462	4.08×10^{-5}
2680	1.74×10^{-7}	1777	6.30×10^{-7}	1277	9.00×10^{-7}	909	1.11×10^{-6}	614	4.35×10^{-6}	578	4.62×10^{-6}
		2221	1.83×10^{-7}	1596	2.89×10^{-7}	1136	5.21×10^{-7}	767	1.12×10^{-6}	722	1.29×10^{-6}
		2777	7.25×10^{-8}	1995	9.58×10^{-8}	1420	9.84×10^{-8}	958	2.44×10^{-7}	903	2.16×10^{-7}

TABLE III - NUMERICAL VALUES OF MEASURED ONE-DIMENSIONAL SPECTRUM FUNCTIONS $U_\infty \geq 20$ fps - Cont'd.

y = 0.300 inch		y = 0.400 inch		y = 0.500 inch		y = 0.50 inch		y = 1.00 inch		y = 1.50 inches	
k	$F(k)/u^2$	k	$F(k)/u^2$	k	$F(k)/u^2$	k	$F(k)/u^2$	k	$F(k)/u^2$	k	$F(k)/u^2$
2.74	5.35×10^{-2}	2.61	5.92×10^{-2}	2.52	6.55×10^{-2}	2.49	6.49×10^{-2}	2.23	7.05×10^{-2}	2.11	7.17×10^{-2}
4.11	4.22	3.92	4.84	3.78	5.11	3.74	5.97	3.35	6.67	3.16	6.48
5.48	3.43	5.22	4.23	5.04	4.22	4.98	4.45	4.46	5.96	4.21	6.14
6.84	3.00	6.53	3.37	6.30	3.66	6.23	4.18	5.58	5.18	5.26	5.02
8.21	2.81	7.84	2.91	7.56	3.27	7.47	3.39	6.69	4.40	6.31	4.36
9.58	2.50	9.14	2.73	8.82	2.72	8.72	3.08	7.81	3.69	7.37	3.97
10.9	2.20	10.4	2.36	10.1	2.44	9.97	2.79	8.92	3.28	8.42	3.36
13.7	1.92	13.1	2.20	12.6	2.05	12.4	2.46	11.2	2.61	10.5	2.58
17.1	1.65	16.3	1.83	15.8	1.58	15.6	1.78	13.9	1.99	13.2	2.16
21.9	1.29	20.9	1.30	20.2	1.22	19.9	1.26	17.8	1.31	16.8	1.55
27.4	1.24	26.1	1.05	25.2	9.10×10^{-3}	24.9	9.41×10^{-3}	22.3	1.08	21.1	1.23
34.2	7.12×10^{-3}	32.7	7.51×10^{-3}	31.5	6.88	31.1	7.07	27.9	8.56×10^{-3}	26.3	7.79×10^{-3}
43.8	5.56	41.8	5.81	40.3	5.22	39.9	4.67	35.7	5.39	33.7	5.76
54.8	3.79	52.2	4.90	50.4	3.77	49.8	3.57	44.6	3.68	42.1	3.44
68.4	2.76	65.3	2.75	63.0	2.55	62.3	2.10	55.8	2.66	52.6	2.17
85.5	2.07	81.6	2.20	78.8	1.67	77.9	1.33	69.7	1.35	65.8	1.45
109	1.38	104	1.54	101	1.15	99.7	8.09×10^{-4}	89.2	8.41×10^{-4}	84.2	9.48×10^{-4}
137	1.16	131	1.10	126	8.00×10^{-4}	125	6.94	112	6.26	105	6.07
171	6.89×10^{-4}	163	5.50×10^{-4}	158	5.55	156	4.07	139	3.89	132	3.64
219	4.59	209	3.56	202	4.11	199	2.19	178	2.10	168	1.86
274	2.67	261	2.10	252	3.33	249	1.01	223	9.48×10^{-5}	211	8.60×10^{-5}
356	1.79	340	1.89	315	1.55	311	4.21×10^{-5}	279	3.98	263	3.36
438	4.13×10^{-5}	418	4.40×10^{-5}	404	2.66×10^{-5}	399	1.10×10^{-5}	357	1.05	337	1.06
548	8.31×10^{-6}	522	7.02×10^{-6}	504	3.88×10^{-6}	498	5.11×10^{-6}	446	5.15×10^{-6}	421	4.55×10^{-6}
684	1.77×10^{-6}	653	1.59×10^{-6}	630	1.39×10^{-6}	623	1.68×10^{-6}	558	1.52×10^{-6}	526	1.43×10^{-6}
855	2.53×10^{-7}	816	1.93×10^{-7}	788	1.50×10^{-7}	779	3.93×10^{-7}	697	3.75×10^{-7}	658	2.88×10^{-7}
				1008	5.55×10^{-8}	997	7.37×10^{-8}	892	8.98×10^{-8}	842	7.53×10^{-8}
								1115	4.87×10^{-8}	1052	5.08×10^{-8}

y = 2.00 inches		y = 3.00 inches		y = 4.00 inches		y = 5.00 inches		y = 6.00 inches		y = 7.00 inches	
k	$F(k)/u^2$	k	$F(k)/u^2$	k	$F(k)/u^2$	k	$F(k)/u^2$	k	$F(k)/u^2$	k	$F(k)/u^2$
2.92	9.57×10^{-2}	1.91	1.02×10^{-1}	1.83	1.08×10^{-1}	1.77	1.20×10^{-1}	1.72	1.13×10^{-1}	1.68	1.16×10^{-1}
3.03	8.38	2.86	8.67×10^{-2}	2.74	1.01×10^{-1}	2.65	1.02×10^{-1}	2.58	1.04×10^{-1}	2.53	8.90×10^{-2}
4.04	7.33	3.81	7.17	3.66	8.52×10^{-2}	3.54	8.84×10^{-2}	3.45	9.15×10^{-2}	3.37	8.22
5.05	5.77	4.77	6.03	4.57	6.65	4.42	6.88	4.31	7.81	4.21	7.60
6.06	5.31	5.72	4.56	5.48	5.79	5.30	5.76	5.17	6.04	5.05	5.97
7.07	4.28	6.67	4.27	6.40	4.97	6.19	5.08	6.03	5.38	5.90	4.74
8.08	3.58	7.63	3.93	7.31	4.03	7.07	3.86	6.89	4.22	6.74	4.09
10.1	3.31	9.53	2.62	9.14	2.96	8.84	2.90	8.61	3.08	8.42	3.47
12.6	2.18	11.9	1.98	11.4	2.20	11.0	2.24	10.8	2.05	10.5	2.28
16.2	1.29	15.3	1.42	14.6	1.45	14.1	1.63	13.8	1.59	13.5	1.49
20.2	1.02	19.1	1.11	18.3	1.03	17.7	1.01	17.2	9.06×10^{-3}	16.8	1.10
25.2	6.99×10^{-3}	23.8	7.13×10^{-3}	22.9	6.96×10^{-3}	22.1	8.14×10^{-3}	21.5	7.20	21.1	8.26×10^{-3}
32.3	4.83	30.5	4.71	29.2	4.81	28.3	5.39	27.6	5.34	27.0	5.58
40.4	2.89	38.1	2.77	36.6	4.16	35.4	2.88	34.5	3.54	34.7	4.05
50.5	1.57	47.7	1.66	45.7	2.16	44.2	2.11	43.1	2.06	42.1	2.16
63.1	1.27	59.6	1.03	57.1	1.08	55.2	1.33	53.8	1.12	52.6	1.24
80.8	8.47×10^{-4}	76.3	9.08×10^{-4}	73.1	8.60×10^{-4}	70.7	9.35×10^{-4}	68.9	8.99×10^{-4}	67.4	1.02
101	6.22	95.3	5.52	91.4	5.54	88.4	6.13	86.1	4.95	84.2	6.88×10^{-4}
126	4.08	119	3.89	114	4.64	110	3.59	108	3.17	105	4.34
162	1.94	153	1.69	146	1.56	141	1.89	138	1.46	135	1.92
202	7.15×10^{-5}	191	7.28×10^{-5}	183	9.00×10^{-5}	177	7.09×10^{-5}	172	6.38×10^{-5}	168	7.41×10^{-5}
252	2.64	238	3.21	229	4.08×10^{-5}	221	3.12	215	2.17×10^{-5}	211	3.19
323	1.02	305	7.14×10^{-6}	292	6.27×10^{-6}	283	1.08	276	9.69×10^{-6}	270	1.11
404	4.18×10^{-6}	381	4.10	366	3.51	354	4.76×10^{-6}	345	3.89	337	4.73×10^{-6}
505	1.27×10^{-6}	477	1.41	457	1.24	442	1.87×10^{-6}	431	1.52	421	1.80×10^{-6}
631	2.60×10^{-7}	596	3.16×10^{-7}	571	2.25×10^{-7}	552	8.72×10^{-7}	538	7.09×10^{-7}	526	9.66×10^{-7}
808	4.68×10^{-8}	763	9.70×10^{-8}	731	7.93×10^{-8}						
1010	2.41×10^{-8}	954	8.13×10^{-8}								

FIGURES

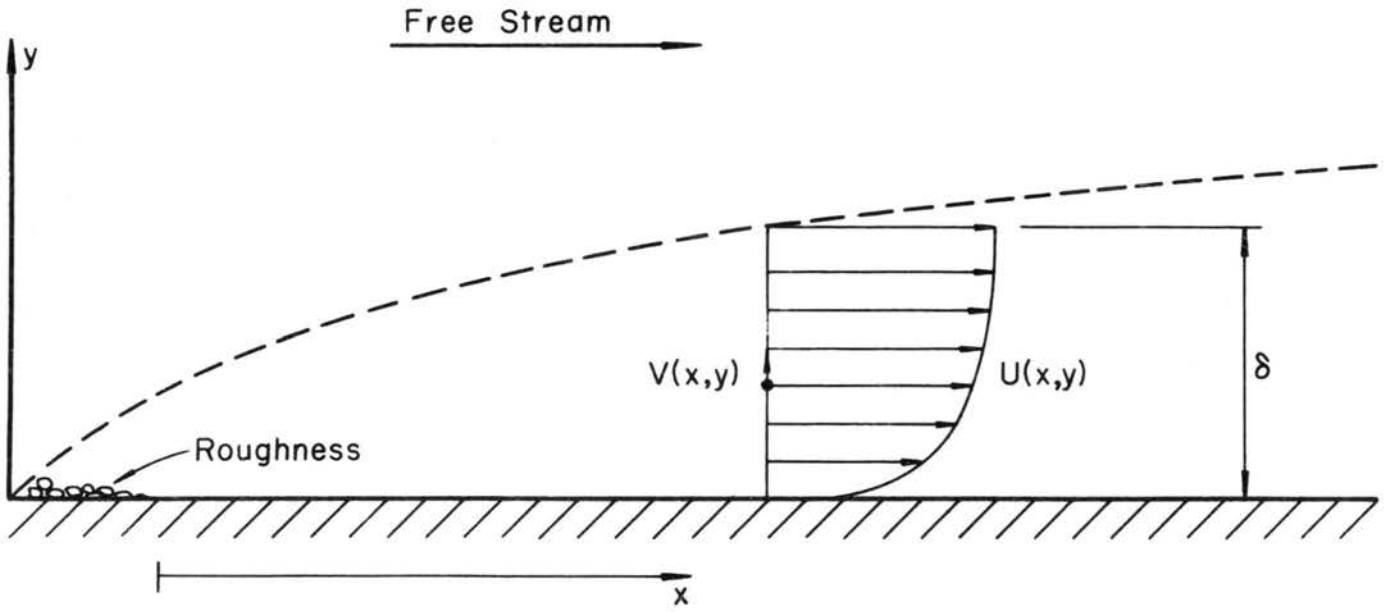

Figure 1. Definition sketch of the boundary layer

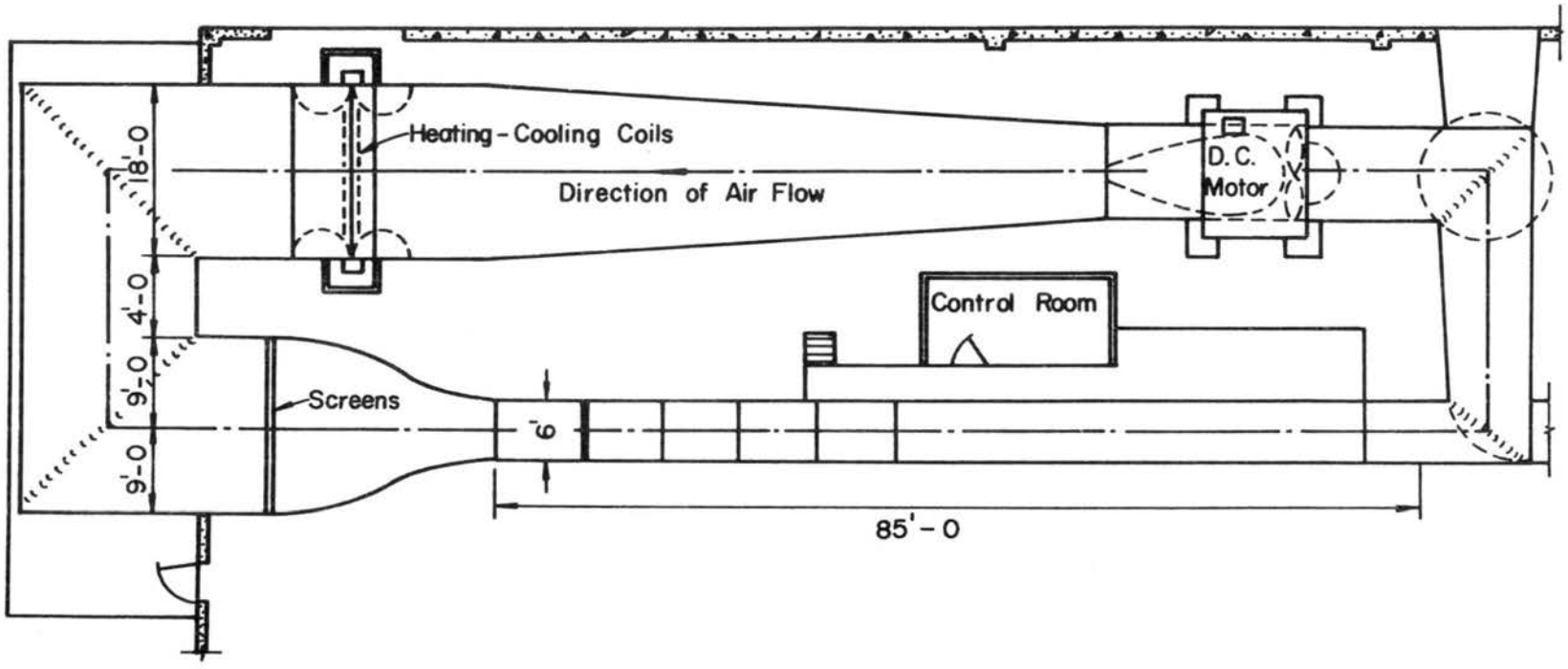

PLAN VIEW

Figure 2. Wind tunnel

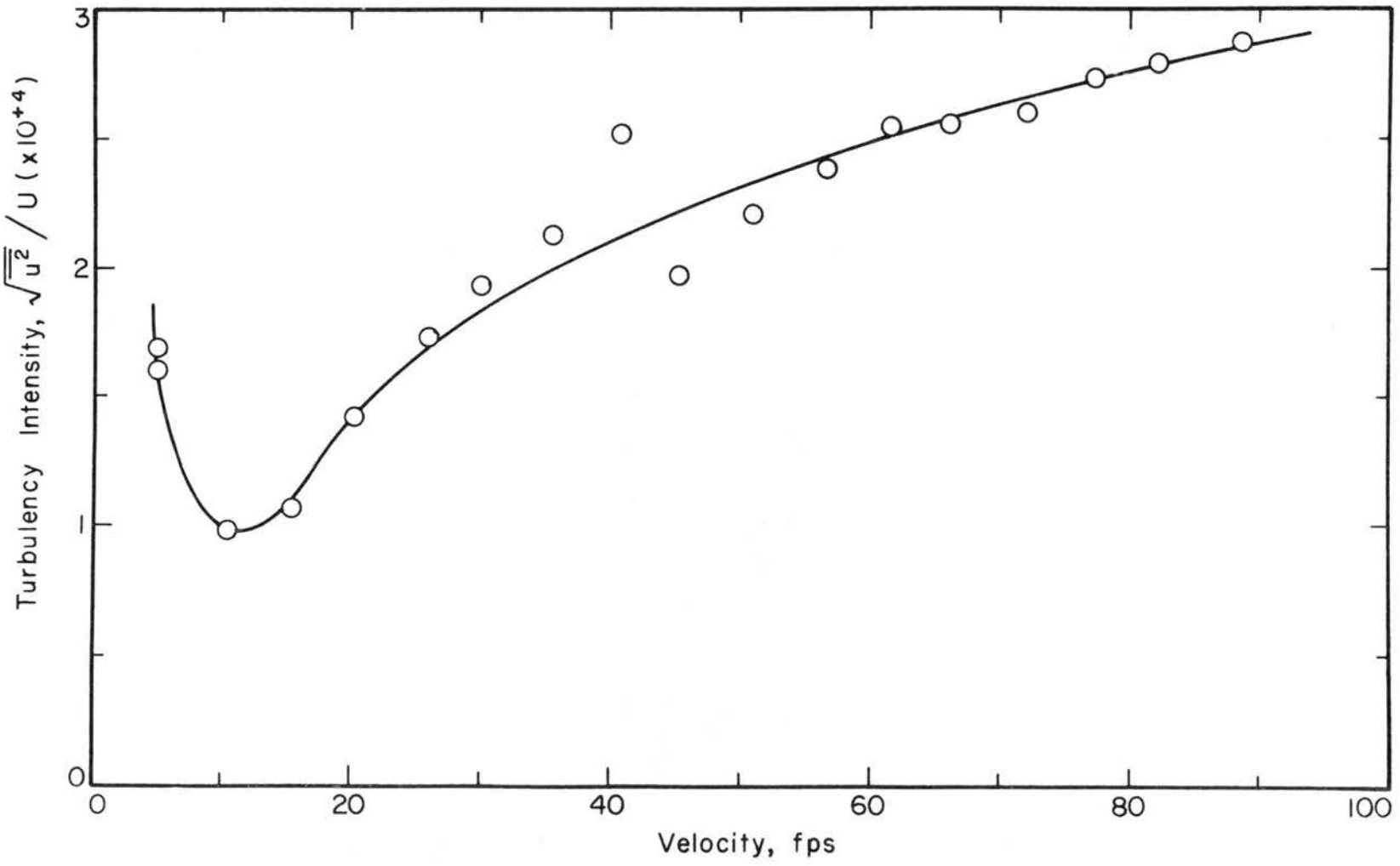

Figure 3. Turbulence intensity in the free stream at the entrance to the test section

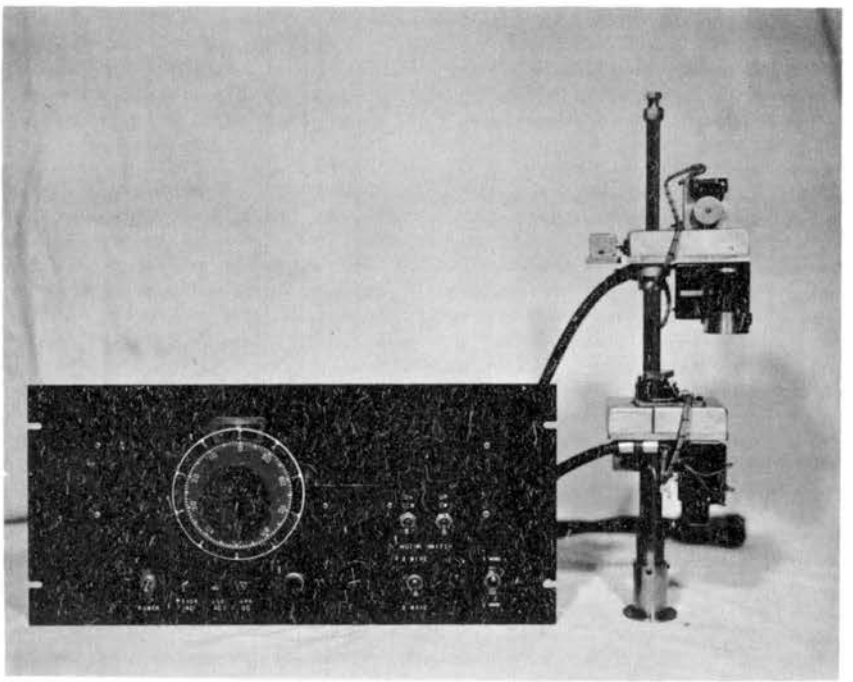

Figure 4. Precision actuator

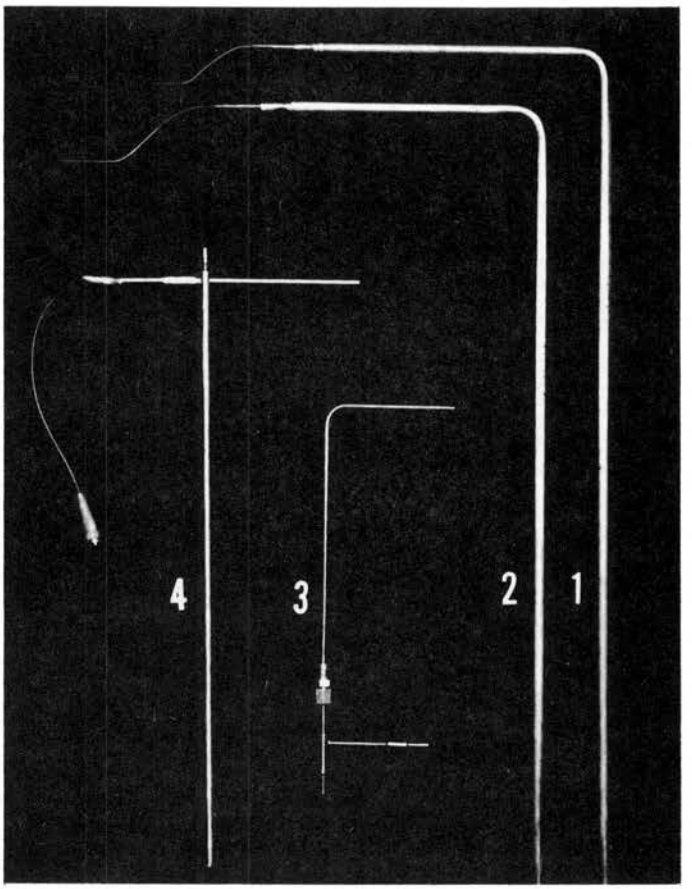

Figure 5. Probes

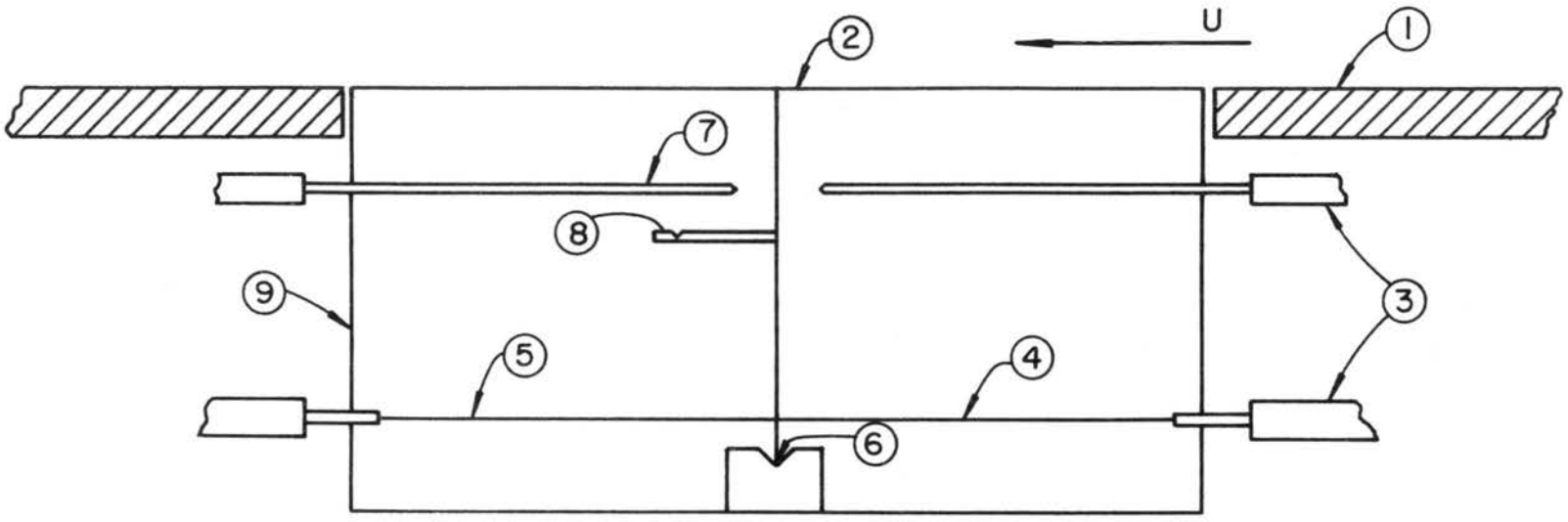

Figure 6. Schematic drawing of wall shear-stress meter (not to scale)

1. Floor of tunnel
2. Shear surface of pivoting element
3. Micrometer movements
4. Active strain wire
5. Reference strain wire
6. Pivots and vee-jewel bearings
7. Locking mechanism
8. Position for calibration weights
9. Housing for pivoting element and micrometers

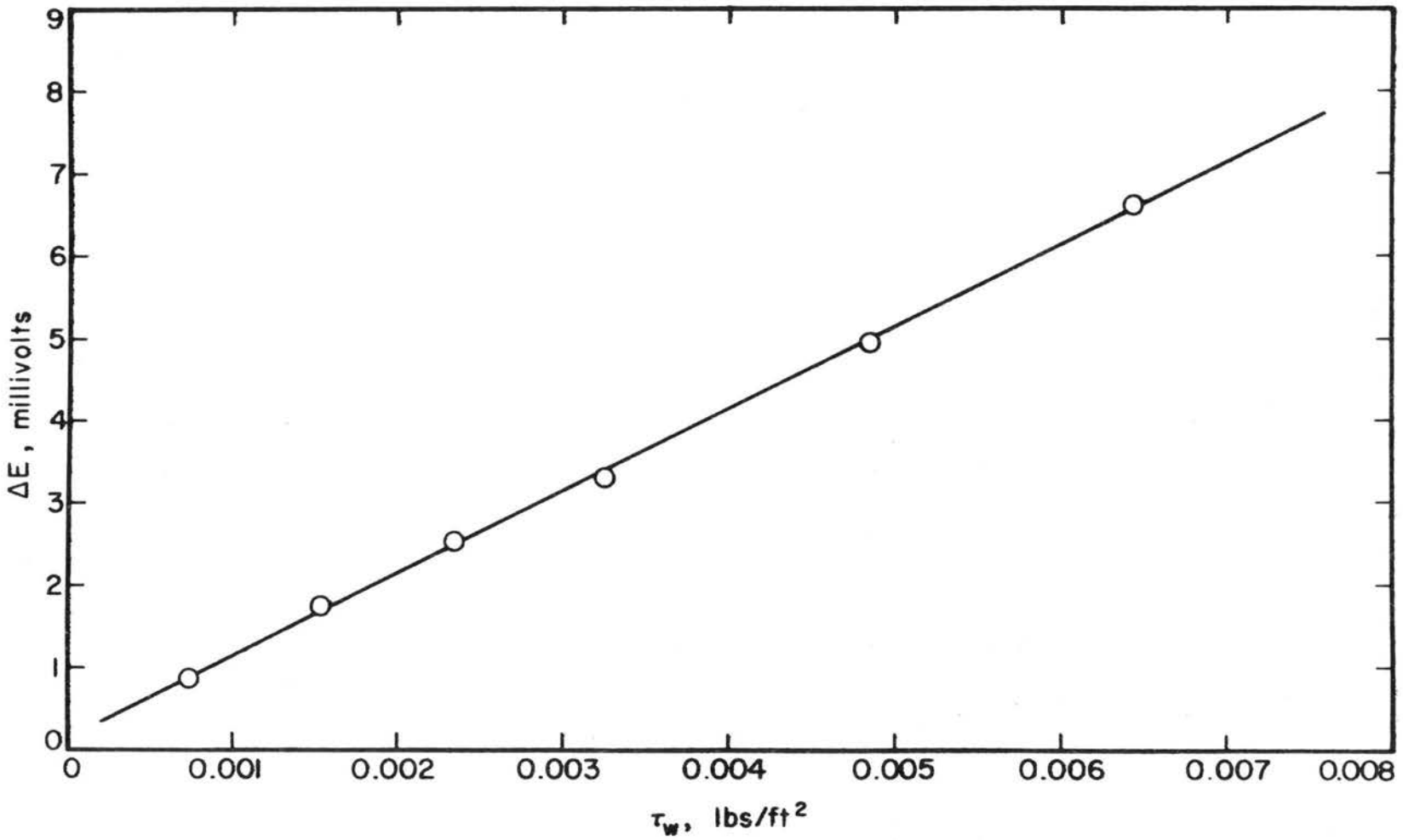

Figure 7. Calibration curve for wall shear-stress meter

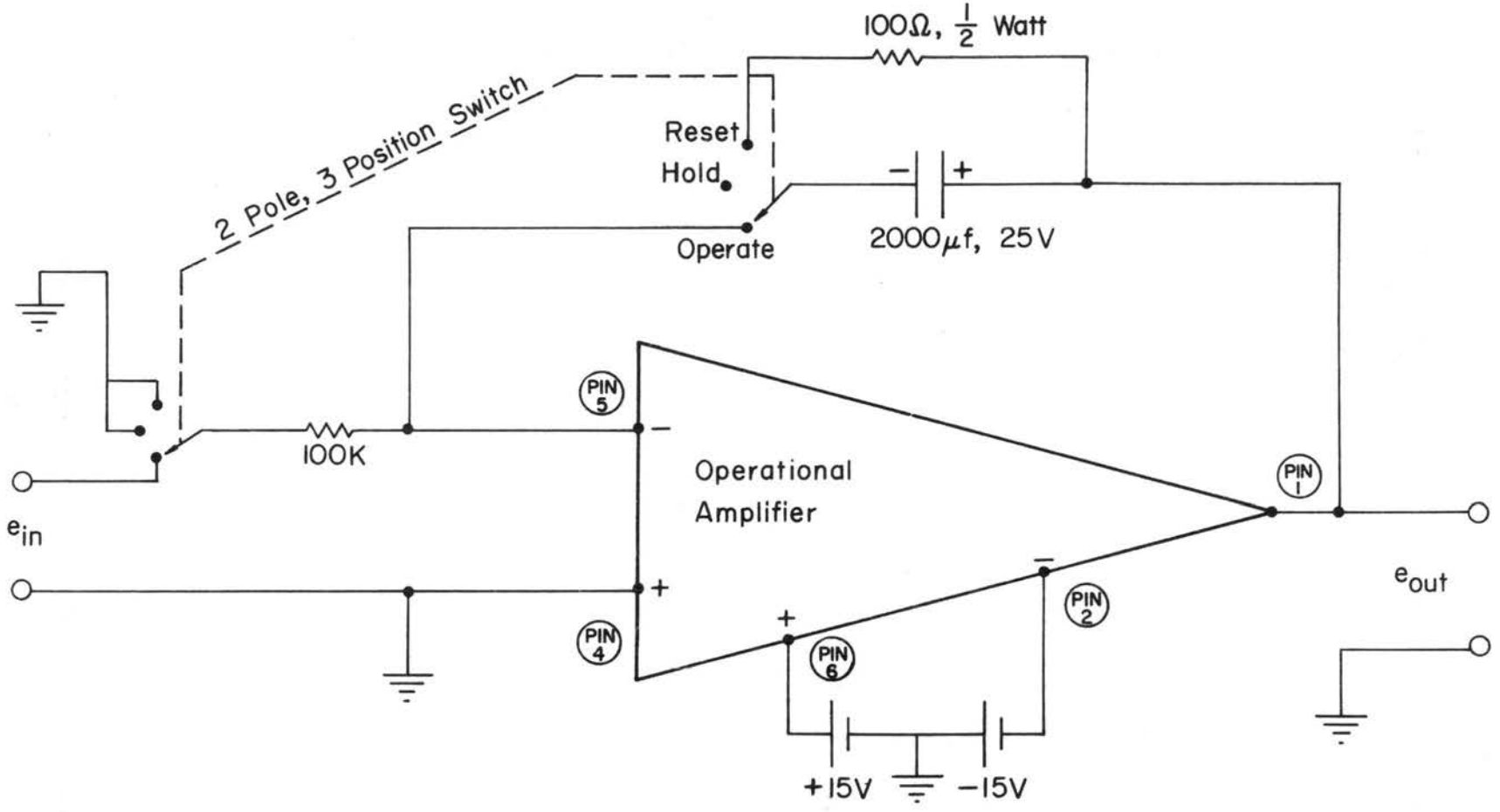

Figure 8. Integrating circuit

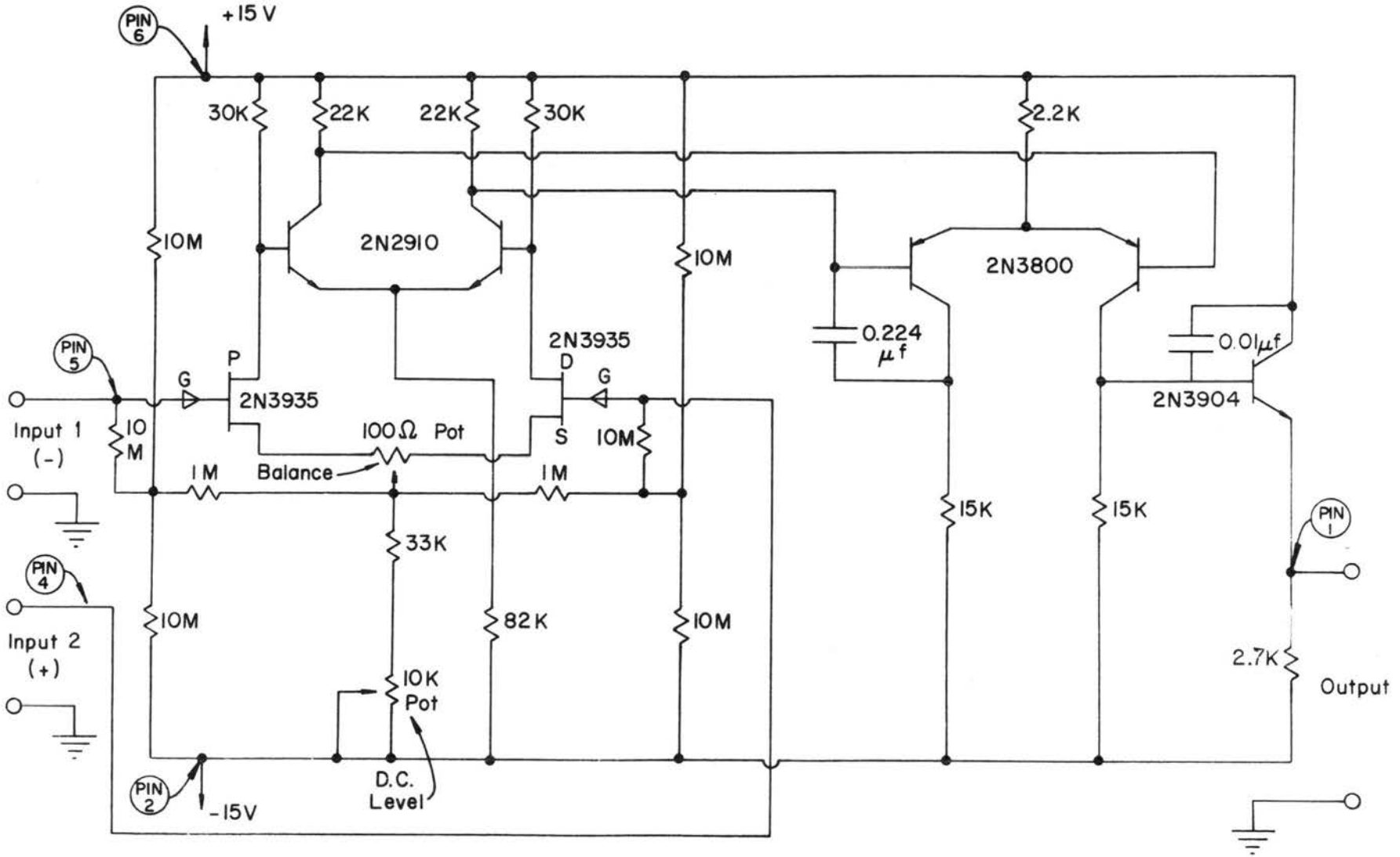

Figure 9. Operational amplifier of integrating circuit

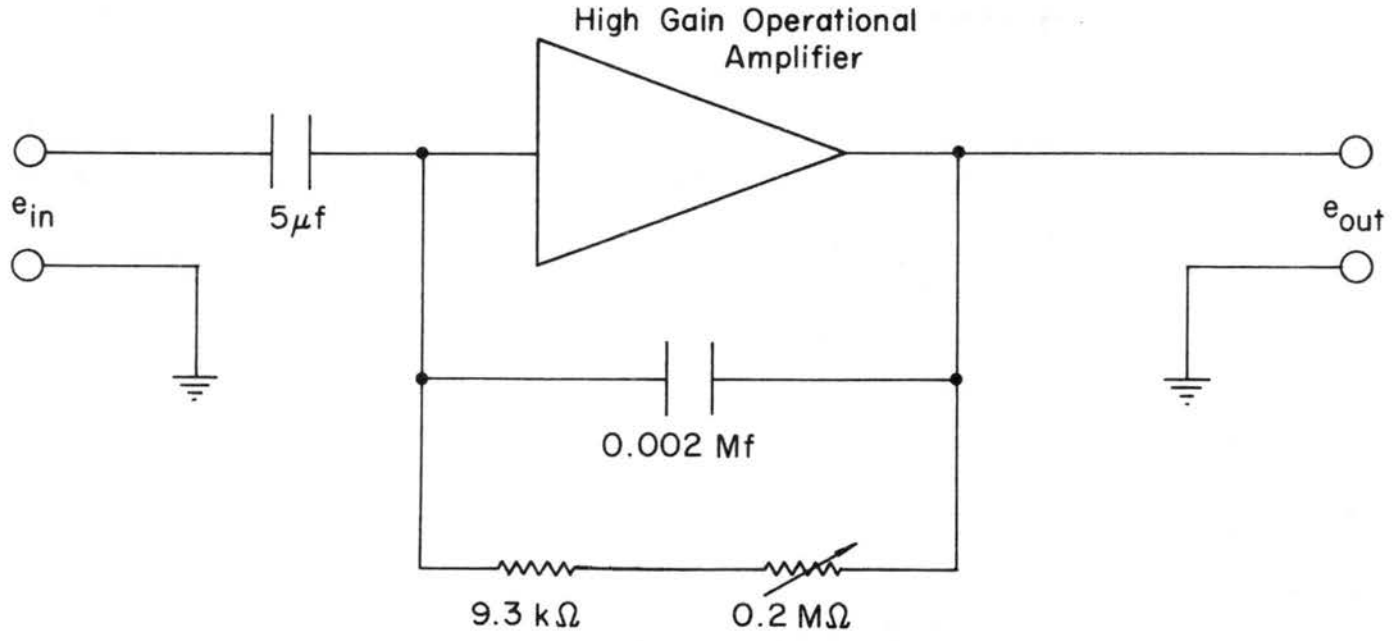

Figure 10. Schematic diagram of differentiating circuit

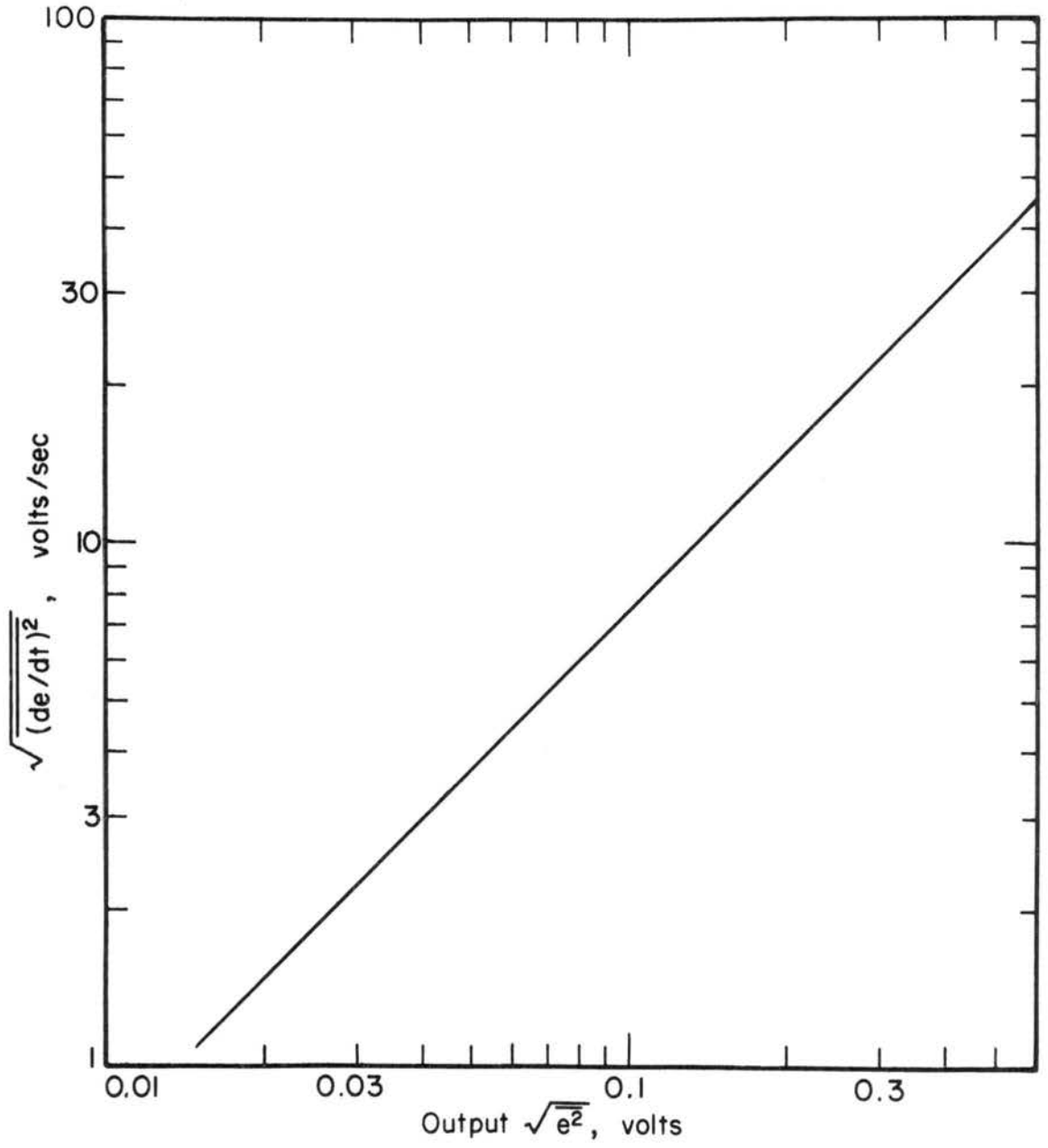

Figure 11. Calibration curve for differentiating circuit

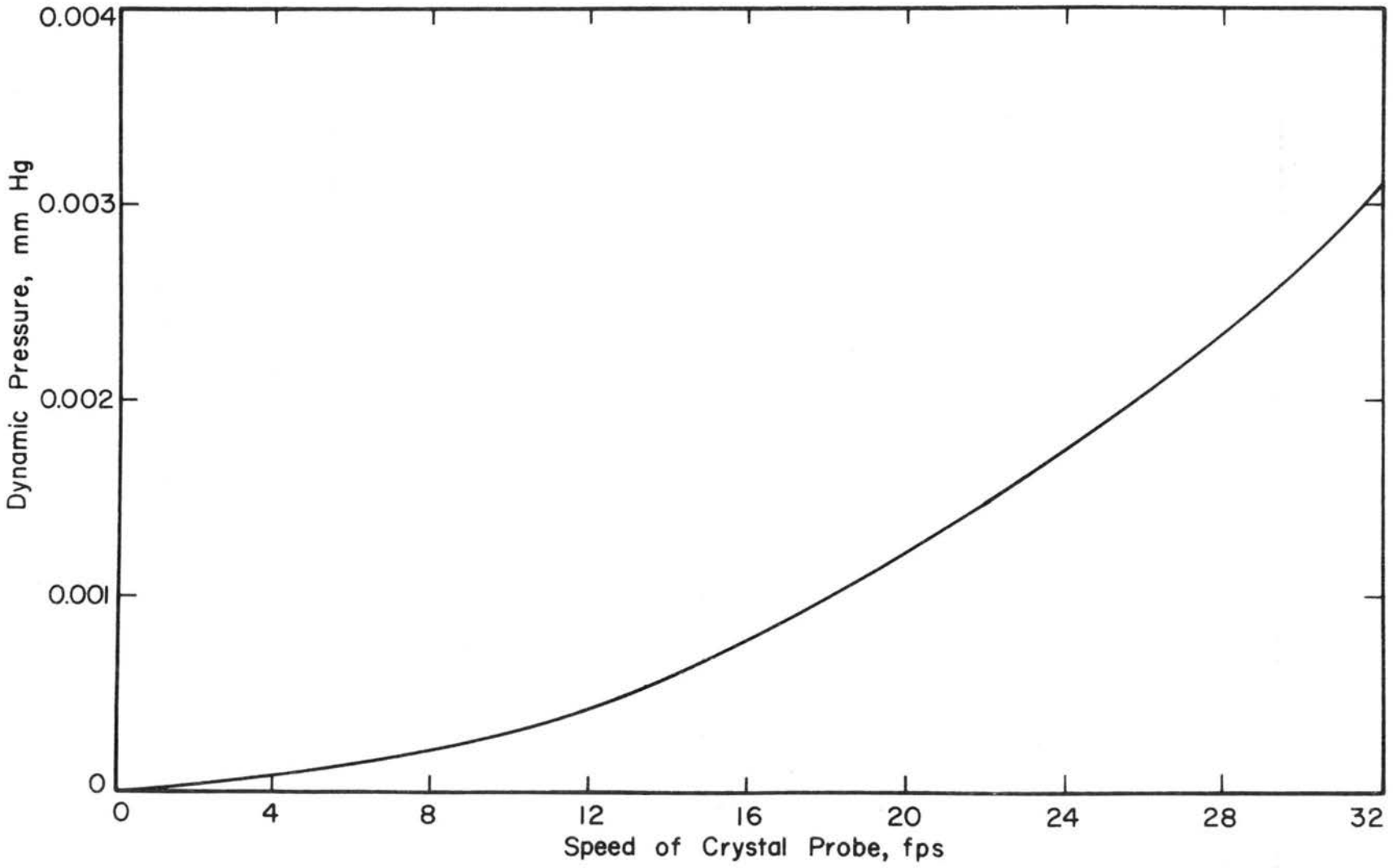

Figure 12. Dynamic pressure due to swirl in tank versus probe speed

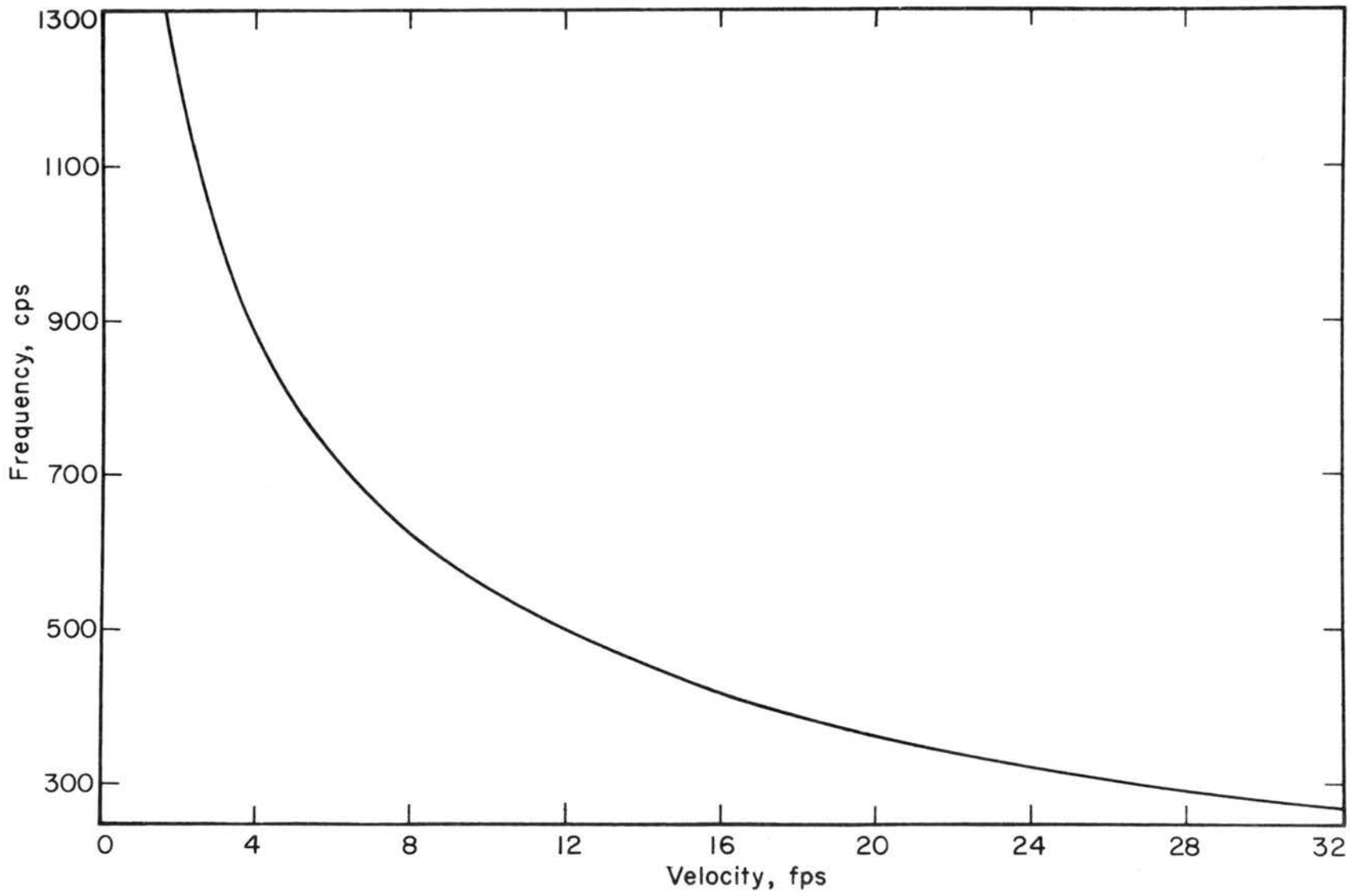

Figure 13. Calibration curve for crystal probe

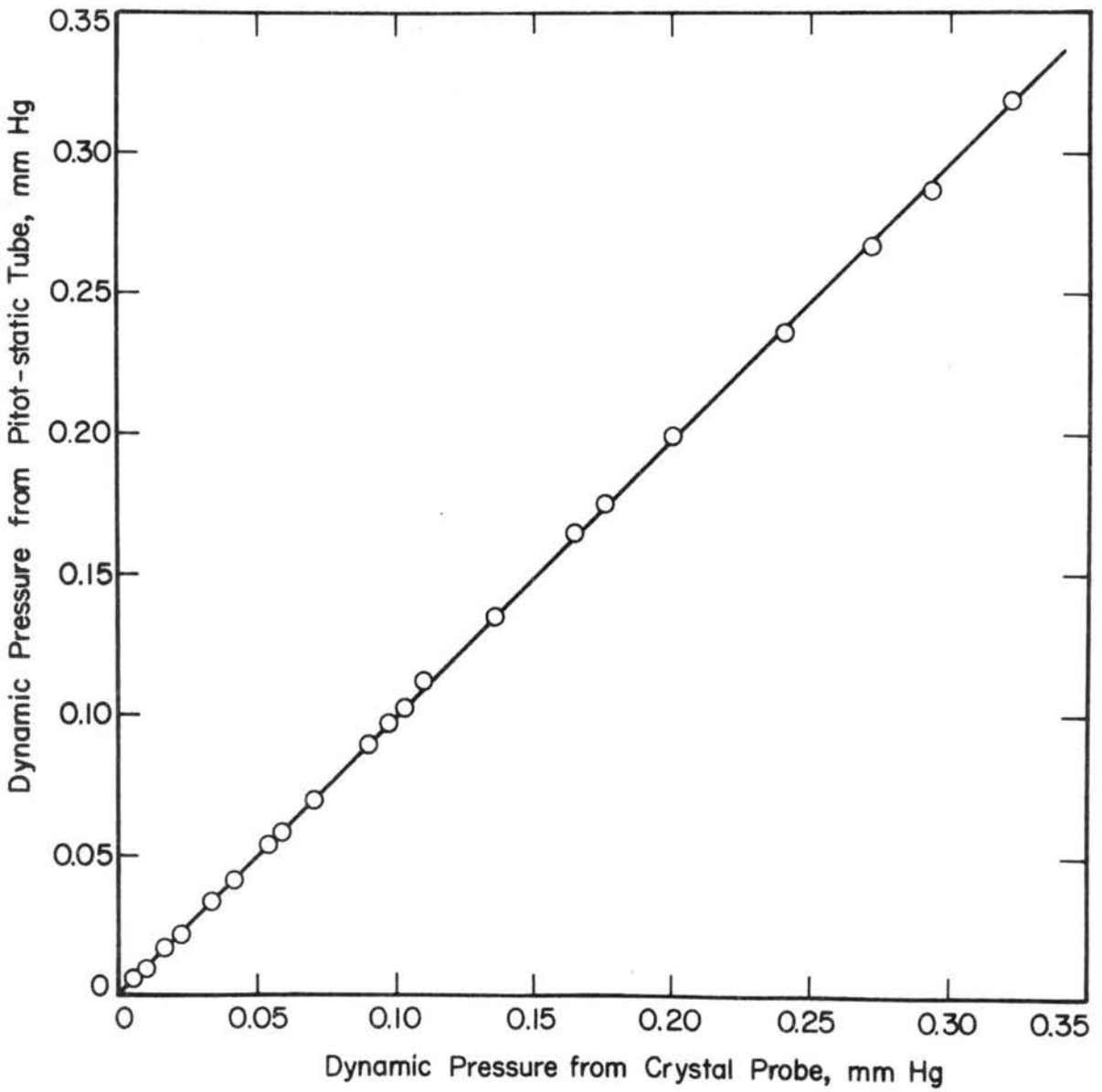

Figure 14. Calibration curve for pitot-static tube

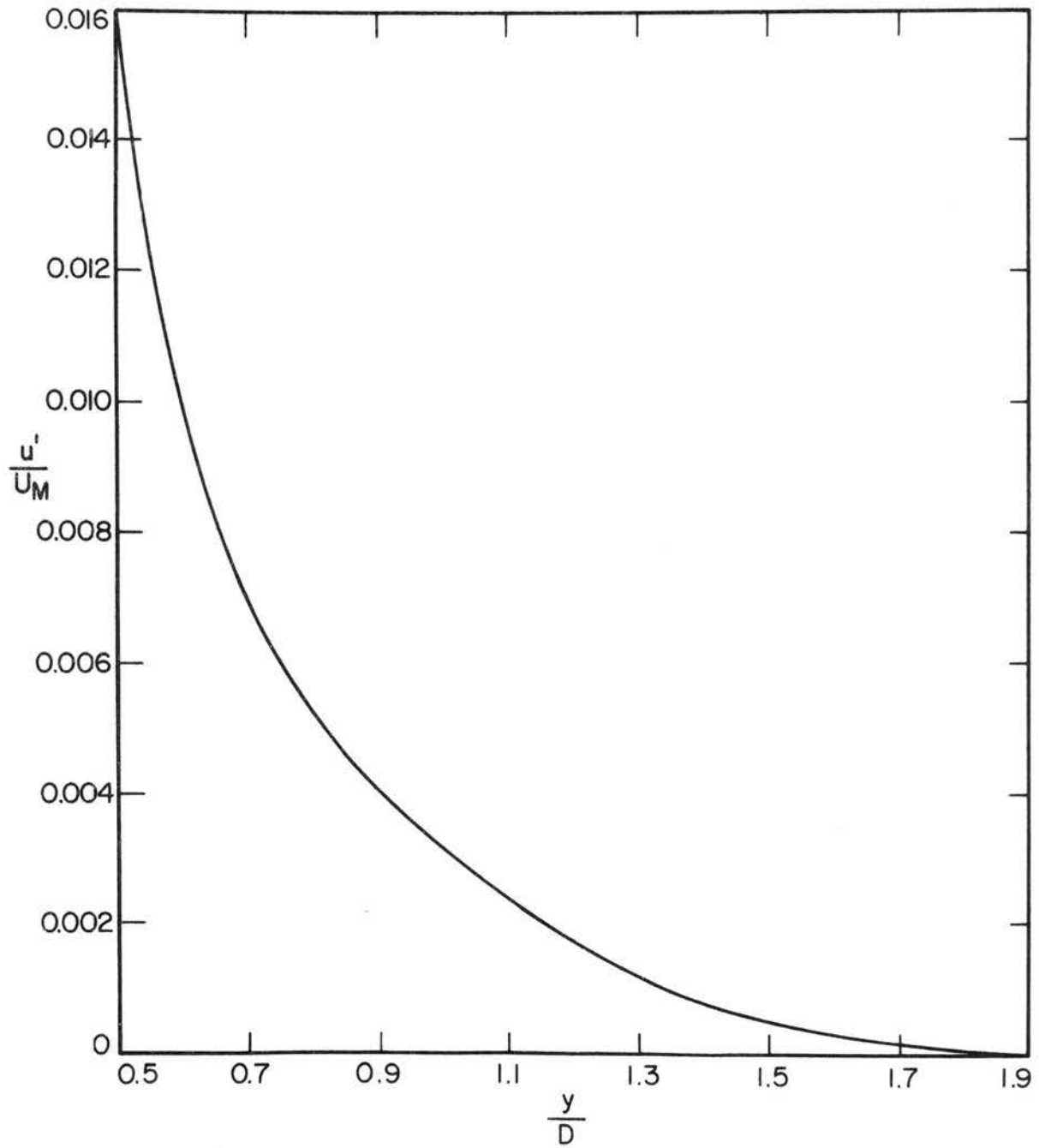

Figure 15. The wall effect expressed as a function of y/D after MacMillan (23)

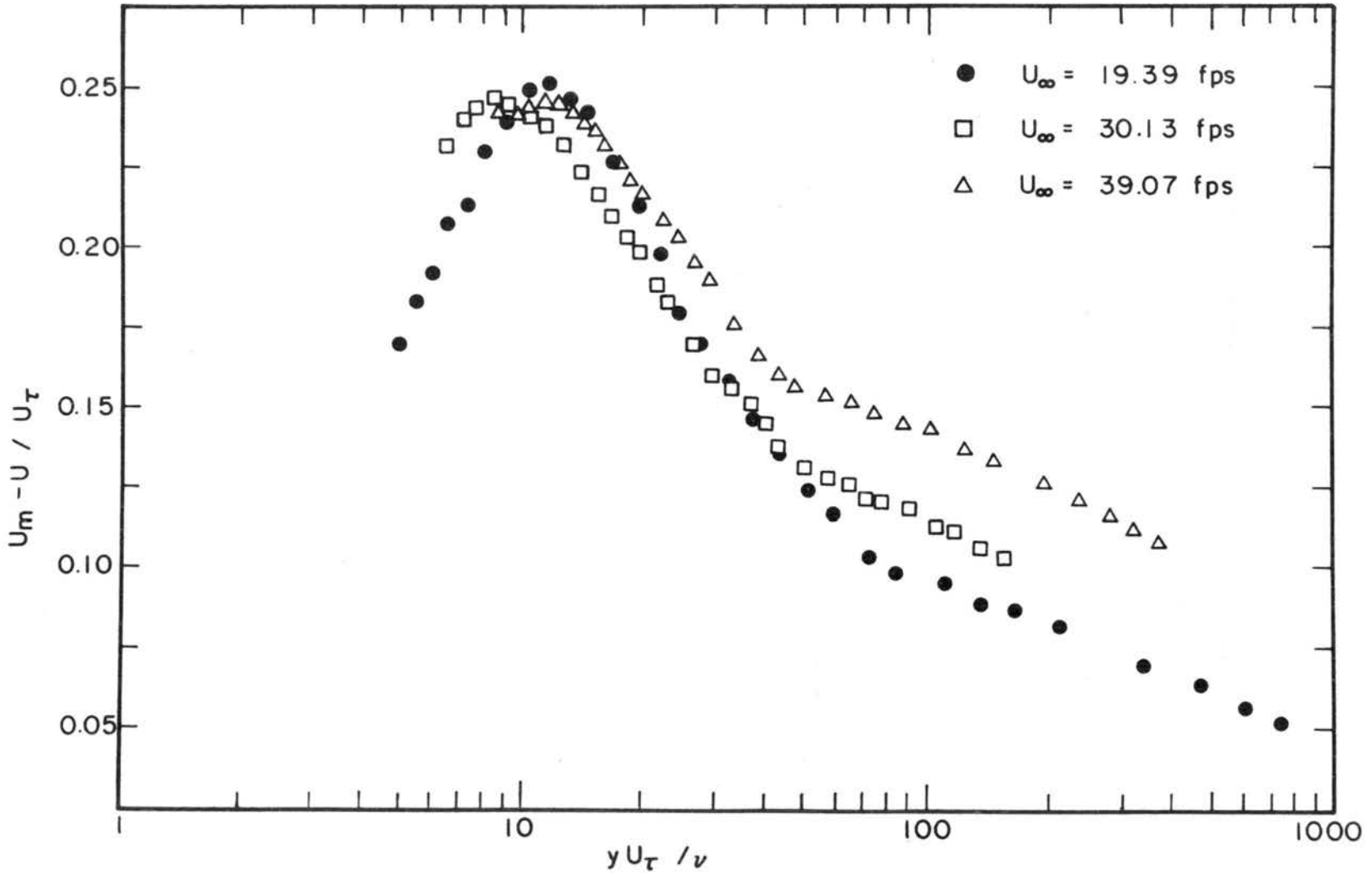

Figure 16. Magnitude of correction for turbulence effects on total-head tube

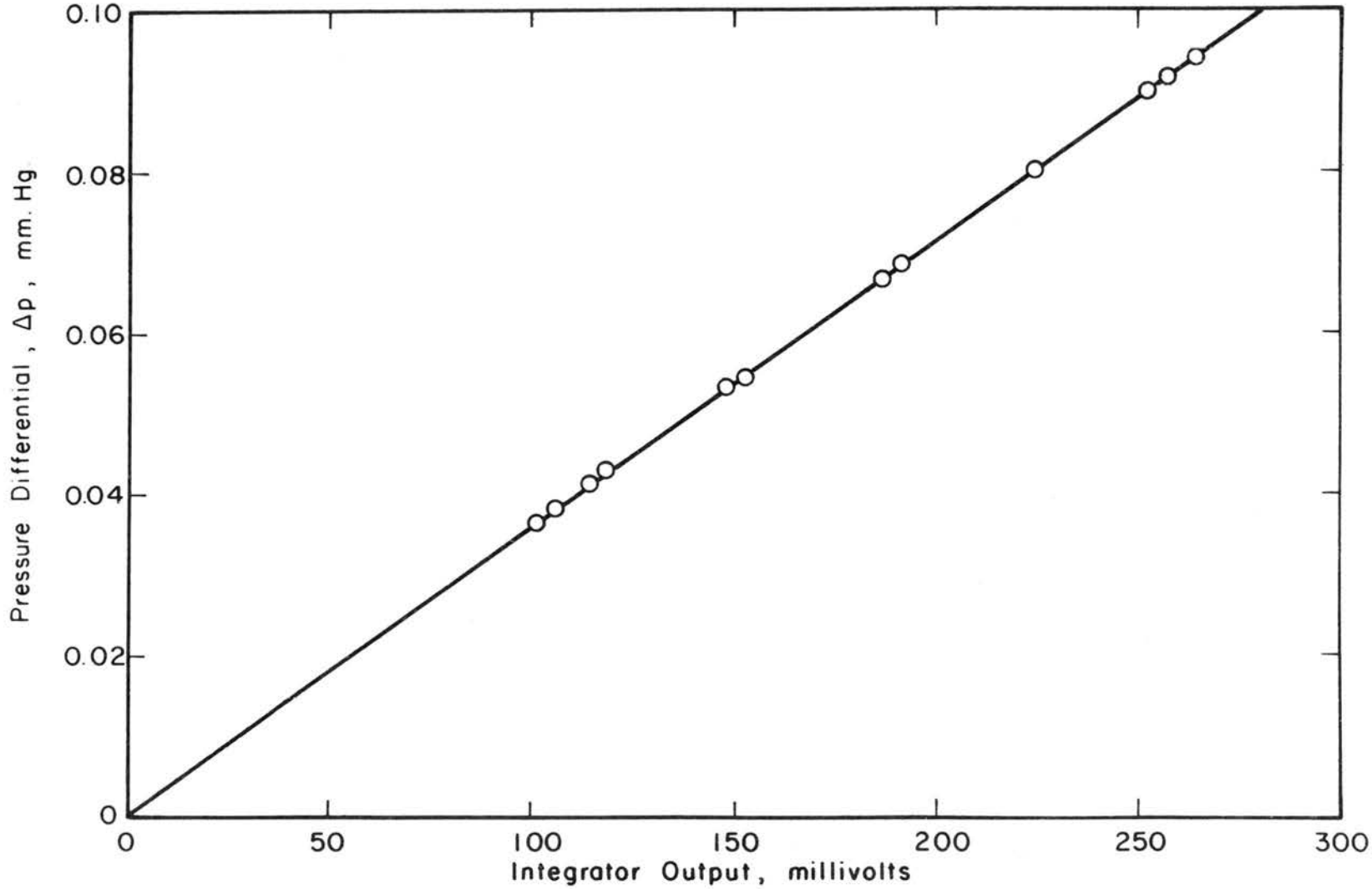

Figure 17. Typical calibration curve of integrator output versus pressure differential from Trans-sonics (0.1 scale). Integration time: 200 seconds

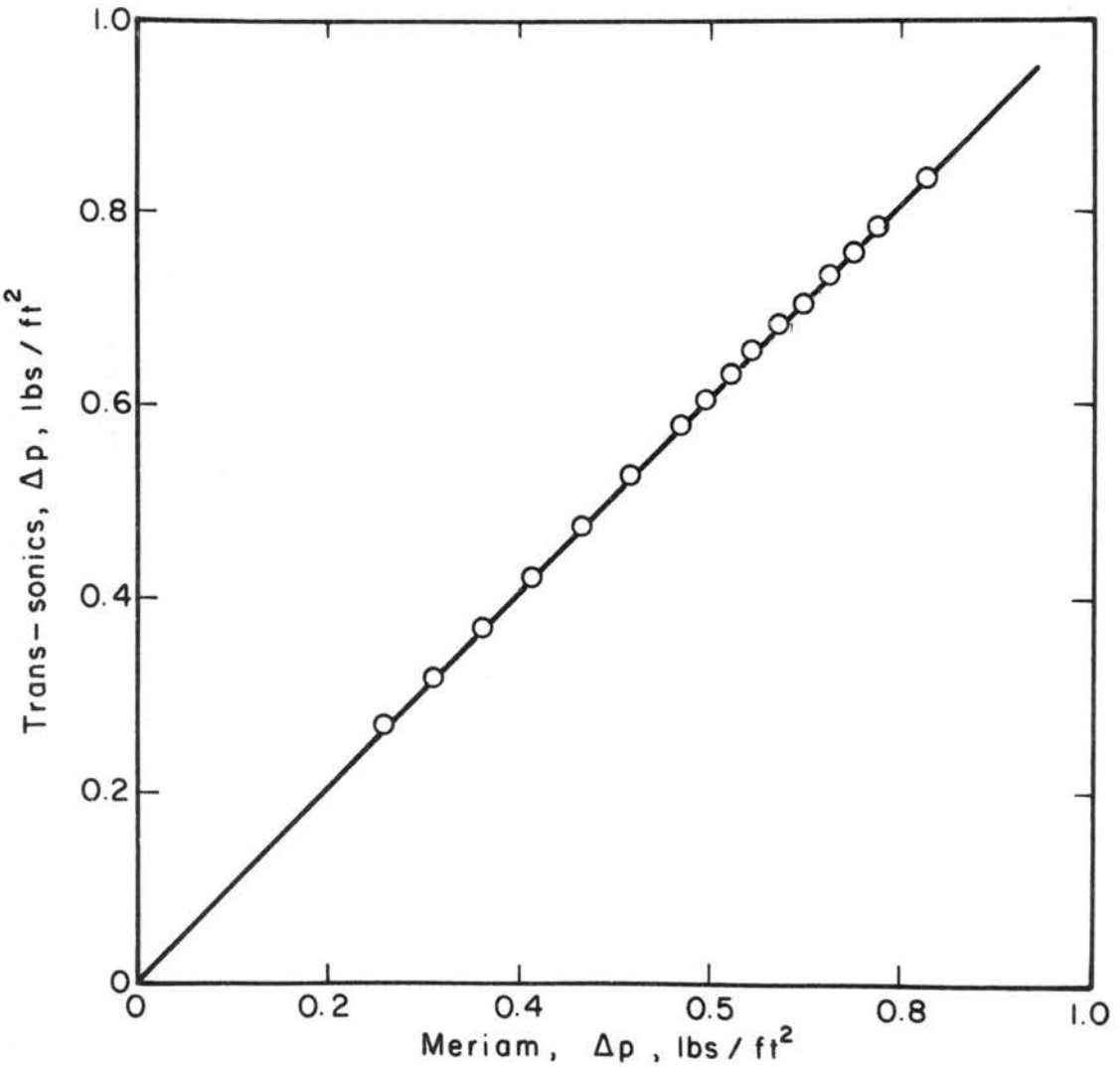

Figure 18. Typical calibration curve of Trans-sonics versus Meriam micromanometer (0.3 scale)

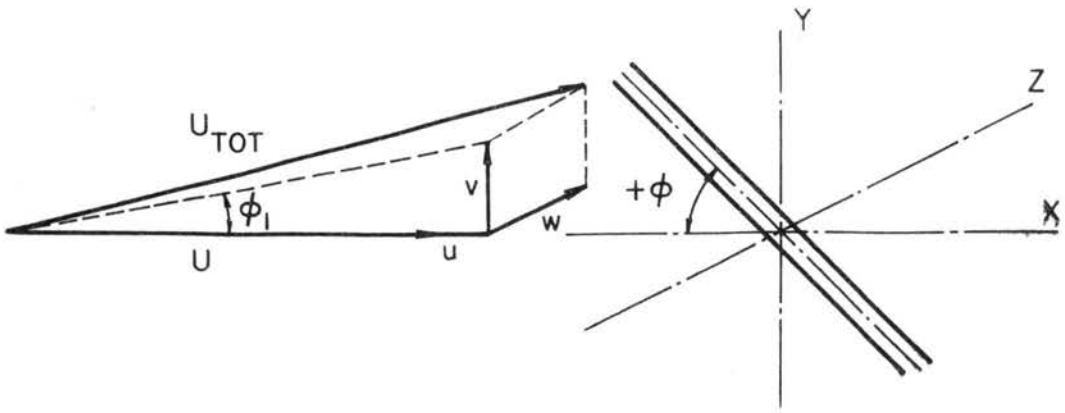

Figure 19. Hot wire yawed to mean flow, $\phi = \phi \quad \psi = 0^0$

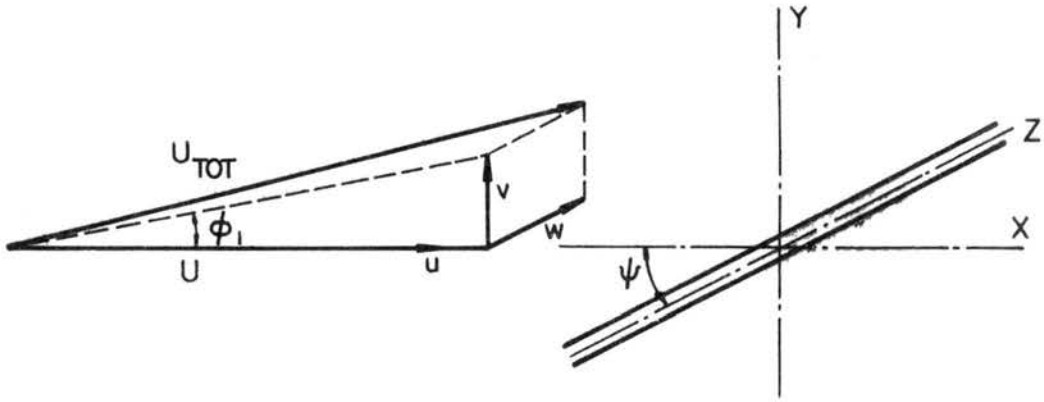

Figure 20. Hot wire normal to mean flow, $\phi = 0^0 \quad \psi = 90^0$

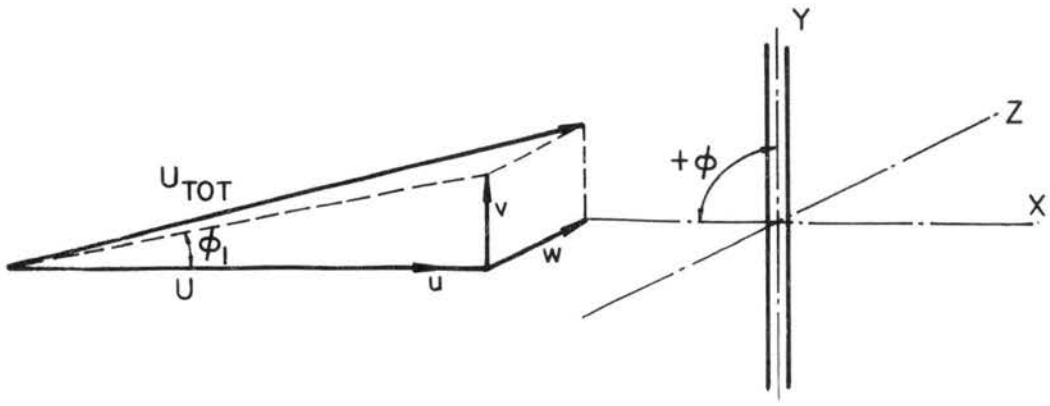

Figure 21. Hot wire normal to mean flow, $\phi = 90^0 \quad \psi = 0^0$

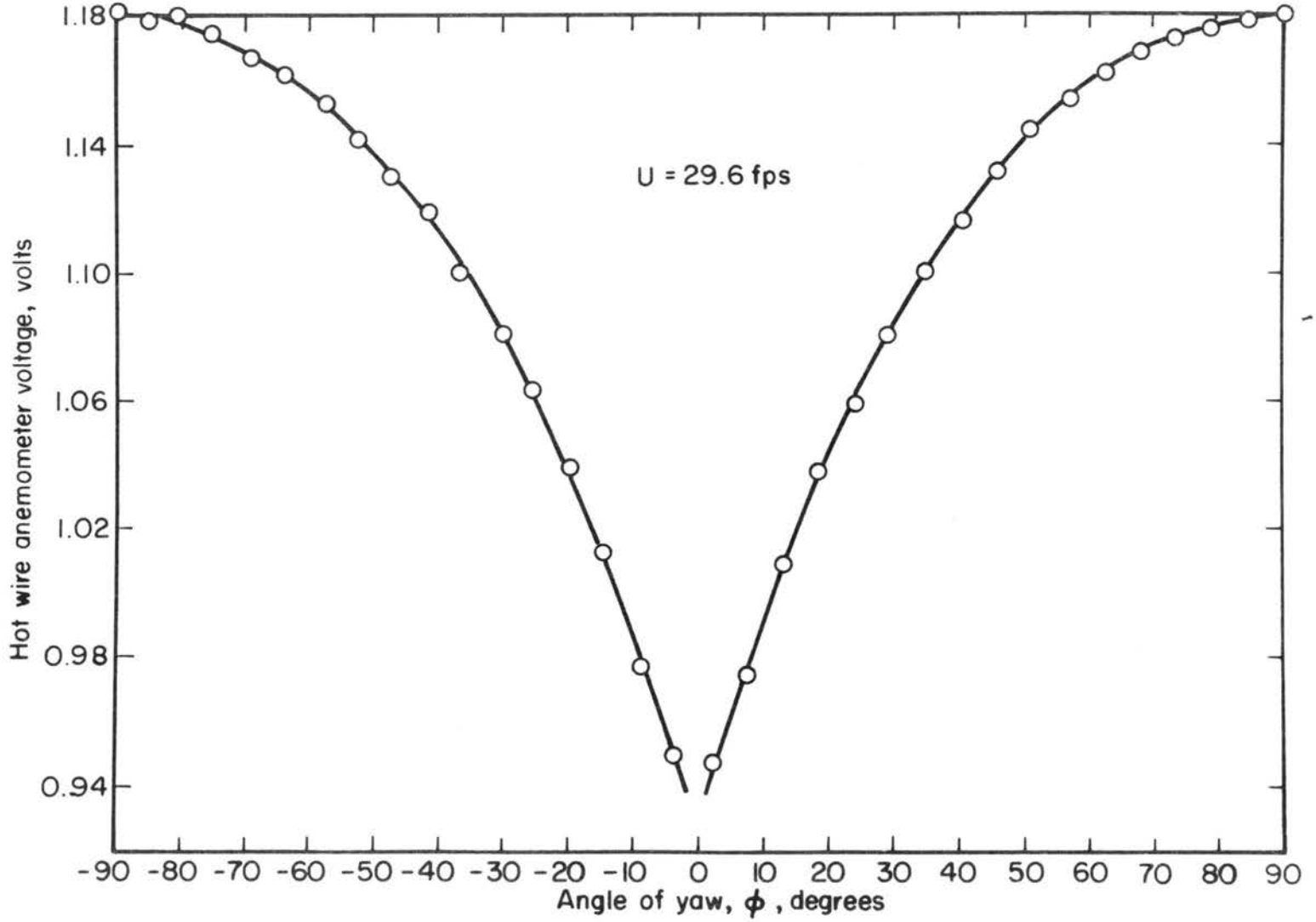

Figure 22. Variation of hot-wire anemometer voltage with angle of yaw

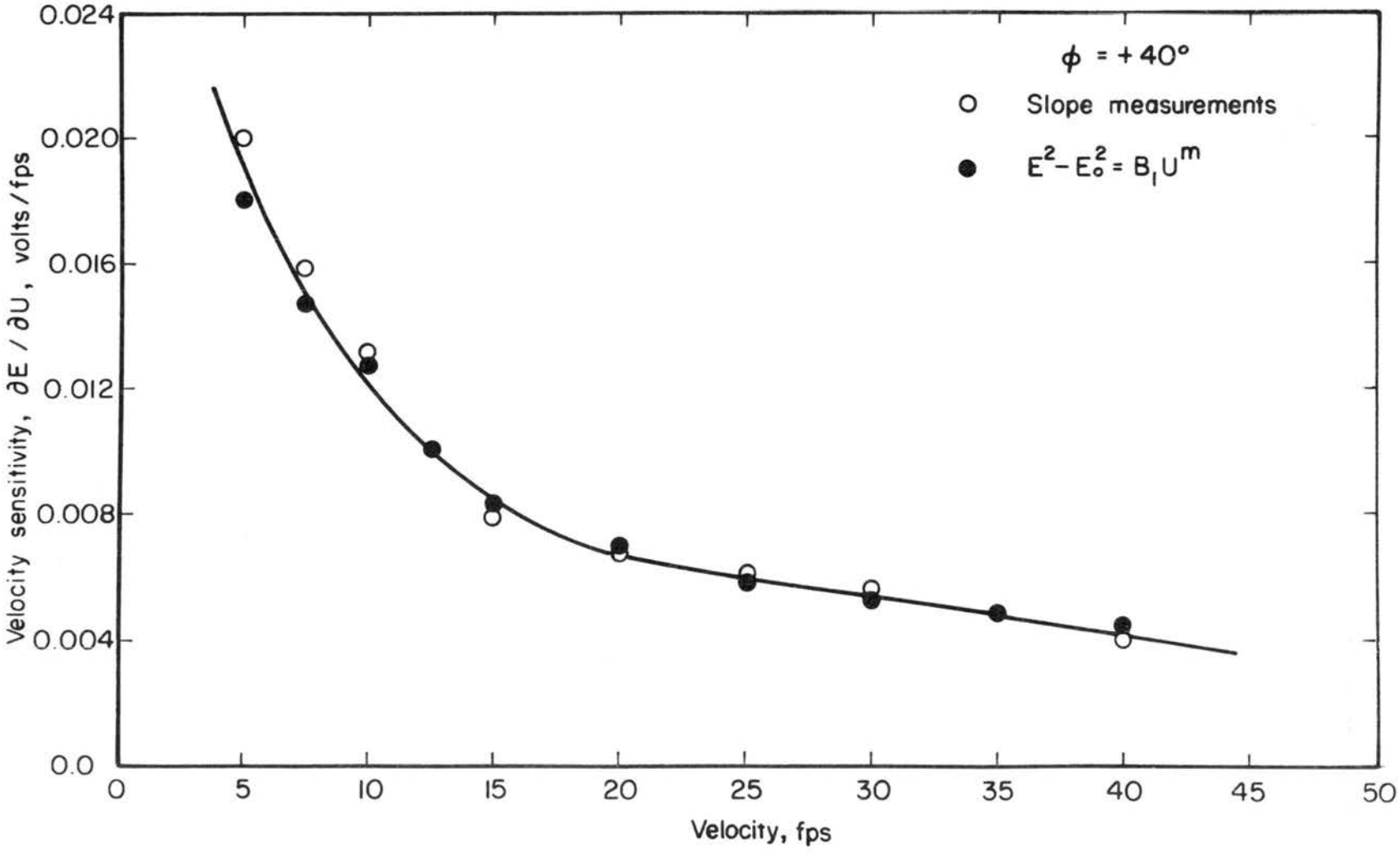

Figure 23. Variation of velocity sensitivity with velocity for angle of yaw $+40^0$

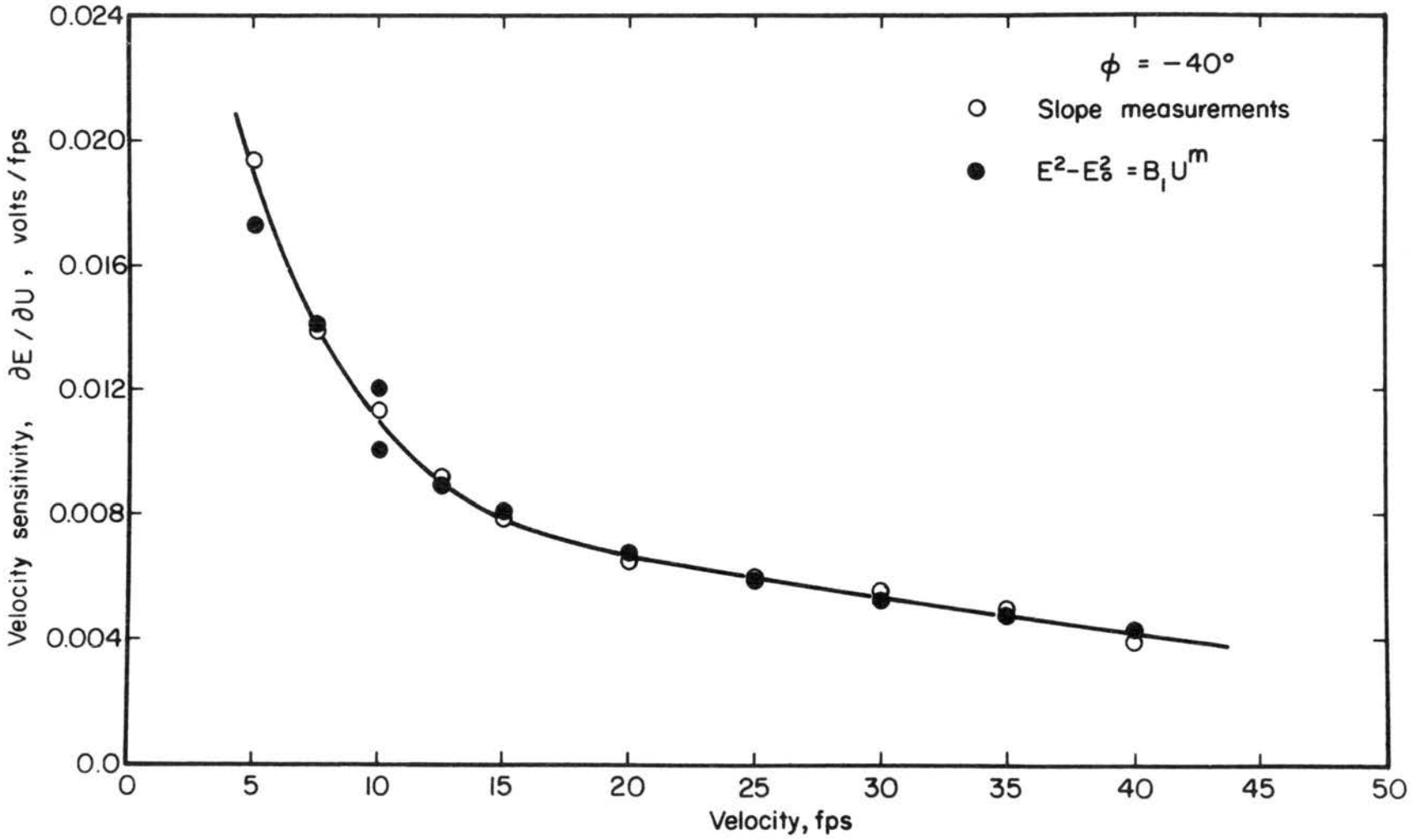

Figure 24. Variation of velocity sensitivity with velocity for angle of yaw -40^{0}

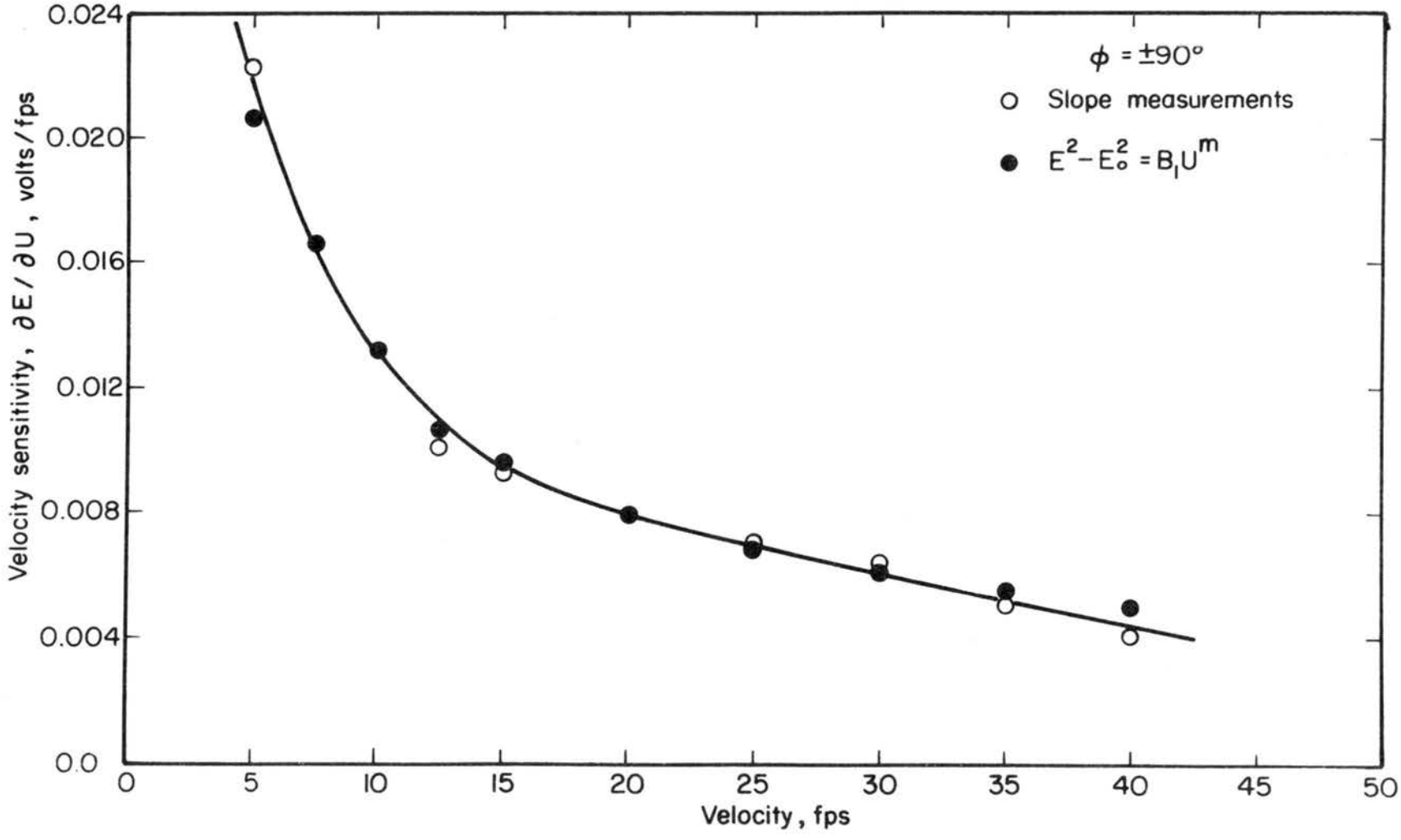

Figure 25. Variation of velocity sensitivity with velocity for wire normal to the mean flow

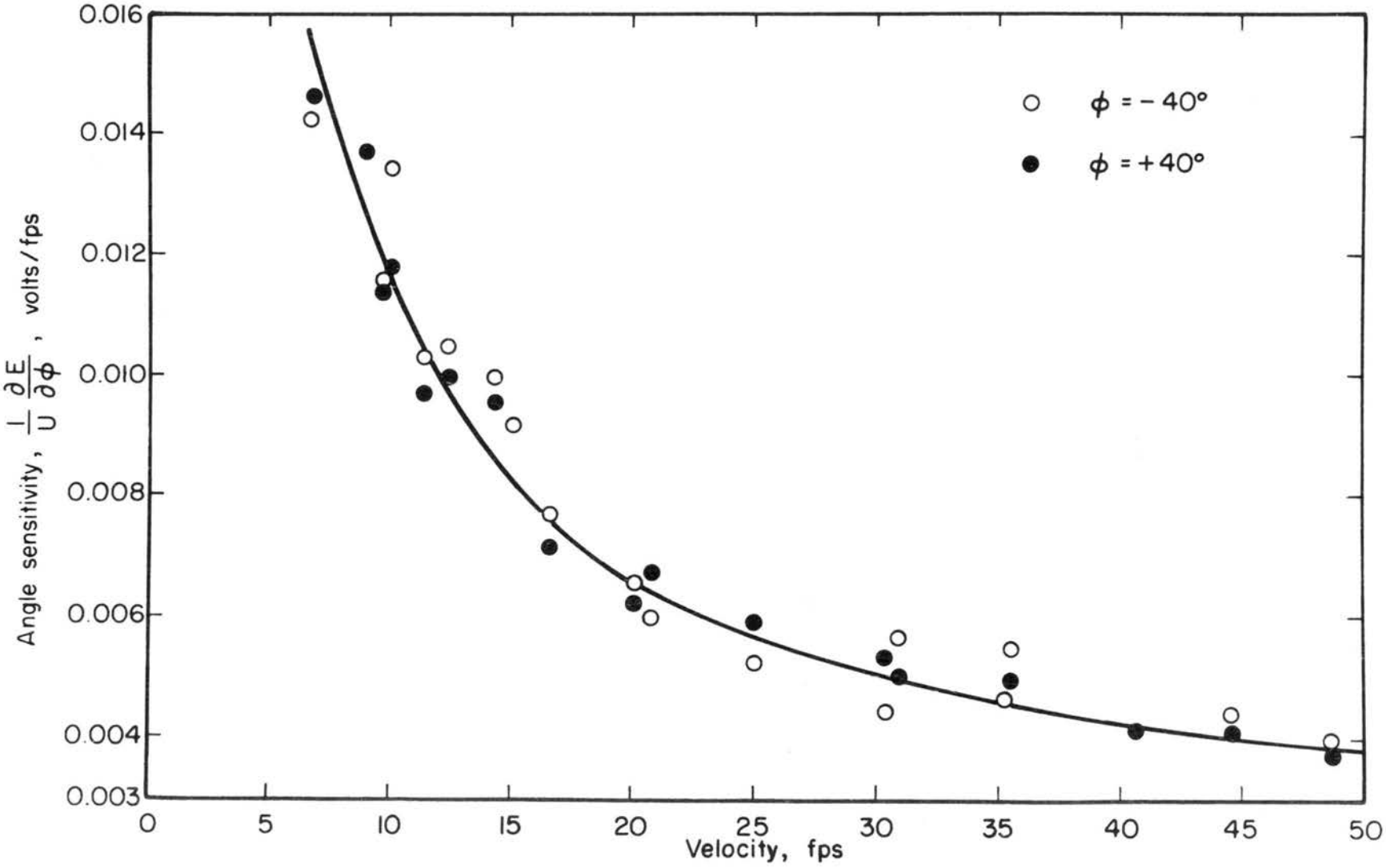

Figure 26. Variation of angle sensitivity with velocity for angles of yaw $\pm 40^0$

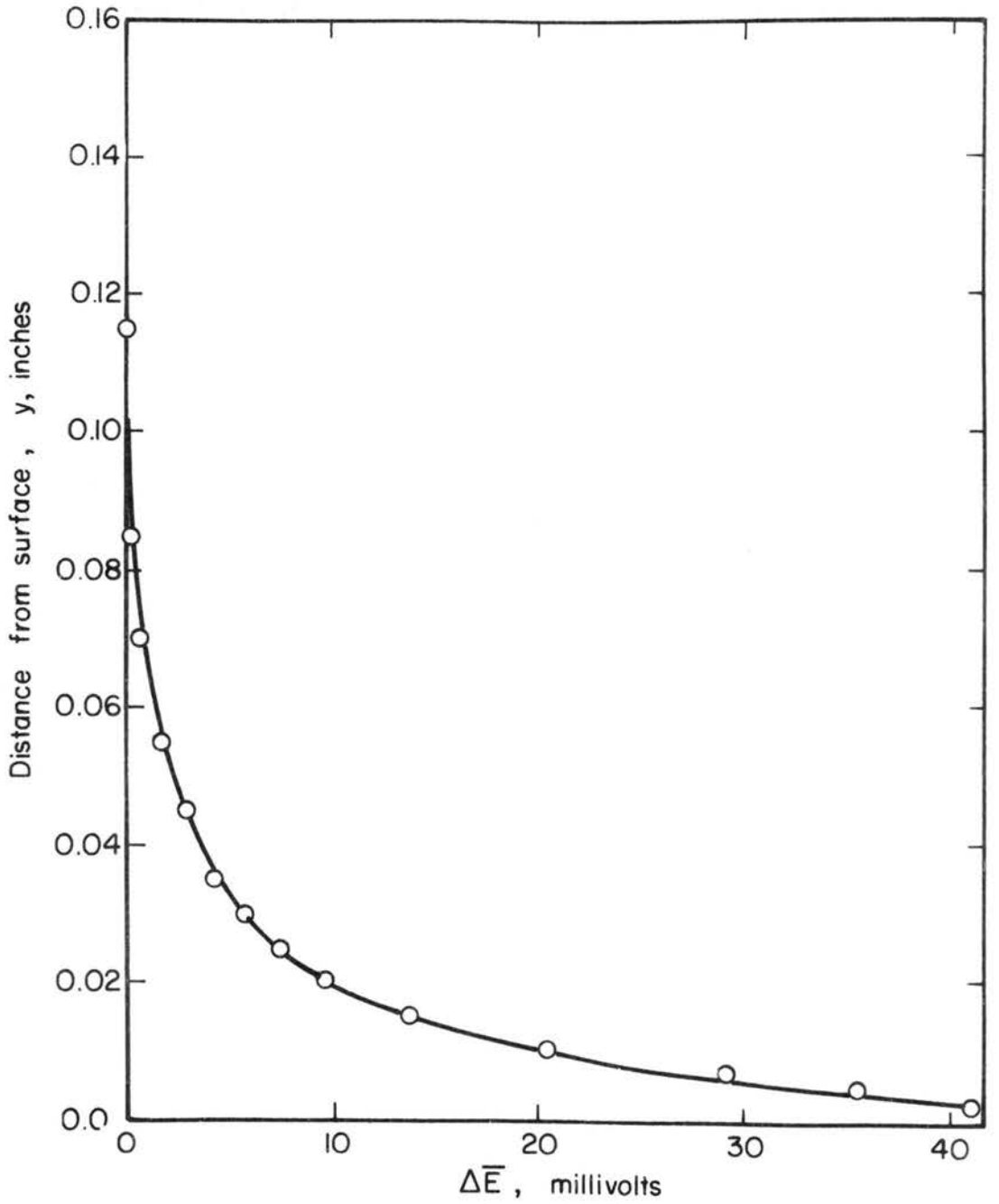

Figure 27. The effect of the solid surface on the heat transfer from a hot wire for no-flow condition

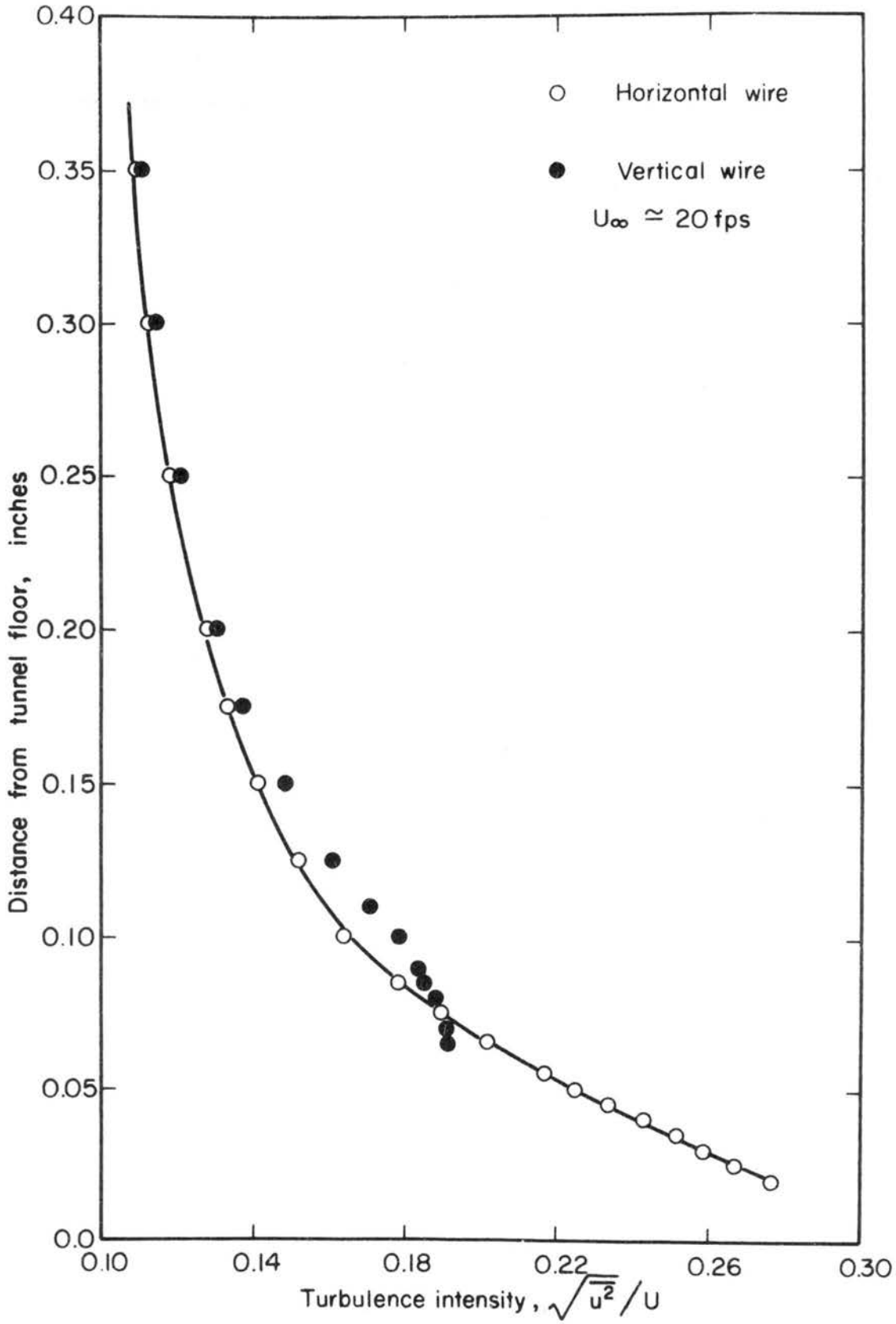

Figure 28. Comparison of turbulence-intensity measurements with a horizontal and vertical hot wire near the tunnel floor

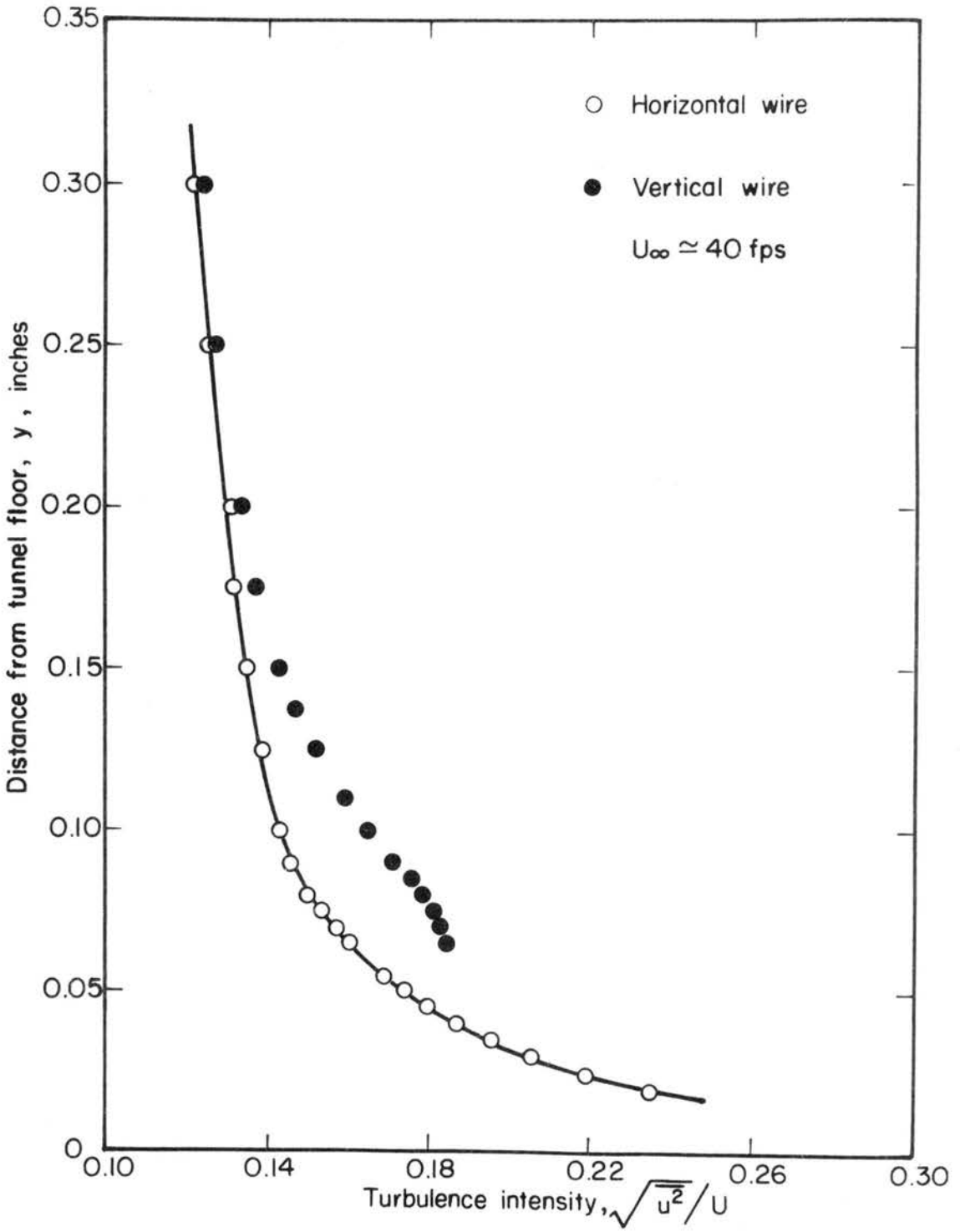

Figure 29. Comparison of turbulence intensity measurements with a horizontal and vertical hot wire near the tunnel floor

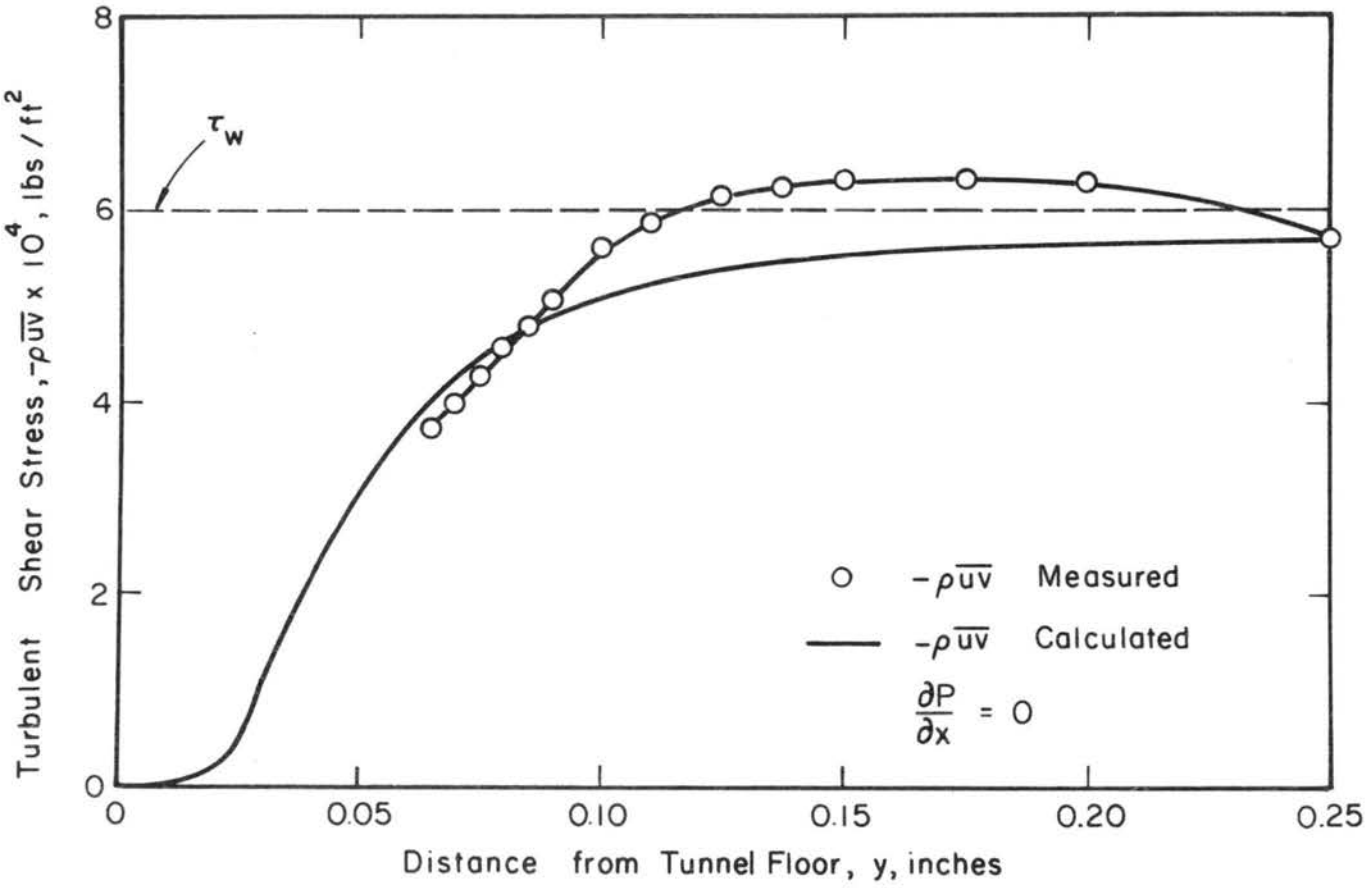

Figure 30. Comparison of measured turbulent shear with mean velocity measurements. $U_\infty \simeq 20$ fps.

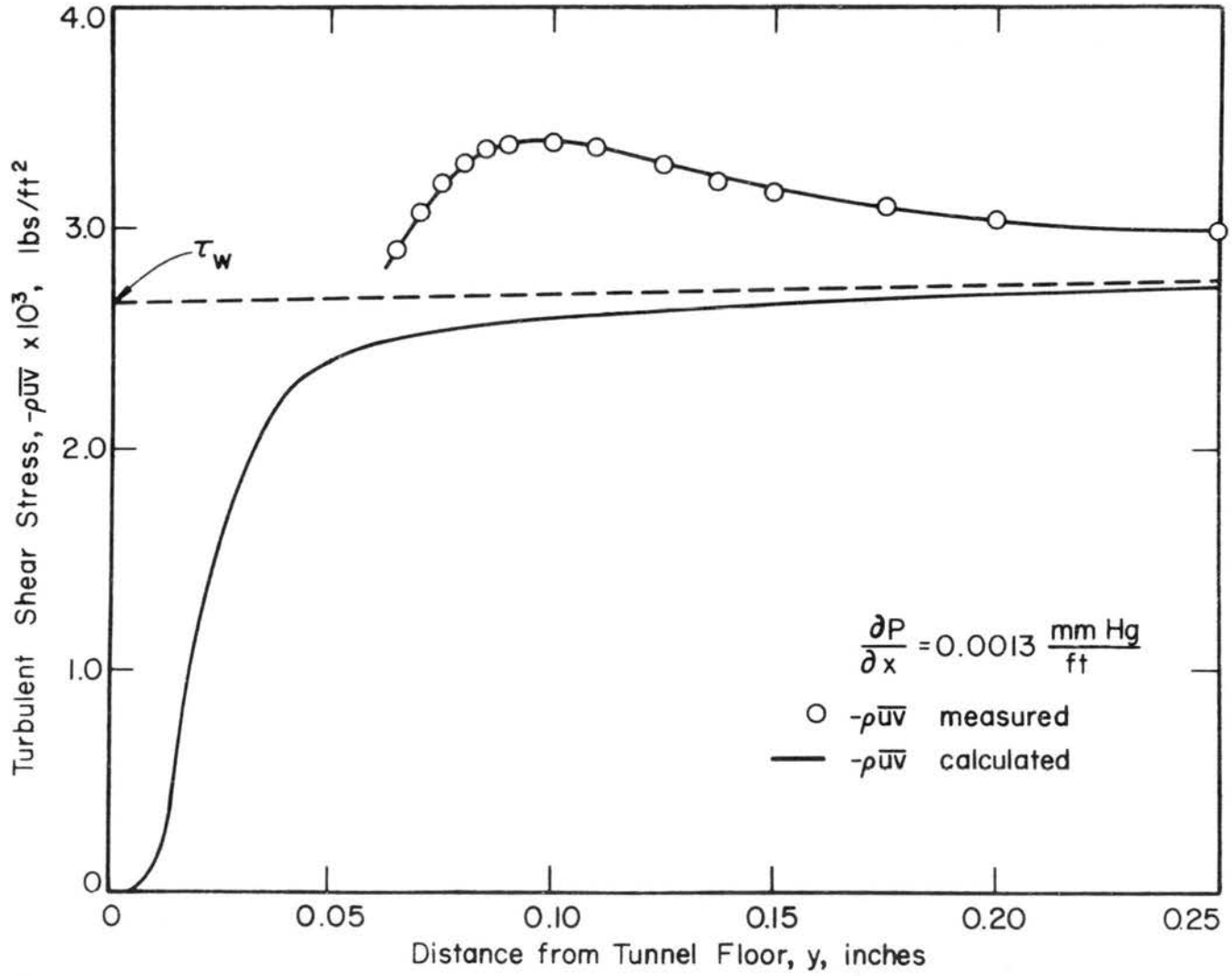

Figure 31. Comparison of measured turbulent shear with mean velocity measurements. $U_\infty \simeq 40$ fps.

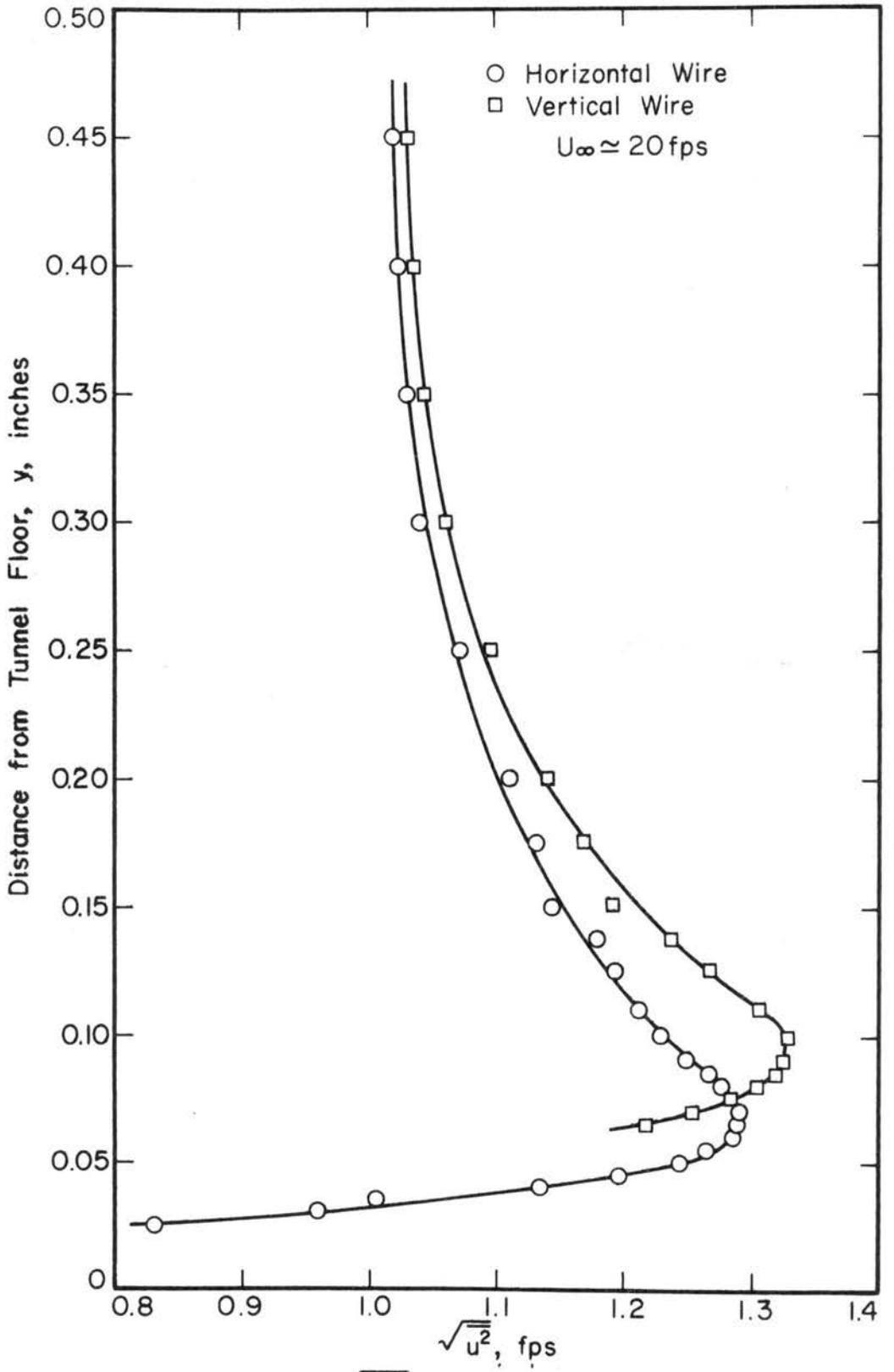

Figure 32. Comparison of $\sqrt{\overline{u^2}}$ measurements with a horizontal and vertical hot wire near the tunnel floor. $U_\infty \simeq 20$ fps.

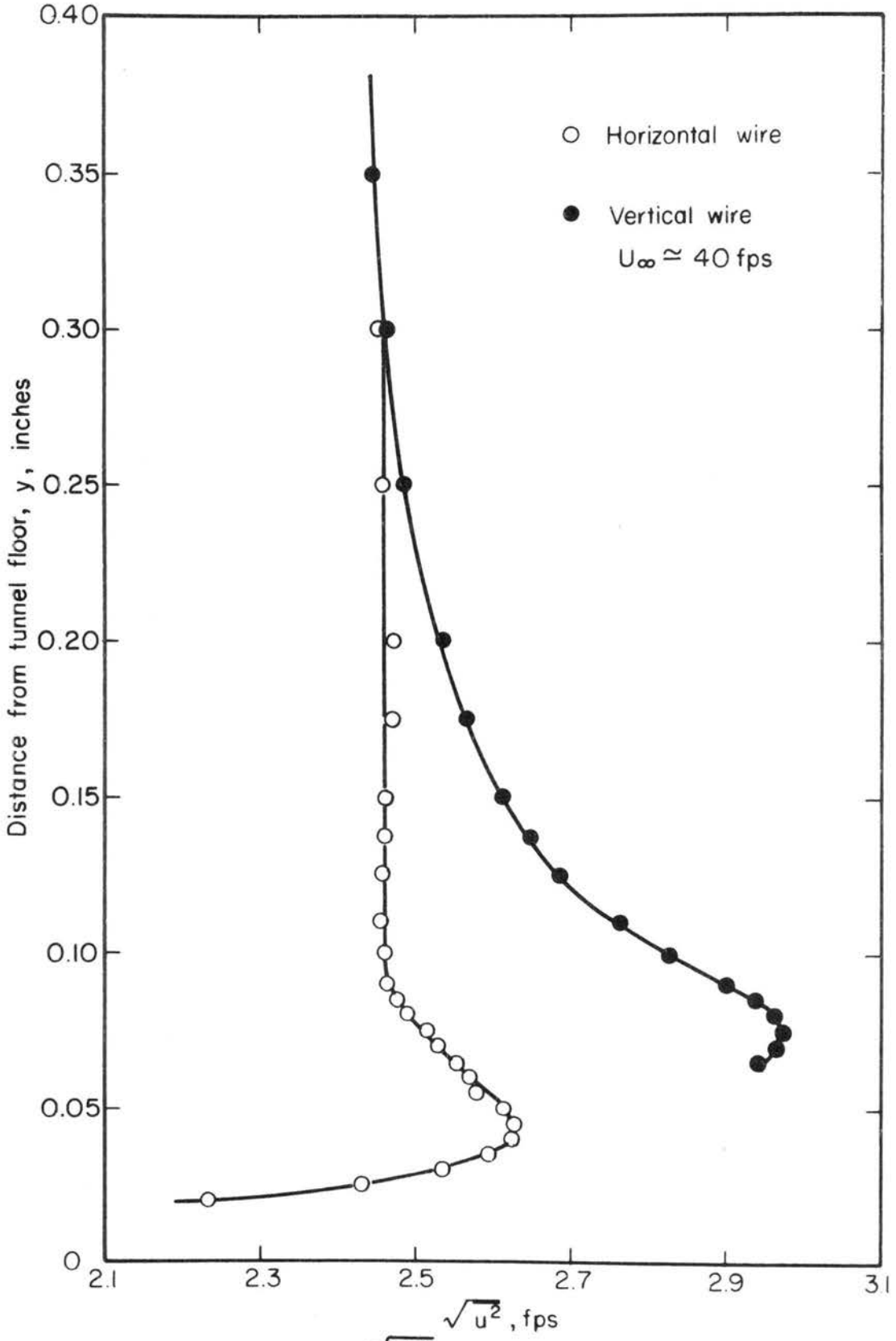

Figure 33. Comparison of $\sqrt{u^2}$ measurements with a horizontal and vertical hot wire near the tunnel floor. $U_\infty \simeq 40$ fps.

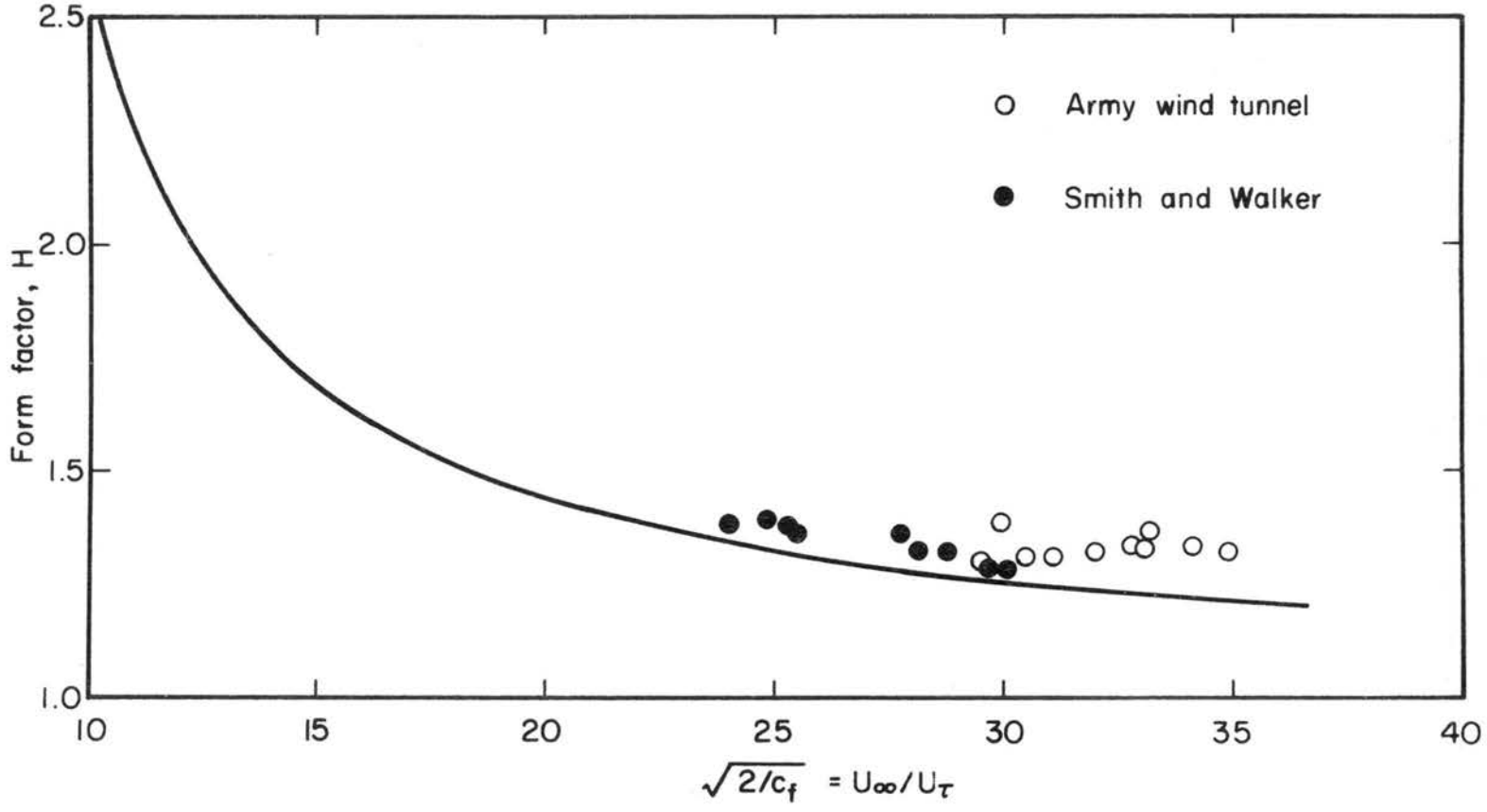

Figure 34. Effect of the skin-friction coefficient on the form factor H for turbulent boundary layers with zero-pressure gradient

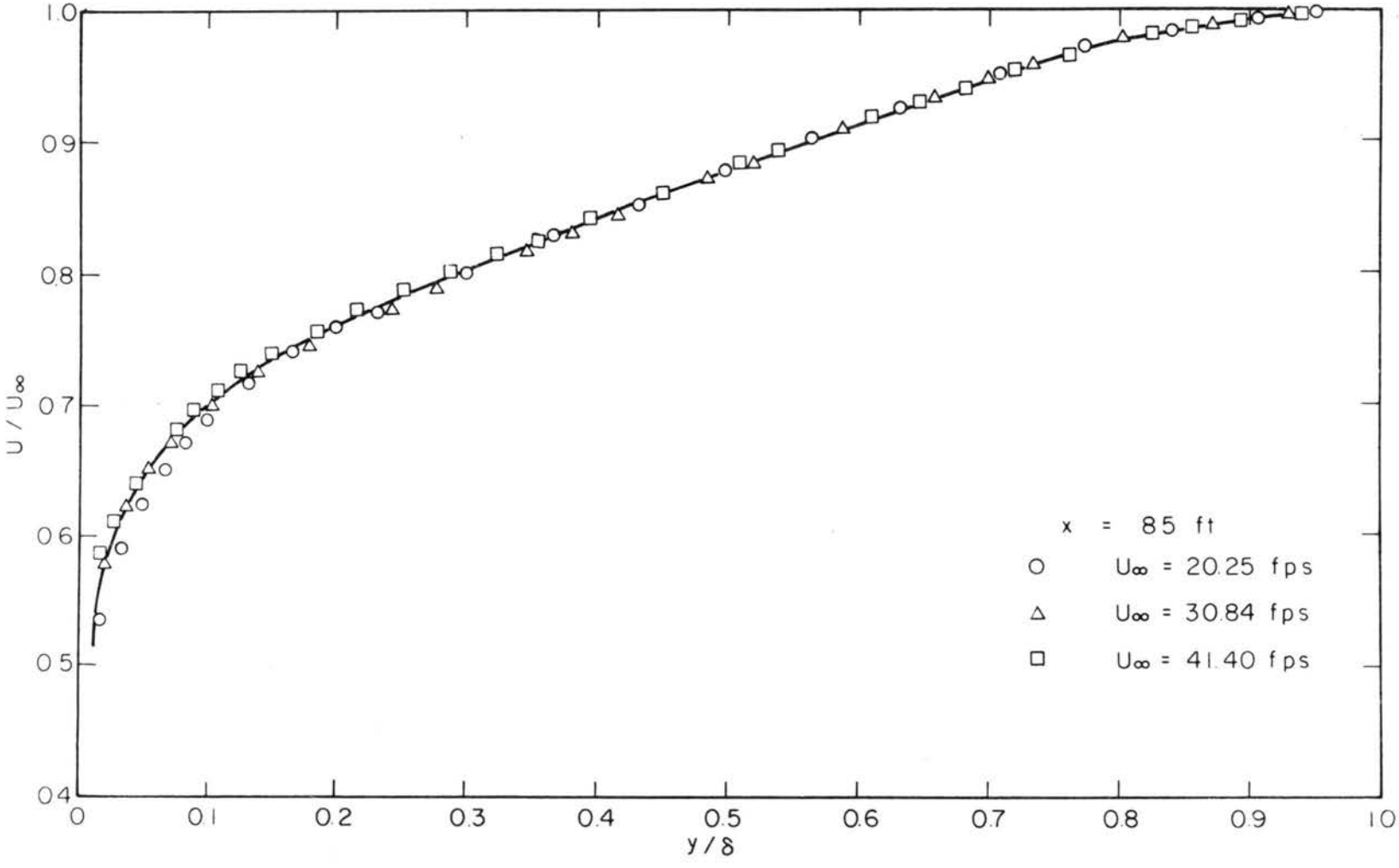

Figure 35. Mean velocity distributions, x = 85 ft.

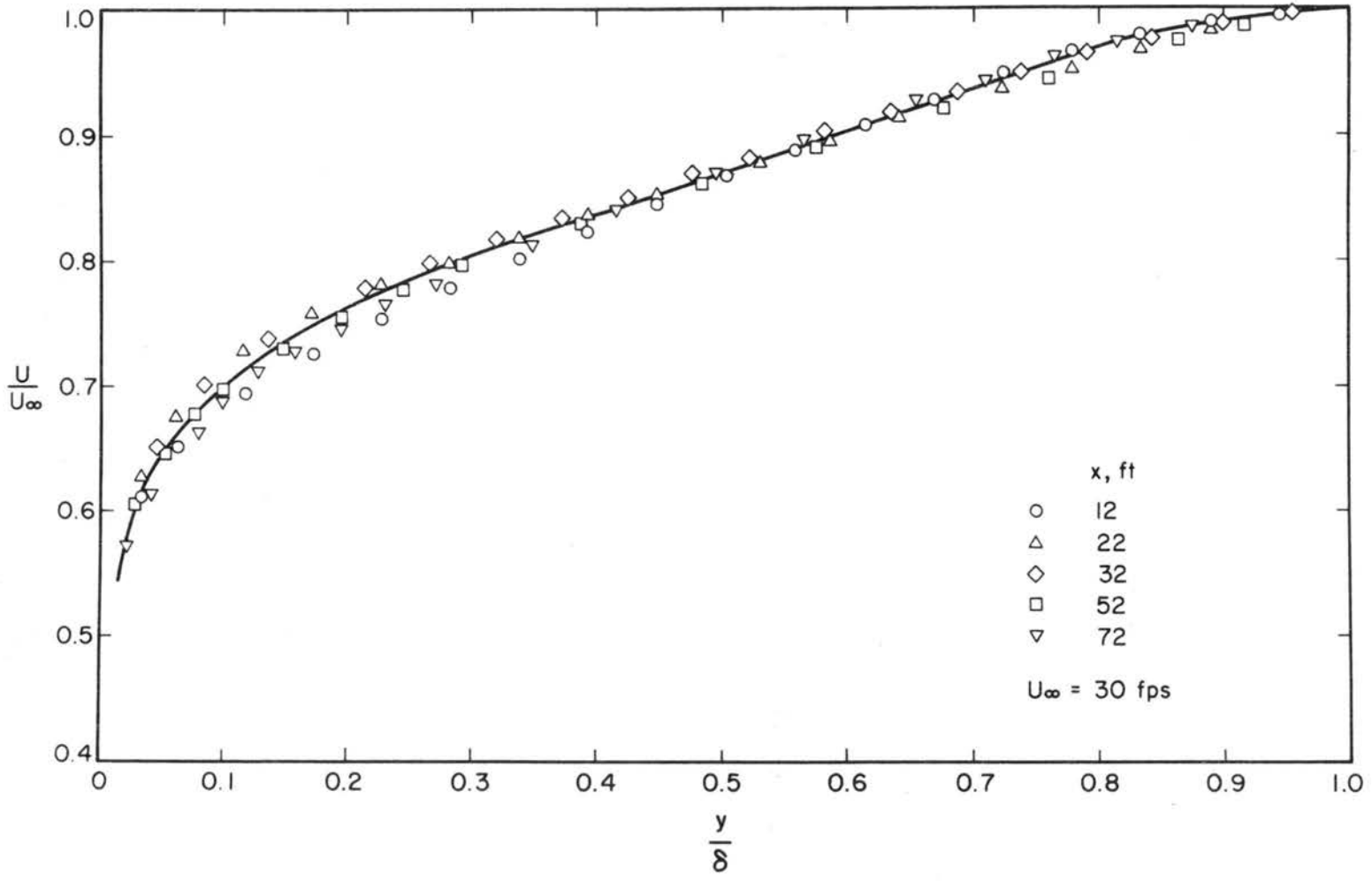

Figure 36. Mean velocity distributions, x = 12, 22, 32, 52, 72 ft.

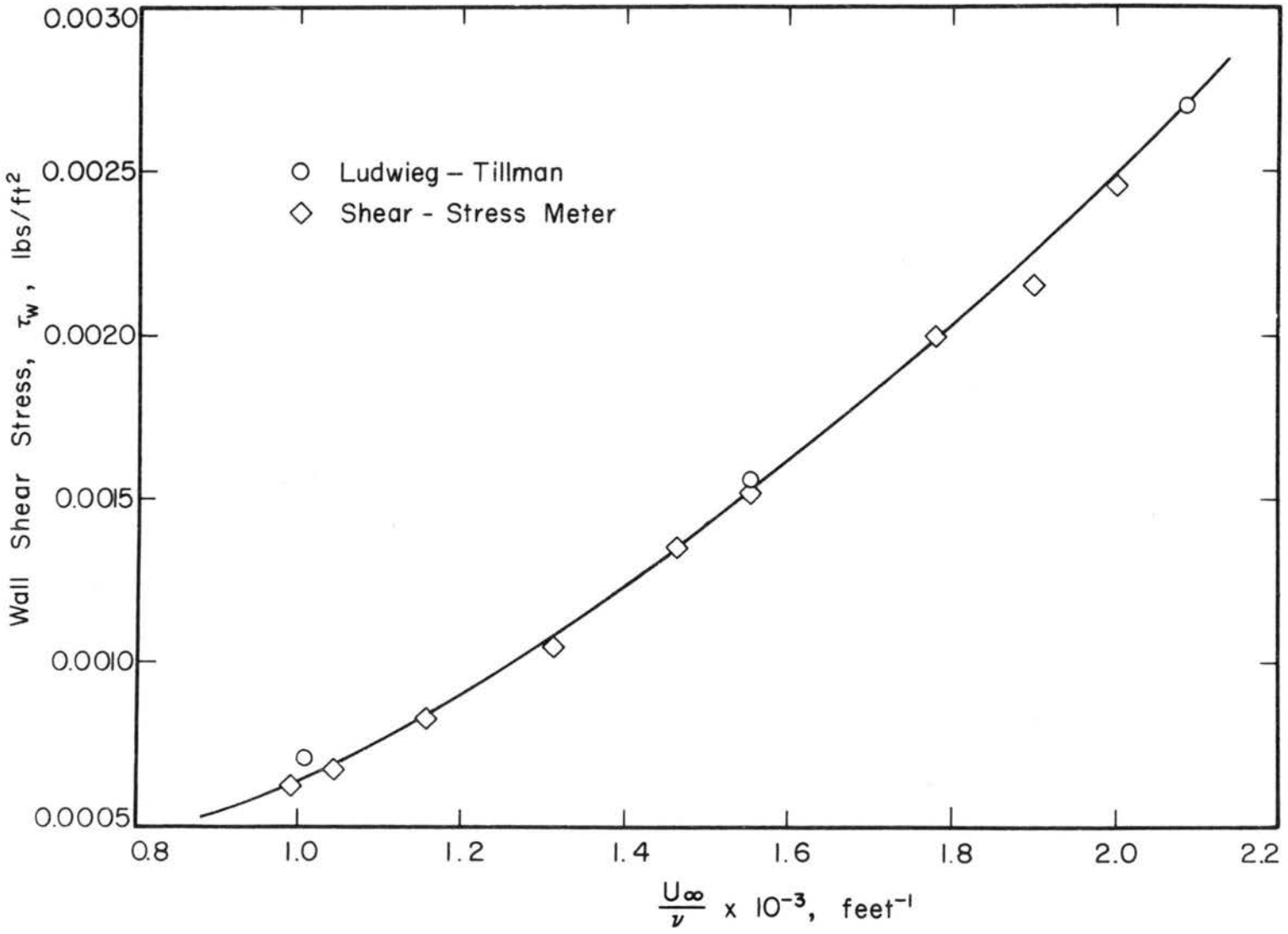

Figure 37. Variation of wall-shear stress with the term U_∞/ν

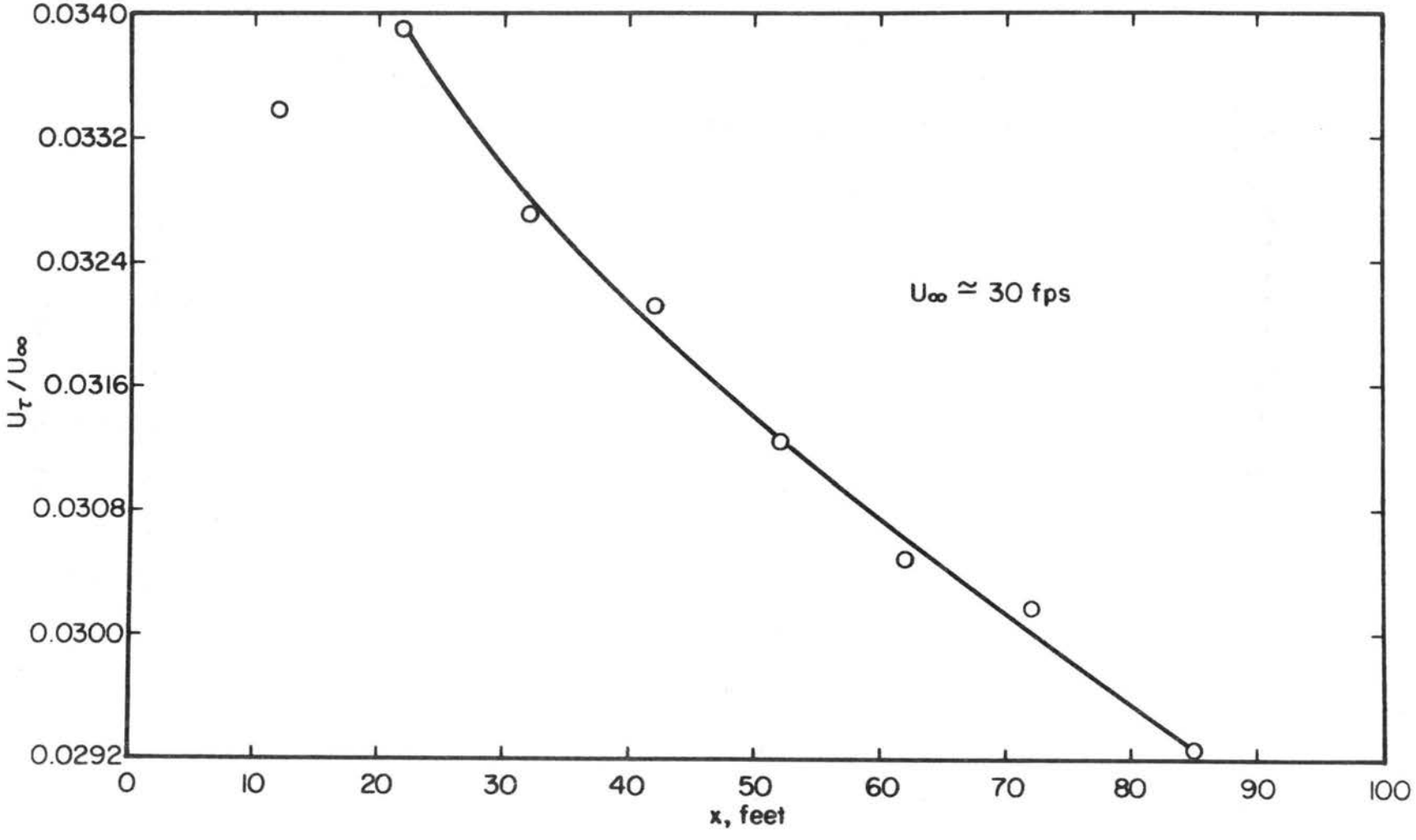

Figure 38. Variation of U_τ / U_∞ with x

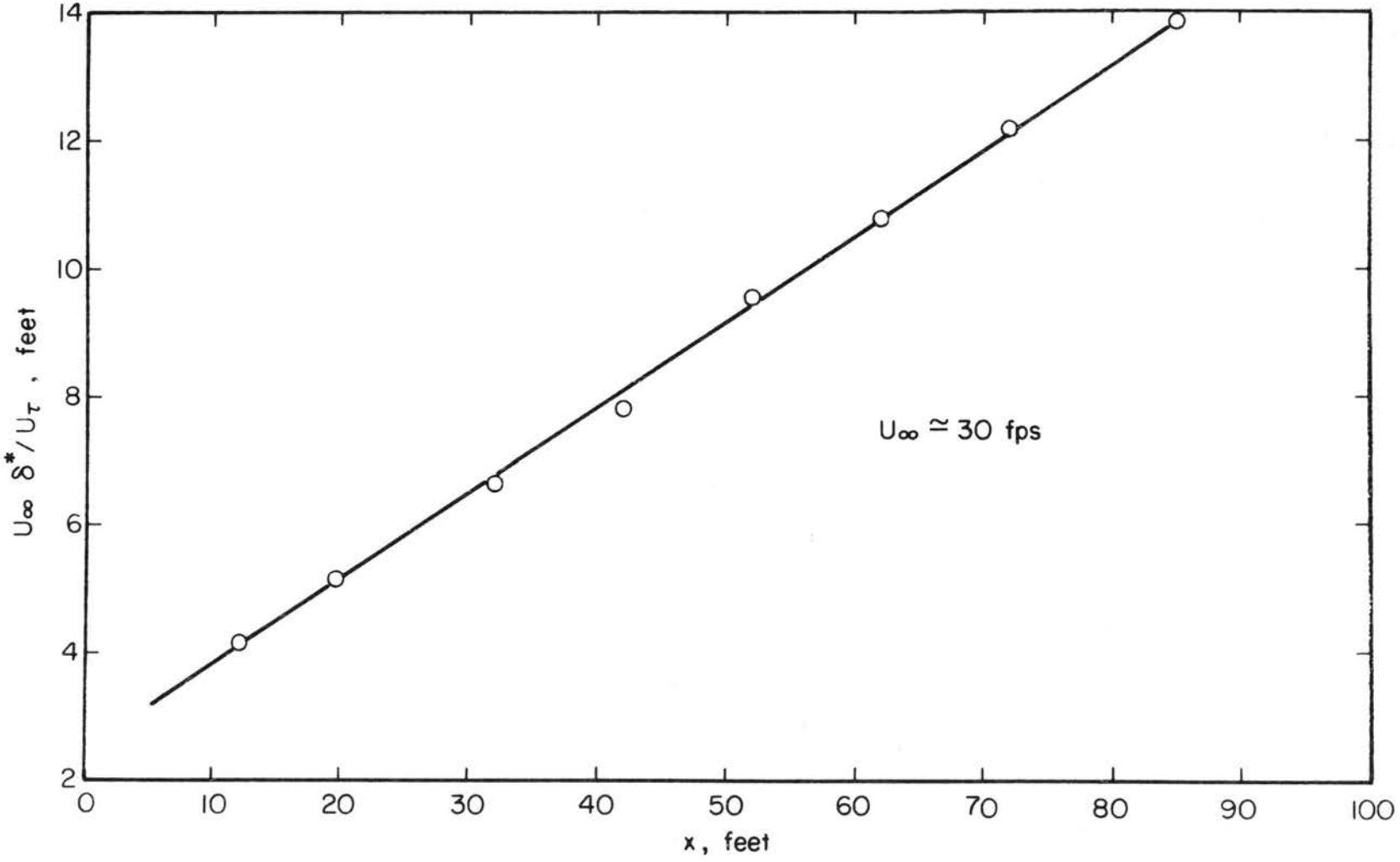

Figure 39. Variation of $U_\infty \delta^*/U_\tau$ with x

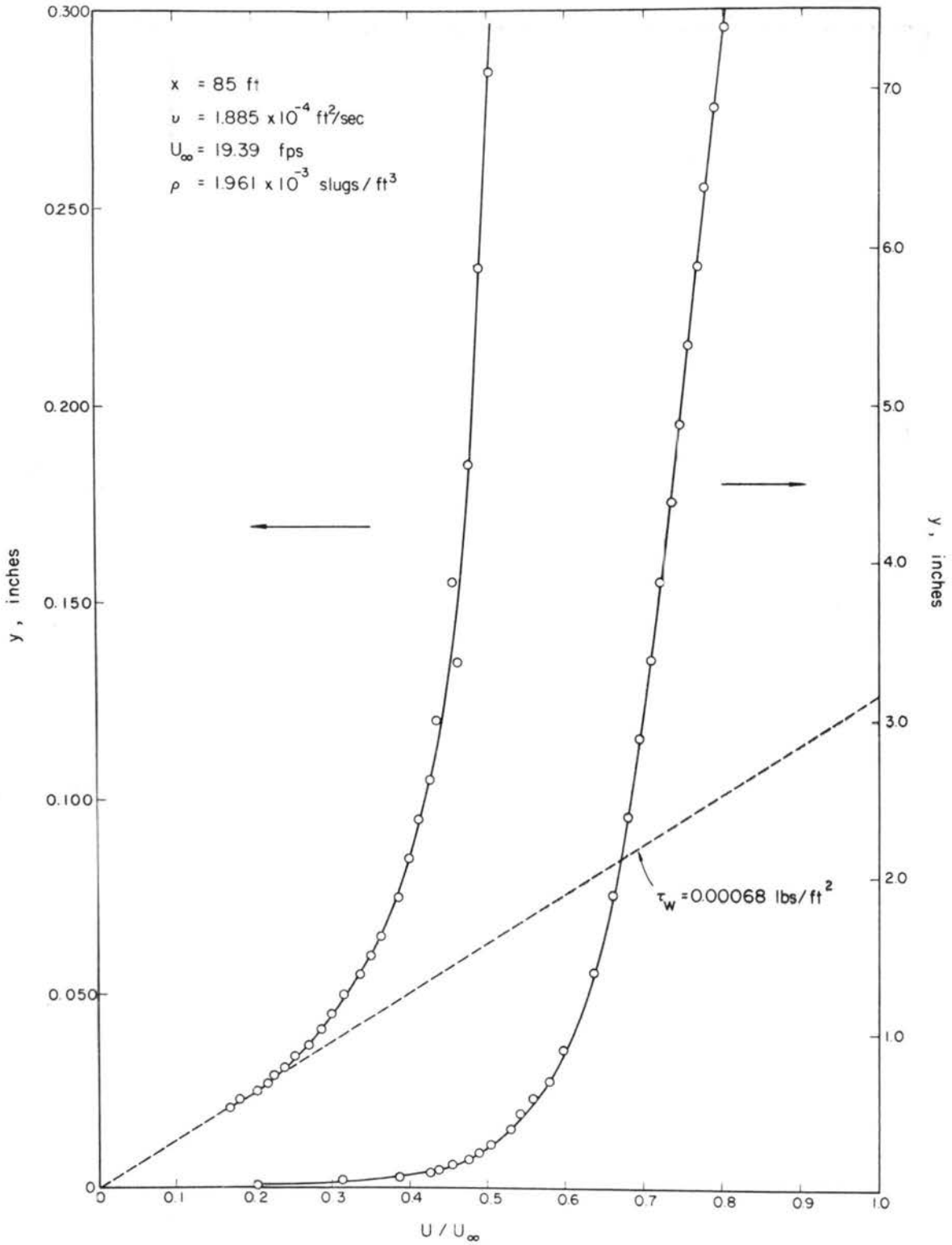

Figure 40. Velocity distribution, U_{∞} = 19.39 fps.

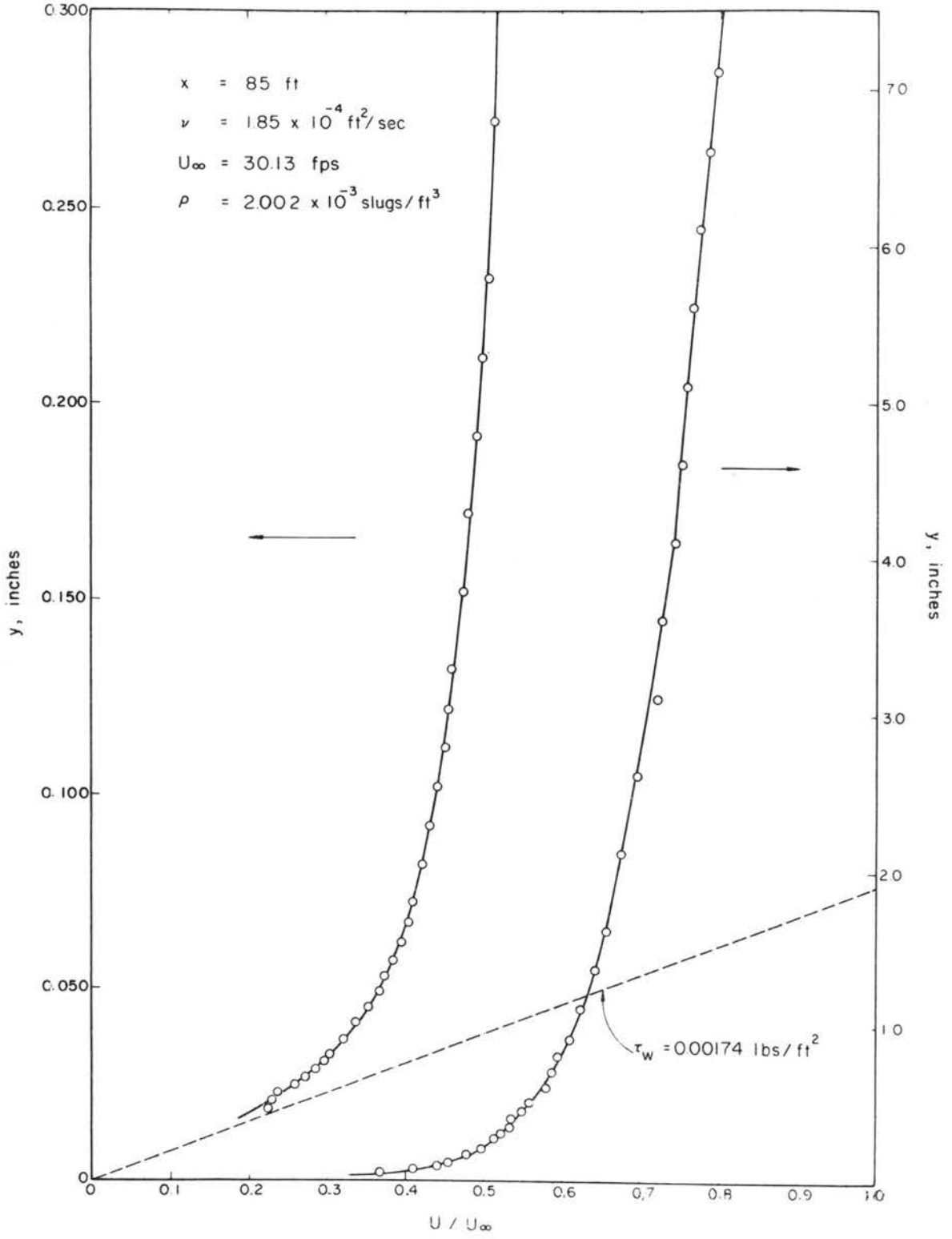

Figure 41. Velocity distribution, U_{∞} = 30.13 fps.

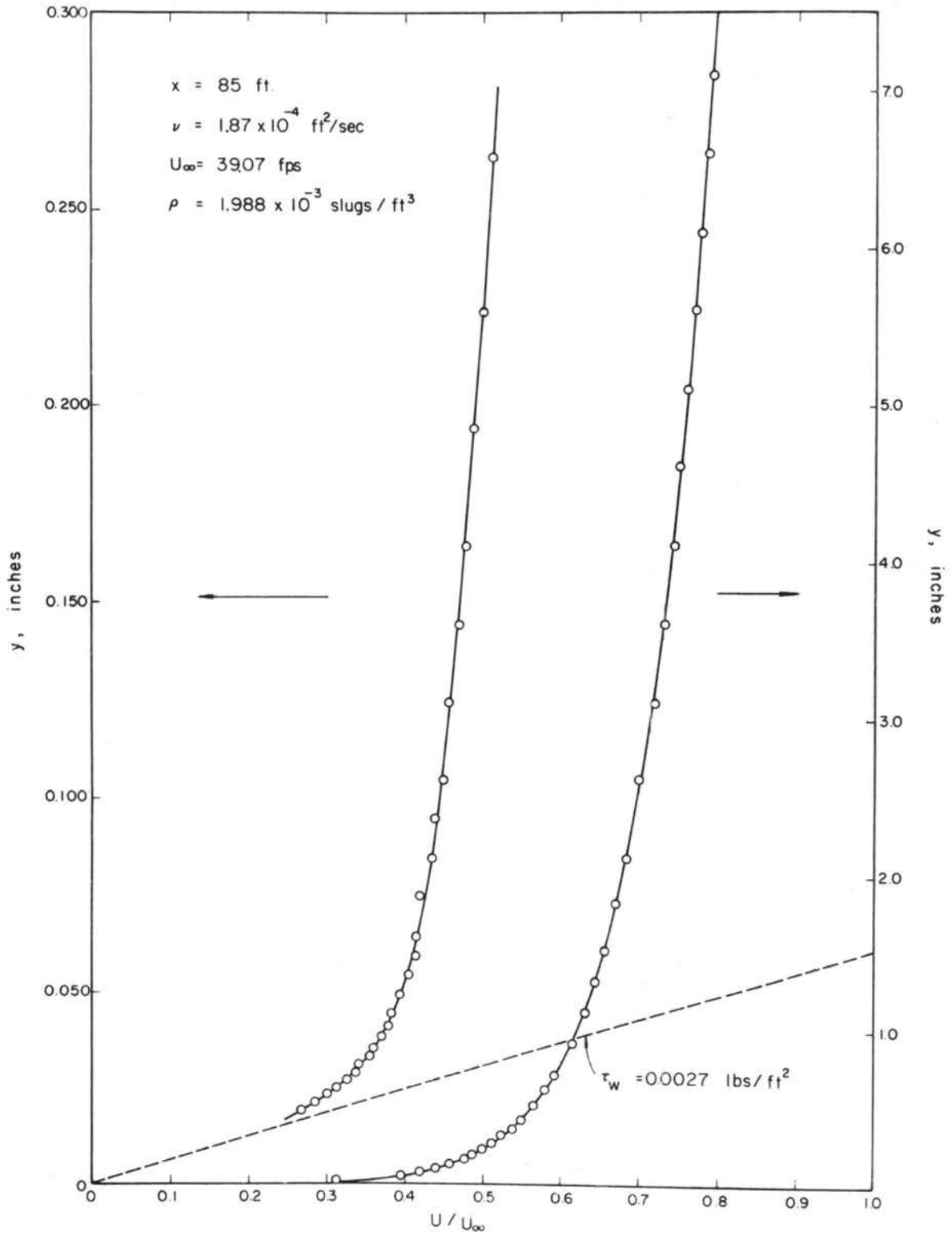

Figure 42. Velocity distribution, U_{∞} = 39.07 fps.

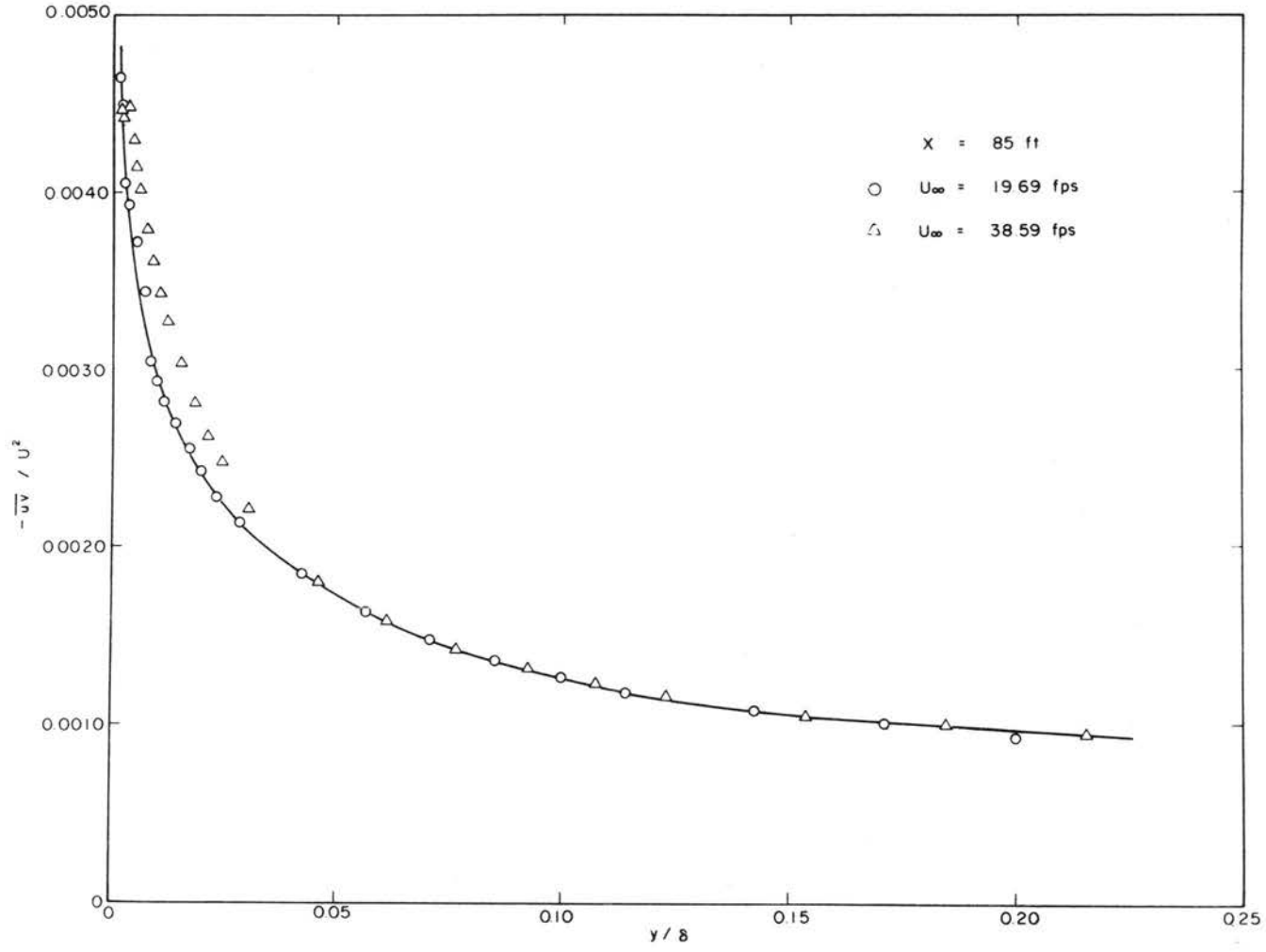

Figure 43. Distribution of term $\frac{-\overline{uv}}{U^2}$

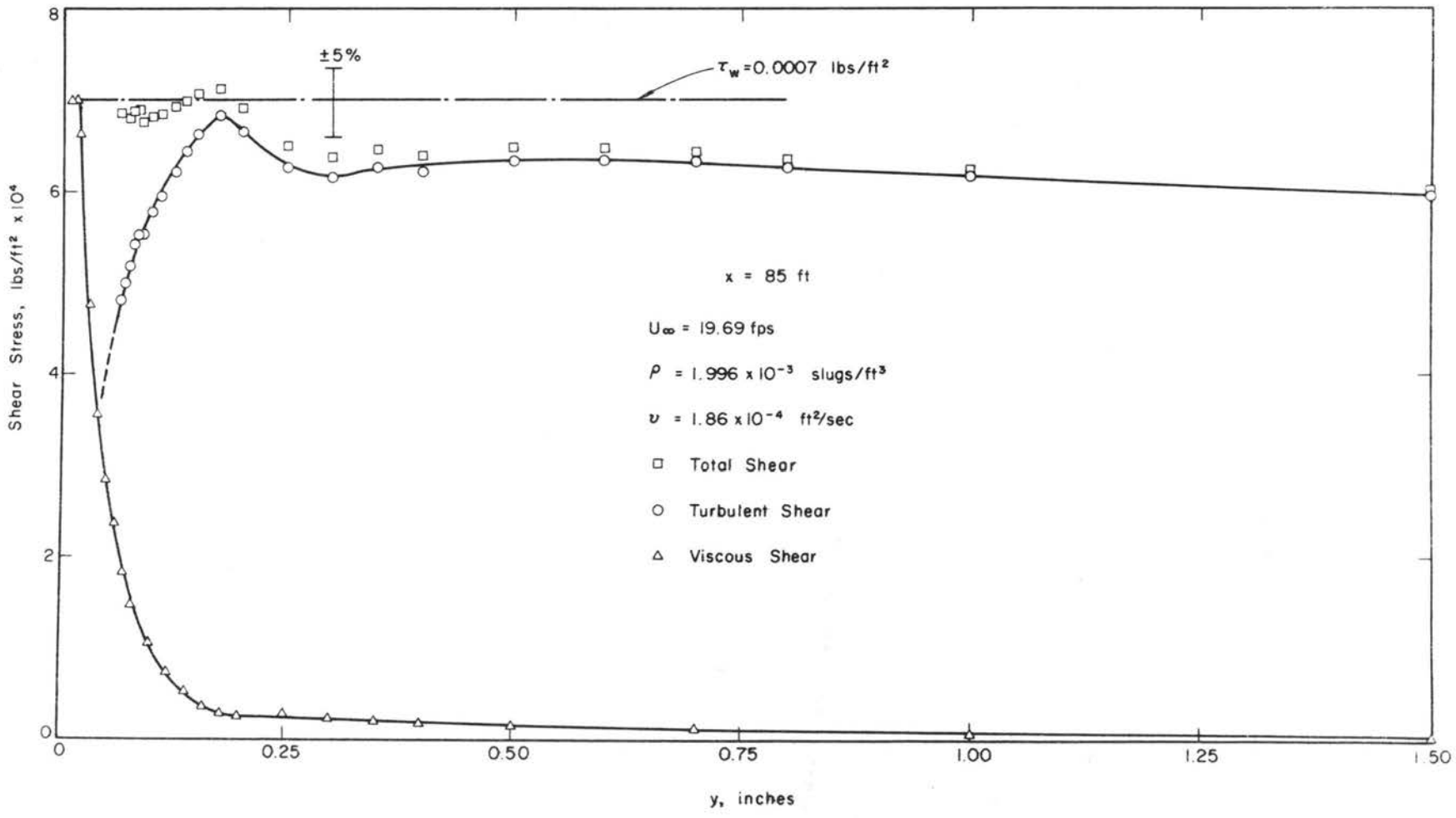

Figure 44. Shear-stress distribution, U_∞ = 19.69 fps.

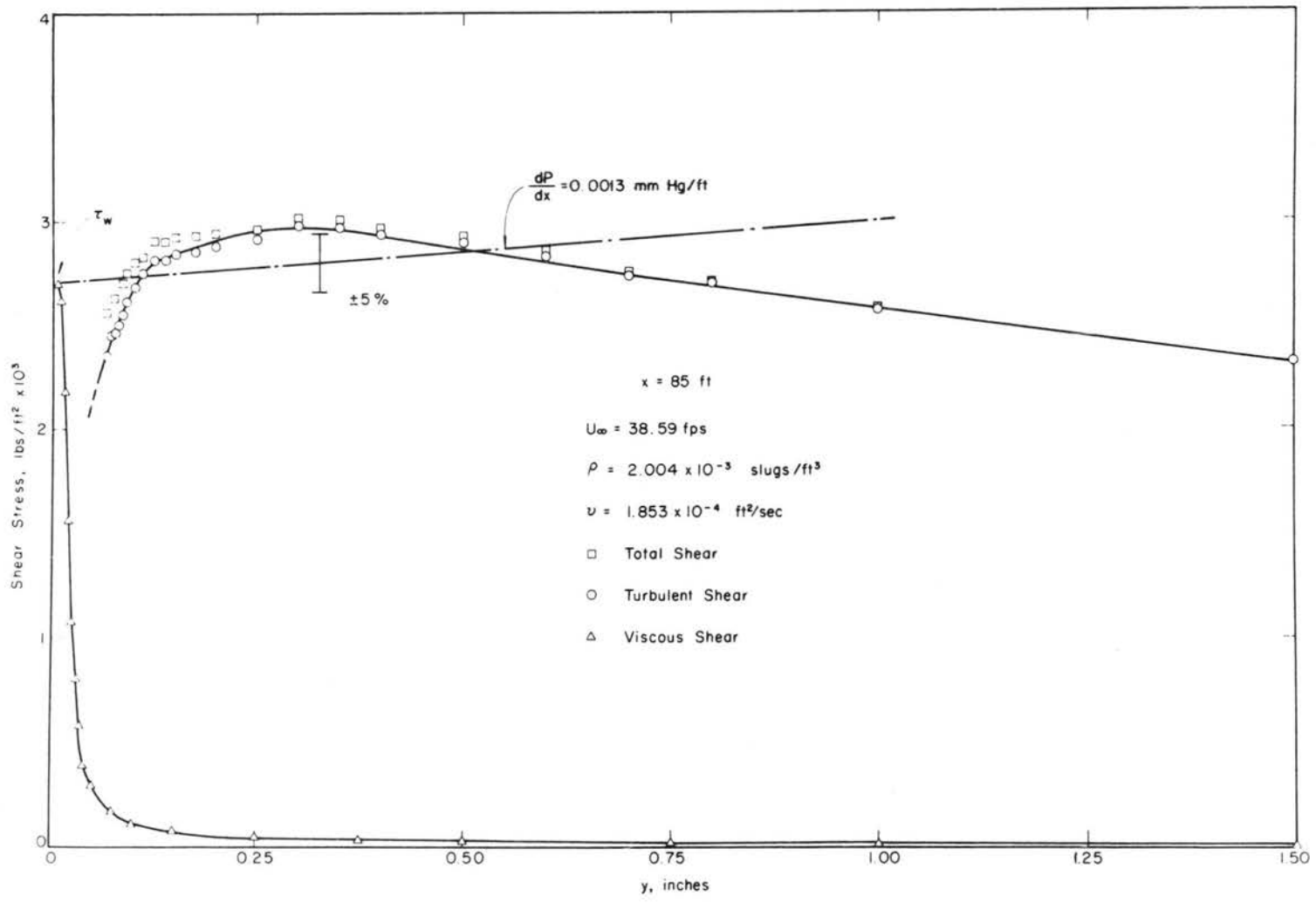

Figure 45. Shear-stress distribution, U_∞ = 38.59 fps.

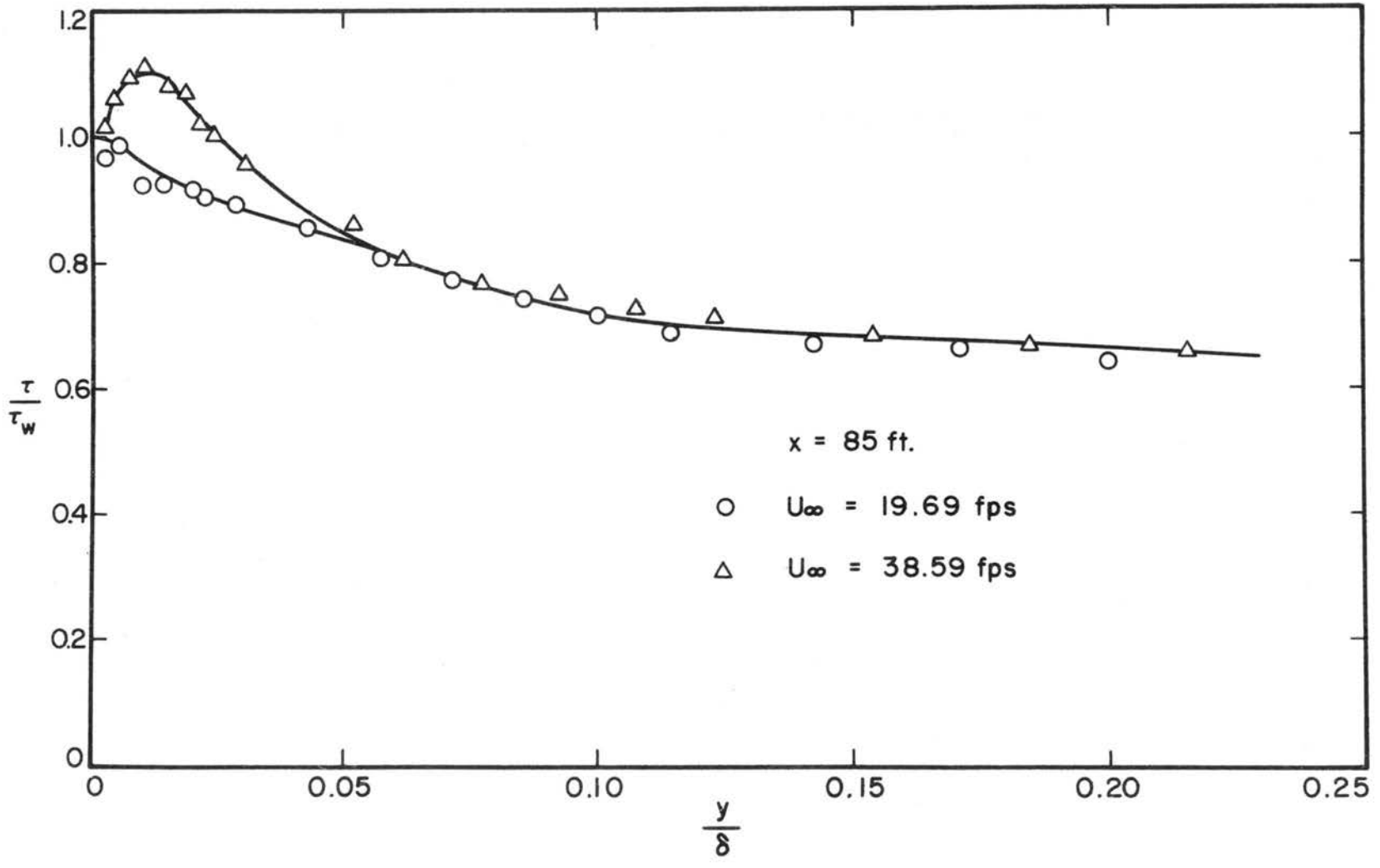

Figure 46. Variation of τ/τ_w with y/δ

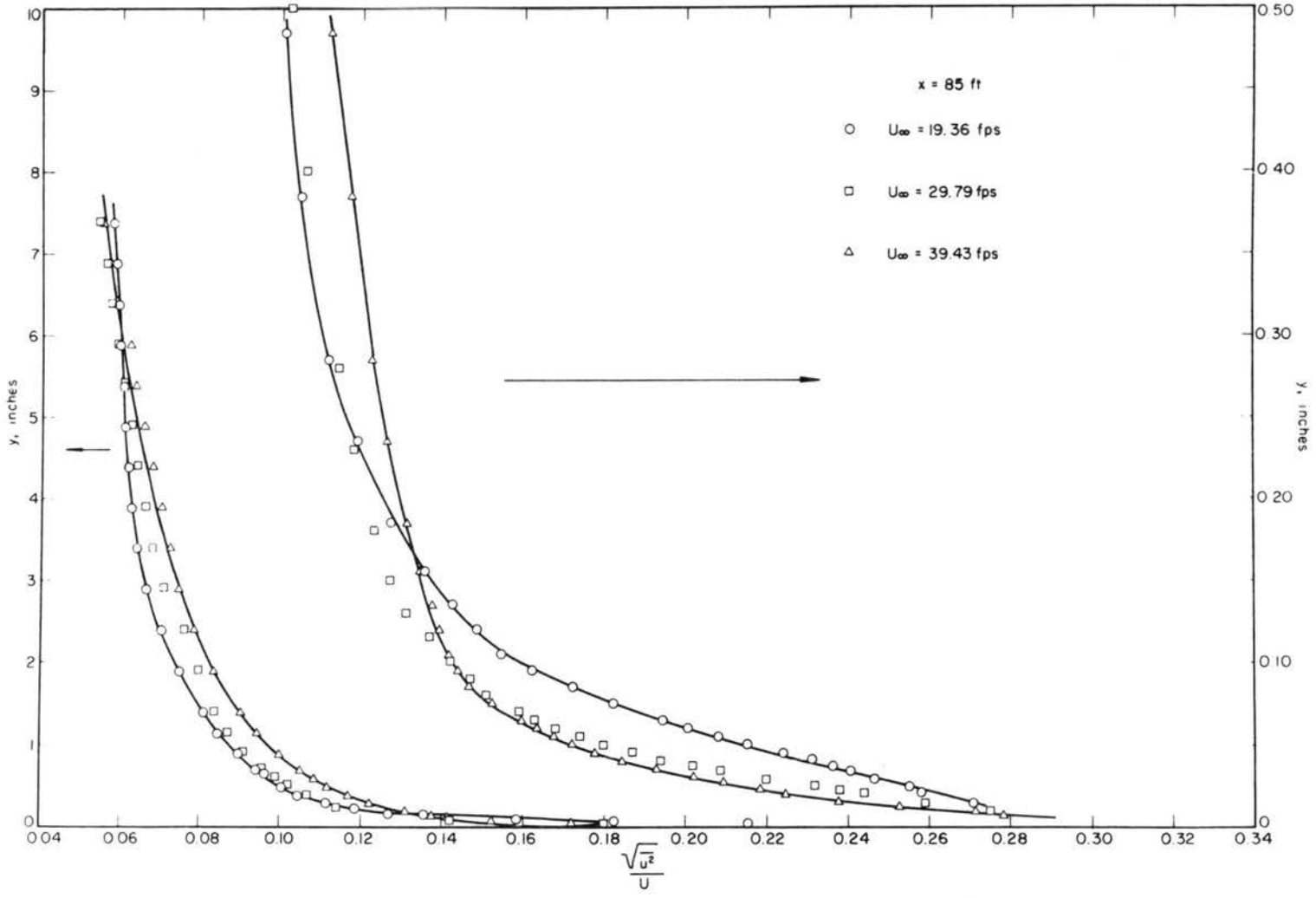

Figure 47. Distribution of turbulence intensity, $\frac{\sqrt{\overline{u^2}}}{U}$

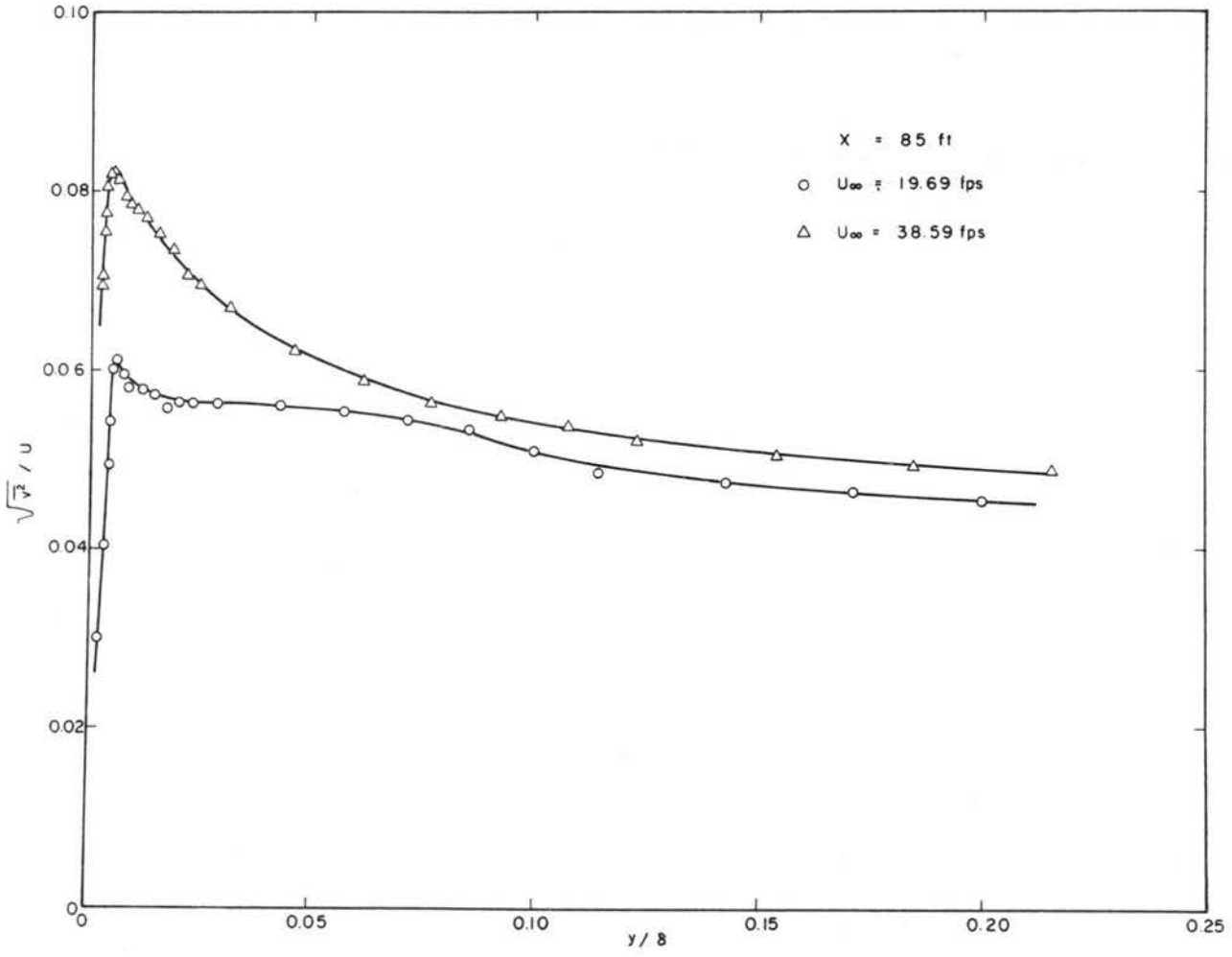

Figure 48. Distribution of turbulence intensity, $\frac{\sqrt{\overline{v^2}}}{U}$

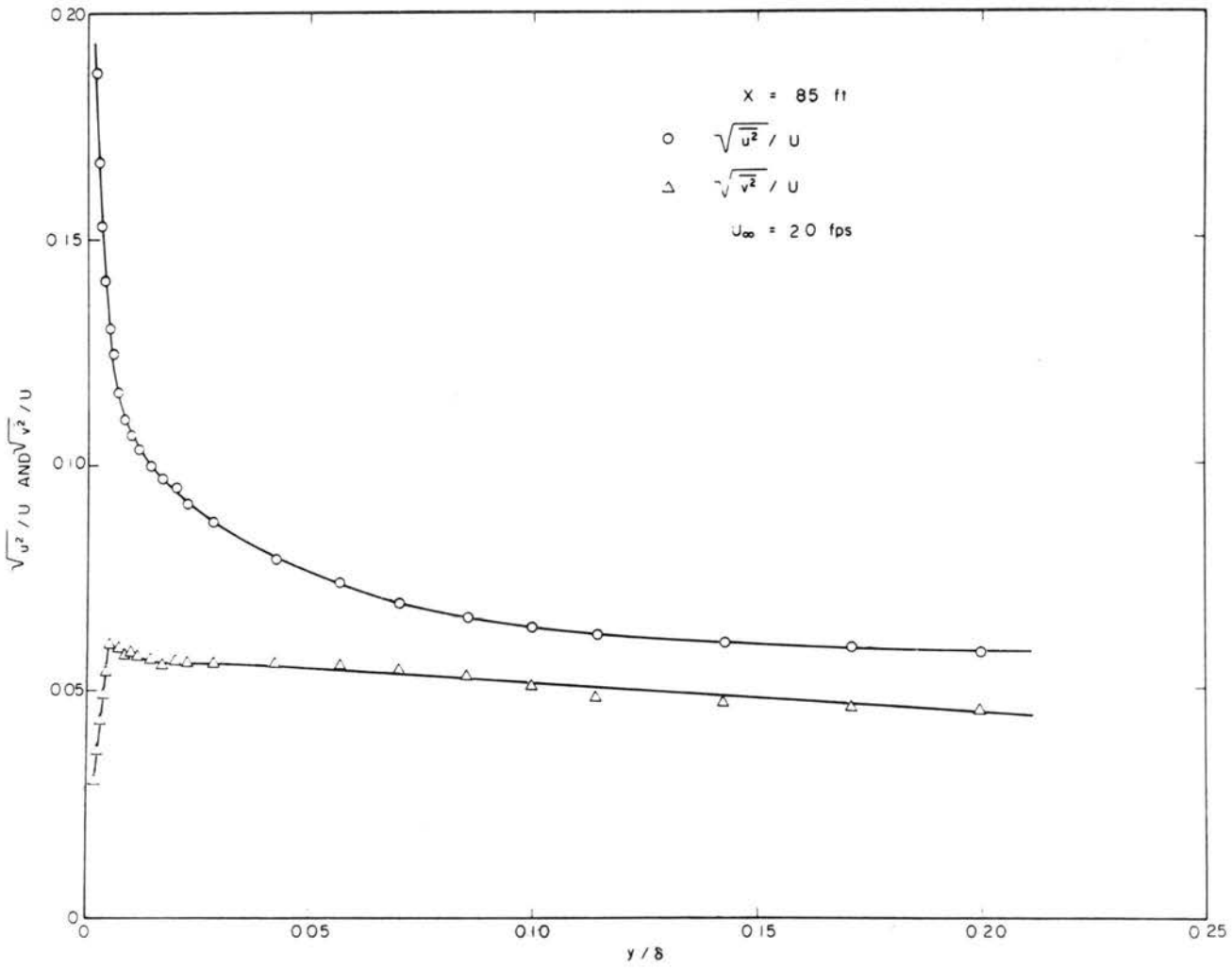

Figure 49. Comparison of turbulence intensities, $U_\infty \simeq 20$ fps.

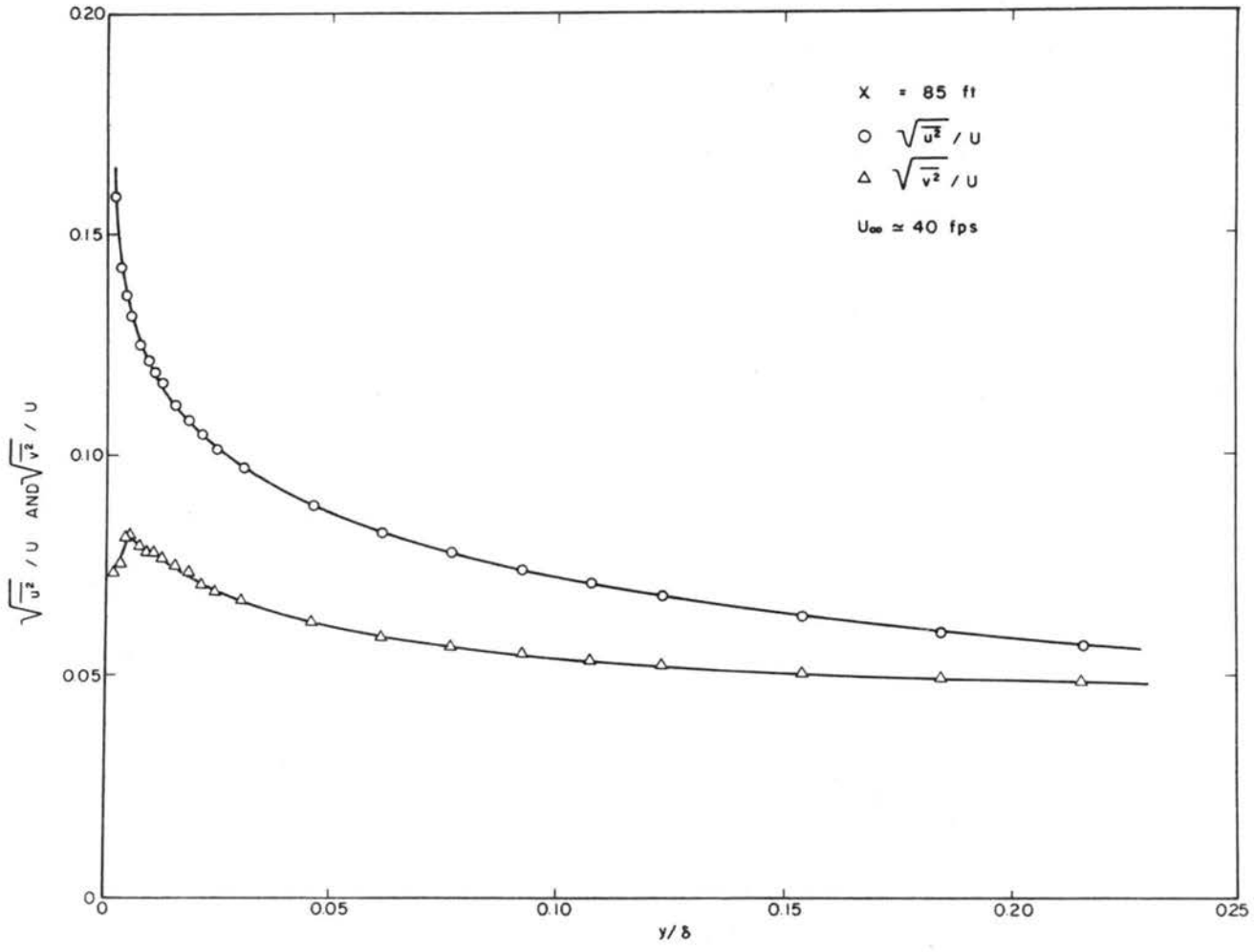

Figure 50. Comparison of turbulence intensities, $U_\infty \simeq 40$ fps.

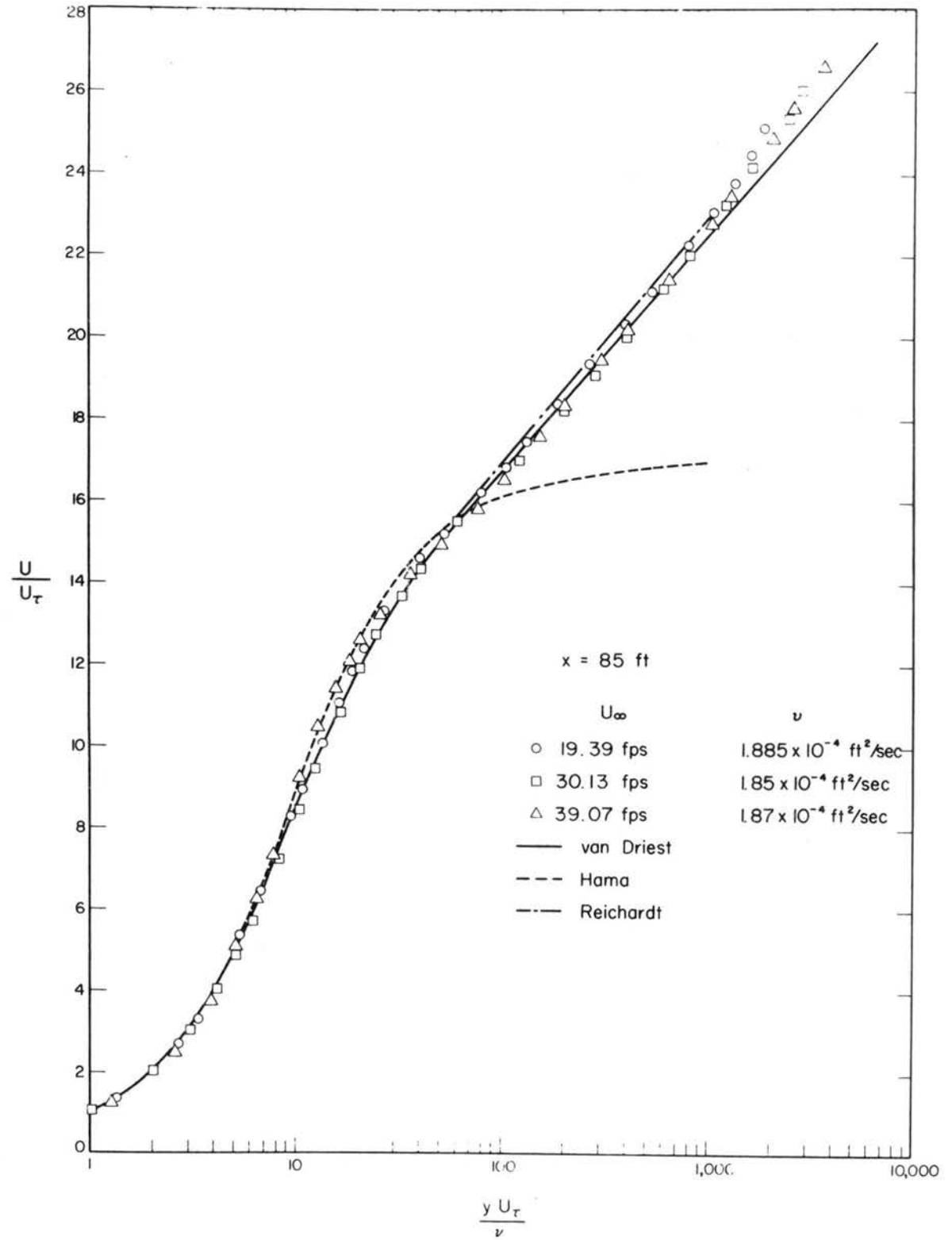

Figure 51. Semilogarithmic plot of mean velocity distribution

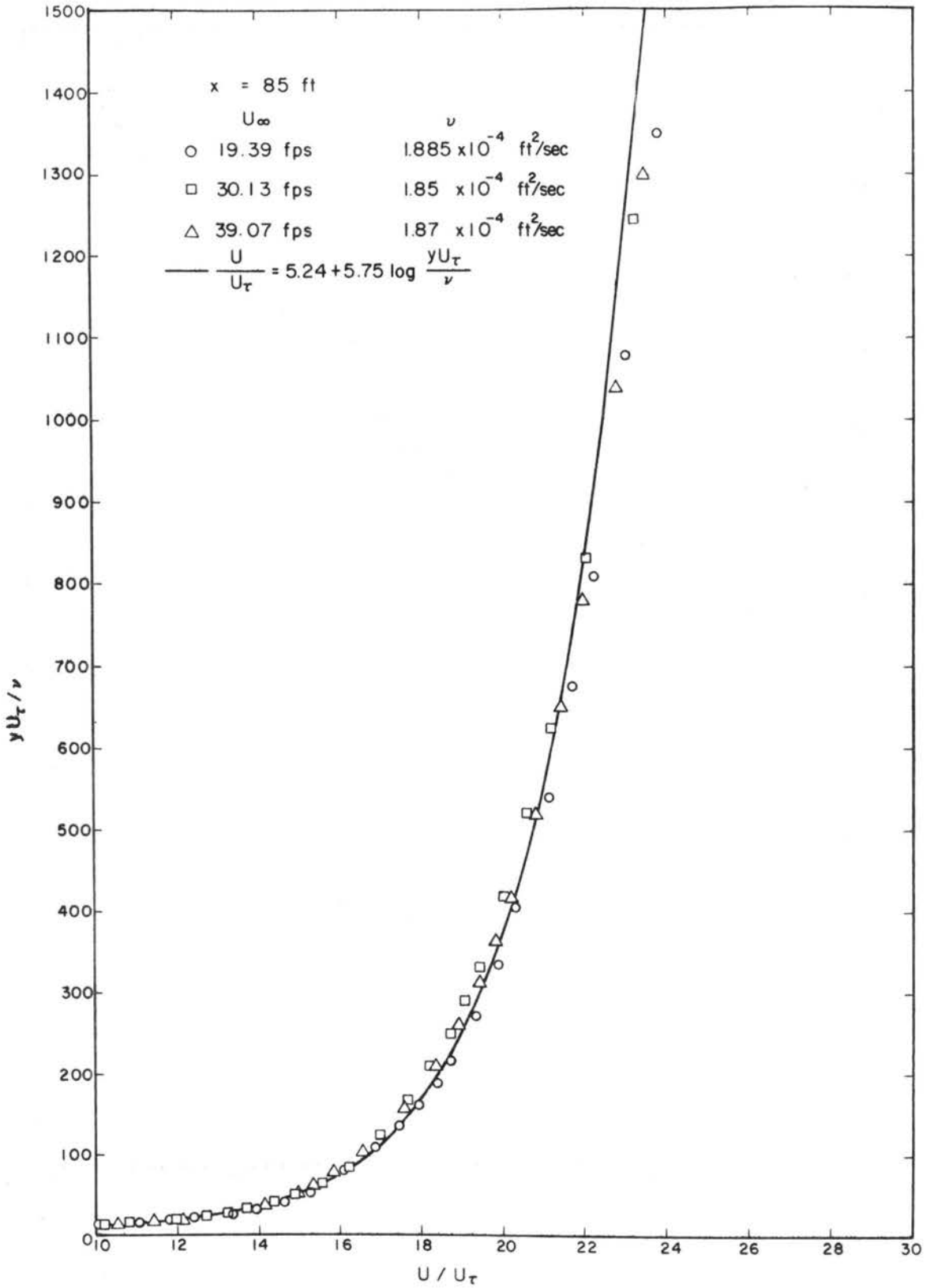

Figure 52. Dimensionless plot of mean velocity

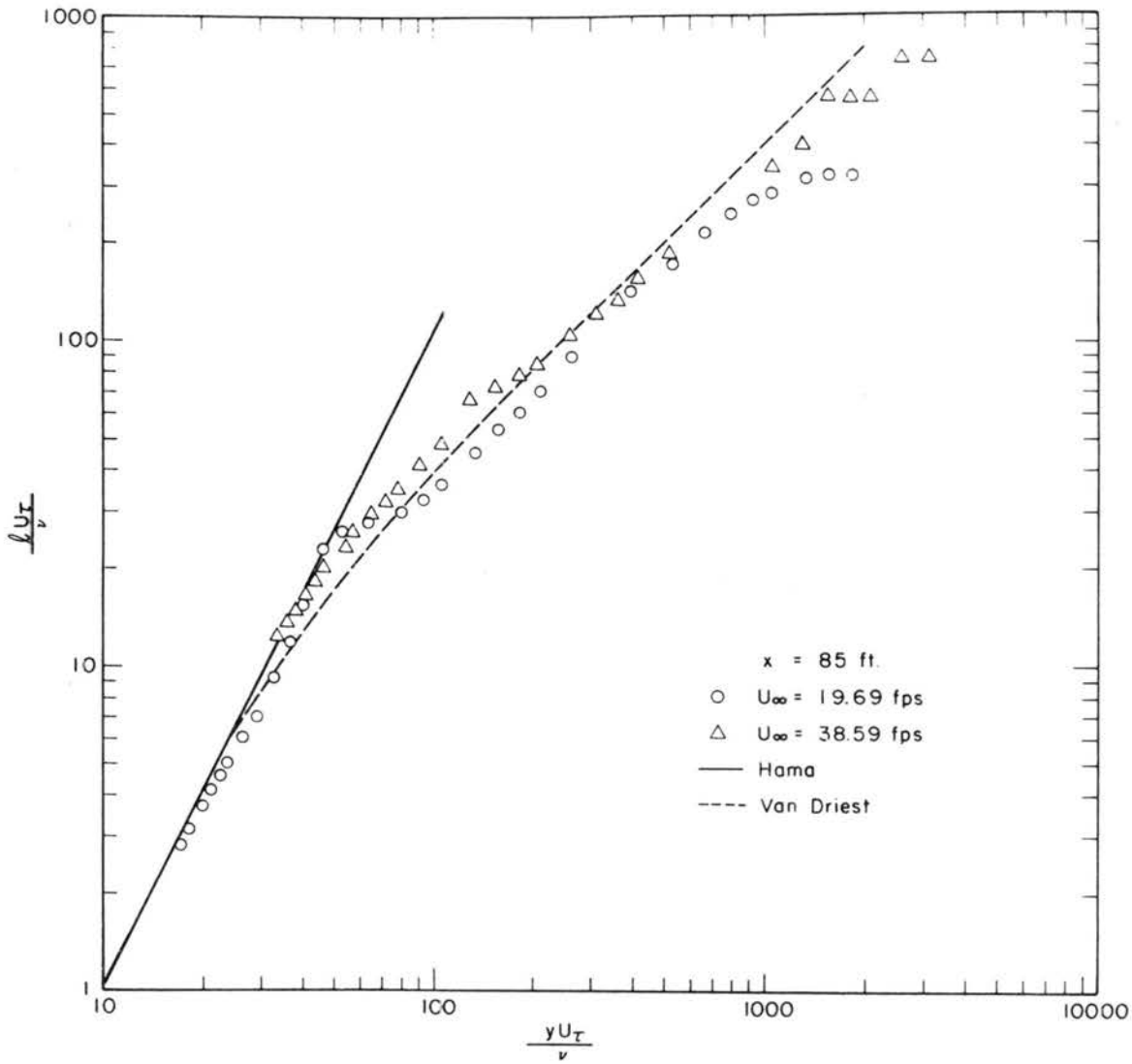

Figure 53. Dimensionless plot of mixing length

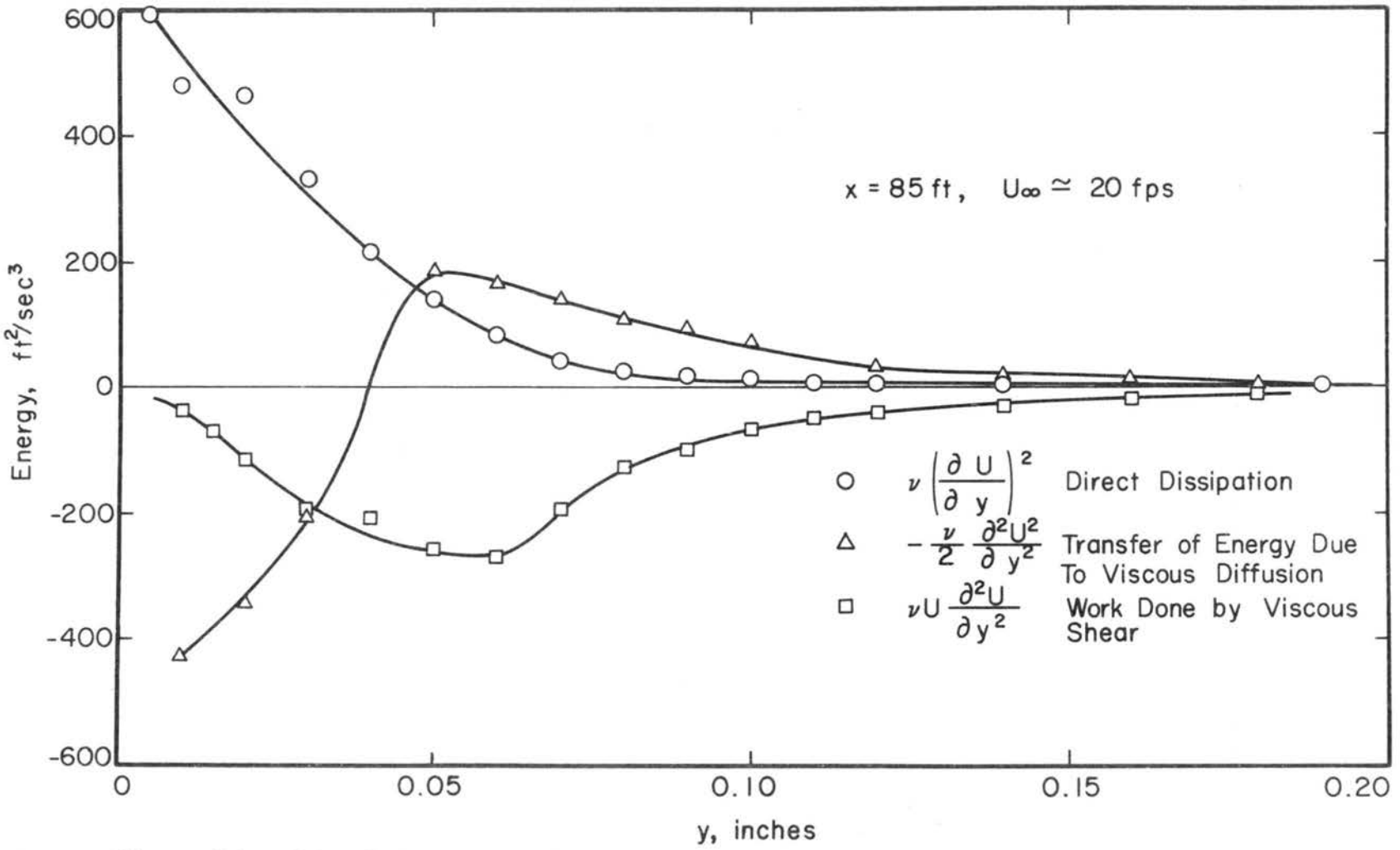

Figure 54. Distribution of the direct dissipation and the transfer of energy due to viscous diffusion in the viscous sublayer

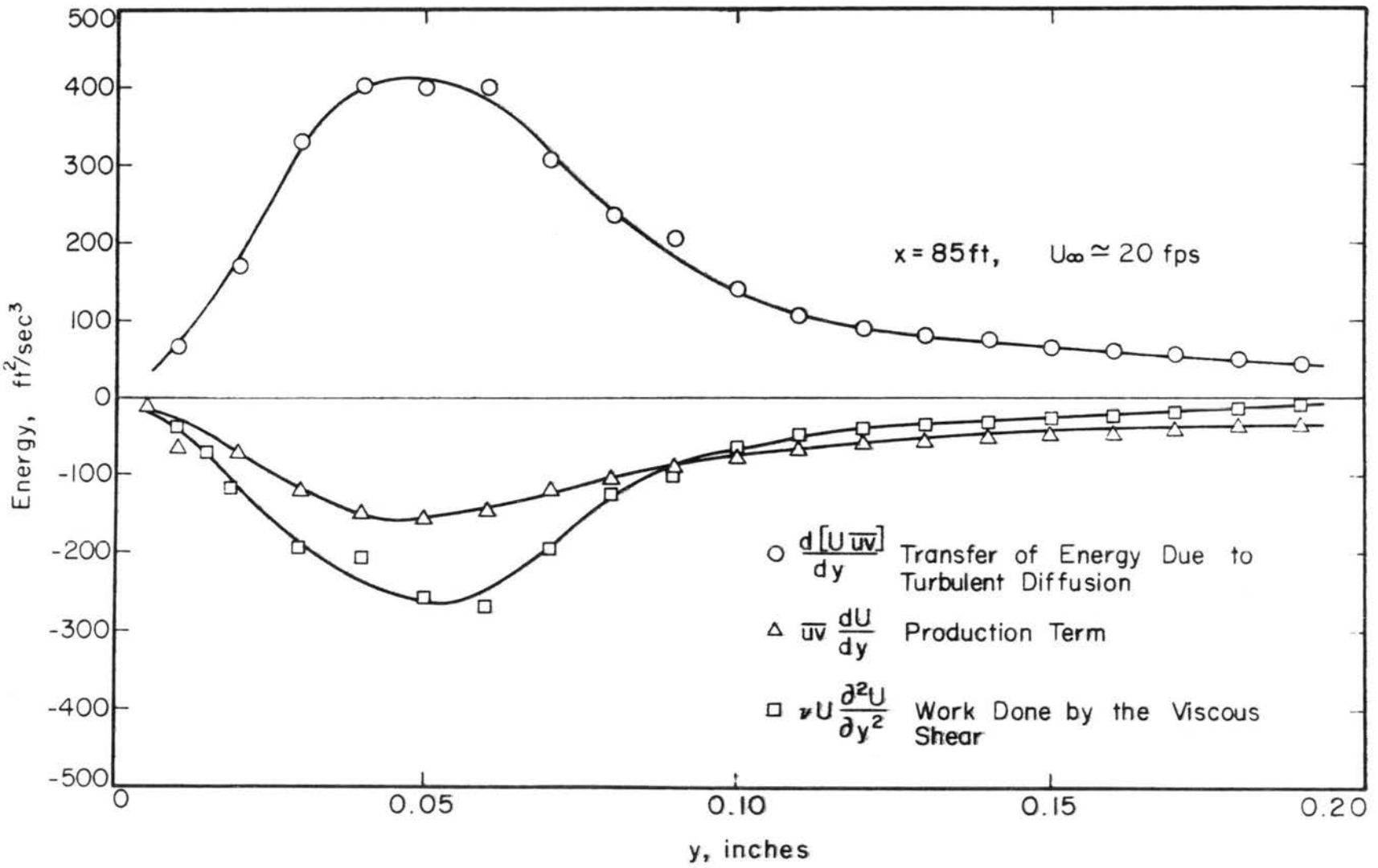

Figure 55. Distribution of the terms appearing in the mean energy equation (5-10) for the viscous sublayer

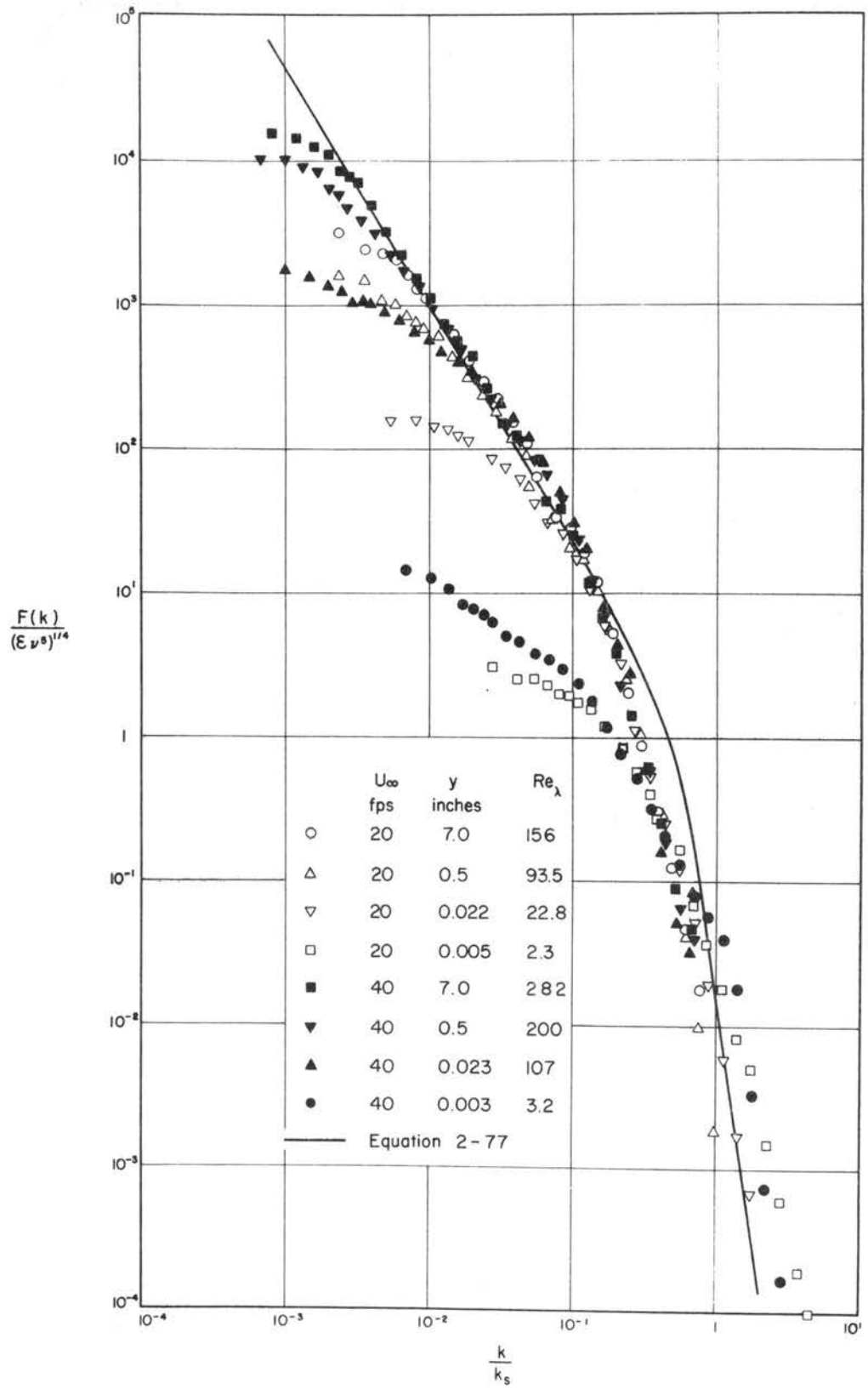

Figure 56. Comparison of energy spectra with Heisenberg's theoretical expression

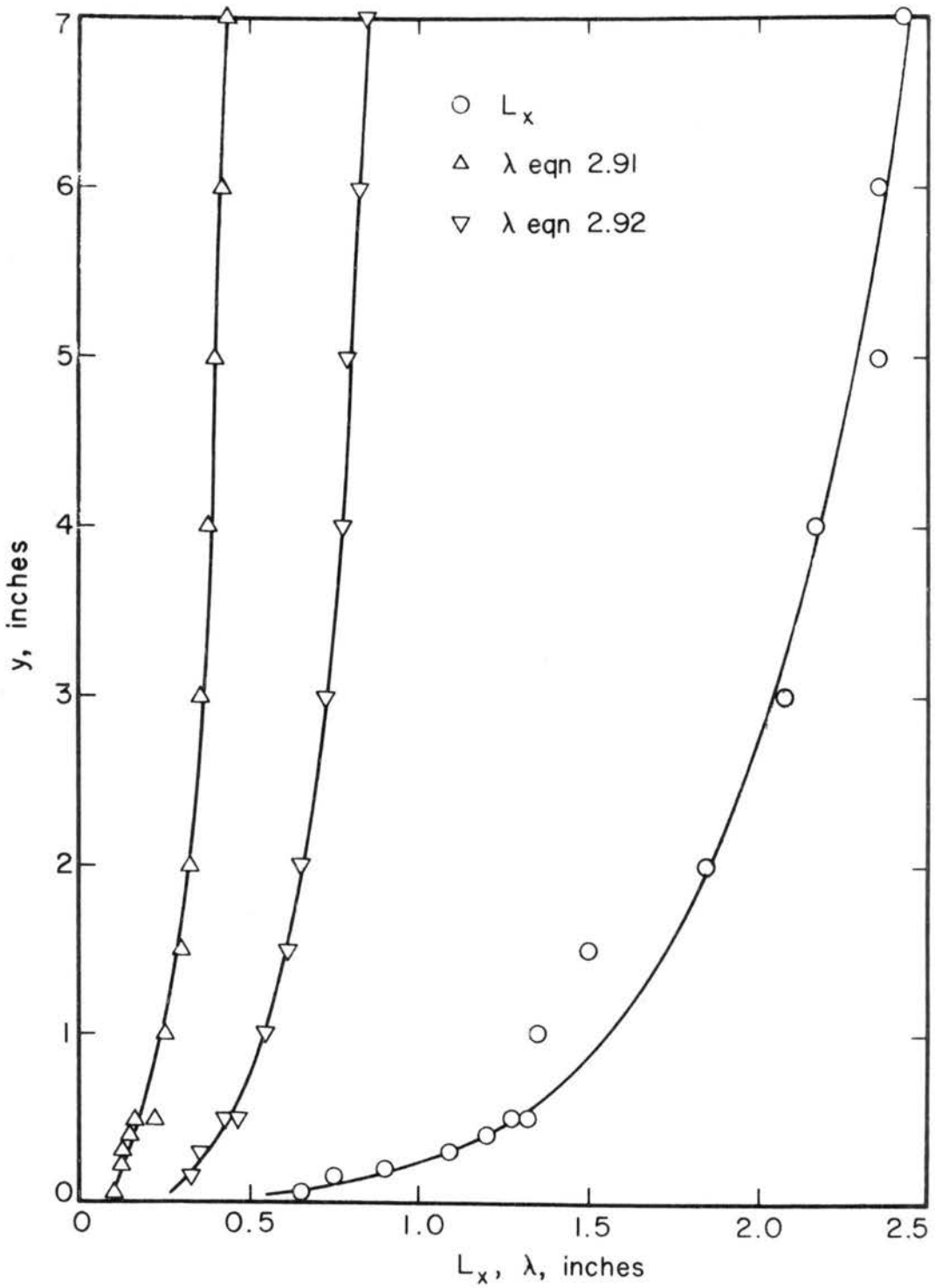

Figure 57. Variation of macro- and micro-scales with distance from wind tunnel floor. x = 85 ft. $U_\infty \simeq 20$ fps.

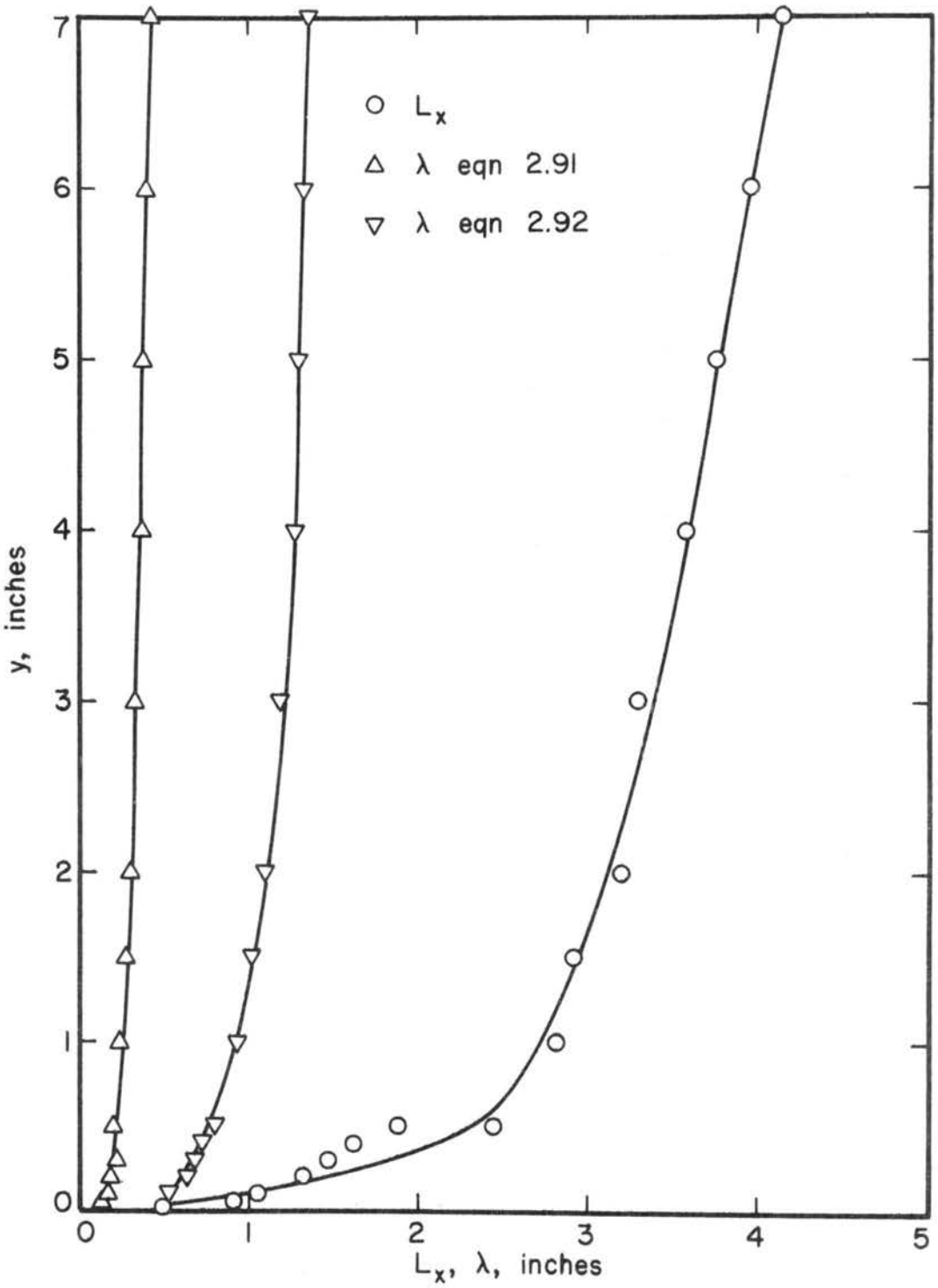

Figure 58. Variation of macro- and micro-scales with distance from wind tunnel floor. x = 85 ft. $U_\infty \simeq 40$ fps.

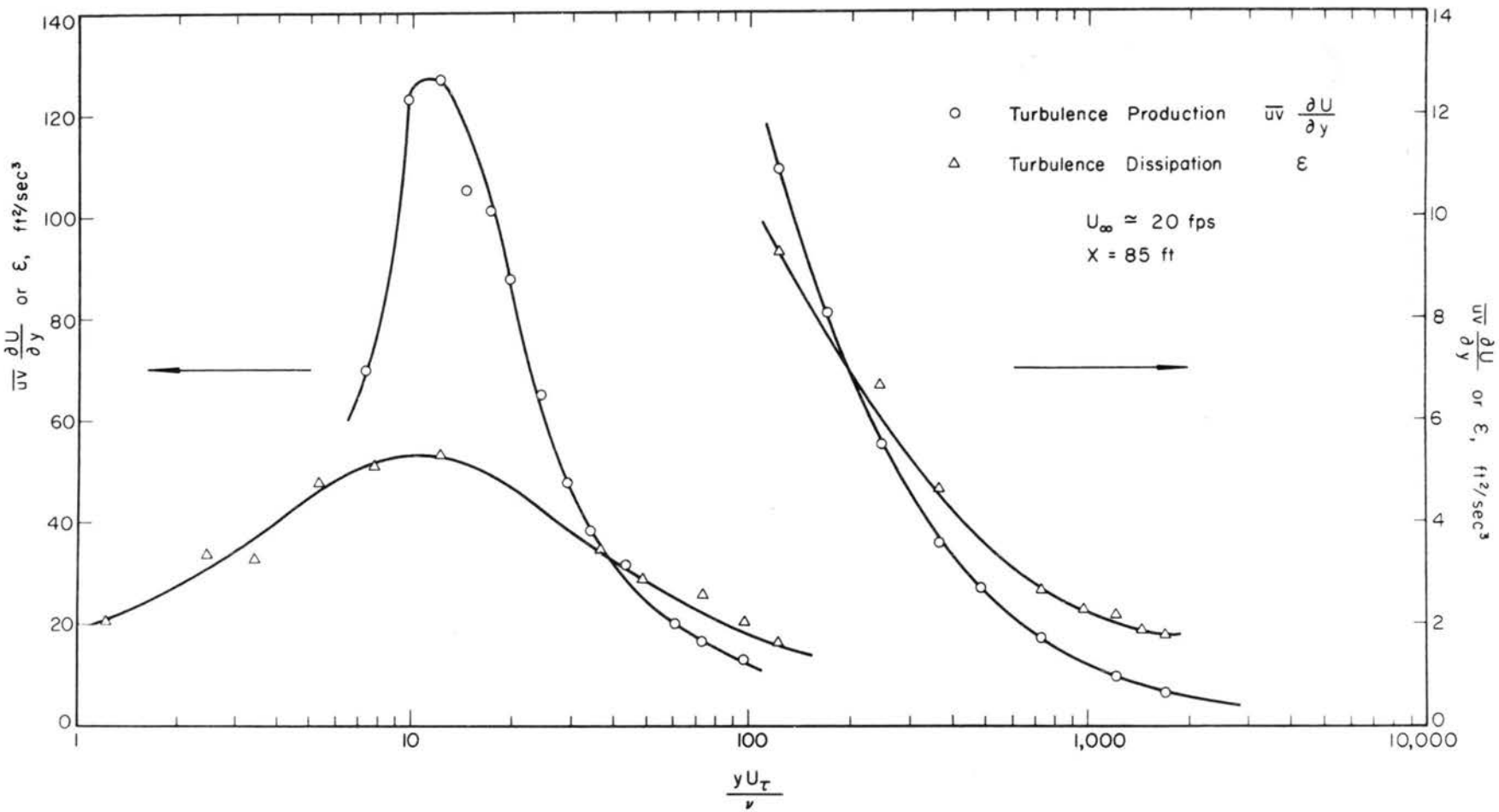

Figure 59. Distribution of production and dissipation of turbulent energy. x = 85 feet. $U_\infty \simeq 20$ fps.

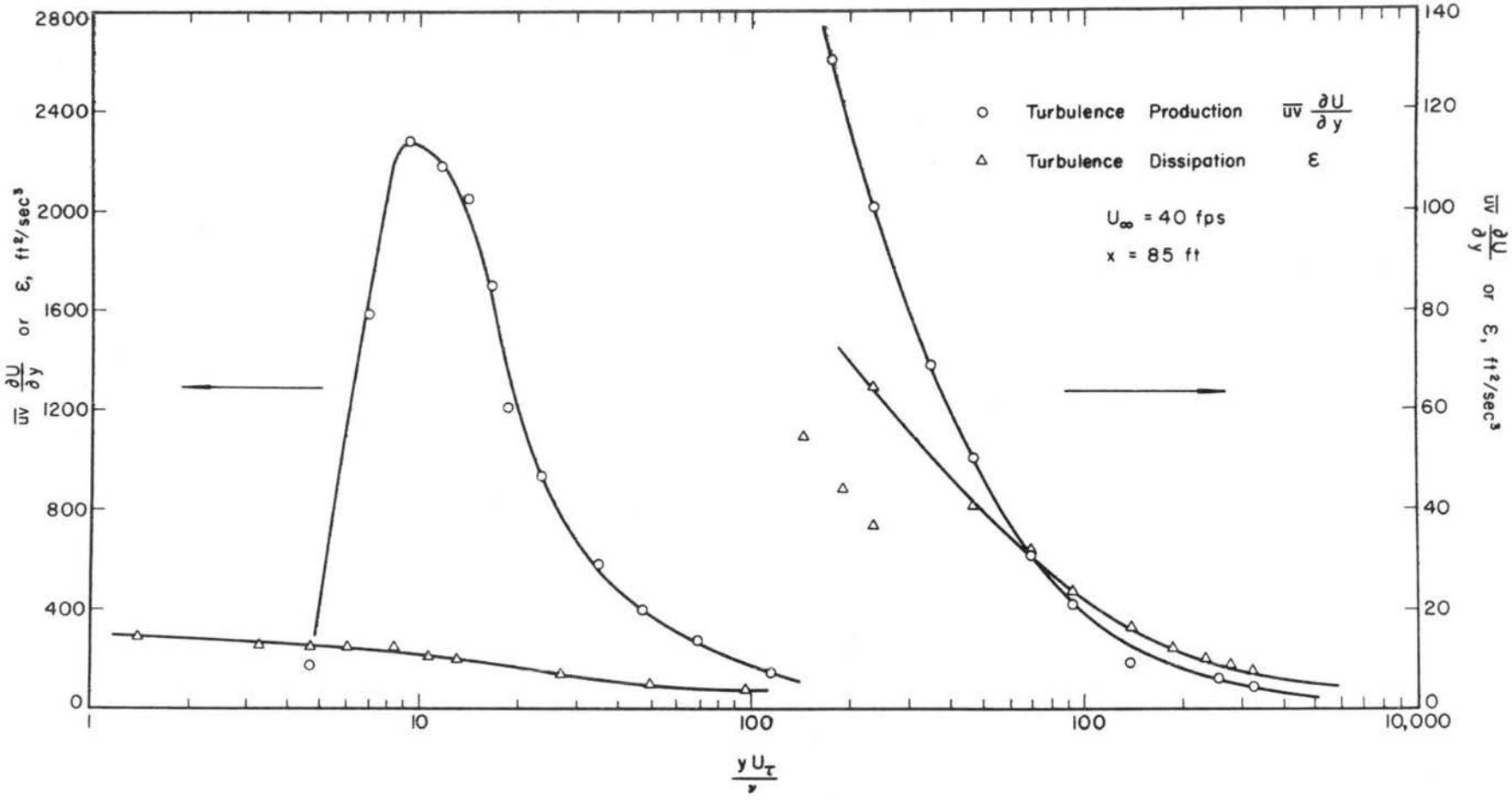

Figure 60. Distribution of production and dissipation of turbulent energy. x = 85 feet. $U_\infty \simeq 40$ fps.

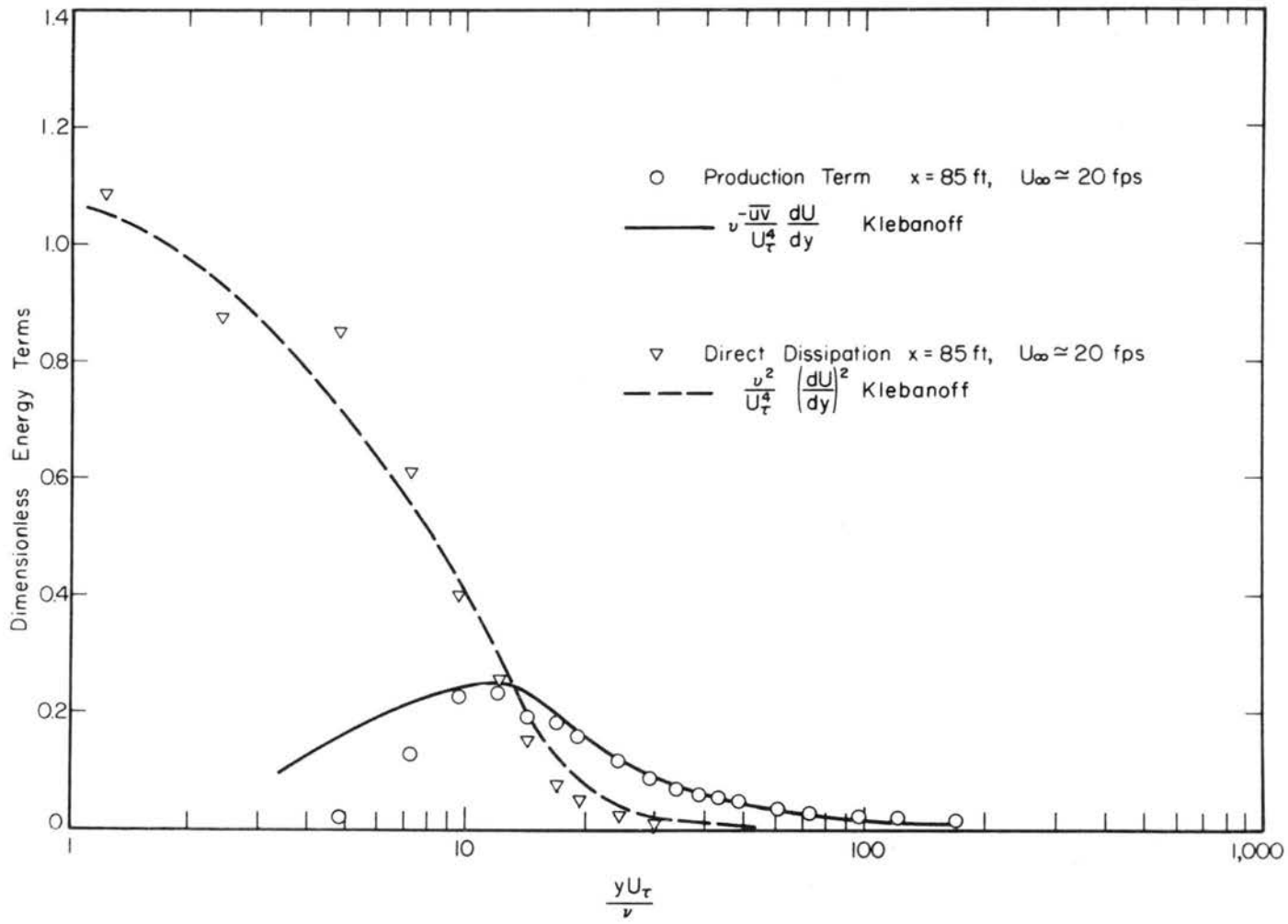

Figure 61. Distribution of production term and direct dissipation in dimensionless form, compared with Klebanoff's results

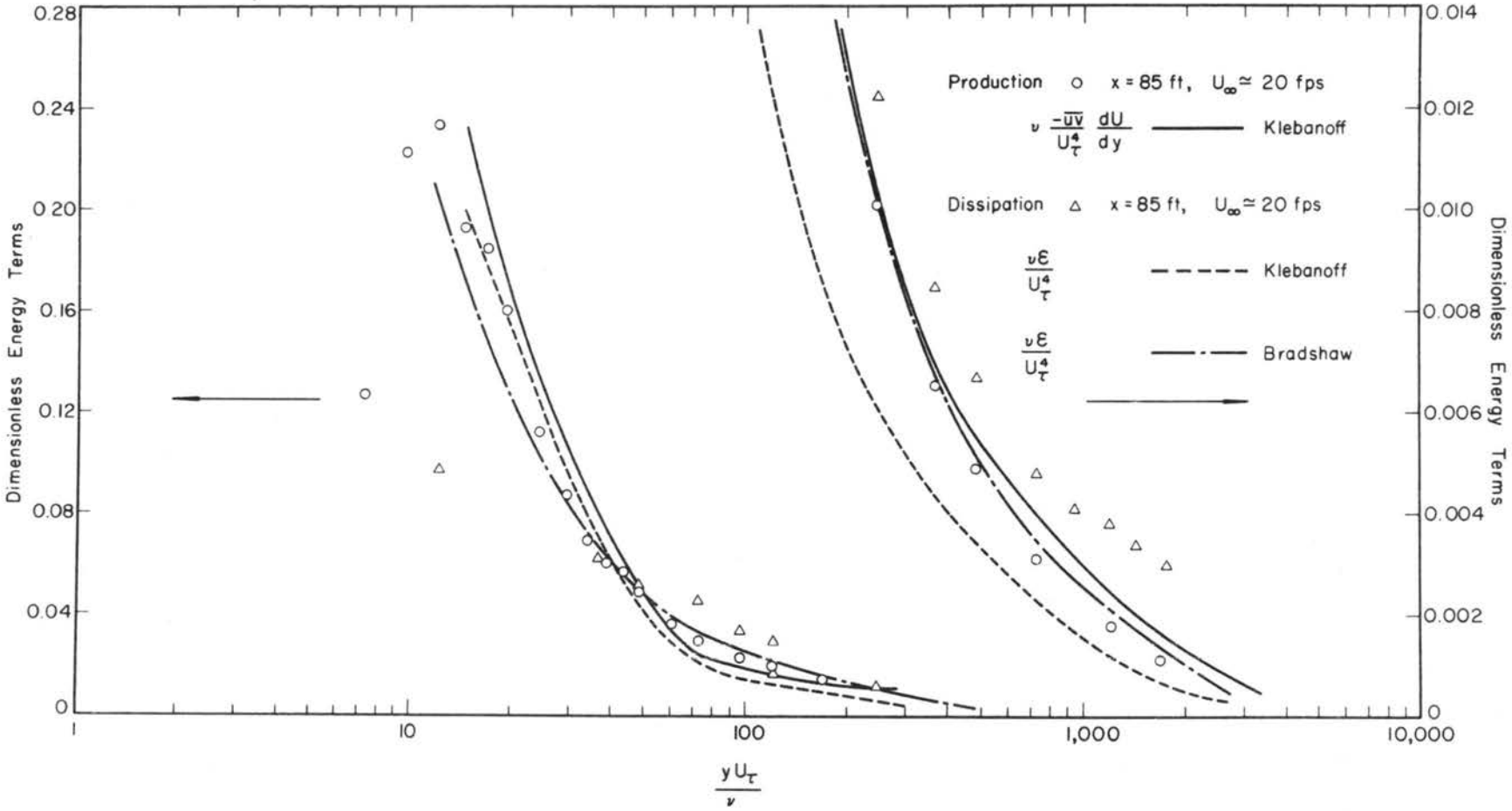

Figure 62. Comparison of production and dissipation of turbulent energy with Klebanoff's results

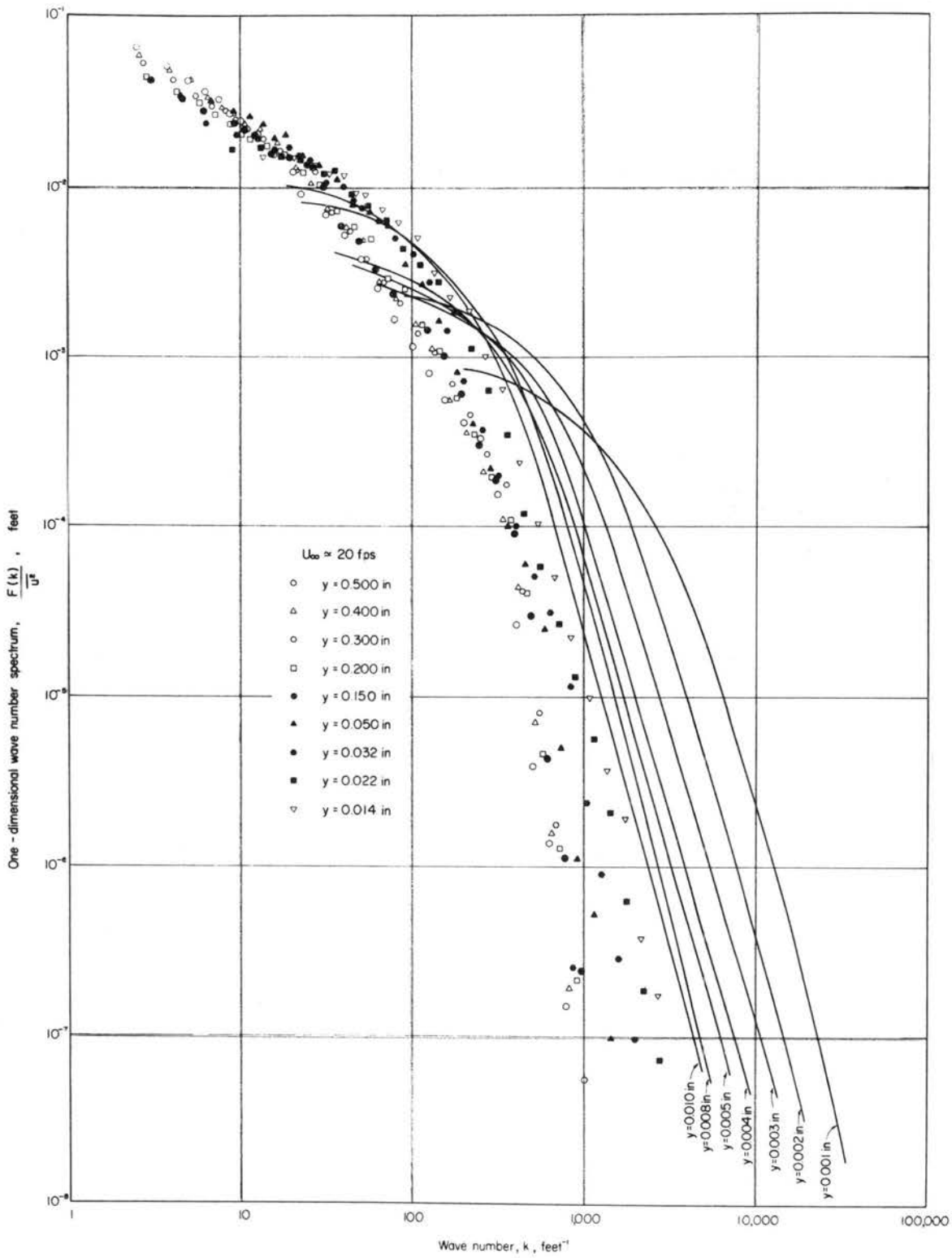

Figure 63. One-dimensional energy spectra measured in the Army wind tunnel at x = 85 feet. $U_\infty \simeq 20$ fps.

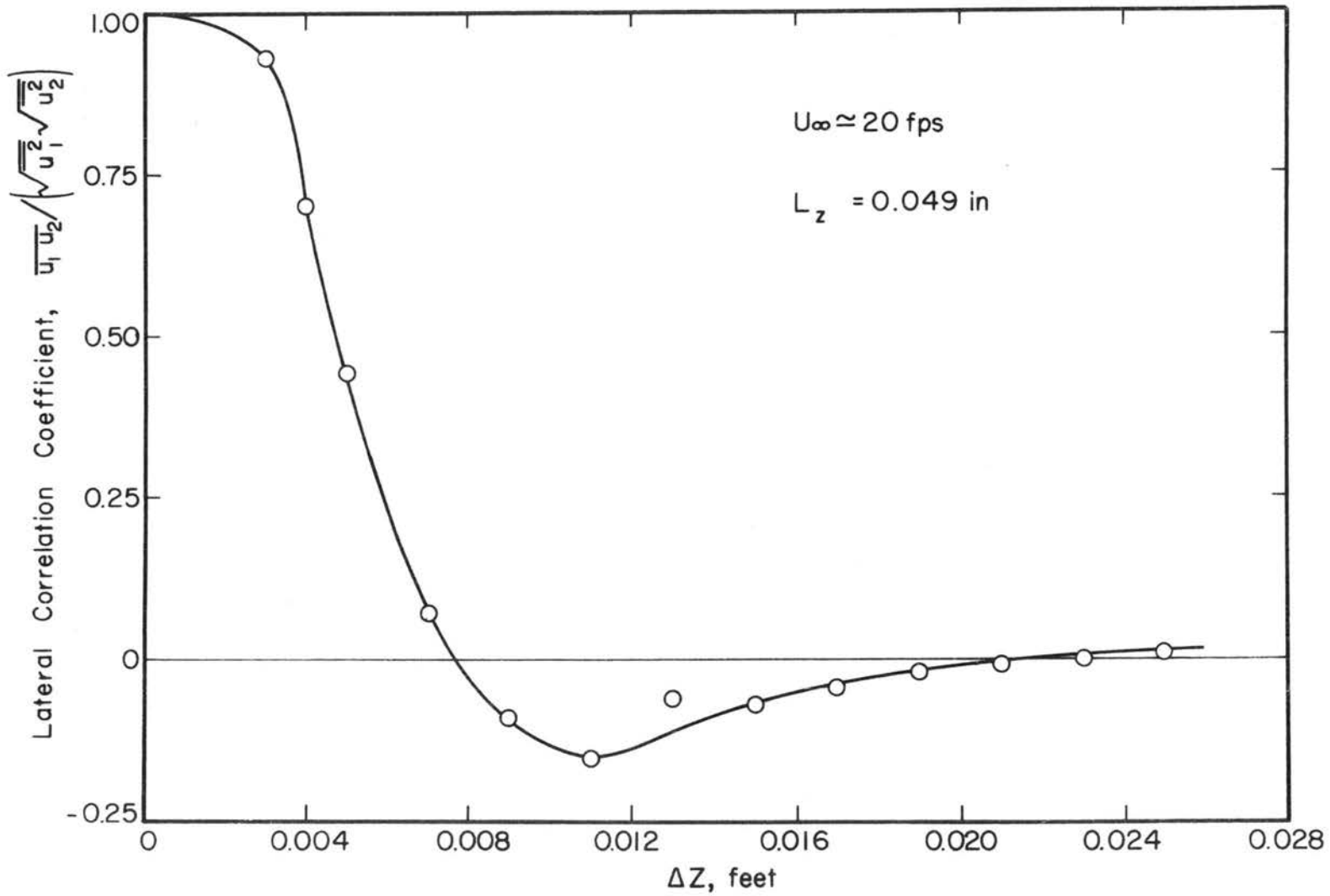

Figure 64. Distribution of the lateral correlation coefficient of the longitudinal velocity fluctuation near the wall. $U_\infty \simeq 20$ fps.

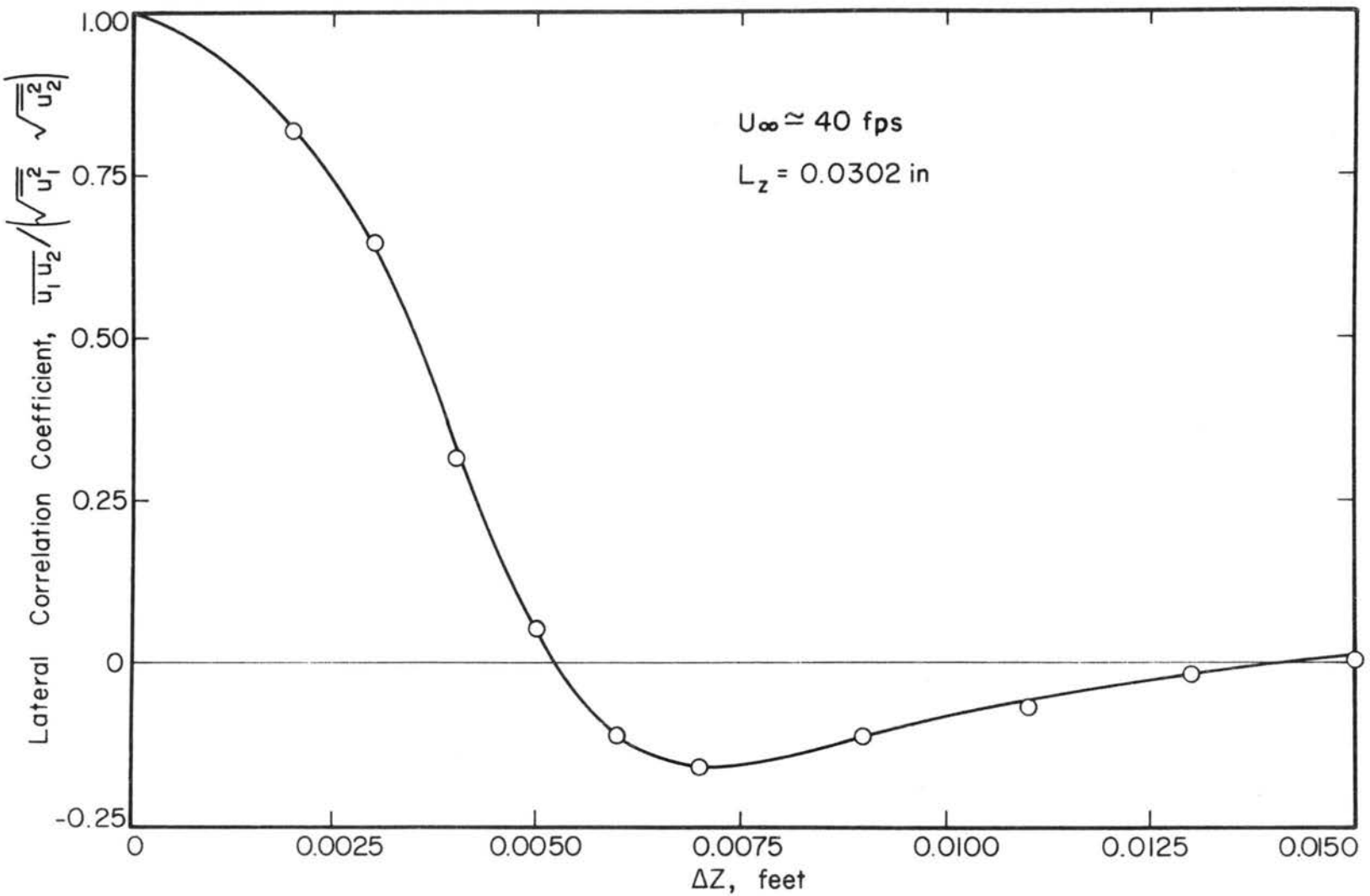

Figure 65. Distribution of the lateral correlation coefficient of the longitudinal velocity fluctuation near the wall. $U_\infty \simeq 40$ fps.

DOCUMENT CONTROL DATA - R&D

(Security classification of title, body of abstract and indexing annotation must be entered when the overall report is classified)

1. ORIGINATING ACTIVITY *(Corporate author)*

Fluid Mechanics Program, College of Engineering
Colorado State University, Fort Collins, Colorado

2a. REPORT SECURITY CLASSIFICATION

Unclassified

2b GROUP

3. REPORT TITLE

VISCOUS REGION OF TURBULENT BOUNDARY LAYER

4. DESCRIPTIVE NOTES *(Type of report and inclusive dates)*

Technical Report

5. AUTHOR(S) *(Last name, first name, initial)*

Tieleman, Henry W.

6. REPORT DATE	7a. TOTAL NO. OF PAGES	7b. NO. OF REFS
December 1967	197	43

8a. CONTRACT OR GRANT NO.	9a. ORIGINATOR'S REPORT NUMBER(S)
DA-AMC-28-043-65-G20	CER 67-68 HWT 21
b. PROJECT NO. 2246	
c.	9b. OTHER REPORT NO(S) *(Any other numbers that may be assigned this report)*
d.	

10. AVAILABILITY/LIMITATION NOTICES

Distribution of This Document is Unlimited

11. SUPPLEMENTARY NOTES	12. SPONSORING MILITARY ACTIVITY
	U.S. Army Materiel Command

13. ABSTRACT

The nature of mean and turbulent motion in the viscous sublayer of a thick boundary layer with zero pressure gradient has been investigated. Measurements have been made of the mean motion, two of the turbulent velocity components, the turbulent shear stress, and spectra of the longitudinal component of the velocity fluctuation. Traverses were made through approximately one-fifth of the boundary layer, which was approximately 32 inches thick. The boundary layer was developed along the floor of the wind tunnel test section for 85 feet.

The turbulent shear stresses and the turbulence intensities were evaluated from a single rotated wire. A detailed account is given of the theory concerning the yawed wire operation. Included are corrections for the results from normal and yawed hot wires when operated in large mean velocity gradients and/or turbulence intensity gradients.

By assuming local similarity, the semilogarithmic velocity distribution can be derived. However, when local similarity is assumed, it is required that $\partial U_\tau / \partial x = 0$ or that $\partial \tau / \partial y = 0$ in the region where the law of the wall is valid. The measurements confirm the existence of a constant shear-stress region near the wall. However, the results show that the constant shear layer does not exist as far out as where semilogarithmic velocity distribution is valid. Cross-checks were made between mean flow measurements, turbulence measurements (Cont'd

DD FORM 1 JAN 64 1473

14. KEY WORDS	LINK A		LINK B		LINK C	
	ROLE	WT	ROLE	WT	ROLE	WT
Turbulent boundary layer Viscous sublayer Turbulent shear stress Viscous shear stress Local similarity Energy density spectra Turbulent energy dissipation						

INSTRUCTIONS

1. ORIGINATING ACTIVITY: Enter the name and address of the contractor, subcontractor, grantee, Department of Defense activity or other organization *(corporate author)* issuing the report.

2a. REPORT SECURITY CLASSIFICATION: Enter the overall security classification of the report. Indicate whether "Restricted Data" is included. Marking is to be in accordance with appropriate security regulations.

2b. GROUP: Automatic downgrading is specified in DoD Directive 5200.10 and Armed Forces Industrial Manual. Enter the group number. Also, when applicable, show that optional markings have been used for Group 3 and Group 4 as authorized.

3. REPORT TITLE: Enter the complete report title in all capital letters. Titles in all cases should be unclassified. If a meaningful title cannot be selected without classification, show title classification in all capitals in parenthesis immediately following the title.

4. DESCRIPTIVE NOTES: If appropriate, enter the type of report, e.g., interim, progress, summary, annual, or final. Give the inclusive dates when a specific reporting period is covered.

5. AUTHOR(S): Enter the name(s) of author(s) as shown on or in the report. Enter last name, first name, middle initial. If military, show rank and branch of service. The name of the principal author is an absolute minimum requirement.

6. REPORT DATE: Enter the date of the report as day, month, year; or month, year. If more than one date appears on the report, use date of publication.

7a. TOTAL NUMBER OF PAGES: The total page count should follow normal pagination procedures, i.e., enter the number of pages containing information.

7b. NUMBER OF REFERENCES: Enter the total number of references cited in the report.

8a. CONTRACT OR GRANT NUMBER: If appropriate, enter the applicable number of the contract or grant under which the report was written.

8b, 8c, & 8d. PROJECT NUMBER: Enter the appropriate military department identification, such as project number, subproject number, system numbers, task number, etc.

9a. ORIGINATOR'S REPORT NUMBER(S): Enter the official report number by which the document will be identified and controlled by the originating activity. This number must be unique to this report.

9b. OTHER REPORT NUMBER(S): If the report has been assigned any other report numbers *(either by the originator or by the sponsor)*, also enter this number(s).

10. AVAILABILITY/LIMITATION NOTICES: Enter any limitations on further dissemination of the report, other than those imposed by security classification, using standard statements such as:

(1) "Qualified requesters may obtain copies of this report from DDC."

(2) "Foreign announcement and dissemination of this report by DDC is not authorized."

(3) "U. S. Government agencies may obtain copies of this report directly from DDC. Other qualified DDC users shall request through _____."

(4) "U. S. military agencies may obtain copies of this report directly from DDC. Other qualified users shall request through _____."

(5) "All distribution of this report is controlled. Qualified DDC users shall request through _____."

If the report has been furnished to the Office of Technical Services, Department of Commerce, for sale to the public, indicate this fact and enter the price, if known.

11. SUPPLEMENTARY NOTES: Use for additional explanatory notes.

12. SPONSORING MILITARY ACTIVITY: Enter the name of the departmental project office or laboratory sponsoring *(paying for)* the research and development. Include address.

13. ABSTRACT: Enter an abstract giving a brief and factual summary of the document indicative of the report, even though it may also appear elsewhere in the body of the technical report. If additional space is required, a continuation sheet shall be attached.

It is highly desirable that the abstract of classified reports be unclassified. Each paragraph of the abstract shall end with an indication of the military security classification of the information in the paragraph, represented as *(TS)*, *(S)*, *(C)*, or *(U)*.

There is no limitation on the length of the abstract. However, the suggested length is from 150 to 225 words.

14. KEY WORDS: Key words are technically meaningful terms or short phrases that characterize a report and may be used as index entries for cataloging the report. Key words must be selected so that no security classification is required. Identifiers, such as equipment model designation, trade name, military project code name, geographic location, may be used as key words but will be followed by an indication of technical context. The assignment of links, rules, and weights is optional.

DOCUMENT CONTROL DATA - R&D

(Security classification of title, body of abstract and indexing annotation must be entered when the overall report is classified)

1. ORIGINATING ACTIVITY *(Corporate author)*	2a. REPORT SECURITY CLASSIFICATION
	2b GROUP
3. REPORT TITLE	
4. DESCRIPTIVE NOTES *(Type of report and inclusive dates)*	
5. AUTHOR*(S)* *(Last name, first name, initial)*	

6. REPORT DATE	7a. TOTAL NO. OF PAGES	7b. NO. OF REFS
8a. CONTRACT OR GRANT NO.	9a. ORIGINATOR'S REPORT NUMBER*(S)*	
b. PROJECT NO.		
c.	9b. OTHER REPORT NO*(S)* *(Any other numbers that may be assigned this report)*	
d.		
10. AVAILABILITY/LIMITATION NOTICES		
11. SUPPLEMENTARY NOTES	12. SPONSORING MILITARY ACTIVITY	

13. ABSTRACT - Cont'd.

and wall shear-stress measurements. The results were compared with existing theories for boundary layer flow near the wall.

Energy spectra of the streamwise turbulence component indicate that the theory of local isotropy can be applied to turbulent shear flows. This is especially true when the boundary layer is allowed to develop for a relatively long time. Measurements indicate that $\sqrt{\overline{v^2}}$ is much closer to $\sqrt{\overline{u^2}}$ in magnitude as compared to the results from small scale boundary layers. This study was made in connection with a program which intends to give criteria for the modeling of atmospheric boundary layers in the wind tunnel.

DD FORM 1 JAN 64 1473

MINIMUM BASIC DISTRIBUTION LIST FOR USAMC SCIENTIFIC AND TECHNICAL REPORTS IN METEOROLOGY AND ATMOSPHERIC SCIENCES

Commanding General (1)
U. S. Army Materiel Command
Attn: AMCRD-RV-A
Washington, D. C. 20315

Commanding General (1)
U. S. Army Electronics Command
Attn: AMSEL-EW
Fort Monmouth, New Jersey 07703

Commanding General (1)
U. S. Army Test and Evaluation Command
Attn: NBC Directorate
Aberdeen Proving Ground, Maryland 21005

Commanding Officer (1)
U. S. Army Ballistics Research Laboratories
Attn: AMXBR-IA
Aberdeen Proving Ground, Maryland 21005

Chief, Atmospheric Physics Division (2)
Atmospheric Sciences Laboratory
U. S. Army Electronics Command
Fort Monmouth, New Jersey 07703

U. S. Army Munitions Command (1)
Attn: Irving Solomon
Operations Research Group
Edgewood Arsenal, Maryland 21010

Commanding Officer (1)
U. S. Army Dugway Proving Ground
Attn: Meteorology Division
Dugway, Utah 84022

Commanding Officer (1)
U. S. Army CDC, CBR Agency
Attn: Mr. N. W. Bush
Fort McClellan, Alabama 36205

Commanding General (1)
U. S. Army Test and Evaluation Command
Attn: AMSTE-EL
Aberdeen Proving Ground, Maryland 21005

Commandant (1)
U. S. Army Signal School
Attn: Meteorological Department
Fort Monmouth, New Jersey 07703

Assistant Chief of Staff for Force Development (1)
CBR Nuclear Operations Directorate
Department of the Army
Washington, D. C. 20310

Director (1)
Atmospheric Sciences Programs
National Sciences Foundation
Washington, D. C. 20550

Assistant Secretary of Defense (1)
Research and Engineering
Attn: Technical Library
Washington, D. C. 20301

R. A. Taft Sanitary Engineering Center (1)
Public Health Service
4676 Columbia Parkway
Cincinnati, Ohio

Dr. Hans A. Panofsky (1)
Department of Meteorology
The Pennsylvania State University
University Park, Pennsylvania

Commanding General (1)
U. S. Continental Army Command
Attn: Reconnaissance Branch ODCS for Intelligence
Fort Monroe, Virginia 23351

Commander (1)
Air Force Cambridge Research Laboratories
Attn: CRZW
1065 Main Street
Waltham, Massachusetts

President (1)
U. S. Army Artillery Board
Fort Sill, Oklahoma 73504

National Center for Atmospheric Research (1)
Attn: Library
Boulder, Colorado

Dr. J. E. Cermak, Head (15)
Fluid Mechanics Program
Colorado State University
Fort Collins, Colorado 80521

Author (1)

Chief of Research and Development (1)
Department of the Army
Attn: CRD/M
Washington, D. C. 20310

Commanding General (1)
U. S. Army Missile Command
Attn: AMSMI-RRA
Redstone Arsenal, Alabama 35809

Commanding General (1)
U. S. Army Natick Laboratories
Attn: Earth Sciences Division
Natick, Massachusetts 01762

Director, U. S. Army Engineer (1)
Waterways Experiment Station
Attn: WES-FV
Vicksburg, Mississippi 39181

Chief, Atmospheric Sciences Research Division (5)
Atmospheric Sciences Laboratory
U. S. Army Electronics Command
Fort Huachuca, Arizona 85613

Commanding Officer (1)
U. S. Army Frankford Arsenal
Attn: SMUFA-1140
Philadelphia, Pennsylvania 19137

Commandant (1)
U. S. Army Artillery and Missile School
Attn: Target Acquisition Department
Fort Sill, Oklahoma 73504

Commanding General (1)
U. S. Army Electronics Proving Ground
Attn: Field Test Department
Fort Huachuca, Arizona 85613

Commanding General (1)
U. S. Army Test and Evaluation Command
Attn: AMSTE-BAF
Aberdeen Proving Ground, Maryland 21005

Office of Chief Communications - Electronics (1)
Department of the Army
Attn: Electronics Systems Directorate
Washington, D. C. 20315

Chief of Naval Operations (1)
Department of the Navy
Attn: Code 427
Washington, D. C. 20350

Director (1)
Bureau of Research and Development
Federal Aviation Agency
Washington, D. C. 20553

Director of Meteorological Systems (1)
Office of Applications (FM)
National Aeronautics and Space Administration
Washington, D. C. 20546

Director (1)
Atmospheric Physics and Chemistry Laboratory
Environmental Science Services Administration
Boulder, Colorado

Andrew Morse (1)
Army Aeronautical Activity
Ames Research Center
Moffett Field, California 94035

Commanding Officer (2)
U. S. Army Cold Regions Research and Engineering Laboratories
Attn: Environmental Research Branch
Hanover, New Hampshire 03755

Mr. Ned L. Kragness (1)
U. S. Army Aviation Materiel Command
SMOSM-E
12th and Spruce Streets
Saint Louis, Missouri 63166

Commanding Officer, U. S. Army (1)
Artillery Combat Development Agency
Fort Sill, Oklahoma 73504

Commander, USAR Air Weather Service (MATS) (1)
Attn: AWSSS/TIPD
Scott Air Force Base, Illinois

Dr. John Bogusky (1)
7310 Cedardale Drive
Alexandria, Virginia 22308

Commanding General (1)
U. S. Army Combat Development Command
Attn: CDCMR-E
Fort Belvoir, Virginia 22060

Commanding General (1)
U. S. Army Munitions Command
Attn: AMSMU-RE-R
Dover, New Jersey 07801

Commanding Officer (1)
U. S. Army Ballistics Research Laboratories
Attn: AMXBR-B
Aberdeen Proving Ground, Maryland 21005

Director (2)
Atmospheric Sciences Laboratory
U. S. Army Electronics Command
Fort Monmouth, New Jersey 07703

Chief, Atmospheric Sciences Office (2)
Atmospheric Sciences Laboratory
U. S. Army Electronics Command
White Sands Missile Range, New Mexico 88002

Commanding Officer (1)
U. S. Army Picatinny Arsenal
Attn: SMUPA-TV-3
Dover, New Jersey 07801

Commanding Officer (1)
U. S. Army Communications - Electronics Combat Development Agency
Fort Monmouth, New Jersey 07703

Commanding General (1)
Deseret Test Center
Attn: Design and Analysis Division
Fort Douglas, Utah 84113

Commandant (1)
U. S. Army CBR School Micrometeorological Section
Fort McClellan, Alabama 36205

Assistant Chief of Staff for Intelligence (1)
Department of the Army
Attn: ACSI-DERSI
Washington, D. C. 20310

Officer in Charge (1)
U. S. Naval Weather Research Facility
U. S. Naval Air Station, Building 4-28
Norfolk, Virginia 23500

Chief, Fallout Studies Branch (1)
Division of Biology and Medicine
Atomic Energy Commission
Washington, D. C. 20545

Director (1)
U. S. Weather Bureau
Attn: Librarian
Washington, D. C. 20235

Dr. Albert Miller (1)
Department of Meteorology
San Jose State College
San Jose, California 95114

Mrs. Francis L. Wheedon (1)
Army Research Office
3045 Columbia Pike
Arlington, Virginia 22201

Commander (1)
Air Force Cambridge Research Laboratories
Attn: CRXL
L. G. Hanscom Field
Bedford, Massachusetts

Harry Moses, Asso. Meteorologist (1)
Radiological Physics Division
Argonne National Laboratory
9700 S. Cass Avenue
Argonne, Illinois 60440

Defense Documentation Center (20)
Cameron Station
Alexandria, Virginia 22314

Office of U. S. Naval Weather Service (1)
U. S. Naval Air Station
Washington, D. C. 20390

Dr. Gerald Gill (1)
University of Michigan
Ann Arbor, Michigan 48103